



**HAL**  
open science

# Valorisation du phosphore des eaux usées des petites stations d'épuration rurales par apatite : détermination des processus pour préciser les dimensionnements des réacteurs

Laura Delgado-González

## ► To cite this version:

Laura Delgado-González. Valorisation du phosphore des eaux usées des petites stations d'épuration rurales par apatite : détermination des processus pour préciser les dimensionnements des réacteurs. Chemical engineering. Université de Lyon, 2020. English. NNT : 2020LYSE1297 . tel-03934652

**HAL Id: tel-03934652**

**<https://theses.hal.science/tel-03934652>**

Submitted on 11 Jan 2023

**HAL** is a multi-disciplinary open access archive for the deposit and dissemination of scientific research documents, whether they are published or not. The documents may come from teaching and research institutions in France or abroad, or from public or private research centers.

L'archive ouverte pluridisciplinaire **HAL**, est destinée au dépôt et à la diffusion de documents scientifiques de niveau recherche, publiés ou non, émanant des établissements d'enseignement et de recherche français ou étrangers, des laboratoires publics ou privés.



N°d'ordre NNT : 2020LYSE1297

## **THESE de DOCTORAT DE L'UNIVERSITE DE LYON**

opérée au sein de  
**l'Université Claude Bernard Lyon 1**

**Ecole Doctorale N° 206**  
**École Doctorale de Chimie de Lyon**

**Spécialité de doctorat** : Génie de procédés  
**Discipline** : Procédés

Soutenue à huis clos le 16/12/2020, par :

**Laura DELGADO-GONZÁLEZ**

---

**Phosphorus valorisation from wastewater of  
small rural wastewater treatment plants by  
apatite: focus on reaction processes to define  
reactors design**

**« Valorisation du phosphore des eaux usées des  
petites stations d'épuration rurales par apatite:  
détermination des processus pour préciser les  
dimensionnements des réacteurs »**

---

Devant le jury composé de :

Arias, C.A.	Professeur, Aarhus University (Danemark)	Rapporteur
Sperandio, M.P	Professeur, INSA de Toulouse (France)	Rapporteur
Dotro, G	PhD, Cranfield University (UK)	Examinatrice
Léonard. D	Professeur, Université de Lyon 1 (France)	Examinateur
Soric, A.	HDR, École Centrale de Marseille (France)	Examinatrice
Molle, P.	Directeur de Recherche, INRAE (France)	Directeur de thèse
Gautier, M.	Maître de conférence, INSA de Lyon (France)	Invité
Troesch, S.	PhD, Responsable R&D Ecobird (France)	Invité



## Résumé

La récupération de phosphore des eaux usées est une problématique importante qui doit être abordée pour éviter l'épuisement de ressources naturelles et l'eutrophisation des milieux aquatiques. C'est aussi un cadre prévu par la normalisation européenne relative au traitement des eaux usées dont l'élimination de phosphore dans les stations d'épuration de plus de 10 000 équivalents-habitants. En France, les réglementations nationales et locales prévoient aussi l'application de limites de rejet contraignants sur le paramètre phosphore pour les petites stations déversant ses eaux en zones sensibles à l'eutrophisation. Les petites stations d'épuration nécessitent des technologies robustes avec peu de maintenance telles que les filtres d'apatite. En France, un certain nombre de filtres d'apatite à échelle réelle ont déjà été mise en œuvre, par contre, le dimensionnement et ses caractéristiques opératoires n'ont pas été optimisés et certains dysfonctionnements sont apparus.

L'apatite est un substrat minéral capable de retenir le phosphore par des phénomènes de précipitation de phosphates de calcium. La composition très similaire entre le substrat et le précipité formé constitue un produit final approprié pour la valorisation de phosphore en tant que matière première pour la fabrication d'engrais. Néanmoins, la précipitation des phosphates de calcium dans les eaux usées implique la participation d'équilibres chimiques complexes qui ne sont pas encore entièrement compris. Ainsi, l'objectif scientifique poursuivi dans le cadre de ce travail de thèse est d'améliorer la compréhension des processus ayant lieu dans les filtres d'apatite. Cela comprend à la fois les performances de rétention et les cinétiques de réaction pour pouvoir fournir, dans un deuxième temps, un dimensionnement amélioré des filtres d'apatite à échelle réelle pour des stations rurales de petite taille.

Dans ce cadre, trois matériaux apatitiques différents ont été étudiés. Le premier matériau consiste en une apatite granulée commercialisée et installée sur une vingtaine de filtres en taille réelle en France depuis 2012. Des retours d'expérience sur ces filtres au préalable à la thèse, montraient des performances très basses et inattendues. Il était donc nécessaire d'établir les causes du dysfonctionnement de ces filtres d'apatite granulée. Cette évaluation a été menée à deux échelles différentes : (1) un retour d'expérience par la réalisation des campagnes intensives sur une sélection de filtres en taille réelle, et (2) par l'expérimentation au laboratoire sur des

colonnes en conditions contrôlées. Les mauvaises performances des apatites granulées pour la rétention de phosphore sur le long terme ont été confirmées. Le produit semble se comporter comme un matériau adsorbent ne permettant pas de déclencher de processus de rétention pérenne.

En conséquence, différents types d'apatites naturelles ont été aussi étudiées comme alternative à l'apatite granulée. La bonne performance de rétention des apatites naturelles avait déjà été mis en évidence par des études préalables. Cependant, des précisions sur les processus ayant lieu et les conditions opérationnelles étaient nécessaires notamment si on considère la variabilité de la composition et les caractéristiques des apatites naturelles en fonction de son origine.

Les apatites naturelles ont donc été testées en colonnes de laboratoire avec des résultats cette fois-ci prometteurs. Les apatites naturelles ont été capables d'initier une rétention de phosphore sur le long terme, en montrant des constantes cinétiques fortes avec de performances de rétention au-dessus de 80% pour des niveaux de rétention assez importants (jusqu'à 17.5 g PO<sub>4</sub>-P/kg matériau). En conséquence, plusieurs dimensionnements ont été ici proposés de manière à pouvoir assurer un rejet respectant le seuil réglementaire pendant 30 ans de vie du filtre.

## Summary

Phosphorus recovery from wastewater is important to reduce sources depletion and eutrophication of natural environments. It is also mandatory according to the European regulation to implement wastewater treatments aiming phosphorus removal, particularly in those greater than 10,000 population-equivalent. In France, small wastewater treatment plants discharging their treated wastewater into sensitive zones to eutrophication are also affected by national and local regulations concerning phosphorus discharge limits. These wastewater treatment plants need robust technologies with low-maintenance requirements such as apatite filters. Some of these full-scale filters already exist in France but their design and operation is not optimised.

The apatite is a reactive mineral able to retain phosphorus onto its surface as calcium phosphate precipitates. The close composition between the reactive substrate and the precipitate would make the resulting product a suitable source for its valorisation in fertilizers production. However, calcium phosphate precipitation in a wastewater solvent involves complex equilibria that are not yet fully understood. Thus, the scientific objective of this thesis work was to enhance the comprehension of phosphorus retention processes taking place in apatite filters, including the assessment of performances and reaction kinetics, in order to provide a better design of full-scale apatite filters for small rural wastewater treatment plants.

In order to achieve these objectives, three different apatite materials were studied. The first apatite material consisted of a manufactured granulated apatite which was commercialised and used in twenty full-scale filters of France since 2012. The first results on these full-scale applications showed performances unexpectedly low considering the predictions based on their design. It was, therefore, necessary to identify the causes leading to the dysfunctions of the granulated apatite filters. The assessment of the granulated apatite as a filtering material was carried out using two different strategies: (1) the implementation of field campaigns on a selection of full-scale filters and (2) the implementation of experiments in fixed-bed laboratory columns to study the processes taking place under controlled conditions. The results of this study confirmed the unsuitability of the granulated apatite for long-term phosphorus retention. The product behaved more as an adsorbent-like material resulting in low long-term performances.

The second and third materials were natural apatites meant to become an alternative to granulated apatite. The suitability of natural apatites for phosphorus retention applications from wastewater was already highlighted in previous works. However, more detailed information about the processes and operational conditions required for the specific application were lacking, especially considering that the composition and characteristics of the natural apatite varies with the origin of the mineral.

The assessment of natural apatites was carried out by fixed-bed laboratory column experiments. The results, in this case, were very promising: natural apatites were able to initiate a long-term removal process providing high kinetic rate constants and high retention performances (>80%) for relatively high phosphorus retention capacities of the filter (up to 17.5 g P-PO<sub>4</sub> /kg material). Consequently, several designs of natural apatite filters were proposed, in order to provide phosphorus retention performances to meet discharging limits for a 30 year-period.

## Acknowledgements

Gracias a todas.os los que de cerca o de lejos han compartido conmigo esta gran aventura. Gracias a mi familia.

This work was supported by the French Water Agency Rhône-Méditerranée-Corse, the French Water Agency Adour- Garonne, Syntea and INRAE.

Ce travail a été financé par l'Agence de l'eau Rhône-Méditerranée-Corse, l'Agence de l'eau Adour- Garonne, Syntea et INRAE.

# Table of content

---

<b>Chapter 1. Literature Review: Introduction</b>	<b>1</b>
1.1. <i>Phosphorus a resource in depletion</i>	1
1.2. <i>Wastewater a new source of P in a circular economy context</i>	6
1.2.1. Phosphorus sources in municipal wastewater	8
1.2.2. Phosphorus forms in wastewater	9
1.3. <i>Phosphorus removal in WWTPs</i>	14
1.3.1. Phosphorus Removal in Small WWTPs	19
1.3.2. Specific reactive materials for phosphorus retention	21
1.4. <i>Phosphorus retention by apatite filters</i>	22
1.4.1. Apatite	25
1.4.2. Reaction rate models	27
1.5. <i>Chapter conclusions</i>	29
1.6. <i>General objectives</i>	31
<b>Chapter 2. Literature Review: Surface reactions</b>	<b>33</b>
2.1. <i>Introduction</i>	33
2.2. <i>Adsorption</i>	33
2.2.1. Sorption types	37
2.2.2. The interface structure.	38
2.2.3. Adsorption mechanisms	41
2.2.4. Kinetics of sorption	43
2.2.5. Sorption isotherms.	44
2.2.6. Sorption thermodynamics	48
2.2.7. Fix-bed sorption models	49
2.2.8. Data analyses	56
2.2.9. Adsorption onto apatite	56
2.3. <i>Surface precipitation</i>	59
2.3.1. Mechanisms of nucleation and crystal growth	62
2.3.2. Thermodynamics of precipitation	68
2.3.3. Kinetics of precipitation	71
2.3.4. Calcium phosphate precipitation onto apatite	77
2.3.5. Parameters influencing phosphate precipitation onto apatite	86
2.4. <i>Chapter conclusions</i>	88
<b>Chapter 3. Materials &amp; Methods</b>	<b>89</b>
3.1. <i>Introduction</i>	89
3.1.1. Analytical techniques	89
3.1.2. Analytical techniques for solid sample characterisation	89
3.1.3. Analytical techniques for liquid samples	95
3.2. <i>Substrate characterisation</i>	96
3.2.1. Substrates	96
3.2.2. Experimental methodology for substrates characterisation	98
3.2.3. Characterisation of the filtering bed	103

3.3.	<i>Column experiments</i>	109
3.3.1.	Experimental setup	109
3.3.2.	Inlet solution	111
3.3.3.	Granulated apatite columns	112
3.3.4.	Natural apatite columns	113
3.3.5.	Chemical analyses and monitoring	115
3.3.6.	Kinetic studies	115
3.3.7.	Tracer tests	117
3.4.	<i>Field campaigns</i>	118
3.4.1.	Full-scale filters	118
3.4.2.	Measurement campaigns	127
<b>Chapter 4.</b>	<b>Results and discussion: Granulated apatite</b>	<b>131</b>
4.1.	<i>Context and objectives</i>	131
4.2.	<i>Article 1. Field campaigns</i>	132
4.2.1.	Introduction	134
4.2.2.	Materials and Methods	136
4.2.3.	Results and discussion	145
4.2.4.	Conclusions	159
4.2.5.	Supplementary information	160
4.3.	<i>Article 2. Granulated Apatite laboratory columns</i>	171
4.3.1.	Introduction	173
4.3.2.	Material & Methods	175
4.3.3.	Results and discussion	179
4.3.4.	Conclusions	189
4.3.5.	Supplementary Information	191
4.4.	<i>Chapter Conclusions</i>	197
<b>Chapter 5.</b>	<b>Results and discussion: Natural apatite</b>	<b>198</b>
5.1.	<i>Context and objectives</i>	198
5.2.	<i>Article 3. Natural Apatite laboratory columns</i>	200
5.2.1.	Introduction	201
5.2.2.	Materials and methods	203
5.2.3.	Results and discussion	210
5.2.4.	Conclusions	222
5.2.5.	Supplementary information	224
5.3.	<i>Article 4. Modelling</i>	232
5.3.1.	Introduction	233
5.3.2.	Material and methods	234
5.3.3.	Results and discussion	239
5.3.4.	Conclusions	246
5.3.5.	Supplementary Information	247
5.4.	<i>Chapter conclusions</i>	248
	<b>Final discussion, conclusions and perspectives</b>	<b>249</b>
	<b>References</b>	<b>261</b>
	<b>Communications</b>	<b>284</b>

# Chapter 1. Literature Review: Introduction

---

## 1.1. Phosphorus a resource in depletion

Phosphorus (P) is an essential element that participates in biological functions of animals and plants. It can be found in cells, blood, bones and teeth, but also in dissolved or suspended forms in water and in the lithosphere as part of soil and rocks. These phosphate rocks are called fossil phosphorites and represent 95% of the P contained in the Earth's crust (Ateeq 2016). Phosphorites might be igneous or magmatic when they originate by thermal processes on the Earth's crust, or sedimentary when they have a biogenic origin. The biogenic fossil P forms by the accumulation of residues from living organisms on the crusts and nodules of the continental shelves which takes place in marine environment over millions of years (Reijnders 2014).

The natural global phosphorus cycle begins with the mechanical abrasion or the chemical dissolution of phosphate rocks. This dissolved P enters the food chain via its incorporation by living organisms. The decomposition of the organic matter (OM) restore P to soil, which is then released to water bodies by erosion (runoff, leaching, mineralisation, weathering). Dissolved and particulate P are transported along the rivers ending up on the coastal sedimentary deposits of the oceans, regenerating P rocks and completing the cycle over thousands of years (Andrieux-Loyer 1997).

Because of the low solubility of mineral P, the dissolved P is a limiting nutrient to the aquatic biota, other microorganisms and plants. In 1845, transformed fossil phosphorites were commercialised for first time as fertilizers in England leading to what was called the "green revolution". Fertilizers were able to supply a surplus of P to soils that increased cropland's productivity. Thus, the demand for fertilizers shot-up over the years leading to a dramatic growth on the production and industrialization of agriculture, more notably in Western Europe and the United States (Reijnders 2014). In 2019, global consumption of fossil phosphorite was estimated to be of 47million tons

as phosphorus pentoxide ( $P_2O_5$ ) (U.S.G.S 2020). Thus, phosphorus has become an important part of the global economy and a requirement for food security worldwide.

Although major application of fossil phosphorites involves fertilizers production (around 85%, Cordell and White (2013)), other minor applications also exist. P is used to produce phosphoric acid, detergents, surfactants, pesticides, food-additives, chelators, pharmaceuticals, metal coatings and paint ingredients, electronics, high functional-plastics, among others (Reijnders 2014).

The main source for phosphorus production is, however, a non-renewable resource at the human time-scale unevenly distributed around the globe. U.S.G.S (2020) has estimated that phosphate rocks reserves<sup>1</sup> were 69,000 million tons in 2019 with a 72% of them localised in Morocco and Western Sahara (Fig.1. 1). Two factors may be worth mentioning at this point: reserves estimations and reserves management. On one hand, remaining reserves estimations are subject to a great variability and uncertainty (Reijnders 2014). Because of the dynamism of available data, predictions evolve with time and differ among authors. Data may depend on the feasibility of the extraction, the discovery of new reserves, the demand/supply rate, as well as, the emergence of new technologies or economic variables that may improve their economic feasibility, among others. These results in estimations of remaining reserves that differ widely between them (confer. Reijnders (2014)) setting up a high level of uncertainty around food security. In addition, consumption of fertilizers is expected to continue growing in the following years in accordance with the growing demand of developing countries or regions as India or South America, which may accelerate P depletion.

---

<sup>1</sup> That part of the reserve base which could be economically extracted or produced at the time of determination. The term reserves need not signify that extraction facilities are in place and operative. Reserves include only recoverable materials U.S.G.S (2020). MINERAL COMMODITY SUMMARIES, U.S Geological Survey..

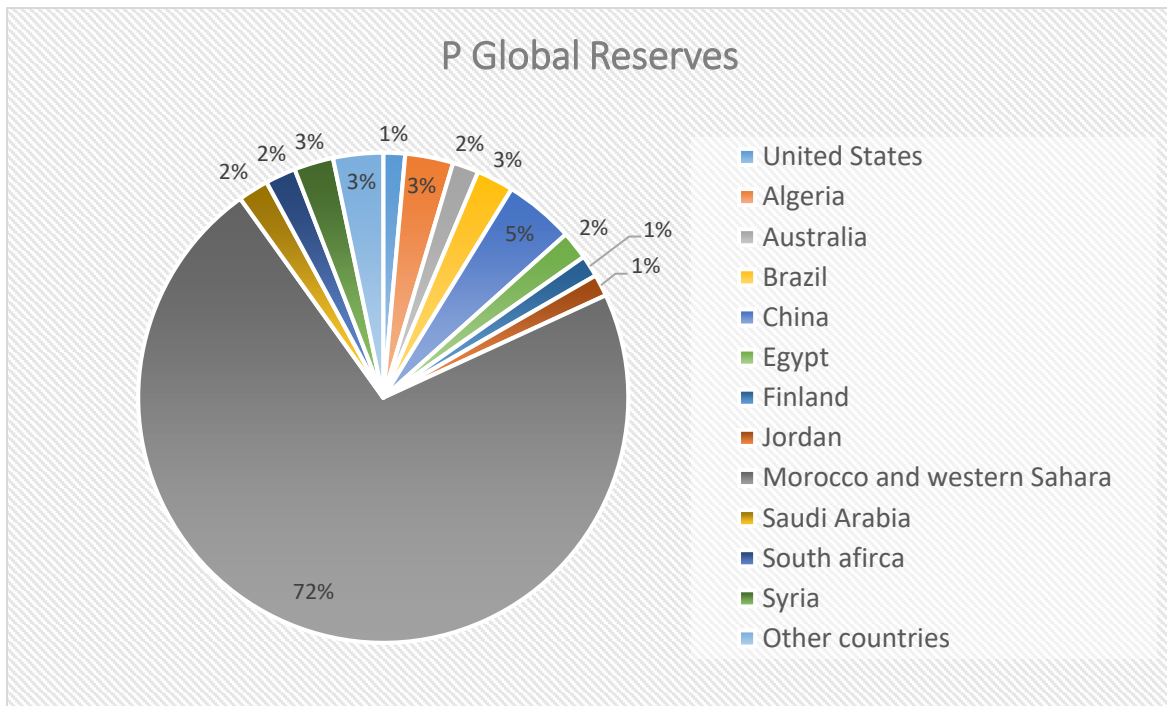


Fig.1. 1. Geographic distribution of estimated remaining global reserves of fossil phosphorites in 2019 (U.S.G.S 2020).

On the other hand, as supply is restricted to several producer countries it may be subjected to geopolitical issues like export policies, war, political instability, etc. which may affect the price or P availability. Consequently, net import countries and regions as Europe have an interest in reducing the demand for fossil phosphorite, and to find new ways of ensure a P supply to agriculture.

In the global food system, P “cycle” begins at the phosphate rock mine where fossil phosphorite is mined, clean and transferred to be processed in the fertilizer industry. The fertilizer is applied to soil in croplands where a fraction of P is taken up by plants and livestock, whilst the reminder P is stored in the soil or transferred to water bodies by erosion. Crops and animals enter the food sector to be transformed and then transferred to the final consumer. P contained in the residues of the food industry usually ends-up as organic waste which is in some cases spread out across landfills, used for compost making or incinerated. The P consumed by humans, on the other hand, continues the cycle in the sewage system as urine and faeces, or in greywater. The wastewater follows some kind of treatment at the Wastewater Treatment plants (WWTPs), but most P still ends-up in oceans, rivers or lakes (Cordell and White 2013).

The rate of production of P residues is far higher than the rate of the regeneration of the phosphate rock, as a consequence, the P cycle is completely linearized.

Despite reserves may not be depleted in the immediate future, researchers agree that a new management strategy needs to be globally applied to de-linearize the phosphorus “cycle” at the human-time scale. In addition, the global food system has shown to be extremely inefficient regarding P. Just one-fifth of mined P-fossils intended for the food sector, are ultimately consumed by the global population (Cordell and White 2013). The substrate is lost and misuse at all levels of its economic lifecycle. P losses include from mining and fertilizer production through food processing, distribution and consumption, to wastewater treatment. Agriculture is, for instance, a major contributor to these losses: soil erosion; run-off; leaching from manure; P sequestration by the soil (P is tightly bound or fixed to other compounds and thus, not bioavailable for crops); overdose of fertilizers to land beyond crop’s requirements; as well as, the incomplete recycling of P residues from crops, harvested crops and manure (Cordell and White 2013, Reijnders 2014). Moreover, a largest fraction of this lost P ends up in water bodies sensitive to eutrophication, as rivers, lakes and groundwater, causing the degradation of aquatic and terrestrial ecosystems.

Preventive measures as international policies and monitoring frameworks are needed in order to: (1) optimize the global P system by reducing the P use to the fundamentals, and by improving the efficiency at all levels of the production system; (2) to reduce dependency on primary P sources (eg. Fossil phosphorites), especially in net import countries, by implementing P recycling strategies for solid waste and wastewater (secondary resources), and (3) to reduce the environmental impact that will ultimately affect food availability. These measures aimed to achieve a sustainable management of this resource to meet long-term food security. Cordell and White (2013) presented an illustrative example of how a set of sustainable measures will help to cope with the predicted increasing demand for P in the food system after achieving the phosphorus peak (Fig.1.2).

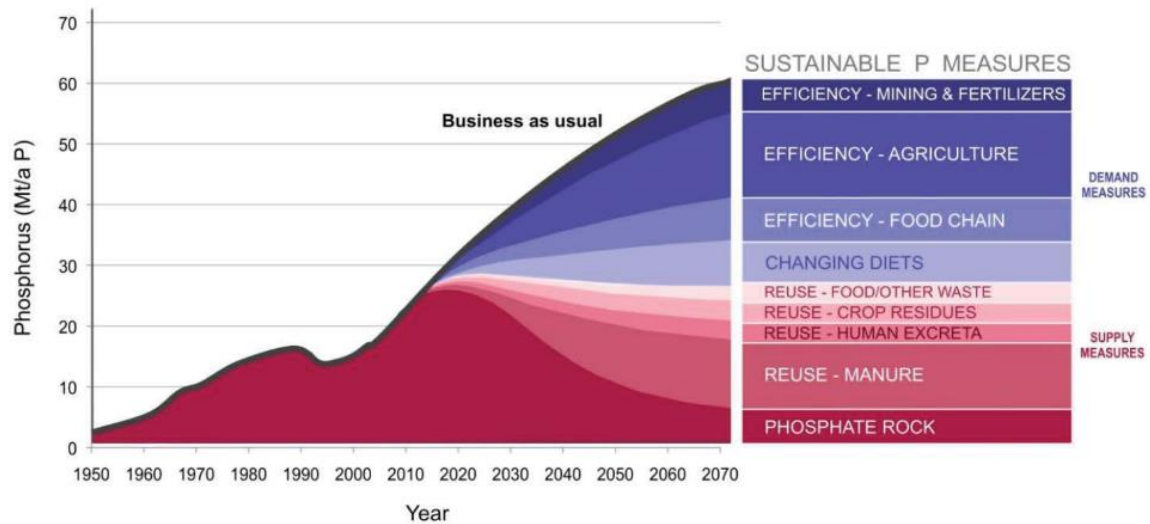


Fig.1. 2. Sustainable phosphorus supply and demand measures for meeting long-term future global food demand (Cordell and White 2013).

From observing Fig.1. 2, it may be noticed that P recycling from wastewater comprises just a small fraction of the total set of required measures; however, in absolute terms this fraction must not be neglected. Of all P consumed by humans just 1% is retained by the global population, whilst the remaining ends up in the sewage system (Reijnders 2014). From a global perspective, human excreta (urine and faeces) generates a significant amount of P per year. Around 3.0 - 3.3 million tons of P may potentially be recovered and reuse, or otherwise lost by the sinking effect of the oceans (Mihelcic et al. 2011). In France, for example, P discharges into the environment from treated wastewater have been estimated in 10,600 tons per year by French Water Agencies in 2012 (Senthilkumar et al. 2014). Nevertheless, if recovered from municipal wastewater, this secondary P source may account from 15 to 22% of the global annual demand for phosphate rocks (Yuan et al. 2012, Science Communication Unit UWE 2013).

Phosphorus discharges into the environment have also environmental repercussions from a local point of view. As P is a limiting nutrient for living organisms, a localised enrichment of the P content of surface waters may leads to an increase of the biological activity for certain species like algae. Algae blooms increase the turbidity of water and cause oxygen content depletion, which results in an increase of aquatic animals' mortality, the impoverishment of the water quality and, in severe cases, the degradation of a whole ecosystem. This nutrient enrichment of water bodies is known

as eutrophication and it may appear at dissolved P contents as low as 10 µg/L in sensitive zones (Ateeq 2016). In all possible future scenarios estimated by van Puijenbroek et al. (2019) global nutrient discharges into surface water will continue to increase. This increase will be mostly caused by an increasing number of inhabitants connected to the sanitation systems in developing countries. Therefore, control measures for eutrophication will demand the implementation of phosphorus removal processes, at least by biological nutrient removal processes, in a near future for all WWTPs.

## 1.2. Wastewater a new source of P in a circular economy context

Since 2000, with the implementation of the European Water Framework Directive (2000/60/EC, OJ L 327), wastewater treatment conception must include an environmental strategy to ensure a “good ecological status” for all waters. New objectives were set to limit the impact of treated wastewater discharges on ecosystems with special attention on nitrogen and phosphorus pollution as major factors favouring eutrophication. Therefore, in the past few decades, sanitation systems have focused on two principal aspects: disease prevention and eutrophication control. In most cases in Europe and other developed regions, wastewater enters the WWTP via a sewer collection system to follow some sort of treatment in order to eliminate pollutants and pathogens. Then, large volumes of potentially valuable diluted pollutants from treated wastewater are discharged and wasted into natural water bodies (Mihelcic et al. 2011). This sanitation system conception appears to be poorly optimized for a world living on credit regarding natural resources. As a consequence, research and engineering address today the transition from wastewater treatment for nutrient removal to wastewater treatment for nutrient recycling and valorisation (Roy 2017). That is, WWTPs are facing the challenge to become Water Resource Recovery Facilities (WRRFs).

Regarding P, a closed-loop approach in wastewater treatments would mean recovering P mainly from urine and faeces to be reused as fertilizer or for fertilizer production. This turns wastewater into a major secondary source for P recovery (Wilfert

et al. 2015). Three strategies are currently being discussed to confront the resource recovery challenge: separation at source, water reuse (fertigation) and resource recovery from sewage systems. The separation at source has great potential since it allows higher concentrations of potentially recovering compounds, which would facilitate the process and increase their efficiency. Nevertheless, this strategy would demand a significant investment to adapt infrastructures in developed countries that already have sewage collectors and a functional sanitation system (Melia et al. 2017). It is, however, an interesting option to assess in developing countries, especially in Africa and Eastern and Southern Asia (Chrispim et al. 2019).

In WWTPs, phosphorus may be recovered from the liquid phase or from the solid phase, as sludge or ashes. Phosphorus recovering technologies from the liquid phase (sludge dewatering liquor and clarified water) were found to be less efficient regarding those from the solid phase (Amann et al. 2018). In contrast, it showed low impacts on emissions and energy demand. The greatest recycling rates were found, however, in sewage sludge ashes (Amann et al. 2018) but such technology is economically feasible just in large WWTPs (Cieřlik and Konieczka 2017). It is worth noting that circularisation of secondary sources like phosphorus does not yet always guarantee a lower environmental impact compared with the current linearized cycle (Amann et al. 2018). For instance, Chrispim et al. (2019) found that the production of sludge-based fertilizers with current technologies has a higher environmental impact than those produced from phosphate rocks because of a higher energy and reactant demand. Thus, a life cycle assessment taking also into account the economic and political context would be appropriate before deciding about the adequacy of a specific P recovery technology for a specific situation, country, or region.

Despite phosphorus recovery still needs to overcome a number of issues (Chrispim et al. 2019), recovery-oriented strategies driven by environmental, economic and geopolitical motivations, push scientific efforts to continue moving in that direction. It will then require the harmonization of policies of the market regulation, as well as, health and environmental protection laws, with the recovery objectives. Despite the interest shown by the European Union in the circularisation of the economy, it is still necessary to build up a regulation framework for the use of recovered phosphorus from wastewater as fertilizers giving it the end-of-waste status for each particular case (Hukari et al. 2016). For instance, the use of secondary sources like struvite or ashes

lack of regulation in Europe despite its proven efficacy for fertilization. Indeed, the use of secondary sources as fertilizers in croplands is not an easy subject because of the environmental and sanitation risk that may accompany this practice. In Europe, some countries have already forbidden the direct application of sludge for agricultural purposes because of the presence of heavy metals, micropollutants and pathogens (Egle et al. 2016, Scholz 2019).

### 1.2.1. Phosphorus sources in municipal wastewater

Total phosphorus (TP) concentration in wastewater normally ranges from 3 to 15 mg TP/L depending on the characteristics of the source (rural or urban areas and their economic activity) and the type of collection system used (combined or separate municipal and storm event) (Senthilkumar et al. 2014), although it will rarely exceed 10 mg P/L (Yuan et al. 2012). For instance, when considering urban wastewater, P content will more likely vary from 6 to 10 mg TP/L (Prochaska and Zouboulis 2006). However, greater variations on TP concentrations can be expected when considering small WWTPs. A study over WWTPs of less than 2000 PE in France reported a mean TP concentration of 9.4 mg P/L in a range of 2.0 to 18.4 (min – max) (Mercoiret 2010).

In terms of specific load, a French survey developed over 247 municipal WWTPs of France in 2007, revealed values of 2.3 g P/d/PE for pure domestic and rural wastewater, and of 2.0 g P/d/PE for urban wastewater. These estimations took into consideration the economic activities of the municipality, which may explain the differences in the results: the P/BOD<sub>5</sub> ratio decreases as the economic activity of the urban area increases, that is, the effluent is more diluted and less charged with organic wastes. The average annual specific P load discharge was therefore estimated in 2.1 g P/d/PE (Stricker and Héduit 2010), and it will be here retained as reference value for design purposes.

There are two main sources of P pollution in domestic wastewater: the human metabolic disposal (faeces and urines) and grey water, which includes phosphorus compounds from detergents and cooking wastes (Table 1.1). This latest contribution to P load has been reduced in the past few decades accordingly to the implementation of regulatory measures banning in particular the use of phosphate-based products in

laundry detergents and automatic dishwasher detergents (Regulation (EC) No 648/2004 (OJ L 104, 8.4.2004); Regulation (EU) No 259/2012 (OJ L 94, 30.3.2012)). However, as shown in Table 1.1 the greatest contribution to the total P load in domestic wastewater effluents derived from metabolic wastes, and thereby a zero P disposal will never be achievable.

Table 1. 1. Daily phosphorus loads contribution per inhabitant classified by source (Kim 2014)

	Black water		Grey water	
	Human metabolic wastes: urine and faeces	Textile detergents and softeners	Dishwasher detergents	Other liquids and wastes from cooking
<b>Daily load</b>	1.2-1.6 g P/inhab/day (it depends on age, genre, diet, medicine and vitamins intake)	0.1 g P/inhab/day (since 2007, Decree n° 2007-491 du mars 2007)	0.2 g P/inhab/day	0.2 g P/inhab/day

### 1.2.2. Phosphorus forms in wastewater

In wastewater, P is classified depending on three major characteristics: (1) size, (2) nature and (3) reactivity (Ateeq 2016) (see Fig.1.3).

In terms of size, two forms can be differentiated, dissolved P and particulate P.

- The **Dissolved fraction** (D) of the total phosphorus, also called soluble fraction, is the one that can pass through a 0.45 µm membrane.
- The **particulate fraction** (p), also called the suspended fraction, is the difference between total phosphorus and the dissolved fraction. It comprises phosphorus particles and phosphorus attached to suspended particles in the water column.

It must be noticed that the composition of dissolved and particulate phosphorus may change according to a dynamic equilibrium:  $P_{\text{dissolved}} \leftrightarrow P_{\text{particulate}}$  (Spivakov et al. 1999).

P can be also classified as mineral or inorganic P and organic P.

- **Organic Phosphorus (OP)** are molecules containing C-O-P and C-P bonds.
- The **Inorganic Phosphorus (IP)** is not associated with any organic molecule. It may be found dissolved as orthophosphates and polyphosphates, or as phosphate mineral particles.

Last category comprises reactivity to some chemical analyses involving colorimetric or specific digestion methods. On that basis, either particulate or soluble, and organic or inorganic compounds can be **Reactive Phosphorus (RP)** or **Non-Reactive Phosphorus (NRP)**. It will be considered as reactive phosphorus if its direct quantification by chemical analyses do not require carrying out a previous oxidation or hydrolysis reaction. Although NRP typically makes up only a small fraction of influent wastewater TP (1–10%), NRP (sNRP in particular) can lead to failures in meeting very low regulatory effluent standards (Venkiteshwaran et al. 2018) for WWTPs.

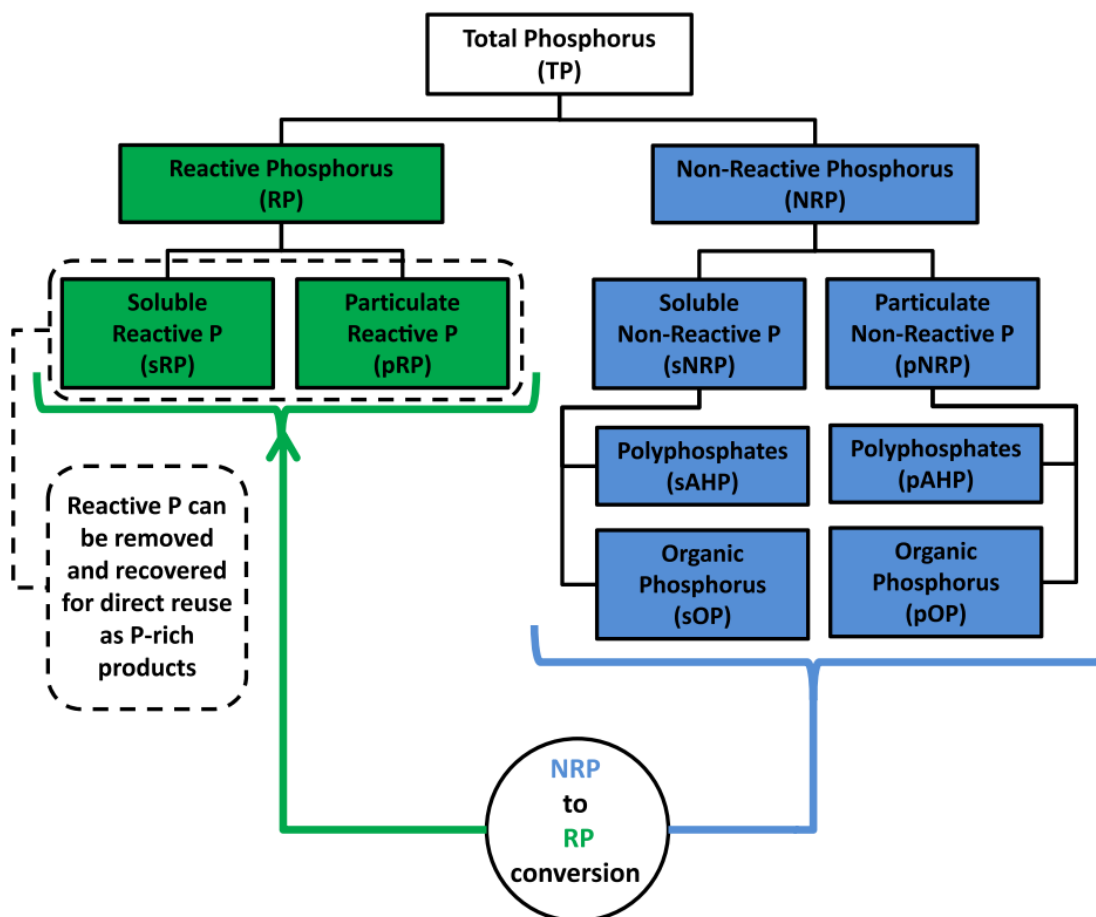
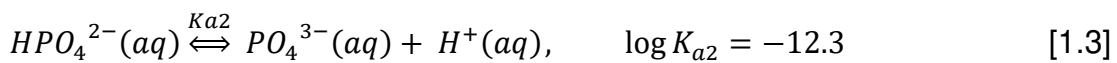
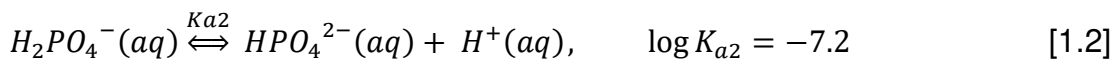
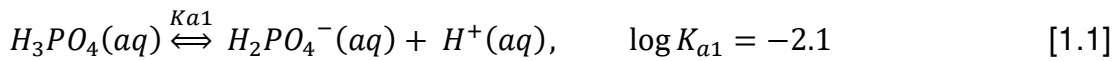


Fig.1. 3. Scheme of the forms of phosphorus found in water. From Venkiteshwaran et al. (2018)

**Soluble Reactive Phosphorus (sRP):** Also called dissolved reactive phosphorus (DRP), this fraction is mostly composed by orthophosphates in all its protonated or deprotonated forms ( $H_3PO_4$ ;  $H_2PO_4^-$ ;  $HPO_4^{2-}$ ;  $PO_4^{3-}$ ) since its speciation is pH dependant (Eq.1.1 , Eq.1.1 and Eq.1.3; Kim (2014)). Considering typical pH values in wastewater ( $5.0 < \text{pH} < 9.0$ ), the predominant species would normally be mono and dibasic phosphates.



In wastewater, orthophosphates are produced through the enzymatic hydrolysis of polyphosphates (Fig.1.4), as well as, of particulate and dissolved organic molecules (bacterial decomposition or mineralization). They may also be released from the solid fraction (minerals) by a modification of the physico-chemical properties of the water as pH (acid environment) or redox potential (reducing environment) (Andrieux-Loyer 1997, Spivakov et al. 1999). Some soluble organic phosphorus components, which are readily hydrolysable, are also considered to be part of the DRP or sRP fraction (Kadlec and Wallace 2009). However, orthophosphates constitute the most abundant and immediately bioavailable fraction in raw wastewater (60 - 86%) (Kim 2014, Comber et al. 2015). They can also easily recombine in solution with metal ions, particularly with  $Fe^{3+}$ ,  $Al^{3+}$ ,  $Ca^{2+}$  and  $Mg^{2+}$ , forming phosphates and or complexes that adsorb phosphorus (Spivakov et al. 1999). Speciation of these inorganic forms depends on pH as shown in Fig.1.5. For pH values under 4, phosphate reacts predominantly with iron (Fe), although for more basic pH, P-Ca and P-Mg complexes will predominate (Molle 2003).

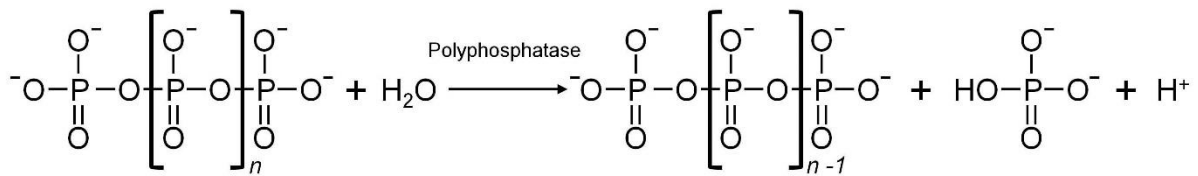


Fig.1. 4. Enzymatic hydrolysis reaction of a polyphosphate by polyphosphatase enzymes to produce phosphates.

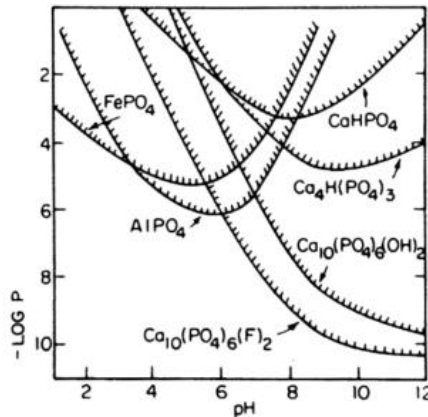


Fig.1. 5. Solubility diagrams of Al, Fe and Ca phosphates depending on pH (Stumm and Morgan 2013)

In the non-reactive category, one can find:

**Soluble Acid-Hydrolysable Phosphorus (sAHP):** These compounds are oxyanion esters, that is, inorganic polymers with P-O-P bonds made of orthophosphates. DAHP comprises linear and cyclic condensed phosphates like polyphosphates ( $\text{H}_{n+2}\text{P}_n\text{O}_{3n+1}$ ) or metaphosphates  $((\text{HPO}_3)_n)$  (Spivakov et al. 1999). This fraction is quantified by the chemical analyses of the orthophosphates formed after acid hydrolysis at  $100^\circ\text{C}$ , which breaks the P-O-P bonds. They are usually found in wastewater derived from additives for water retention in meat and cheese industry and from detergents due to their chelating power. A representative compound in this category is sodium triphosphate (STP) which is typically used for water softening (sequestration of  $\text{Mg}^{2+}$  and  $\text{Ca}^{2+}$  ions) (Kim 2014, Ateeq 2016).

**Dissolved/soluble Organic Phosphorus (DOP/sOP):** This fraction is constituted by molecules presenting C-P and C-O-P bonds, which convert to orthophosphates only under harsh digestion (oxidation processes). Most of DOP molecules come from the living beings by either urine and fecal excretions or from bacterial cell lysis.

Components in this category are organic soluble molecules as nucleic acids (DNA or RNA); molecules participating in the energy transfer at cellules like AMP, ADP and ATP (adenosine mono, di and triphosphate); phospholipids; phosphoproteins; and some known complexing agents (chelates) like phosphonates ( $C-PO(OR)_2$ ) and phytic acid (Andrieux-Loyer 1997, Kim 2014, Ateeq 2016). Phosphonates are refractory P-compounds that cannot be eliminated by conventional wastewater treatments. They are typically man-made products like herbicides (Glyphosate), bleach-containing detergents and pharmaceuticals (Ateeq 2016). On the other hand, the phytic acid is a molecule naturally present in some cereals, which can react with some metallic ions (Ca, Zn, Cu, Co, Mn, Fe) to form insoluble salts. For instance, calcium phytate is usually used to de-ironized the wine.

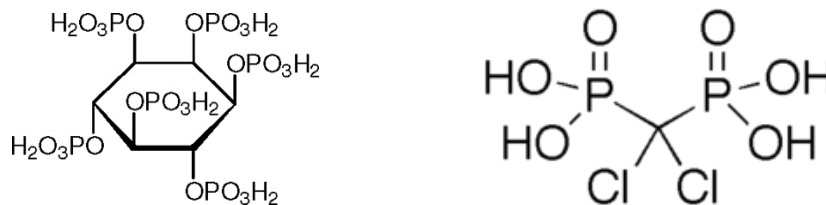


Fig.1. 6. a) molecular structure of phytic acid ( $C_6H_8O_{24}P_6$ ) (Egbuna and Ifemeje 2015); b) Chlondronic acid bisphosphonate, pharmaceutical drug to treat osteoporosis.

**Total Particulate Phosphorus (TPP).** This fraction comprises the phosphorus associated with suspended matter covering from true particle (visible by optical microscope) to colloidal matter as hydrated inorganic solids, large organic macromolecules or organic - inorganic complexes (Broberg and Persson 1988). It may be reactive or non-reactive phosphorus.

The organic fraction is constituted of cells of animals and plants, bacteria and the organic detritus from cell's degradation or fragmentation, this is, organic macromolecules that may flocculate forming aggregates. Another organic particulate component includes organic-inorganic coprecipitates or the inclusion of P by metal (Ca, Al, Fe, Mn) - phosphorus binding into organic aggregates (Broberg and Persson 1988).

The mineral fraction is made of phosphates that may precipitate in the presence of calcium and magnesium. The most common precipitates in wastewater are calcium

phosphates as hydroxyapatite ( $\text{Ca}_5(\text{PO}_4)_3\text{OH}$ ) and struvite ( $\text{NH}_4\text{MgPO}_4 \cdot 6\text{H}_2\text{O}$ ), although precipitation of phosphates of iron and aluminium is also possible. Phosphorus can also co-precipitate with some solid mineral phases such as ferric oxyhydroxide ( $\text{FeO}(\text{OH}) \cdot n\text{H}_2\text{O}$ , eg. monohydrated iron oxide  $\text{Fe}(\text{OH})_3 = \text{FeO}(\text{OH}) \cdot \text{H}_2\text{O}$ ), aluminium hydroxides (eg. Gibbsite,  $\text{Al}(\text{OH})_3$ ), aluminosilicates (eg. clays) or calcium carbonates (calcite,  $\text{CaCO}_3$ ), by adsorbing physically or chemically onto their surfaces (Andrieux-Loyer 1997, Kadlec and Wallace 2009).

The existence of colloids of particle-size lower than  $45 \mu\text{m}$  and the existing dynamic equilibria between particulate and dissolved components, can make it difficult to draw a clear line for PP and DP. For instance, Broberg and Persson (1988) pointed out that just cells can be easily considered as true particles whereas detritus and minerals can attain a very small particle-size sinking into the colloidal region. A schematic representation of the distribution of PP with size is shown in Fig.1.7.

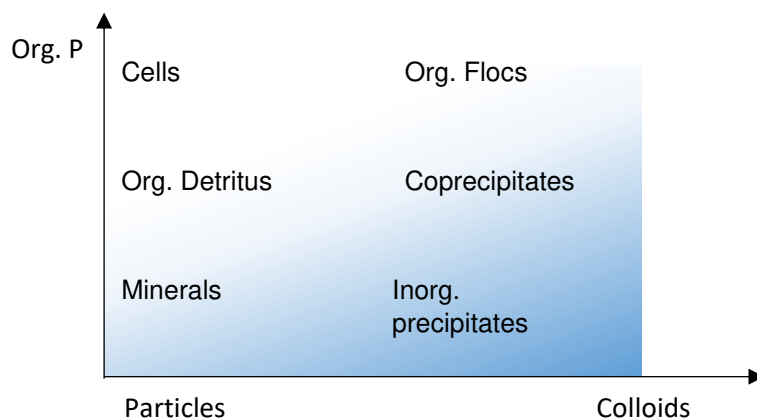


Fig.1. 7. Components of particulate phosphorus distributed as a function of size and nature. Adapted from Broberg and Persson (1988).

### 1.3. Phosphorus removal in WWTPs

Typical WWTP conception aims the removal of phosphorus in order to meet phosphorus emission thresholds. The national French regulation states P limits for large and very large WWTPs in the orders of 22<sup>nd</sup> June 2007 and 21<sup>st</sup> July 2015 in accordance with the European Directives 91/271/CEE and 2000/60/CEE concerning urban waste water treatment and the establishment of a Community water framework, respectively. The regional institutions and local authorities dictate the legislation concerning phosphorus for small and medium size WWTPs discharging treated

wastewater in sensitive zones to eutrophication. A new revised version of the French watershed considered as sensitive zones was requested by the government in 2019, and must be published during 2020<sup>2</sup>. Environmental concerns like the capacity for climate change resilience, the preservation of ecosystems and water quality or the urbanisation pressure, are driving forces leading to continuous extension of sensitive zones in the last decades. For instance, much of the metropolitan French territory is already considered as a sensitive zone (Fig.1. 8).

The regulation establishes annual averages of phosphorus discharge limits at 2 and 1 mg TP/L for all WWTPs between 10,000 p.e (excluded) and 100,000 p.e (included) and for WWTPs > 100,000 p.e, respectively. When WWTPs between 10,000 and 100,000 p.e are in sensitive zones TP removal performance must be at least of 80%. In small WWTPs, regulations on the maximum discharge threshold vary widely (eg. < 1.0 or > 4.0 mg TP/L) and there may be seasonal considerations to take into account. The supplementary treatment is increasingly important in small rural WWTPs to preserve surface water quality (Brix et al. 2001) and stringent discharge limits are expected to be demanded in the years to come (Shepherd et al. 2016, Ye et al. 2017).

---

<sup>2</sup> <https://www.actu-environnement.com/ae/news/revision-zones-sensibles-eutrophisation-stations-epuration-33594.php4>

## Annexe 4 Les zones sensibles

La liste des zones sensibles est disponible à l'adresse: <http://assainissement.developpement-durable.gouv.fr/services.php>

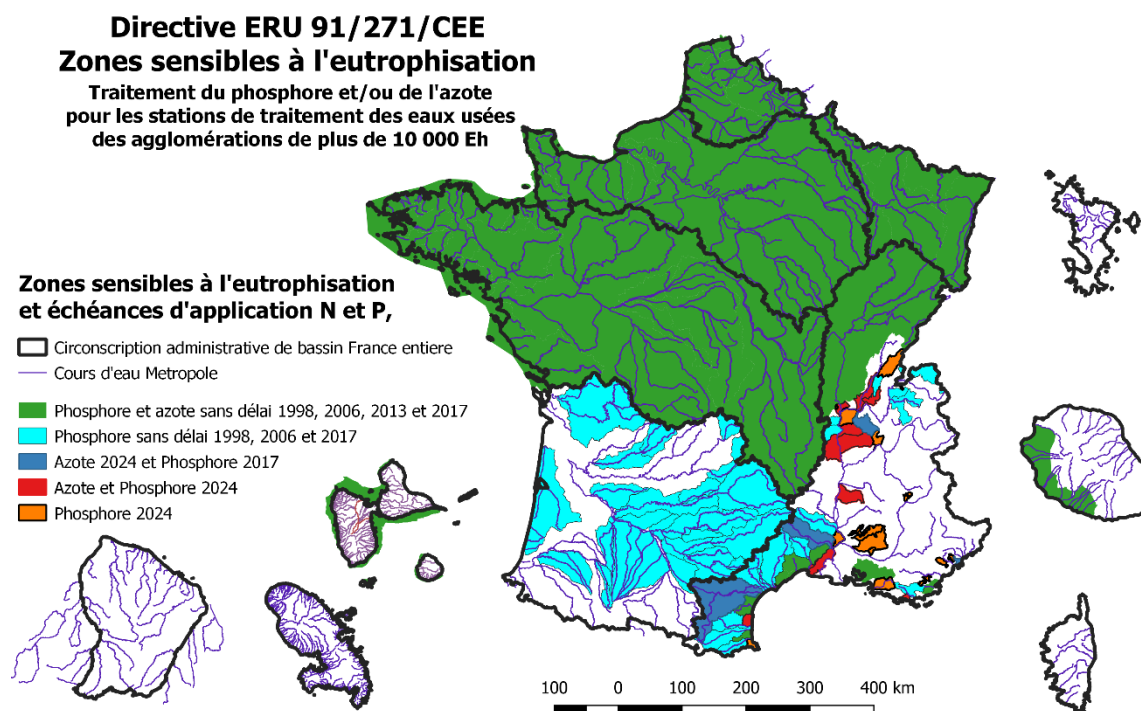


Fig.1. 8. Map of French watersheds declared as sensitive zones. Last update in 2017 with the addition of sensitive zones in the Rhone-Mediterranean region.

Conventional treatments for phosphorus removal may be physical operations, chemical and biological processes, or a combination of them. Physical operations like filtration or sedimentation are usually part of pre-treatment and primary treatment stages at the WWTP, which get rid of some of the particulate phosphorus fraction (mostly organic). It is then followed by biological processes relying on the incorporation of dissolved phosphorus by biomass, either for growth (bacteria, algae, plants) or for bioaccumulation as polyphosphates by specific bacteria (Bellier et al. 2006). In the first case, classical systems are activated sludge, biofilters, ponds or wetlands. However, when stringent P discharge conditions apply ( $< 2$  mg TP/L), the enhanced biological phosphorus removal (EBPR) system is a popular option (Wilfert et al. 2015). By including an anaerobic phase to the classical activated sludge system, microorganisms are exposed alternatively to aerobic and anaerobic stages that favours the growth of phosphorus accumulating organisms (PAOs). These bacteria metabolise polyphosphates increasing the amount of P cumulated in the biomass. Optionally, a chemical phosphorus removal (CPR) process may be applied. CPR is the precipitation

of P compounds that react to the addition of aluminium, iron and calcium salt (Table 1.2). CPR systems may be used at any stage of a conventional WWTP (even if its implementation at a final stage limits chemical consumption due to competition with organic matter) to enhance the phosphorus removal capacity of the plant. This process, however, entails an additional cost from the use of chemical reactants and increases the sludge production (Melia et al. 2017).

Table 1. 2. Characteristics of conventional metals used for phosphorus precipitation (CPR) in wastewater treatments. From Melia et al. (2017).

Element	Optimal pH	Most common precipitate	Advantages	Disadvantages
<b>Fe</b>	4.5 – 5.0	Strengite ( $\text{FePO}_4 \cdot 2\text{H}_2\text{O}$ )	Relative inexpensive	Precipitate unsuitable for use as fertilizer
			Effective in the precipitation of phosphorus	Expensive
<b>Al</b>	~ 6.0	Variscite ( $\text{AlPO}_4 \cdot 2\text{H}_2\text{O}$ )	Most effective precipitant	Precipitate unsuitable for use as fertilizer
			At pH 6, both biological and treatment and precipitation with Al could be operated	Toxic effect on biomass on doses over 60 mg/L
<b>Ca</b>	>10.5	Hydroxyapatite ( $\text{Ca}_5(\text{PO}_4)_3\text{OH}$ )	Relative inexpensive	High pH requirement which can cause detrimental conditions for biological treatment
			Similarities between precipitate and rock	Additional neutralisation step may be required
			Suitable for use in industry and potentially suitable as fertilizer	Large volume of generated sludge

When using either of both techniques, phosphorus is removed from the water line with the sludge. Sludge from EBPR process, or bio-P sludge, may be used after dewatering directly onto the agricultural land as a fertilizer. As good as conventional fertilizers, the accumulation of heavy metal and other chemicals and the potential biological contamination start to prevent its use. In some countries of Europe bio-P sludge fertilization is already forbidden (eg. Switzerland (Schoumans et al. 2015) or Germany except from rural WWTPs (Scholz 2019)). On the other hand, the sludge derived from

CPR processes would be also inconvenient since Al is toxic to plants and Fe-P solids have low bioavailability (Melia et al. 2017).

These issues have led to the implementation of P recovery processes. Technologies for phosphorus recovery may be applied on the solid (primary and secondary sludge and ashes) or in the liquid phase (sludge dewatering stream: anaerobic digestion, wet-chemical extraction from the sludge or wet-chemical extraction from sewage sludge ash) (Melia et al. 2017). In anaerobic digestion (methanization), P may be recovered from a concentrated supernatant. Acidic or basic solvents are added to the sludge or the incinerated sludge to re-dissolve P and obtain a concentrated liquor. For all the three cases, crystallisation processes are required to transform the recovered P concentrated liquid phase into valuable fertilizer products like calcium phosphate (CaP) and struvite. Indeed, because of the dirtier nature of the sludge P recovery would demand complex recovery processes, the use of chemicals and/or great amounts of energy resulting in high operational costs (Ye et al. 2017). All the same, the recovered P may still contain toxic by-products, heavy metals, organic micropollutants and other components that may complicate its valorisation as a fertilizer (Amann et al. 2018).

Optionally, sorption-based filters seeking phosphorus recovery may be applied to the liquid phase of a WWTP; either to the water line or to side streams from sludge dewatering or sludge liquors. When stringent regulatory effluent standards apply, a tertiary treatment stage may be carried out based on physicochemical processes like adsorption, crystallisation, electrodialysis and ion-exchange but also micro and ultrafiltration membrane processes (Venkiteshwaran et al. 2018). A large variety of materials to promote P sorption are currently being studied (See section 1.3.2), but their high cost still prevents these technologies to be applied in full-scale especially concerning large WWTPs (Melia et al. 2017).

Although technologies for P removal like EBPR are considered mature technologies, those seeking P recovery are still at a young development stage (Yuan et al. 2012). In addition, a majority of them apply associated with the EBPR process (Egle et al. 2016, Cieřlik and Konieczka 2017) which together with other intensive systems may be less suitable for small WWTPs. Phosphorus removal and recovery in small-scale WWTPs is still an unsolved problem (Vohla et al. 2011).

### 1.3.1. Phosphorus Removal in Small WWTPs

Wastewater treatment systems for small communities require taking into consideration some of their particularities. Generally, small WWTPs cannot count on permanent and specialised on-site technicians. Consequently, the use of simple treatment processes requiring low maintenance and low cost is usually considered. Although intensive systems like activated sludge are still extensively used, nature based systems like treatment wetlands (TW) are gaining popularity (Bellin 2016). In France, more than 4,000 TW (Martinez-Carvajal et al. 2019) have been built since the 90s to treat WW of small and medium size communities (< 5000 PE). TW are simple, reliable and efficient systems to treat carbon (C) and nitrogen (N) pollution with low energy and maintenance requirements (Morvannou et al. 2015, Kania et al. 2019). The main disadvantage of TWs is their higher land footprint compared with intensive systems. Nevertheless, they show a lower environmental impact than, for example, activated sludge systems (Garfi et al. 2017). TW systems are, indeed, suitable for small plants of rural areas.

In subsurface flow treatment wetlands, wastewater flows through a porous media, made of conventional substrates like gravel or sand (Yang et al. 2018). The treatment of wastewater is carried out through a compendium of different processes: physical retention of suspended solids (SS), biological degradation of organic matter (OM) and nitrogen, assimilation of nutrients by the plants and bacteria and physicochemical retention of dissolved components inside the media.

Concerning P, microorganisms and plants are capable to assimilate and store a fraction of this phosphorus. However, organic matter mineralization releases back P into the effluent and the amount retained by plants is negligible unless a great land footprint is used (Harouiya et al. 2011, Molle et al. 2011). The major contribution to P retention is usually carried out by adsorption and precipitation on the filter media (Vohla et al. 2011) and to some extent on the OM (Gilbin et al. 2000, Molle et al. 2011). Phosphorus retained by surface interactions depends mostly on the capacity of the substrate to retain P and thus, in the particular composition of the media. With gravel, this capacity has been shown to be limited (Wang et al. 2020). Otherwise, sand filters were reported to have up to 99% P removal but do not always ensure a long-term retention (Wang et al. 2020). For soil type substrates, which is not recommended to use in TW, P retention is associated with Fe and Al concentrations as well as the

presence of OM, leading to a great variability in P performance results (Wang et al. 2020). Indeed, the use of conventional substrates may compromise reliable long-term phosphorus removal (Vohla et al. 2011) and low discharged concentrations.

To solve the issue of phosphorus retention and recovery in TW, three major solutions have been proposed: (1) the use of specific substrates as a filter media in the TW to enhance P retention (Yang et al. 2018), (2) CPR and (3) the use of reactive filter media as a tertiary treatment for P retention (Hamisi et al. 2019).

As for intensive systems, the use of chemical reactants is an effective solution to precipitate phosphorus. When used as a tertiary treatment to minimize the amount of reactant needed, an additional unit is required to allow the settlement of the sludge produced. Optionally, the sludge may be recirculated to the first stage of treatment accumulating with the surface deposit of the filter or stored and treated using a specific system. In Kim et al. (2013), the dosing of  $\text{FeCl}_3$  in between a pre-treatment stage, consisting of a tricking filter and a TW, was proposed. The retention of the sludge produced would be then carried out at the first stage of a lower footprint TW (0.8 -1.1 instead of 1.2 – 1.5  $\text{m}^2$  /PE). The use of CPR systems for P retention will certainly allow to reach low P concentrations in the effluent when stringent regulation thresholds apply. However, the use of reactants will increase the operational costs, the dosing unit makes the operation more complex from a technical point of view and finally, P must be recovered from the mineralized sludge of the TW filter.

The use of reactive materials for phosphorus retention has been object of intensive research in the last two decades. When applied as a filter media for TW, substrates may also seek for good performances of other pollutants like N, organic compounds and heavy metals (Yang et al. 2018, Wang et al. 2020). The biggest drawbacks of specific substrates in TW is a premature saturation of the phosphorus retention capacity (PRC) of the filter compared to the lifespan of a well operated TW, as well as, a premature internal clogging. This may be solved by adding the so-called P-filter as a tertiary treatment in the WWTP (Hamisi et al. 2019). After successive stages of TW, the SS, OM, N and particulate P loads are usually reduced to the minimum, thus reducing the risk of clogging. This configuration would also allow the renewal of the exhausted media once it has attained its maximum PRC while the TW still operates properly. Of course, the use of a tertiary stage P reactive filter may not be limited to TWs but it may be potentially applied to all kind of WWTPs.

### 1.3.2. Specific reactive materials for phosphorus retention

Vohla et al. (2011), Yang et al. (2018) and then Wang et al. (2020) have carried out comprehensive reviews about specific conventional and emerging substrates to enhance phosphorus removal in TW. Substrates have been classified based on their origin as natural products, man-made products and industrial by-products. Lately research has focused in modifications of some substrates that have already shown P binding capacity to enhance their capabilities (eg. Thermal treatment, coating, mixing with other substrates). However, the associated production costs may still be counterproductive to a large-scale application (Melia et al. 2017).

The suitability of a material is measured in first place by its phosphorus retention capacity (CPR). When it reaches its maximum value the substrate is said to be saturated. The sorption capacity depends on their relatively high content of calcium (Ca) (Vohla et al. 2011), Fe, Al together with their oxides and hydroxides. Phosphorus is retained by adsorption and/or precipitation processes, however, the specific reaction mechanisms may vary among the substrates (eg. Ligand exchange ( $\text{OH}^-$  replaced by  $\text{PO}_4^{3-}$ ), ion-exchange, electrostatic interactions, seeded precipitation, dissolution/re-precipitation processes, etc. (Chapter 2). Using substrates based solely in adsorption mechanisms, one has to consider the need of a desorption phase (or washing) to regenerate the sorption capacity of the substrate once exhausted, which may be a cycle of several days, weeks or months according to substrate capacities. This may complicate the operation and will most certainly require the use of chemicals, which may not be the better option for small WWTPs. The PRC of other substrates may rely on their capacity to dissolve  $\text{Ca}^{2+}$  (to coprecipitate as calcium phosphates) and so their efficiency may drop off when all  $\text{Ca}^{2+}$  has dissolved (eg. calcite (Molle et al. 2003) or steel slag (Barca et al. 2013)). For substrates based on seeded precipitation mechanisms, the filter may reduce its efficiency for P removal after years of operation because of the chemical clogging of the filter.

The exhaustion of the PRC of a substrate may have different origins related with their reaction mechanism but there are other factors (environmental, biomass development, affinity for other pollutants, etc.) that may influence the lifespan of the filter. Vohla et al.

(2011) concluded that most tested substrates have attained PRCs close to saturation after 5 years operation.

Another important aspect of substrates is their particle size distribution. Generally, fine substrates show better retention than coarse materials because of a greater specific surface area (SSA). Since reaction mechanisms depend on interface interactions, the greater the surface available the higher the P sorption capacity. A high SSA may also be attained through porous particles (internal pores). However, the hydraulic performance also needs to be considered since a fine particle-size-distribution may lead to a rapid clogging of the filter. Consequently, a compromise needs to be found between the particle size and the P retention efficiency. In conclusion, the PRC of a substrate depends on the particle size distribution, the porosity, the hydraulic conductivity, specific surface area, as well as, the substrate's nature and its content of Al, Fe or Ca ions (Ádám et al. 2006, Blanco et al. 2016).

Finally, the saturation of the PRC and the frequency needed for replacement/regeneration of a substrate define an important aspect of the economic feasibility of the process. Complicated operations, use of chemicals and/or expensive substrates will also increase the cost resulting in less suitable options especially for small WWTPs. Other criteria to evaluate the adequacy of a filter media for P retention are the local availability of the substrate and its revalorisation potential. The applicability of the recovered P or saturated media as a fertilizer or for fertilizer production needs to be considered on behalf of the circularisation of P. Aspects like the bioavailability of the retained P or the potential pollution of croplands with heavy metals will also determine the selection of a sorption substrate against another.

#### 1.4. Phosphorus retention by apatite filters

Previous studies have assessed the capability of mineral apatite (FAP,  $\text{Ca}_5(\text{PO}_4)_3\text{F,Cl,OH}$ ) for phosphorus retention from wastewater (Joko 1984, Jang and Kang 2002, Molle et al. 2005, Bellier et al. 2006, Harouiya et al. 2011b, Harouiya et al. 2011a, Molle et al. 2011) showing high PRC and long-term retention. Apatite allows irreversible retention of P by seeded precipitation of calcium phosphates (CaP) evolving ultimately into hydroxyapatite (HAP), the most stable CaP phase (Chapter 2).

Joko (1984) was first imagining a process for P removal from wastewater based on seeded precipitation of CaP onto apatite. He carried out batch, column and pilot experiments with granular crystals prepared from phosphate rocks showing the efficiency of apatite to retain phosphorus from secondary wastewater effluent. The pilot plant consisted of an up-flow packed bed reactor of 0.9 m<sup>3</sup> fed by a sewage secondary effluent. The pH was adjusted to values in a range of 8.5 - 9.0 by lime addition (Ca(OH)<sub>2</sub>) acting also as a source of calcium ions. During a 200-days monitoring, P outlet concentrations stayed below 1 mg PO<sub>4</sub>-P/L during the whole experiment with influent concentrations in the range of 1 to 10 mg PO<sub>4</sub>-P /L. The operation of the filter included an air-water backwashing to recover the permeability lost by the presence of suspended solids. The study concluded that operating in the metastable zone, phosphate rock crystals were able to promote the nucleation of apatite precipitates in a wastewater environment.

Jang and Kang (2002) examined the capacity of calcinated cow bones to crystalize phosphorus from wastewater as HAP. The authors studied the influence of temperature and alkalinity stating that temperatures above 20°C would positively affect the rate constant, instead the presence of carbonate would have a negative effect on the crystallization process. All the same, they concluded that the material presented good capacity for P removal.

In Molle et al. (2005) the differentiation of two reaction mechanisms depending on the PRC of the material, was suggested. Adsorption would govern the reaction rates for low PRC values and precipitation would follow for higher PRC being the predominant mechanism for long-term retention. Scanning Electron Microscopy (SEM) images would have also confirmed the formation of hydroxyapatite (HAP) as the precipitated CaP phase. This work was followed by Harouiya et al. (2011)<sup>a,b</sup>, whom assessed the P retention potential of several types of natural apatite to treat wastewaters of small communities in TW plants. The work presented the importance of apatite composition on the efficiency of P retention identifying high apatite content phosphate rocks (>90% apatite) as rich quality materials for P retention. Instead for those with low apatite content, P retention was shown to be less efficient since the reaction rates were slower.

In Molle et al. (2011) some design rules for apatite filters were suggested. Substrates with high apatite content were evaluated in laboratory pilot columns reaching a PRC of 13.9 g PO<sub>4</sub>-P/kg of apatite and showing outlet concentrations still below 1 mg TP/L

(total phosphorus). Applying a security factor to the design, a 0.5 m<sup>2</sup>/PE filter should allow a P removal up to concentrations lower than 1 mg TP/L for 15 years working in hydraulic saturation conditions and for influent COD concentrations below 150 mg/L. It was also reported that natural phosphate rocks of high apatite content generally present a fine particle size distribution. To limit risks regarding hydraulics, it was recommended to use vertical filters, against the horizontal filters, because of their greater surface sections (Molle et al. 2011).

The design and development of a granulated apatite product in order to control the particle size distribution of the media (Troesch et al. 2016) was also proposed as a solution to avoid hydraulic risks. The granulated apatite would reduce the risk of a premature clogging that might be associated with the use of a substrate with a finer particle size distribution, i.e. natural apatites. The manufacture process is similar to the production of fertilizer pellets and assures a particle size of 3-8 mm. This material was commercialised by a fertilizer industry and used for the treatment of P in 20 full-scale patented filters in France to treat municipal sewage. The first results from the early stages of operation of some of these granulated apatite filters were reported to be satisfactory but results of the long-term operation were still needed (Troesch et al. 2016).

The importance of the apatite origin was also noticed by Bellier et al. (2006). Sedimentary apatites would present better P retention than igneous apatites. It was believed that a higher density of igneous apatites would explain a lower internal porosity (lower SSA available for reaction) and thus a lower performance. No correlation with the P content and the retention capacity of the material was made though. Instead, the work highlighted that a calcium source provided by other minerals from the gangue would enhanced P retention as CaP.

The major advantage of using such a substrate is that the precipitated CaP phases (mainly HAP) are close in composition to the phosphate rock seed, which is used for fertilizer production. This may simplify the acceptance and adoption of this secondary P source for the use as fertilizer or for fertilizer production. Spreading the recovered CaP directly in land (e.g. acidic soils) may provide slow and more efficient P release. Nevertheless, further research in that specific area needs to be carried out in order to draw reliable conclusions. In addition, apatite is known to have important interactions with heavy metals and radionuclides that may result in strong binding capacities with

Cd, Co, Hg, Sr, Pb, U (Kaplan and Knox 2004, Xu et al. 2019). This may also involve the release of heavy metals previously adsorbed from wastewater due to sorption sites competition (Kaplan and Knox 2004), as well as the release of those metals already present in the apatite crystalline structure (isomorphic substitutions). Harouiya et al. (2011)<sup>a,b</sup> followed the variation of some trace metal concentrations of the influent and effluent of pilot columns showing adsorption of Cu, Se, Zn and Hg and releasing of As, Cd and U. Apatite/metal interactions would mostly depend on: the concentration of trace metals in the apatite; the presence of metals in soil; and the redox conditions of the pore water. Then the use of apatite, either in wastewater or in soil, may involve both positive and negative effects from the sorption or release of heavy metals that must be investigated carefully.

#### 1.4.1. Apatite

The stoichiometric composition of pure apatite is  $\text{Ca}_5(\text{PO}_4)_3\text{Cl}$  for chlorapatite (CIAP),  $\text{Ca}_5(\text{PO}_4)_3\text{OH}$  for hydroxyapatite (HAP) and  $\text{Ca}_5(\text{PO}_4)_3\text{F}$  for fluorapatite (FAP). However, pure stoichiometric apatite is not frequent because of the several isomorphic substitutions allowed by its hexagonal crystalline lattice (Fig.1. 9). The ions may be partial or completely replaced by other ones of similar charge and size leading to solids with apatite structure of general formula  $\text{Me}_5 (\text{XO}_4)_3\text{Y}$ . Possible substitutions are present in Table 1.3. The so-called carbonated apatite represents an important group of apatite that includes minerals as francolite and dahllite, biological apatites (teeth and bones) and phosphate rocks (Elliott 2013). In particular, the most abundant apatite in phosphate rocks (or phosphorites) is the carbonated fluorapatite (C-FAP). These deposits are formed by the reaction of guano with calcareous rock or by the accumulation of sediments precipitated from the sea. In phosphate rocks, C-FAP are less well crystallized (micro-crystalline structure) and allow many substitutions which may result in a variety of different compositions.

Table 1. 3. Possible isomorphic substitution in apatite structure. Me stands for metal, X for non-metal and Y for halogen (except for the hydroxyl ion). Adapted from Bengtsson (2007) and Fihri et al. (2017)

Me	XO <sub>4</sub>	Y
Ca <sup>2+</sup>	PO <sub>4</sub> <sup>3-</sup>	F <sup>-</sup>
Al <sup>3+</sup>	SiO <sub>4</sub> <sup>4-</sup>	OH <sup>-</sup>

<b>Na<sup>+</sup></b>	CO <sub>3</sub> <sup>2-</sup>	Cl <sup>-</sup>
<b>Cd<sup>2+</sup></b>	SO <sub>4</sub> <sup>2-</sup>	Br <sup>-</sup>
<b>Pb<sup>2+</sup></b>	AsO <sub>4</sub> <sup>3-</sup>	I <sup>-</sup>
<b>Mg<sup>2+</sup></b>	CrO <sub>4</sub> <sup>3-</sup>	Br <sup>-</sup>
<b>Ba<sup>2+</sup></b>	MnO <sub>4</sub> <sup>3-</sup>	S <sup>2-</sup>
<b>Na<sup>+</sup></b>	VO <sub>4</sub> <sup>3-</sup>	O <sup>2-</sup>
<b>K<sup>+</sup></b>	HPO <sub>4</sub> <sup>2-</sup>	CO <sub>3</sub> <sup>2-</sup>

In C-FAP, carbonates may replace the fluoride ion, which is called an A-type substitution or they may replace the phosphate anion, which is a B-type substitution (Ca<sub>5</sub>(PO<sub>4</sub>, CO<sub>3</sub>)<sub>3</sub>(F, CO<sub>3</sub>)). There may be C-FAP with just A substitutions, with just B substitutions or with both kinds (Lafon et al. 2003). B-type substitutions involve the loss of fluoride and calcium cations causing distortions of the crystal lattice or a loss of the apatite hexagonal symmetry (Leroy and Bres 2001). As a result, the carbonated apatites present a higher solubility than pure H, Cl or FAP (Zhu et al. 2009).

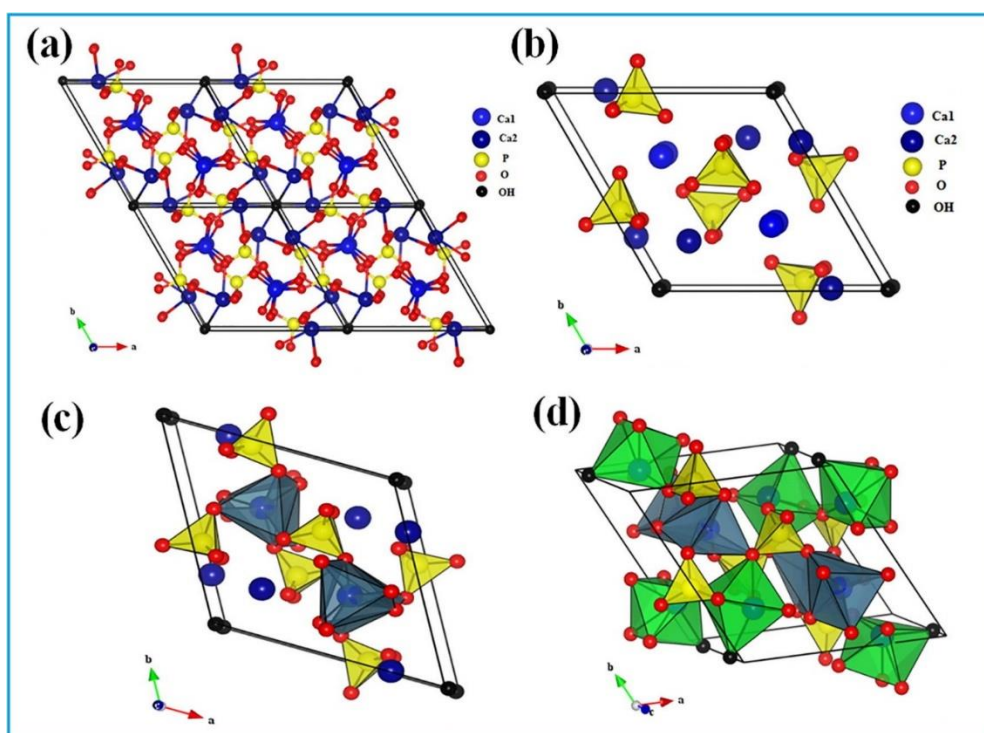


Fig.1. 9. (a) Projection of a unit cell of HAP; (b) projection showing the arrangement of octahedrons [Ca(1)O<sub>6</sub>] in the HAP structure; (c) projection showing the sequence of octahedral [Ca(1)O<sub>6</sub>] and tetrahedral [PO<sub>4</sub>] in the HAP structure; and (d) projection showing the sequence of octahedral: [Ca(1)O<sub>6</sub>] and [Ca(2)O<sub>6</sub>], and also tetrahedral [PO<sub>4</sub>] in the HAP structure. From Fihri et al. (2017).

### 1.4.2. Reaction rate models

Chemical and biological degradation in wastewater treatment is often represented by chemical engineering reaction kinetics. They present the advantage of simplifying flow and reaction processes, hence they are easy-to-use models for designers. On the other hand, they do not allow to represent the complexity of the mechanisms involved (it works as a black box). In this work, two different reaction rate models are used: the k-C\* model (Kadlec and Knight 1996) and the N-k-C\* model (Kadlec and Wallace 2009).

#### 1.4.2.1. The k-C\* model

The k-C\* model (Eq.1.4) assumes a first order kinetics for P retention, the existence of a background concentration and the hydrodynamics of an ideal plug flow reactor. The evolution of P concentration (C, mg PO<sub>4</sub>-P/L) with the hydraulic retention time (HRT) represented by t (h) can be then obtained by the following expression:

$$C = (C_0 - C^*)exp(-k_v t) + C^* \quad [1.4]$$

where C<sub>0</sub> is the inlet concentration of phosphorus, k<sub>v</sub> (h<sup>-1</sup>) the volumetric kinetic rate coefficient and C\* (mg PO<sub>4</sub>-P/L) the background concentration. k<sub>v</sub> and C\* are the parameters of the model. The kinetic rate coefficient does not depend on the hydraulic loading rate or the inlet concentration (Gajewska et al. 2013). The concept of a background concentration, applied to P retention on apatites, involves an equilibrium concentration derived from adsorption and precipitation processes (the lower attainable concentration).

The k-C\* model has been extensively used to describe phosphorus retention in hydraulically saturated treatment wetlands (eg. free water surface TW, (Kadlec and Wallace 2009)) since the existence of a phosphorus gradient. It has been also previously used for modelling struvite formation (Quintana et al. 2008). In Harouiya et al. (2011)<sup>a,b</sup>, this model was proposed for modelling the P retention in apatite filters showing a good correlation with experimental results.

In the works of Harouiya et al. (2011)<sup>a,b</sup> and Molle et al. (2011), adsorption and precipitation were the two different processes considered responsible for P retention onto mineral apatite. A representation of the estimated  $k_v$  (from the k-C\* model) with PRC allowed to observe an evolution of the  $k_v$  value which was claimed to account for a change in the processes taking place (Fig.1. 10). Adsorption processes are fast reactions involving high  $k_v$  values. It is then assumed to be the dominating reaction for low PRC values. As the adsorption sites deplete, the precipitation reactions become the predominant process and the one prevailing considering long-term operation. The slower kinetics associated with such process would lead to a pseudo-stabilization of the parameter  $k_v$  with increasing PRC.

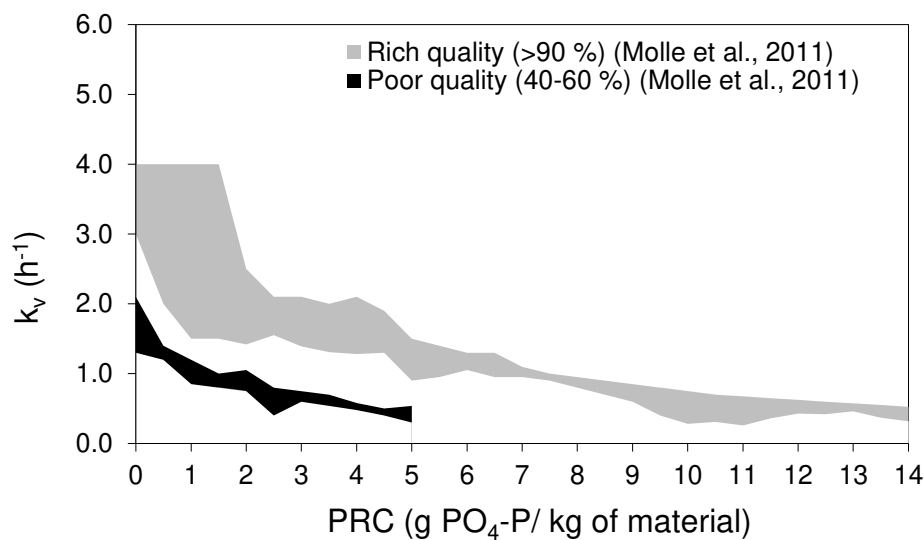


Fig.1. 10. Evolution of the kinetic constant with the phosphorus retention capacity of the media for mineral apatite of different quality. Source: Molle et al. (2011)

#### 1.4.2.2. The N-k-C\* model

The tank-in-series (TIS) reaction rate model is a combination of the k-C\* model (first order kinetics and background concentration) with the hydrodynamics of a TIS model. The TIS hydrodynamic model considers that the flow conditions of the system result from N completely stirred-tank reactor (CSTR) in series. The greater is the value of N the closer is the hydrodynamics to a plug flow. For N = 1 the system operates as a

CSTR. From  $N = 50$  the hydrodynamics approach plug flow conditions. As the model parameters are  $N$ ,  $k$  and  $C^*$  it is here referred as the  $N$ - $k$ - $C^*$  model in analogy with the  $k$ - $C^*$  model and to differentiate the reaction rate model from the hydrodynamic model. The  $N$ - $k$ - $C^*$  model is described by Eq.1.5.

$$C = (C_0 - C^*) \left(1 + \frac{k_v t}{N}\right)^{-N} + C^* \quad [1.5]$$

Compared to the plug flow assumption of the  $k$ - $C^*$  model, the  $N$ - $k$ - $C^*$  model might provide a more realistic representation of the actual hydrodynamics in apatite filters.

## 1.5. Chapter conclusions

The need for phosphorus recovery from secondary sources like wastewater has become evident in order to avoid the depletion of phosphorus sources. The increasing pressure on natural ecosystems due to anthropogenic pollution also pushes regulators to include the obligation for phosphorus treatment even in small WWTPs. Traditional systems for phosphorus retention are expensive, poorly adapted to small WWTPs and the phosphorus recovery is usually not easy to implement. Therefore, the use of filters with reactive media has gained interest for such applications due to its simplicity and the possibility of phosphorus recovery. Many substrates have already been tested but long-term removal (more than five years) is often lacking. In France, apatite filters were previously suggested as a technological solution for long-term phosphorus removal in small WWTPs. As an extensive system, is particularly adapted to treatment wetlands plants, extensively used in France, and requires little maintenance. The retention of phosphorus is provided by means of adsorption and seeded precipitation of calcium phosphates, which allows phosphorus recovery in the fertilizer industry. Natural apatites showed to be efficient in phosphorus removal and capable of achieving phosphorus retention capacities up to 13.9 g  $\text{PO}_4\text{-P/kg}$  material in laboratory tests. The major concern for the use of natural apatite filters involved the risk of a premature clogging due to the fine particle-size distribution of the substrate. To overcome that, a granulated apatite product with a higher particle size distribution was implemented in full-scale filters after some short laboratory tests. First results from full-scale systems

announced good phosphorus retention performances, however, the long-term retention capabilities of such systems remained unknown.

## 1.6. General objectives

In such a global economic-political and environmental context, the circular economy of resources is of importance. When considering the domain of wastewater treatments in particular of rural and small communities, research is still to be done to promote circularity. With phosphorus being a depleting resource that needs to be reused, the apatite filter constitutes one of these solutions. In this document, apatite filters are assessed in order to determine their actual capacity to become a technological solution for the retention and recovery of phosphorus from wastewater in the framework of small and medium-size communities. The general objectives of this study are:

- To determine the suitability of different apatite products for the retention of phosphorus from wastewater, in terms of their retention capacity, performances and kinetics.
- To draw the advantages and limits of the different apatite materials studied, as well as the methodology applied for their assessment.
- To provide a comprehensive evaluation of the processes involved in phosphorus retention from wastewater, identifying the mechanistic differences developed that could be related to the nature and characteristics of the particular material and/or the influence of the environmental conditions in the solute/substrate system.
- The discussion around the possibilities and constraints in the design of full-scale apatite filters for the particular case of small wastewater treatment plants.

To address this general objectives this dissertation is organized in the following chapters:

- Chapter 2: explains the fundamentals of the surface interactions involved in phosphorus retention on a reactive media with an especial emphasis in the particular interactions between apatites and phosphates in wastewater. The chapter briefly reviews the different studies carried out about phosphorus retention by apatites in the particular framework of wastewater treatments.

- Chapter 3: a detailed presentation of the extensive experimental work carried out and methodologies and techniques applied is shown here. The experimental work is composed of a significant part dedicated to substrate characterization on one hand; long-term laboratory experiments with fixed-bed columns for the assessment of different apatites products; and, the evaluation of full-scale systems by field experiments carried out over two years.
- Chapter 4: Results of this study are presented in the form of scientific articles. This chapter is dedicated to the presentation of the results followed by a comprehensive discussion of the experimental work carried out on granulated apatite, which includes an assessment of full-scale and laboratory systems.
- Chapter 5: This final chapter is dedicated to the experimental results of laboratory columns filled with natural apatites. It ends up by presenting a characterization method and first steps towards the development of a mechanistic model.

At the end, a discussion concerning the design of full-scale filters based on laboratory results is presented to draw the limits and advantages of the experimental approach here developed. The discussion finishes with the main conclusions and perspectives derived from this work.

## Chapter 2. Literature Review: Surface reactions

---

### 2.1. Introduction

In a solid material, the atoms located at the surface present a different coordination number than those located in the bulk of the solid. With all the valencies occupied, bulk atoms show electroneutrality and thus, a low energy state. On the other hand, the surface atoms with unsaturated valencies show an accentuated reactivity because of their higher energy state. When in contact with a liquid solution, the atoms of the solid at the solid-liquid interface will tend to lower this surface energy by:

- (1) coordinating with atoms of the liquid phase (solvent or solute) or
- (2) by reducing the surface area per volume of solid, which implies the growth of the solid.

The reactions taking place at the interface between the solid surface and the liquid phase are called surface reactions and may be two (forward/reverse reaction): adsorption/desorption and dissolution/precipitation. Adsorption is a two dimensional process (Anderson and Rubin 1981) where solute ions form a one-layer cover onto the surface of the solid. Further sorption may lead to a three dimensional process or nucleation that will eventually form a precipitate. A clear line differentiating the end and the beginning of the reactions is difficult to draw since one process may lead to the other (Anderson and Rubin 1981). However, both processes exhibit different characteristics that will be more broadly discussed in sections 2.2 and 2.3.

### 2.2. Adsorption

Adsorption is the primary surface reaction described as the accumulation of matter at the solid-liquid interface (Stumm 1992). When a solid is in contact with a liquid phase, surface atoms will coordinate with either solvent molecules or solute ions leading to a charge accumulation at the solid-liquid interface and therefore to the occurrence of an

electrostatic potential (Kallay et al. 2010). Three concepts may be described at this point:

- Active surface sites, which are the functional groups of the solid surface.
- Potential determining ions, which normally are  $H^+$  and  $OH^-$  ions from the solvent when the solvent is water.
- Counterions, solute ions of opposite sign charge with respect to the solid-liquid interface.

The exposition of the surface of a solid material like a metal oxide (MO, simplest system) to water, originates charging reactions. The active surface sites of the solid ( $\equiv MO^z$ , where  $\equiv$  indicates bond of the functional group to the bulk of the solid and  $z$  is the charge number) react with the surrounding medium (the water) by coordinating with the potential determining ions ( $H^+$  and  $OH^-$  for the MO). This originates an hydroxylated/protonated surface like shown in Fig. 2.1 (Anderson and Rubin 1981) and in Eq. 2.1 and 2.2 (Kallay et al. 2010). The protonation of an anionic functional group is also described in Eq. 2.3 and examples of charging reactions for other functional groups or even for hydrophobic surfaces are also pictured in Fig. 2.2. These interactions are responsible for the accumulation of charge at the interface (surface charge density,  $\sigma_0$ ) and for the existence of a surface potential ( $\psi_0$ ).



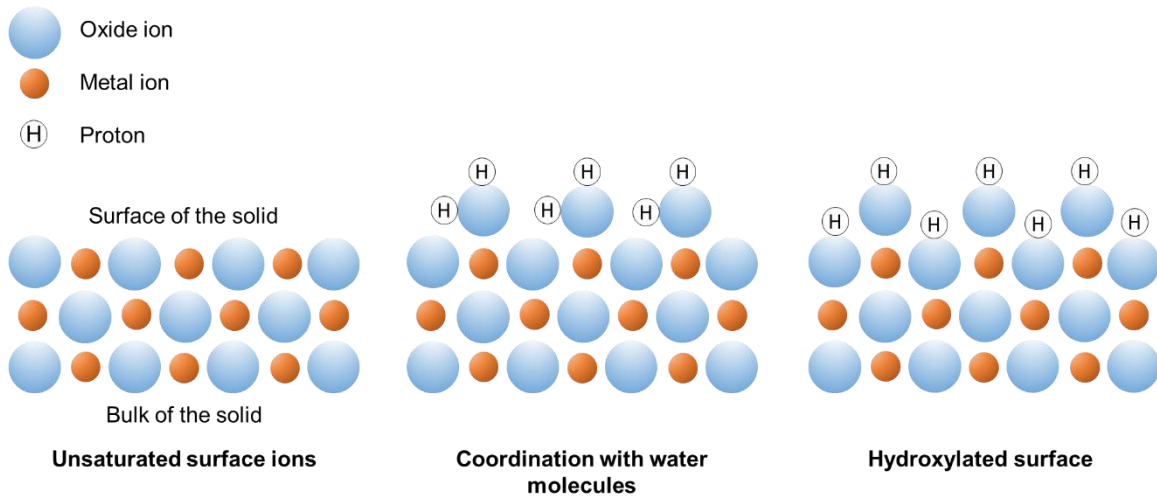


Fig. 2. 1. Cross section of a surface layer of a metal oxide. The hydration of the surface results in hydroxylated cations. Adapted from Anderson and Rubin (1981).

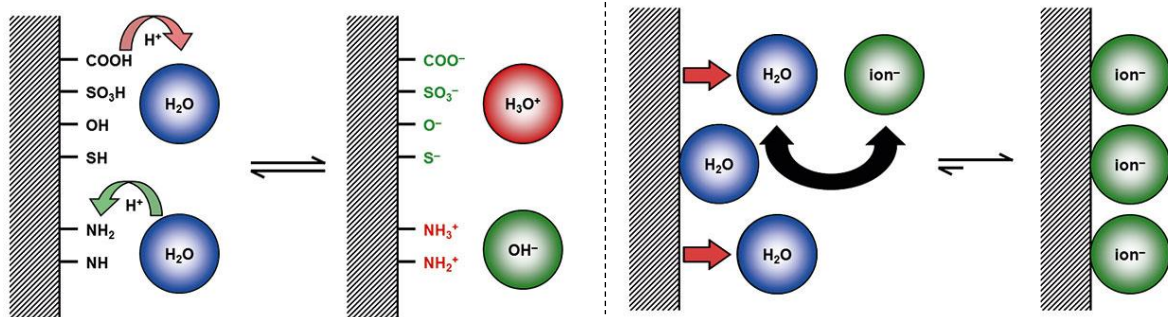


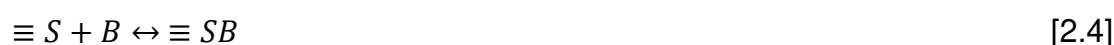
Fig. 2. 2. Charge formation at the solid-liquid interface for: left) a hydrophilic material with acidic or basic functional groups; right) a hydrophobic material without functional groups. From: <https://wiki.anton-paar.com/fr-fr/potentiel-zeta/>.

As a consequence of the hydration of functional groups at the surface of the solid, the interface exhibits acid/base properties which, of course, depend on the pH of the solution. The pH value at which the surface charge is zero ( $\sigma_0 = 0$ ) is called the point of zero charge ( $\text{pH}_{\text{zpc}}$ ). For a solution pH below the point of zero charge, the surface will be protonated and so positively charged (e.g. excess of  $\text{MOH}_2^+$ ). For a solution pH above the point of zero charge, the surface will be deprotonated and, thus, negatively charged (e.g. excess of  $\text{MO}^-$ ).

When considering surface reactions, solid phases may be understood as inorganic or organic polymers, with monomer units that repeat in a three dimensional association,

as it was suggested with the schematic representation of MO in Fig. 2.1. Of course, a real solid do not reproduce a perfect association of monomers. It may have isomorphic substitutions in the bulk and surface of its lattice, as well as, surface defects (incomplete layers of atoms on the surface, e.g. steps, kinks) that will also intrinsically affect the surface charge of the solid (Speed 2016). In addition, a single mineral may present different types of surface sites which may use different reaction mechanisms to interact with the solution (Payne et al. 2013). The major inorganic surface functional groups are oxygen atoms bound to silicates and hydroxyl groups (Sparks 2003).

In a solution, the presence of solutes partially compensates the charge at the interface ( $\sigma_0$ ) by the adsorption of counterions of opposite charge (metal ions or ligands). These adsorption reactions are generally explained by the Surface Complexation Model (SCM), where the ionic species of the solution will distribute influenced by electrostatic forces and those close enough to the solid surface may bind to the surface sites establishing a thermodynamic equilibrium (Eq 2.4, where B accounts for a molecule and  $\equiv S$  for a surface site (Kallay et al. 2010)). Taking again the example of metal oxide surfaces adsorbing a cation ( $C^+$ ) or an anion ( $A^-$ ), it will result in the complexes showed in Eq 2.5 and 2.6 (Kallay et al. 2010). A surface complex is therefore a stable molecular entity resulting from the interaction of a sorbate (solute) with a surface site (Sparks 2003).



The reaction with ions from the solution may take place under different reaction mechanisms. Surface complex formation may involve the loss of protons or a ligand exchange ( $OH^-$  per L). Simple cases of these kinds of adsorption are shown in Eq. 2.7 and 2.8, respectively (Stumm 1992). The coordination of surface sites with solutes may also be multiple (double, triple) analogously to complexation reactions in solution, however it is also possible that two surface sites can attach to one ion. These all coordination possibilities are shown in Eq. 2.9. Table 2.1 also shows the most important adsorption equilibria according to Stumm (1992).

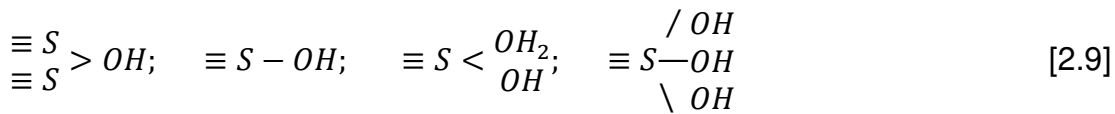
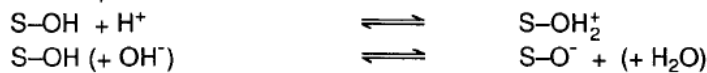


Table 2. 1. Examples of adsorption reactions: Surface Complex Formation Equilibria. Source: Stumm (1992).

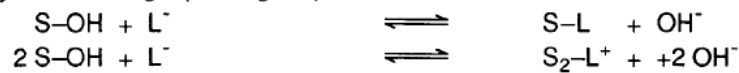
**Acid base equilibria**



**Metal binding**



**Ligand exchange ( $L^- = \text{ligand}$ )**



**Ternary surface complex formation**



### 2.2.1. Sorption types

Solute ions may bind to the surface by:

- Specific adsorption (chemisorption)
- Non-specific adsorption (physisorption)

Eq. 2.7 and 2.8 describe examples of specific adsorption where the solute is directly bind by ionic or covalent bonds to the functional group at the surface. Such bonds involve a significant rearrangement of electron density in both sorbate and sorbent. This kind of process are often exothermic with typical energy release around 200kJ/mol ((Atkins and De Paula 2006)), however, the enthalpy change for coordination and chemical bonds is  $> 40\text{kJ/mol}$  (Patel 2019). The formed complex, with different chemical structure and properties than the solute before the reaction, is called an inner-sphere complex. This complex is formed directly onto the surface of the solid replacing

$\text{OH}^-$  and  $\text{H}^+$  resulted from the hydration of the surface. Chemisorption is just possible in monolayer, is often irreversible and does not depend on the surface charge or ionic strength (Sparks 2003). It is also the one kind involve in precipitation reactions (find another reference).

Longer distance interactions, like Van der Waals or hydrogen bonds, may also establish between functional groups and solutes which, in this case, keep their solvating molecules (hydration shell). This originates a layer with immobile water and solutes, at a distance of a couple of water molecules form the surface. Physically sorbed molecules keep their chemical integrity, that is, no significant redistribution of electron density in either the molecule or at the substrate surface occurs. The enthalpy change of physisorption is considered to be lower than 40kJ/mol (Kara et al. 2003). Eq. 2.5 shows an example of this kind of interactions. Bonds where water molecules separate solute ions from functional groups are then called outer-sphere complex and, contrary to specific adsorption, it can stand multiple adsorption layers. It is usually a faster process than chemisorption, it is reversible and it depends on surface charge and the ionic strength of the solution (Sparks 2003). Both types, inner and outer-sphere complexes, are pictured in Fig. 2.3.

### 2.2.2. The interface structure.

Since there is a surface potential at the interface plane (the inner surface potential  $\psi_0$ ), there must be a potential distribution from the interface to the bulk of the liquid phase where the potential is assumed to be zero (Fig. 2.3). This distribution is characterized by some planes and layers depending on the model considered (Kovacevic et al. 2007). The simplest model to explain the electrochemical behaviour of solid-liquid interfaces was suggested by Helmholtz in 1879 and was called the Electrical Double Layer (EDL). Such model considered just two rigid planes of charge: the solid surface on one hand, and the ions of opposite charge together with their solvating molecules in contact with the surface, on the other hand. After that, several contributions have been made by Gouy-Chapman, Stern or Graham among others, transforming the primitive conception of the EDL in a more sophisticated one. For instance, Gouy and Chapman introduced the concept of a diffuse layer where the charge distribution would

decrease exponentially from the surface to the bulk of the solution. The diffuse layer would have a different concentration of ions than the bulk of the solution and it would consider the motion resulted from thermal energy. Later on, Stern additionally proposed the concept of adsorption onto specific sites.

Since the 70s, the models based on surface complexation to explain the interface structure have replaced the previous models. Surface complexation models (SCM) explain the electric double layer based on the chemistry and thermodynamics of the interactions. Some of them are the constant capacitance model (CCM), the triple-layer model (TLM), the generalized two layer, or the one-pK model among others. Major common characteristics of these models reside on the consideration of surface charge balance and density, electrostatic potential terms, equilibrium constants and capacitances. The most significant difference is the description of the double layer, i.e. the planes and position of the inner and outer complexes in them, the equations, and relationships between surface charge and surface potential (Sparks 2003). Among all the variety, one may choose, indeed, the model that better suits a specific case.

In 2000, Kallay proposed the General Model of Electrical Interfacial Layer (GM-EIL) schematically represented in Fig. 2.3. This model claims to include all the conventional models to describe solid-liquid interfaces when choosing the correct parameters (Kovacevic et al. 2007), reason why it has been taken here as an example of a SCM.

The GM-EIL model is described by 4 planes and 3 layers. The charge ( $\sigma_0$ ) and potential ( $\psi_0$ ) of the inner surface plane (the 0-plane) is determined by the characteristics of the active surface sites and their interactions with the potential determining ions. The counterions, bonded to the functional groups (inner-sphere complex), are located at the  $\beta$ -plane ( $\psi_\beta$ ) so that the layer between the surface and this plane is the inner Helmholtz layer. The outer Helmholtz layer, which hosts the outer-sphere complexes, extends from the  $\beta$ -plane to the d-plane where it finds the onset of the diffuse layer. The potential developed at the d-plane ( $\psi_d$ ) affects the charge distribution of the diffuse layer where the interactions are just electrostatic. The diffuse layer of the GM-EIL share the same characteristics described by the model of Gouy-Chapman.

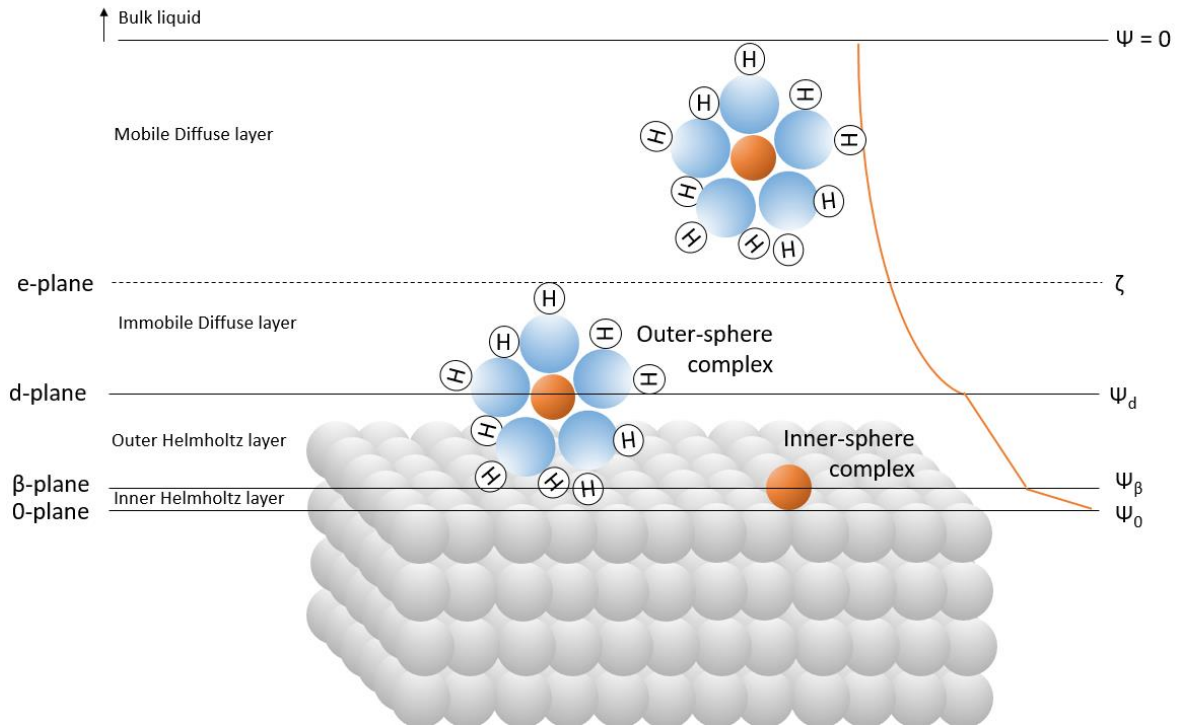


Fig. 2. 3. Scheme of the interface structure according to the General Model of Electrical Interfacial Layer. Adapted from (Kallay et al. 2010).

In the diffuse layer, there is a combination of counter-ions and of co-ions (ions with the same charge as the surface charge). Contrary to the counterions, co-ions have a lower concentration in the diffuse layer than in the bulk of the solution due to repulsive interactions with respect to the surface charge (Speed 2016). The net charge of the surface ( $\sigma_0 + \sigma_\beta = \sigma_s$ ) may be compensated by the charge of the diffuse layer to achieve the electroneutrality of the system (Eq. 2.10).

$$\sigma_0 + \sigma_\beta + \sigma_d = 0 \quad [2.10]$$

Finally, there is the shear plane within the diffuse layer, which defines the line between the stationary liquid and the mobile liquid at the interface. This is the electrokinetic plane or e-plane defined by the  $\zeta$ -potential (also called the zeta potential in the literature). Contrary to the GM-EIL model, for the EDL model the onset of the diffuse layer would be located in the shear plane, so that all the diffuse layer would be mobile.

Finally, it is worth mention that not just pH influences interactions at the solid-liquid interface but temperature and the ionic strength, too. Indeed, an increase of the ionic

strength in the solution constrains the diffuse layer (Speed 2016). This affects the potential and the charge at the d-plane ( $\psi_d, \sigma_d$ ) and at the e-plane ( $\zeta$ ) (Kallay et al. 2010).

### 2.2.3. Adsorption mechanisms

Considering the existence of an interface with a particular structure, the adsorption process cannot be solely described in terms of the surface reaction itself, as represented in the previous equations (Eq. 2.1 – 2.9), but also in terms of mass transport. The whole adsorption process involves several chronological steps describing the mass transfer of the solute from the bulk of the solution to the solid surface where it adsorbs. These steps are known as the adsorption mechanism (Plazinski et al. 2009, Xu et al. 2013, Patel 2019):

- (1) External diffusion: solute is transported from the bulk of the solution to the external limit of the diffusive layer by advection, axial dispersion or diffusion.
- (2) Film diffusion: the solute is transported by molecular diffusion through the film (diffuse layers) to the immobile layer at the surface of the sorbent. It is a concentration gradient driven process.
- (3) Intra-particle diffusion: It includes surface diffusion and pore diffusion. Most adsorbate ions migrate from the surface through pores where there is a greater specific surface area.
- (4) Adsorption-desorption reaction (surface reaction)<sup>3</sup>: Film diffusion may lead to the physical attachment of the solutes onto the surface of the sorbent (surface adsorption). Following intra-particle diffusion, sorbates can also react at the specific sites within the porous structure of the sorbent (pore adsorption or intra-particle adsorption).

The whole process involves three mass transport steps which are actually considered as the adsorption mechanisms together with the surface reaction. The slowest step will be the rate-determining step of the overall adsorption process. Sometimes a

---

<sup>3</sup> Despite the actual surface reaction is that resulting from chemisorption, the term “surface reaction” is used in this context to encompass both kinds of adsorptions (physisorption and chemisorption) in order to differentiate this mechanism from diffusion mechanisms.

combination of several mechanisms can also decide the overall rate of adsorption. A typical rate-controlling mechanism is the intra-particle diffusion. On the contrary, the external mass transport is often neglected. Film diffusion, as the previous step for adsorption, can significantly affect the overall sorption rate and even become the rate-determining step. Its impact is reduced with increasing flow rate and increasing concentration gradient as it follows the Fick's law (Plazinski 2010). Surface reactions have quite often a much faster rate than the other transport mechanisms but they can affect, in some cases, the overall rate and chemisorption, in particular, can significantly weight on adsorption rates (Plazinski et al. 2009, Xu et al. 2013).

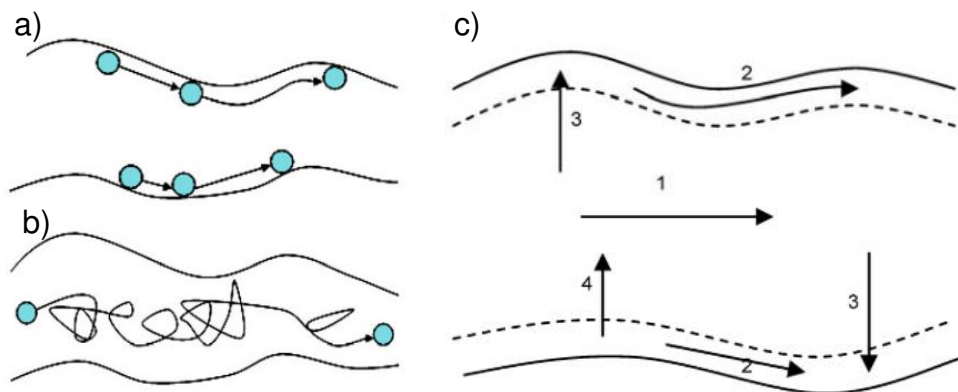


Fig. 2. 4. Schemes of basic adsorption and diffusion steps inside de pore: a) surface diffusion: b) pore diffusion; combination of intra-particle diffusion and adsorption (1. Pore diffusion; 2. Surface diffusion; 3. Adsorption; 4. Desorption). Adapted from (Xu et al. 2019)

A number of factors affect, indeed, the overall adsorption rate; the specific characteristics of the sorbate and the sorbent, as well as, the operation conditions (eg. the adsorbate concentration, the amount of adsorbent, the flow turbulence in solution, temperature pH, etc.). In addition, as adsorption is a time dependent process, the diffusion rate of each stage may vary with time. For instance, in a batch reactor, film diffusion may be fast at the beginning of the adsorption process because of the strong concentration gradient but slows close to as long as solute concentration lowers in the bulk of the solution. Therefore, in order to properly design adsorption processes it is necessary to be able to predict the rate at which this process will take place (Hashemian et al. 2013).

#### 2.2.4. Kinetics of sorption

The transient feature of the sorption process requires an overall rate law capable of explaining the behaviour of the mechanisms involved. Several kinetic models are available for this purpose. Despite, sorption kinetics depends on many factors, simple kinetic models are generally enough to describe the sorption systems successfully. The models can be classified as adsorption reaction or surface reaction models and adsorption diffusion models (Ebelegi et al. 2020). The most commonly applied are the following: the pseudo-first order kinetic model, the pseudo-second order kinetic model and the intra-particle diffusion model. The two first kinetic models are based on the assumption that surface reaction governs the overall rate reaction (Plazinski et al. 2009). For the last case, the complex mechanism of intra-particle diffusion is the rate-determining step.

##### 2.2.4.1. Pseudo-first order kinetics.

Also called the Lagergren model, the rate law is described by Eq. 2.11.

$$\frac{dq_t}{dt} = k_1(q_e - q_t) \quad [2.11]$$

Where  $q_t$  and  $q_e$  account for the amount of sorbed solute per mass of sorbent (mg/g) at time  $t$  and at equilibrium, and  $k_1$  ( $\text{min}^{-1}$ ) is the rate constant of the pseudo-first order equation. The sorbed amount is calculated as the difference in solute concentration at the liquid phase at  $t = 0$  (initial concentration) and  $t = i$  with  $i$  going from 0 to the final time at equilibrium, divided by the sorbent mass. The integration considering  $q_t = 0$  at  $t = 0$  as boundary gives the linearized expression of Eq. 2.12 (Tie et al. 2017).

$$\log(q_e - q_t) = \log q_e - \frac{k_1}{2.303} t \quad [2.12]$$

Plotting the left term of the equation as a function of time allows to determine  $k_1$  and  $q_e$  from the slope and intercept, respectively. It describes well the kinetics of any system where the adsorption rate is proportional to the distance from equilibrium (Marczewski 2010).

#### 2.2.4.2. Pseudo-second order kinetics

A pseudo second order kinetics assumes that the rate of the process depends on the sorption capacity but not the sorbate concentration. Its linearized form is described by Eq. 2.13.

$$\frac{t}{q_t} = \frac{t}{q_e} + \frac{1}{k_2 q_e^2} \quad [2.13]$$

Where  $k_2$  (g/(mg·min)) accounts for the rate constant of pseudo second-order equation. By representing  $t/q_t$  vs time,  $q_e$  and  $k_2$  can be determined from slope and intercept, respectively. The rate-determining step of the sorption processes following the pseudo-second order kinetic is the chemisorption step (Tie et al. 2017).

#### 2.2.4.3. Intra-particle diffusion model

Neither the pseudo-first order nor the pseudo-second order kinetics take into account the diffusion mechanisms (Wu 2007). When the intra-particle diffusion mechanism is the rate-determining step of the sorption process, the rate law applied follows the expression in Eq. 2.14.

$$q_t = k_i t^{0.5} \quad [2.14]$$

Where  $k_i$  (mg/(g·min<sup>0.5</sup>)) accounts for the intra-particle diffusion rate coefficient. It can be calculated from the slope of the plot of  $q_t$  vs  $t^{0.5}$ . If the regression is linear and passes through the origin, then intra-particle diffusion is the sole rate-limiting step, otherwise it can be involved but it is not the solely rate-controlling step (Wu 2007).

#### 2.2.5. Sorption isotherms.

The rate of the adsorption process is an important parameter for designing purposes, but a suitable adsorbent/adsorbate system requires a large adsorption capacity, too. Adsorption kinetics describes the time needed for a particular system to attain the equilibrium, i.e. its adsorption capacity. Thus, the adsorption capacity is defined by the thermodynamics of the adsorption system. During adsorption the mass transfer process proceeds until a dynamic equilibrium state between the residual solute

concentration in the bulk of the liquid and the solute concentration in the solid is attained, this is, the adsorption equilibrium. At equilibrium, the reaction rate of adsorption is the same as for desorption, so that equals amounts of solute adsorb and desorb simultaneously. The equilibrium relationship between the amount of solute adsorbed onto the surface of the solid ( $q$  in mol/unit mass or unit mass/unit mass) and the ion activities (or concentration,  $C$  in mol/unit volume or unit mass/unit volume) at the bulk of the solution at constant temperature depicts a sorption isotherm. The sorption isotherm describes a curve that follows the general equation:

$$q = f(C) \quad [2.15]$$

Sorption isotherms are defined according to the shape of the  $q$  vs  $C$  curve (Fig. 2.5) and they can be classified according to four main types (Giles et al. 1974):

- The “C” isotherm: The ratio between the amount of residual solute in solution and the amount of solute retained onto the solid (the distribution coefficient,  $K_d$ ) is constant at any concentration, which traces a line with zero-origin. This behaviour may result from a proportional increase of active sites with increasing adsorbate concentration.
- The “L” isotherm:  $K_d$  diminishes for increasing concentrations. This forms a concave curve with a plateau meaning that the solid material has a limited sorption capacity. The curve may clearly reach the asymptote (saturation of the solid-strict plateau) or not (without strict plateau). The most used isotherm in soils.
- The “H” isotherm: A particular case of the “L” isotherm, the  $K_d$  coefficient attains the plateau very fast because of a great affinity between the solid and the solute compound.
- The “S” isotherm:  $K_d$  draws a sigmoidal curve which is indicative of the presence of several and opposing mechanisms.

The exact nature of the mechanisms involve in the retention of the solute onto the solid phase cannot be derived from isotherm data. However, one can get an idea of the mechanisms that may be implied, the surface properties or the affinity of the compounds involved (Foo and Hameed 2010). Some models, resulting in the isotherm curves previously described, have been developed – Langmuir, Freundlich, BET,

Temkin, etc. as well as modifications of these models. In some cases these models have theoretical foundation and in other cases are just empirical models.

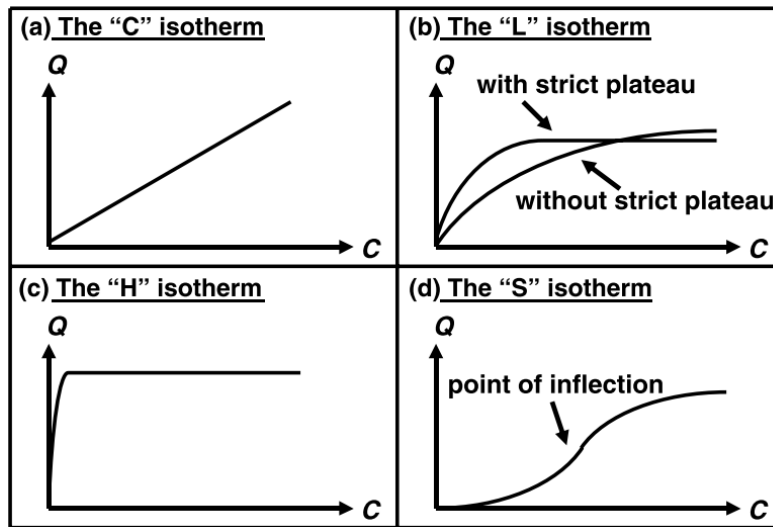


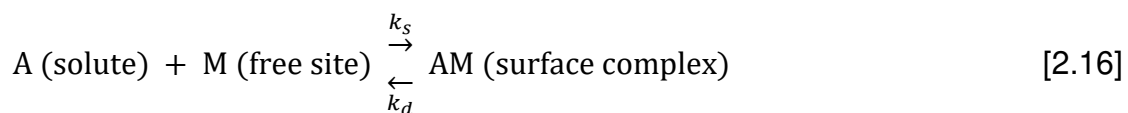
Fig. 2. 5. Main types of isotherm curves according to their shape (Limousin et al. 2007).

### 2.2.5.1. The Langmuir model.

The simplest model is based on three assumptions.

- Adsorption just proceeds in a monolayer coverage (limited adsorption capacity,  $Q_{max}$ ) retaining just one molecule per sorption site
- Sorption sites are equivalent and the surface is perfectly uniform (flat)
- There is no interactions of adsorbed molecules, which means that all sites are energetically independents.

Considering the equilibrium reaction of Eq. 2.16,



Where  $k_s$  and  $k_d$  are the rate constants of the sorption and desorption reaction respectively.

$$\frac{k_s}{k_d} = K_L = \frac{[\text{surface complex}]}{[\text{solute}] \cdot [\text{free site}]} = \frac{q_e}{C_e(q_{max} - q_e)} \quad [2.17]$$

Where  $K_L$  (L/mg) is the adsorption equilibrium constant related to the affinity of binding sites,  $C_e$  (mg/L) is the equilibrium concentration of the solute at the liquid phase,  $q_e$  (mg/g) is the solute equilibrium concentration at solid-phase,  $q_{max}$  (mg/g) is the maximum theoretical amount of solute for a complete monolayer coverage and thus,  $q_{max} - q_e$  is the remaining concentration of free sites. Reorganizing, Eq. 2.18 represents the Langmuir isotherm (L-type) and Eq. 2.19 is the linearized equation (Hashemian et al. 2013).

$$q_e = q_{max} \frac{K_L C_e}{1 + K_L C_e} \quad [2.18]$$

$$\frac{C_e}{q_e} = \frac{1}{q_{max} K_L} + \frac{C_e}{q_{max}} \quad [2.19]$$

By representing  $C_e/q_e$  as a function of  $C_e$ , one can determine  $K_L$  from the intercept with the vertical axis and  $q_{max}$  from the slope of the isotherm. Then, the distribution coefficient, defined as  $K_d = q_{max} K_L$  (L/g), can be also determined. Since ionic and covalent surface reactions can only exist in monolayer, the Langmuir isotherm has been traditionally used to describe chemisorption processes.

Modifications of the basic Langmuir model exist to include for example multisite or competitive sorption (Limousin et al. 2007, Foo and Hameed 2010). However, the simple nature of this model still implies some limitations. (1) Since surface are not completely flat but contain imperfections, the energy of the active sites is not identical. In consequence, the first surface complexes would rather be formed where the highest amount of energy can be released leading to the more stable bond. (2) The coverage of the surface involve a change in the surface charge and thus, interactions between the adsorbed species. Since these interactions may be repulsive, the energy released when new complex are formed is lower than for reactions in a fresh surface. That is, the affinity of the solute for the solid changes with increasing surface coverage. Therefore, most of the assumptions of the model are not applicable in many cases, e.g. heterogeneous surfaces as soils. Still, the Langmuir model can successfully qualitatively described adsorption isotherms of many systems.

### 2.2.5.2. The Freundlich Model

The Freundlich equation (Eq. 2.20), although completely empirical, adds some complexity to model. The use of an exponential parameter involves a change in the affinity of the surface for the solute as the coverage increases. In addition, it admits a multilayer adsorption, reversibility and non-uniform coverage (Foo and Hameed 2010).

$$q_e = K_F C_e^n \quad [2.20]$$

Where the equation parameters are the Freundlich constant  $K_F$  (L/kg) and the heterogeneity factor  $n$  (ad.). The equation may also be written with the exponent equal to  $1/n$ . The isotherm is a non-strict L-type curve, i.e. it does not predict an adsorption maximum. The linearized equation is described by Eq. 2.21.

$$\log q_e = \log K_F + n \log C_e \quad [2.21]$$

Freundlich isotherm is largely used for physical chemical adsorption, and although traditionally used for heterogeneous systems, it can also handle homogeneous surfaces (Xu et al. 2013). It is a successful model to predict adsorption of organic compounds. In this case as well, the Freundlich equation has followed several modifications to include for example competitive adsorption. Despite its popularity, one may criticize its lack of thermodynamic fundamentals (Foo and Hameed 2010).

Other popular models are the Tempkin or the Brunauer–Emmett–Teller (BET) model, more adapted for predictions of gas-solid equilibria but less appropriate for solid-liquid interfaces. Confer to Limousin et al. (2007) and Foo and Hameed (2010) for extended reviews of adsorption isotherm models and the modifications developed for more than 100 years.

### 2.2.6. Sorption thermodynamics

The energetic changes of the sorption process are assessed through thermodynamic parameters as the Gibbs free energy change ( $\Delta G^\circ$ ), the entropy change ( $\Delta S^\circ$ ) and the change in enthalpy ( $\Delta H^\circ$ ). This is a useful tool to determine the nature of the sorption reaction, i.e. whether it is a physisorption or a chemisorption reaction (Wu 2007). The sorption process can be represented by the general chemical reaction in Eq. 2.22:

$$S_l \rightleftharpoons S_s \quad K = \left( \frac{[S_s]}{[S_l]} \right)_{equilibrium} = \frac{C_0 - C_e}{C_e} \quad [2.22]$$

Where  $S_l$  is the sorbate in the liquid phase and  $S_s$  is the sorbate in the solid phase. Since adsorption isotherms are built from equilibrium data, in some cases the model constants can be interpreted as equilibrium constants (e.g. the Langmuir constant (Wu 2007)). The equilibrium constant from Eq. 2.22 is related to the thermodynamic parameters through the Eq. 2.23 and 2.24. By representing the equilibrium constant at different temperatures as a function of the inverse of temperature, one can determine through the Van't Hoff equation (Eq.2.24) the thermodynamic parameters  $\Delta S^\circ$  and  $\Delta H^\circ$  from the slope and intercept of the vertical axis. Then the spontaneity (spontaneous if  $\Delta G^\circ < 0$ ) and so the feasibility of the process can be also calculated from Eq. 2.23.

$$\Delta G^\circ = -RT \ln K \quad [2.23]$$

$$\ln K = \frac{\Delta S^\circ}{R} - \frac{\Delta H^\circ}{RT} \quad [2.24]$$

Thermodynamically favoured sorption reactions are typically exothermic reactions ( $\Delta H^\circ < 0$ ). Nevertheless, spontaneous endothermic sorption reactions have been observed (Ebelegi et al. 2020). Indeed, the entropic contribution to the spontaneity of the process may be significant (Kara et al. 2003). A positive  $\Delta S^\circ$  involves an increasingly degree of freedom at the interface as a result structural changes due to chemisorption (Wu 2007, Ebelegi et al. 2020).

Other useful thermodynamic relationships might be the Clausius-Clapeyron equation or the Arrhenius equation in order to calculate the adsorption enthalpy change and the activation energy, respectively (Kara et al. 2003, Ebelegi et al. 2020).

### 2.2.7. Fix-bed sorption models

Its relative low cost and high efficiency has turned continuous fixed-bed sorption columns into a widely used process to treat pollution of water and wastewaters (McKay 1995). Most industrial systems aiming pollutant removal by adsorption processes are, indeed, fixed-bed filters (Patel 2019). Before the design and operation of a full-scale fix-bed sorption system, the sorption capacity of an adsorbent/adsorbate couple needs to be evaluated. Sorption isotherms are built from batch tests that provide initial

information about the suitability of a specific substrate for the removal of a particular pollutant and its maximum sorption capacity. However, since adsorption columns do not operate in chemical equilibrium and they may present preferential flow patterns, batch experiments cannot provide accurate enough data (Samarghandi et al. 2014). A continuous column experiment is then necessary to determine the characteristic parameters for the scale-up design and operation of the system (eg. amount of adsorbent, system size requirements, contact time, lifespan). That is, a dynamic fixed-bed test.

In a fixed bed system, the water is continuously flowing through the media (the adsorbent) at a constant rate. The pollutant concentration in solution and on the solid phase depends on position and time according to the mass transfer zone (MTZ), the zone of the bed where active adsorption occurs. The pollutant enters the bed and adsorbs almost completely on the first media layers where adsorption sites are available and the pollutant concentration is high. As the adsorption proceeds, the sites of the first layers deplete and the mass transfer zone travels along the column until the whole bed is saturated. Indeed, upstream and downstream the MTZ there is no mass transfer process (Fig. 2.6). Saturation occurs when the concentration of adsorbate on the solid is in thermodynamic equilibrium with the concentration of the inlet solution (Mustafa and Ebrahim 2010). Therefore, when the saturation approaches, the outlet concentration increases until it equates the concentration at the inlet of the column.

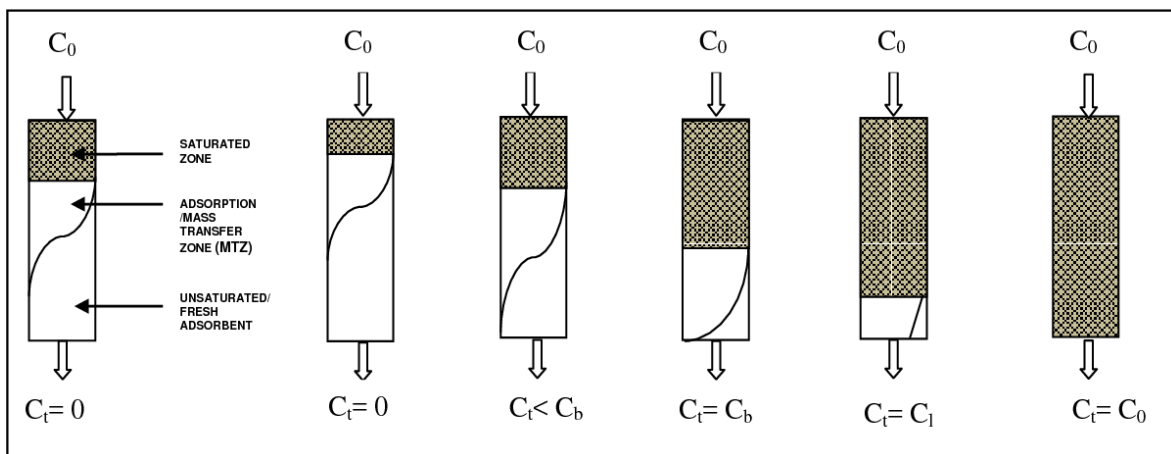


Fig. 2. 6. Schematic representation of the evolution with time of the MTZ wave front, the saturated zone and the fresh adsorbent zone through the fixed-bed column.

The whole process can be described by a breakthrough curve (BTC) (Fig. 2.6). It represents the concentration ratio between the concentration of the pollutant in the effluent at a time  $t$  and the inlet concentration of the pollutant ( $C_t/C_0$ ) as a function of the effluent volume passed through the filter (pore volume). The BTCs can be also expressed as the pollutant concentration in the effluent vs. the elapsed time, or by the ratio  $C_t/C_0$  vs. time, and it describes from the breakthrough point to the saturation of the filter. According to the MTZ,  $C_t/C_0$  is initially zero since all the adsorbate is retained. When outlet concentration attains a detectable level ( $C_b, t_b$ ) or a predefined value which is usually the current legislation limit of a specific contaminant (Lee et al. 2014) or  $C_t/C_0 = 0.05$  (Chowdhury 2013). At this point, the system has attained the breakthrough point indicating that the substrate needs to be replaced/regenerated. Then the breakthrough curve evolves rapidly up to the operating limit point corresponding to a concentration ratio of 0.9 ( $C_i, t_i$ ). At the end of the experiment, the  $C_t/C_0$  ratio must be close to the unit since the adsorption capacity of the substrate is exhausted and so  $C_t = C_e$  (the exhaustion point)  $\approx C_0$ .

The breakthrough capacity and the exhaustion capacity are defined as the mass of sorbate retained per mass of sorbent at the breakthrough and at the exhaustion points, respectively. For industrial-scale applications, the need for replacement and so the sorption capacity of the column is usually calculated as the 50% of the breakthrough curve ( $C_{0.5}, t_{0.5}$ ) (Chowdhury et al. 2015). The form of the breakthrough curve defines, indeed, the characteristics of the adsorption process and so its lifespan (Samarghandi et al. 2014). It depends on the inlet concentration, the flow-rate and the depth of the column (Samarghandi et al. 2014, Chowdhury et al. 2015).

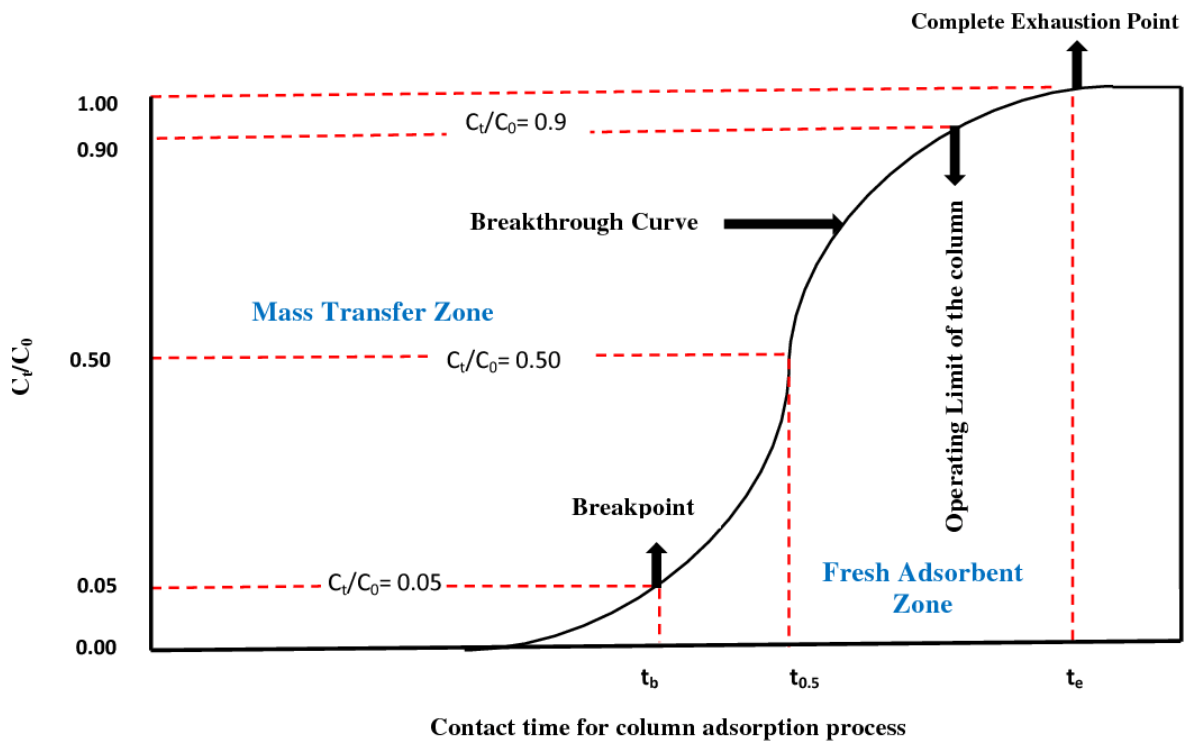


Fig. 2. 7. Scheme of breakthrough curve characteristics (Chowdhury et al. 2015)

The BTCs can be predicted quantitatively by the use of mathematical models in order to design and optimized full-scale fixed bed systems (Lee et al. 2014). A number of models are available. Most models predict the BTC based on the mass conservation law, adsorption kinetics and equilibrium relationship, this is, equilibrium isotherms, axial dispersion, diffusion resistances and reaction kinetics (Xu et al. 2013, Patel 2019). Most of them require numerical methods to solve them but some of them can be solved analytically. Some of the most commonly used models are presented hereafter (Baral et al. 2009, Lee et al. 2014, Patel 2019).

### 2.2.7.1. Thomas Model

The Thomas model (Thomas 1948) combines the Langmuir kinetic model with a second order reversible reaction and plug flow hydraulic regime (no axial dispersion) according to Eq. 2.25. It is, thus, a model based on surface reaction theory.

$$\frac{C_t}{C_0} = \frac{1}{e^{k_T q_0 \frac{X}{Q} - k_T C_0 t} + 1} \quad [2.25]$$

Where  $k_T$  (L/(mg·min)) is the Thomas sorption rate constant,  $q_0$  (mg/g) is the sorption capacity per unit mass of sorbent,  $X$  (g) is the mass of sorbent in the column,  $Q$  (mL/min) is the volumetric flow rate,  $C_0$  (mg/L) is the influent concentration,  $C_t$  (mg/L) is the effluent concentration at time  $t$  (min). The Thomas equation can be linearized resulting in the expression of Eq. 2.26.

$$\ln\left(\frac{C_0}{C_t} - 1\right) = k_T q_0 \frac{X}{Q} - k_T C_0 t \quad [2.26]$$

The Thomas model generally describes sorption processes limited by surface reaction. Nevertheless, it has been demonstrated its applicability for diffusion-limited system too (Mustafa and Ebrahim 2010).

#### 2.2.7.2. Bohart-Adams Model

Also called the bed-depth service time model (BDST) (Bohart and Adams 1920), it is based on the hypothesis that sorption rate is determined by the surface chemical reaction between sorbate and remaining sorbent with no diffusion considered (Samarghandi et al. 2014, Patel 2019). It assumes a proportional relationship between the adsorption rate and both the remaining capacity of the adsorbent and the solute concentration (Lee et al. 2014). Several expressions of this model are available, which derive from expression in Eq.2.27:

$$\frac{C_t}{C_0} = \frac{e^{k_{BA} C_0 t}}{e^{k_{BA} N_0 \frac{Z}{U}} - 1 + e^{k_{BA} C_0 t}} \quad [2.27]$$

and in its linearized form:

$$\ln\left(\frac{C_0}{C_t} - 1\right) = \ln\left(e^{k_{BA} N_0 \frac{Z}{U}} - 1\right) - k_{BA} C_0 t \quad [2.28]$$

Where  $k_{BA}$  (L/ (mg·min)) accounts for the Bohart-Adams rate constant,  $N_0$  (mg/L) is the sorption capacity per unit volume,  $Z$  is the bed depth (cm),  $U$  (cm/min) is the linear flow velocity,  $C_0$  (mg/L) is the influent concentration,  $C_t$  (mg/L) is the effluent concentration at time  $t$  (min).

The Thomas model and the Bohart-Adams model are mathematically equivalent. Therefore, one can determine the model parameters of the other by applying the

relationships of Eq. 2.30 and 2.31 from a simplified version of the BA model (Eq. 2.29) (Lee et al. 2014):

$$\frac{C_t}{C_0} = \frac{1}{e^{k_{BA}N_0\frac{Z}{U}-k_{BA}C_0t}+1} \quad [2.29]$$

$$k_T = k_{BA} \quad [2.30]$$

$$q_0 = \frac{N_0ZS}{1000X} \quad [2.31]$$

Where ZS is the volume of the fixed bed column and ZS/X is the reciprocal of the bulk density of the sorbent ( $\rho_b$ ).

Finally, the expression for the properly called BDST model is shown in Eq. 2.32.

$$t_b = \frac{N_0}{C_0U}Z - \frac{1}{k_{BA}C_0} \ln\left(\frac{C_0}{C_t} - 1\right) \quad [2.32]$$

Where  $t_b$  is the service time or breakthrough time. This expression allows then to describe the relationships between the breakthrough time and the depth of the column.

### 2.2.7.3. Yoon-Nelson Model

The Yoon- Nelson Model (Yoon and Nelson 1984) analyses the breakthrough performance of the column by presuming that the decreasing rate of adsorption for each adsorbate molecule is directly proportional to the probability of adsorbate adsorption and the probability of adsorbate breakthrough on the adsorbent. Therefore, this theoretical assumption implies that there is no involvement of the properties of adsorbate, type of adsorbent or any physical features of the adsorption bed (Patel 2019). The model is described by the expression in Eq.2.33.

$$\frac{C_t}{C_0} = \frac{1}{e^{k_{YN}(t_{0.5}-t)}+1} \quad [2.33]$$

And in its linearized version as Eq.2.34:

$$\ln\left(\frac{C_0}{C_t} - 1\right) = k_{YN}t_{0.5} - k_{YN}t \quad [2.34]$$

Where  $k_{YN}$  ( $\text{min}^{-1}$ ) is the Yoon-Nelson rate constant,  $t_{0.5}$  (min) is the time for 50% of adsorbate breakthrough,  $C_0$  is the influent concentration,  $C_t$  (mg/L) is the effluent

concentration at time t (min). The Yoon-Nelson model is mathematically equivalent to the Bohart-Adam model and so to the Thomas model. Thus, the model parameters can be calculated from the following expressions.

$$k_{YN} = k_{BA}C_0 = k_T C_0 \quad [2.35]$$

$$t_{0.5} = \frac{N_0}{C_0 U} Z = \frac{N_0 Z S}{1000 C_0 U} \quad [2.36]$$

$$t_{0.5} = \frac{q_0 X}{C_0 Q} \quad [2.37]$$

#### 2.2.7.4. Clark model

The Clark model (Clark 1987) uses the laws of mass-transfer in combination with Freundlich equilibrium isotherm under the consideration of plug flow (dispersion is neglected).

$$\frac{C_t}{C_0} = \left( \frac{1}{Ae^{-rt} + 1} \right)^{\frac{1}{n-1}} \quad [2.38]$$

And its linearized form:

$$\ln \left[ \left( \frac{C_0}{C_t} \right)^{n-1} - 1 \right] = -rt + \ln A \quad [2.39]$$

Where A (ad.) and r (min<sup>-1</sup>) are the Clark model constants, n is the Freundlich constant (ad) determined from the adsorption isotherm, C<sub>0</sub> is the influent concentration, C<sub>t</sub> (mg/L) is the effluent concentration at time t (min).

#### 2.2.7.5. Modified dose-response model

The modified dose response model (MDRM) by Yan et al. (2001) is an empirical model that reduces the error between the prediction and the experimental data of the Thomas model especially for very short or very long operation times.

$$\frac{C_t}{C_0} = 1 - \frac{1}{\left( \frac{C_0 Q t}{q_0 X} \right)^a + 1} \quad [2.40]$$

$$\ln\left(\frac{C_t}{C_0 - C_t}\right) = a \ln t + a \ln\left(\frac{C_0 Q}{q_0 X}\right) \quad [2.41]$$

Where  $a$  (ad.) accounts for the modified dose-response model constant,  $q_0$  (mg/g) is the sorption capacity per unit mass of sorbent,  $X$  (g) is the mass of sorbent in the column,  $Q$  (mL/min) is the volumetric flow rate,  $C_0$  is the influent concentration,  $C_t$  (mg/L) is the effluent concentration at time  $t$  (min). The  $a$  constant increases with bed height, decreasing flow rate and decreasing initial concentration of the sorbate (Gokhale et al. 2009).

### 2.2.8. Data analyses

The goodness of the predictions is usually examined by the determination of statistical parameters. Among the most popular for the assessment of linear and non-linear regressions are the sum of square errors (SSE) (Eq. 2.42), the coefficient of determination ( $R^2$ ) (Eq. 2.43) and the chi-square coefficient ( $X^2$ ) (Eq.2.44) (Foo and Hameed 2010, Lee et al. 2014, Ebelegi et al. 2020).

$$SSE = \sum_{i=1}^m (y_e - y_c)_i^2 \quad [2.42]$$

$$R^2 = \frac{\sum_{i=1}^m (y_c - \bar{y}_e)_i^2}{\sum_{i=1}^m (y_c - \bar{y}_e)_i^2 + \sum_{i=1}^m (y_c - y_e)_i^2} \quad [2.43]$$

$$X^2 = \sum_{i=1}^m \left[ \frac{(y_e - y_c)^2}{y_c} \right]_i \quad [2.44]$$

Where  $y_c$  is the predicted data obtained from the model,  $y_e$  is the experimental data, and  $\bar{y}_e$  is the average of experimental data.

### 2.2.9. Adsorption onto apatite

After reviewing the main concepts and models used to describe adsorption processes, it is the moment to focus the discussion on the particular substrate of interest, the apatite, and its capacity for phosphorus sorption from wastewater. A limited number of work relative to phosphate adsorption onto apatite is available in literature. Molle et al. (2005) used the Langmuir model and the Freundlich model to analyse batch

equilibrium data of phosphorus (P) sorption onto apatite. Two sedimentary apatites with differences in the particle size distribution were tested. Both models showed a good correlation with the experimental data ( $R^2 > 0.97$ ) and the theoretical maximum sorption capacity estimated by the Langmuir parameter  $q_{\max}$  was of 4.76 g PO<sub>4</sub>-P/kg apatite. No differences were observed as a result of the differences in particle size distribution. From the representation of the distribution coefficient  $K_d$  vs  $q$  resulting in a convex curve, the author suggested the implication of two different surface reactions during the experiment: adsorption and precipitation.

Bellier et al. (2006) predicted P adsorption capacities of sedimentary and igneous apatites by using the Langmuir model over a phosphate concentration of 5 to 150 mg PO<sub>4</sub>-P/L. The adsorption capacities of the four different apatites tested were in the range of 0.41 to 0.28 g PO<sub>4</sub>-P/kg apatite suggesting that the affinity of apatites for P was limited and below expectations regarding the previous works. A slight difference was noticed, however, regarding the geological origin of the apatite. The sedimentary apatite showed better adsorption capacity than the igneous apatites and authors assigned these results to the lower specific density of the sedimentary apatite.

Leng et al. (2019) also examined the P retention capacity of cow-bone ashes thought as a synthetic phosphate rock, which major composition was hydroxyapatite (13% P). Sorption isotherm data was confronted to both Langmuir and Freundlich model. Langmuir model showed a better regression than Freundlich model and allowed to estimate the maximum theoretical sorption capacity in 75 mg/g at pH 8 and initial phosphate concentration of 100 mg/L. The major P removal process was claimed to be precipitation.

The assessment of P sorption capacity of apatite by sorption isotherms may provide useful information for the comparison of such substrate with others. However, the limitations of this kind of data to predict long-term retention in full-scale fixed-bed systems need to be considered. The goodness of the correlation with the Langmuir model for all cases would suggest that chemisorption is the main sorption surface reaction taking place. Such adsorption, however, would rapidly lead to nucleation and crystal growth and so precipitation will become the most important process for phosphorus retention onto apatite.

The authors agreed to claim that phosphorus sorption on apatite, although considered an important process, it would mostly act just as an initial process leading to further retention by precipitation of calcium phosphates, the latter becoming the predominant process when considering a long-term retention. Thus, on the following the most important concepts about the thermodynamics and kinetics of precipitation/dissolution reactions will be discussed.

### 2.3. Surface precipitation

Precipitation results from the reaction of various solutes in a liquid solution to form a solid phase. Despite it can occur spontaneously in the bulk of a solution, it is usually induced by sorption processes onto surfaces (Fig. 2.8), and therefore so called surface precipitation. Such precipitation is defined as the accumulation of material onto a surface resulting in a three-dimensional structure (Ertl 2009). Indeed, all kinds of surface precipitation are initiated by a sorption process (Anderson and Rubin 1981) and the continuum between both processes depends on the extent of surface coverage. For a low surface coverage ratio, the formation of surface complexes leads the process. As surface coverage increases, some aggregates form on the surface so that both sorption and precipitation take place simultaneously. Later on, at higher surface loadings, precipitation becomes the dominant process (Sparks 2003). On the other hand, precipitation is an important and complex process itself which worth to be discussed in more detail.

Classical theories divide the precipitation process in 3 fundamental steps: (1) supersaturation; (2) nucleation and (3) crystal growth (Hlabse and Walton 1965, Karapinar et al. 2006). Supersaturation is the state for which, for a given temperature, a solution contains more dissolved solute than that given by the equilibrium saturation value (Richardson et al. 2002) respect to a specific solid phase. If such supersaturation occurs, the system tends to equilibrium by precipitating the solute in excess. The precipitation process begins then, with the formation of a nucleus, a visually perceptible three-dimensional accumulation of material. After that, additional deposition of the constituent ions into the crystal lattice of the nuclei may eventually lead to crystal growth until equilibrium is reached (Ohlinger et al. 1999).

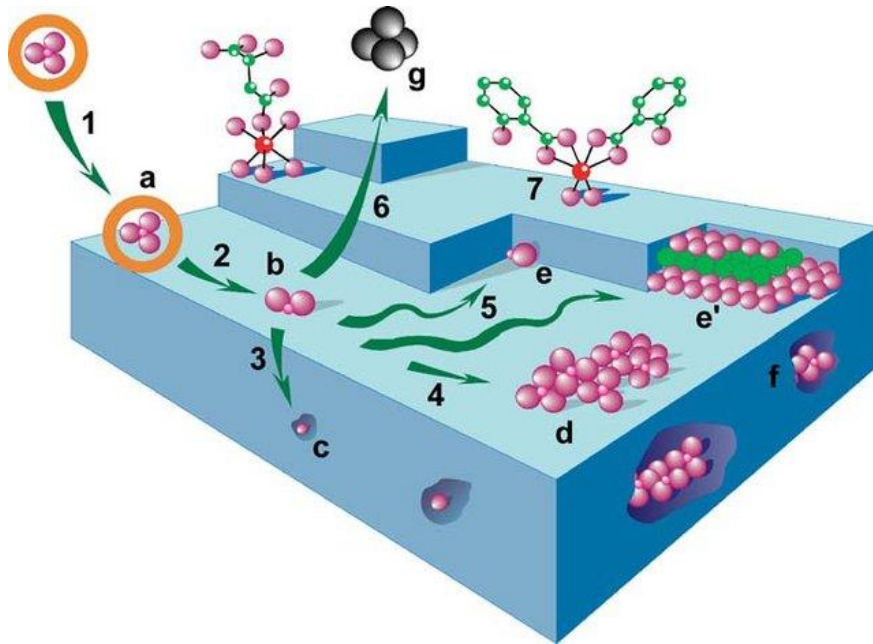


Fig. 2. 8. Scheme of the continuum between sorption and surface precipitation processes. The sorption process initiates with the physical adsorption of a particle forming an outer-sphere complex (a), which can evolve to an inner-sphere complex (b) involving the loss of hydration molecules (2). Once the particle is chemically bond to the surface several processes can take place: isomorphous substitution within the mineral lattice (c); formation of a surface polymer (d), or adsorption on a ledge (e and e'); desorbed back in solution, either as a result of dynamic equilibrium or as a product of a surface reaction (e.g. redox)(g). The particles retained on a ledge or nucleating as a surface polymer will contribute to lattice growth ending up embedded in the crystal, surface precipitation (f). The numbers in the image account for mass transfer processes: film diffusion (1 and 6); diffusion into the lattice (3) lateral diffusion (4 and 5). (Panfili 2004)

Three different types of nucleation exist: primary homogenous nucleation, primary heterogeneous nucleation and secondary nucleation. In the absence of impurities or surface influences, the birth of a crystal can take place spontaneously in the bulk of a solution, and is called primary homogeneous nucleation (Peng et al. 2018). The presence of impurities or seed materials in contact with the solution lowers the required activation energy for surface nucleation to occur. Indeed, precipitation will rather take place onto a surface than in the bulk of a solution. Two kinds of surface nucleation can be distinguished depending on the nature of the surface catalysing the process: primary heterogeneous nucleation and secondary nucleation. In the first kind, any impurity or foreign particle (container walls, dust...) can act as a catalyser for the foundation of embryo nuclei (Ohlinger et al. 1999). In secondary nucleation, however, the seed particles are crystals of the same composition as the precipitate under consideration (Botsaris 1976, Richardson et al. 2002), which requires a much lower supersaturation than primary nucleation to occur.

Finally, another distinction can be made when the precipitate is constituted of both the solute species from the solution and the dissolved species from the same mineral serving as catalyser as a result of its own interactions with the liquid phase. The process is then called coprecipitation. It is, indeed, a dissolution-reprecipitation process that takes place when, parallel to the diffusion of the solute to the vicinity of the surface, the substrate dissolves resulting in chemical changes at the interface: the concentration of various solutes increases generating variations in pH and increasing supersaturation (Godelitsas and Astilleros 2011). Such changes lead to the heterogeneous nucleation of a new solid phase with different composition than the catalyst (Sparks 2003). This kind of process is useful in the sequestration of metals. The term coprecipitation is also used for the simultaneous precipitation of different solid phases because of the presence of various dissolved ions that cause supersaturation for more than one solid phase (Prieto et al. 1997); or due to the incorporation of foreign particles in the lattice of the precipitate (isomorphic substitutions) (Sposito et al. 1989). In all these cases, the resulting precipitate is generally a solid solution (SS).

A SS is a non-stoichiometric and homogeneous solid phase with minor substituents distributed uniformly in the lattice (Prieto et al. 2016). For example, coprecipitation of a calcite-hydroxyapatite solid solution because of the coexistence of carbonates, phosphates and calcium ions in a saturated solution. The resulting SS would be a sort of carbonated hydroxyapatite. Another example would be the isomorphic substitution of Sr in the lattice of hydroxyapatite because of the presence of Sr traces in a solution saturated with calcium and phosphates. A solid solution is, indeed, a metastable solid phase which can follow successive dissolution-recrystallization processes driven by the thermodynamics of the end-member (the most stable pure solid phase) until its stoichiometric composition is attained (e.g. the strontianite-calcite metastable solid solution will tend to release Sr until just calcite is present in the solid phase) (Prieto et al. 1997). Of course, this process can take a long time to complete.

## 2.3.1. Mechanisms of nucleation and crystal growth

### 2.3.1.1. Homogenous nucleation

In a supersaturated solution, solute ions in molecular thermal agitation or in convective movement collide with each other and form reversible aggregates, the so called embryos. Such embryos are able to continue growing or to resorb depending on the interfacial tension developed. When the aggregates are formed of few particles, interfacial surface per volume of the aggregate is high, and so it is the interfacial tension associated (Fritz and Noguera 2009). If the embryo achieves a volume large enough that the free energy developed by the aggregation exceeds the interfacial tension, the growth will continue until the formation of a nucleus (Fig. 2.9). Imagining aggregates as spheres according to the classical theories (devoid of any chirality consideration), the stabilisation of the aggregate is achieved at a critical size characterised by a critical radius  $r_c$  whose value depends in the degree of supersaturation. However, the degree of supersaturation evolves during the nucleation process and so it does the critical radius (Fritz and Noguera 2009). Supersaturation is usually high at the beginning of nucleation and decreases as the solute is incorporated into new nuclei and/or used for crystal growth. In the same way, the critical radius is small for initial high supersaturations and increases with supersaturation reduction. Such evolution results in a race where those nuclei formed at sufficient speed that the critical radius for a specific supersaturation is attained remains stable and continue to grow, but those who does not re-dissolved and incorporate into greater nuclei (Anderson and Rubin 1981).

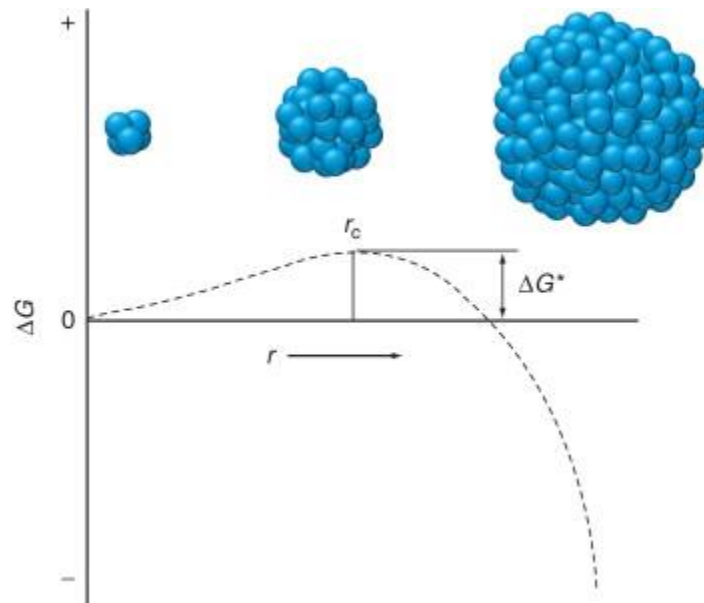


Fig. 2. 9. Classical picture of aggregation, nucleus formation, and beginning crystal formation from supersaturated solution;  $r$  is the radius and  $r_c$  is the critical radius at which point aggregation leads to overall stabilization (Kellogg and Leeman 2012).

### 2.3.1.2. Heterogeneous precipitation

Mechanisms of heterogeneous nucleation are still not completely understood (Elliott 1988, Richardson et al. 2002). The process is believed to be started by adsorption of molecules onto preferential sites on whatever surface (dust, container walls, suspended solid particles, lattice-mismatching crystals) in contact with a supersaturated solution (Richardson et al. 2002, Kamano et al. 2014). Lattice accidents and imperfections are responsible for creating these effective nucleation sites. The maximum contact that can be provided between the surface and the ion the more effective the nucleation site (cavity > step > flat face, in decreasing order of effectiveness, see Fig. 2.10) (Anderson and Rubin 1981).

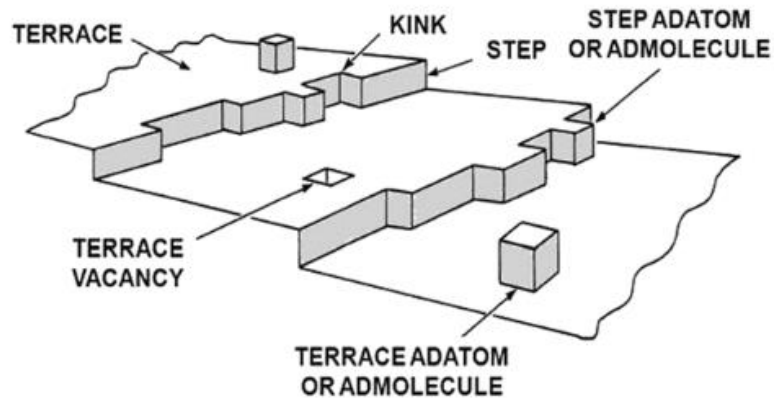


Fig. 2. 10. Structural defects of a crystal surface at the nanoscale (nanotopography).

The presence of a surface reduces the interfacial energy between the liquid and the nucleus since a part of it is in contact with the solid-nucleus interface (Anderson and Rubin 1981, Elliott 1988, Liu 2001). Some of the hypothesis used to explain this effect are: the interfacial energy developed between two solids is lower compared with a solid and a liquid, and is zero when the seed and the nucleus have identical composition (secondary nucleation); the solubility in the vicinity of the surface is lower with regards to the bulk of the solution because of an also lower dielectric constant; activity of surface precipitate lower than 1; among other reasons.

As a consequence of a reduced interfacial energy, the energy barrier to overcome to allow nucleation is reduced, and the critical nucleus size can be achieved at lower saturation ratios. How much effective is this reduction of the energy barrier depends on the contact angle between the solid surface and the nucleus. The nucleation may be built either in a 2-dimensional structure or in a 3-dimensional growth or island growth depending on the magnitude of the contact angle (Liu and Dandy 1995). When it is greater than zero, the cohesion forces are greater than the adhesion forces leading to the 3-dimensional nucleus. Inversely, a contact angle equal to zero leads to a layer-by-layer growth. The opposite case happens when the contact angle equals  $\pi$ , this is, no contact exists at all between the nucleus and the surface. Homogeneous nucleation can be understood, indeed, as a specific case of heterogeneous nucleation (Liu 2001).

### 2.3.1.3. Secondary nucleation

In secondary nucleation, the crystal surface participates actively in the formation of nuclei by possibly two different mechanisms: one originating in the solution and the other one on the crystal. In the former case, the nuclei forms due to the properties of the solution layer adjacent to the surface. The embryos formed in the supersaturated solution are attracted to the surface of the seed crystal by van der Waals forces where, in great concentration, are able to coagulate to form nuclei of bigger size than the critical size (Agrawal and Paterson 2015). Then the nuclei may be remove from the surface by fluid shear or collision. This is known as the Embryo Coagulation Secondary Nucleation theory. This mechanism is affected by supersaturation in two different ways: (1) the critical size of the nucleus decreases with increasing supersaturation; (2) the thickness of the adsorbed layer increases with increasing supersaturation so that, more embryos are available for the nucleation.

When the nucleation originates directly on the surface of the crystal, lattice structural defects as seen for heterogeneous nucleation induced preferential site precipitation. Depending on several aspects like local supersaturation conditions, fluid hydrodynamics or the microscopic roughness (microtopography) of the surface, the precipitation onto the surface can evolve as clusters or as an apparent continuous layer (Fig. 2.11). The clusters can take a dendritic or needle form that can be removed from the seed surface by mechanical forces (fluid shear or collision) in agitated crystallisers systems (Agrawal and Paterson 2015) or continue to grow to macroscopic dimensions in fixed-bed systems. Clusters are usually formed as a result of a fast growth induced by high levels of supersaturation and mass transfer (diffusion) controlled grow rates (Botsaris 1976).

The deposition can also be carried out in more or less constant layers over the seed surface. Solute ions adsorbed onto the previously mentioned surface sites and become an integral part of the seed crystal lattice (integration), e.g. the adsorption onto a molecular step making it larger or completing it (Fig. 2.12). The precipitate is then made of superposed sorbed ion layers that become an integral part of the seed crystal. As the composition of the seed and the sorbent are the same, such sorption reactions are part of the precipitation process contributing, indeed, to crystal growth (Anderson and Rubin 1981, Sparks 2003).

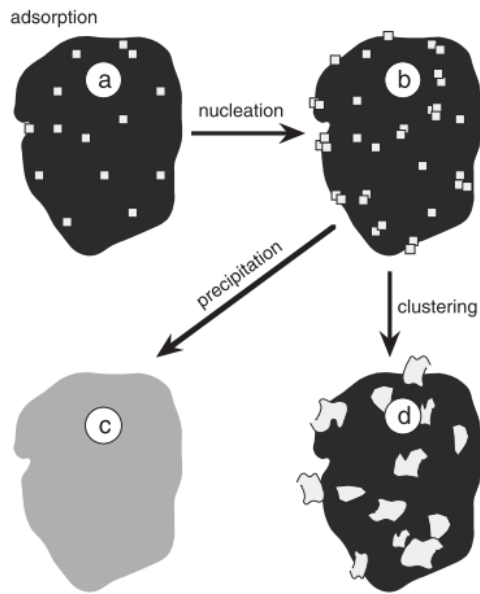


Fig. 2. 11. Evolution of sorption phenomena with surface coverage (Sparks 2003)

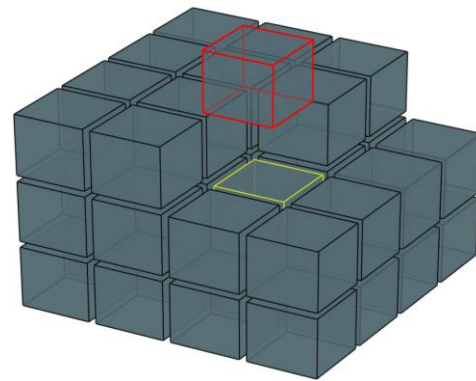


Fig. 2. 12. Adsorption of a solute particle in the edge of a molecular step contributing to the lattice growth.

Most of the literature concerning secondary nucleation has been developed from, or addressed to, industrial crystallising processes. In batch-agitated crystallisers most nuclei formed at the surface of the seed crystal are ejected (Fig. 2.13), due to mechanical forces (agitation, collision...), again to the bulk of the solution where they continue to grow. These ejected nuclei are said to be secondary nucleated. When considering surface precipitation in a fixed-bed column, these mechanical forces do not apply and the nuclei formed onto the surface of the seed material remains on the surface contributing, indeed, to its crystal growth.

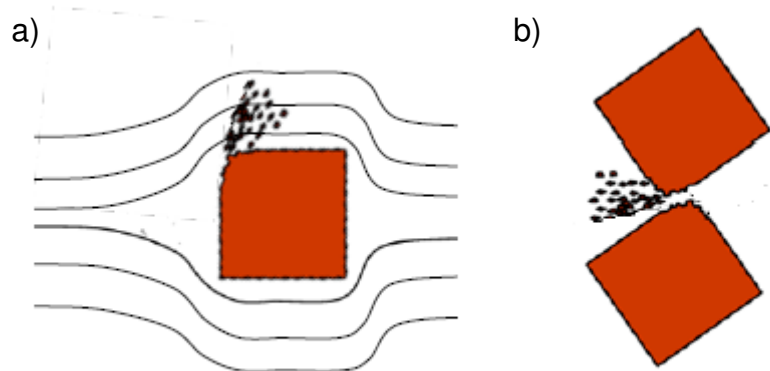


Fig. 2. 13. Examples of nuclei removal from the surface of a seed crystal by a) fluid shear, b) collision. The ejected particles are secondary nucleated nuclei that will continue to grow separated from their parent's seed in a crystalliser.

#### 2.3.1.4. Crystal growth

Crystal growth involves the incorporation of new particles in the crystal lattice in such a way that the crystal size increases at the macroscopic scale. Such process involves three successive steps: (1) the mass transport from the bulk of the solution to the crystal/solution interface by diffusion through the diffuse film; (2) the adsorption of the solute onto the surface sites (imperfections/accidents); and (3) the integration of the adsorbed particle into the lattice (Anderson and Rubin 1981). In crystal growth the activation energy required is derived from the release of the hydration molecules of the adsorbed ion and so the growth rate is usually reaction limited or interface controlled. The diffusion limited growth rate is however also possible for low saturation ratios.

Since the density of the imperfections like dislocations or steps is usually high, crystal growth may occur simultaneously from many points of the crystal leading to the appearance of a surface roughness. In cases where supersaturation is high, a fast precipitation can even result in the formation of macroscopic dendrites (Botsaris 1976). A crystal can continue to grow or age until it achieves a thermodynamic equilibrium between the solid phase and the solution by successive dissolution and re-precipitations steps. This thermodynamic equilibrium would imply the formation of a unique large crystal. However, as for any system approaching equilibrium, the reaction rate becomes very low and long times are needed to attain it. This is particularly true for solid phases with low solubility (Anderson and Rubin 1981).

### 2.3.2. Thermodynamics of precipitation

A basic understanding of precipitation thermodynamics, as well as, the kinetic and mechanistic aspects that define and govern precipitation performances is required (Godelitsas and Astilleros 2011). On the following, a basic explanation of these aspects will be given.

For any chemical reaction, its equilibrium state is described by a thermodynamic equilibrium constant. In the case of precipitation/dissolution reactions, this constant is called the solubility product ( $K_{sp}$ ) and it is defined as the product of activities of the species ( $a_i$ ) participating in the reaction raised by their stoichiometric numbers ( $\nu_i$ ) at equilibrium.

$$K_{sp}^{\circ} = \prod_i a_i^{\nu_i} \quad [2.45]$$

The reaction equilibrium is also described by the change of the Gibbs free energy,  $\Delta_r G$ , at constant pressure, which depends on the reaction entropy,  $\Delta_r S$ , and enthalpy,  $\Delta_r H$  and is related to the equilibrium constant as shown in Eq.2.46.

$$\Delta_r G^{\circ} = \Delta_r H^{\circ} - T\Delta_r S^{\circ} = -RT \ln K_{sp}^{\circ} \quad [2.46]$$

Where R accounts for the ideal gas constant, T is the absolute temperature,  $^{\circ}$  refers to standard conditions ( $P = 10^5 \text{Pa}$ ) of the extensive properties. As a thermodynamic constant, the value of the solubility product depends on temperature. The van't Hoff equation allows the correction of the  $K_{sp}$  as a function of temperature as shown in Eq; 2.47 and 2.48 (integrated form).

$$\frac{d}{dT} \ln K_{sp} = \frac{\Delta H^{\circ}}{RT^2} \quad [2.47]$$

$$\ln \frac{K_{sp,2}(T_2)}{K_{sp,1}(T_1)} = \frac{-\Delta H^{\circ}}{R} \left( \frac{1}{T_2} - \frac{1}{T_1} \right) \quad [2.48]$$

For any conditions other than the standard conditions, the Gibbs free energy for a homogenous nucleation is described by:

$$\Delta_r G_{hom} = \Delta_r G^{\circ} + RT \ln \prod_i a_i^{\nu_i} = -RT \ln \frac{IAP}{K_{sp}} \quad [2.49]$$

Where IAP is the free Ionic Activity Product for a specific precipitate compound. The relationship between the ion activity product and the solubility product constant is known as the saturation ratio ( $\Omega$ ).

$$\Omega = \frac{IAP}{K_{sp}} \quad [2.50]$$

Which can also be expressed as the saturation index (SI):

$$SI = \log \frac{IAP}{K_{sp}} \quad [2.51]$$

SI measures the deviation of a dissolved salt from its equilibrium state. When  $SI > 0$  ( $\Delta_rG < 0$ ) the solution is supersaturated with regard to a specific and stoichiometric solid phase and it will spontaneously tend to equilibrium ( $SI = 0$  or  $\Delta_rG = 0$ ) by the precipitation of the excess solute. If  $SI < 0$  the dissolution of the solid phase will take place (since  $\Delta_rG > 0$ , so the backward reaction is spontaneous. The SI assesses, indeed, the supersaturation level of a solution with respect to a particular precipitate phase and its spontaneous tendency to precipitate or dilute.

A typical approximation in the determination of the saturation ratio is to consider the system at an ideal state. In such a case, the activity, defined as the activity coefficient of the specie multiplied by its concentration (Eq. 2.52), can be approximated to the concentration. Indeed, the activity coefficient, which determines the deviation from the ideal state, is one for an ideal solution. As the ideal state of a solute is defined as the absence of interactions with other solutes, this kind of approximation just applies for dilute solutions (below  $10^{-2}$  mol/L) (Kallay et al. 2011).

$$a_i = \gamma_i C_i \approx C_i \quad [2.52]$$

When non-ideality needs to be considered, one can use the Debye-Hückel equation or the Davies equation to calculate the activity coefficient.

It can be also common to speak of supersaturation in absolute terms. When the approximation applies, the absolute supersaturation ( $\Delta C_i$ ) is defined by the expression in Eq. 2.53; where  $C_i$  is the solution concentration of the specie  $i$  and  $C_i^{eq}$  accounts for the equilibrium state (Richardson et al. 2002, Baillon et al. 2015).

$$\Delta C_i = C_i - C_i^{eq} \quad [2.53]$$

Precipitation is therefore a thermodynamically driven process that depends on the solubility of the most stable pure solid phase (or end-member in SS) and the free energy change. Since the chemical potential is, indeed, the partial molar Gibbs energy with respect to the specie  $i$ , another thermodynamic expression for supersaturation can be given, as shown in Eq. 2.54. In other words, the driving force for nucleation is the change in the chemical potential ( $\Delta\mu$ ) (Ohlinger et al. 1999).

$$\Delta_r G = \sum_i v_i \mu_i \quad ; \quad \mu_i = \left( \frac{\partial G}{\partial n_i} \right)_{T,p,n} \quad ; \quad \frac{\Delta\mu}{RT} = - \ln \frac{IAP}{K_{sp}} \quad [2.54]$$

The same as for the Gibbs free energy, the system is supersaturated when  $\Delta\mu < 0$ .

Based on the degree of supersaturation, two states are possible: labile or unstable supersaturation, and metastable supersaturation. As shown in Fig. 2.14, these zones are delimited by two different curves: the supersolubility curve defines the limit between the labile and metastable zone; instead, the solubility curve defines the limit between the unsaturated zone where precipitation is not possible and the supersaturated metastable zone. Conditions at the labile or unstable supersaturation allow the primary homogenous nucleation (spontaneous). Conditions at the metastable supersaturation only allow catalyzed nucleation and crystal growth. Thus, precipitation processes based on primary heterogeneous or secondary nucleation take place at the metastable zone, which requires lower levels of supersaturation.

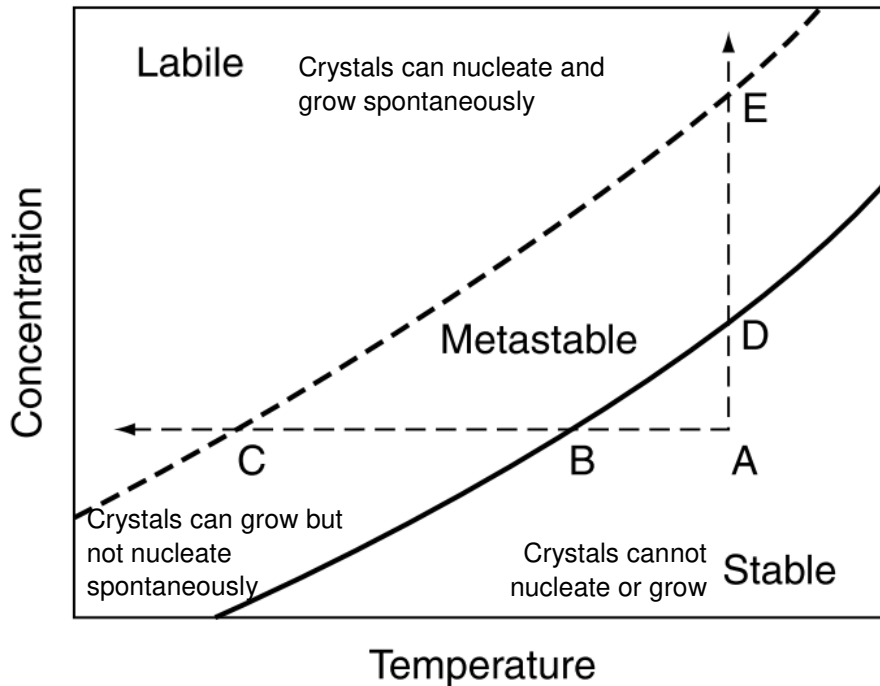


Fig. 2. 14. Solubility supersolubility diagram (concentration vs temperature): the continuous line represents the solubility curve and the break line the supersolubility curve. (Richardson et al. 2002)

The previously discussed thermodynamic expressions just give information of the willingness of a system to spontaneous precipitation, but nothing is said about how much precipitate is formed or the size of the crystals. One could use the kinetic expressions for this purpose.

### 2.3.3. Kinetics of precipitation

Despite precipitation is a thermodynamically driven process, reaching equilibrium can take a long time. The most thermodynamically favored solid phase may not be the most kinetically favored, leading to the formation of metastable intermediates going from the amorphous phase to the final stable phase (Chung et al. 2008). This phenomena is known as the Ostwald's step rule (Ostwald 1897). Passing through intermediate states involves the smallest amounts of free energy release per step but also requires the lowest amount of activation energy, as shown in Fig. 2.15, which makes this transient pathway thermodynamically feasible (Chung et al. 2008). Sufficiently low activation energies can lead to these transitions by simple atomic

displacements in the lattice structure caused by thermal fluctuations. Examples of systems following the Ostwald's step rule are the polymorphs of crystals: its kinetically favored metastable form can grow rapidly at high supersaturations forming stable large crystals and preventing nucleation of the most thermodynamically favored form (Anderson and Rubin 1981). Thus, kinetic and mechanistic factors play a major role in the determination of the precipitates composition, size and shape,

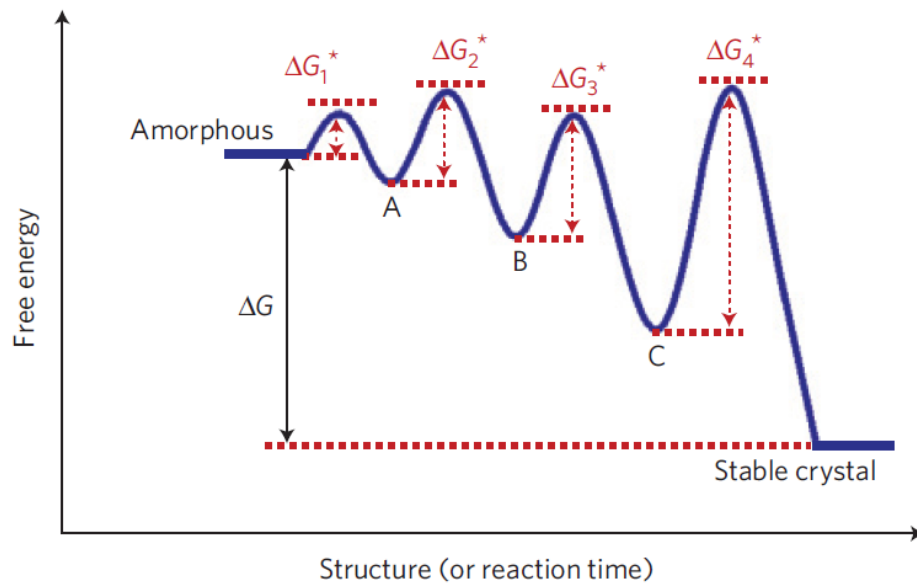


Fig. 2. 15. Schematic diagram of a transition pathway during crystallization.  $\Delta G$  indicates the driving force from amorphous to a stable final solid phase through the metastable intermediate phases (A, B, C). The activation energy required for each step is indicated as  $\Delta G_i^*$  where  $\Delta G_1^* < \Delta G_2^* < \Delta G_3^* < \Delta G_4^*$ . (Chung et al. 2008)

Precipitation kinetics can be separated into two phases: nucleation and growth (Ohlinger et al. 1999). The relevance of each phase in the overall reaction rate will depend on the system conditions.

In homogeneous precipitation, there is a time lapse between the mixing of precipitate constituents in a supersaturated solution and the appearance of the first measurable precipitates known as the induction period. Both nucleation and crystal growth occur during the induction time, however, nucleation is usually the rate-determining step of the whole process and so, it is usually assumed to be the essential step affecting the kinetics at initial times of the process (Ohlinger et al. 1999, Richardson et al. 2002). For primary nucleation, it can be calculated from the inverse of the determined nucleation rate (Ohlinger et al. 1999, Peng et al. 2018).

### 2.3.3.1. Nucleation kinetics

In homogenous nucleation, the previously described competition between the interfacial tension developed and the free energy of formation is the major kinetic driver of the process (Fritz and Noguera 2009). The most well-known model in the description of precipitation or crystallisation processes is based on classical nucleation theory (CNT) proposed by authors as Gibbs, Volmer and Weber. The CNT model is based on the concept of overcoming an energetic barrier (activation energy) to allow the formation of a nucleus. Although more recent models have overcome some limitations of the CNT model, e.g. the two step nucleation theory (Kamano et al. 2014), a full discussion of the subject exceeds the scope of this work. On the following, the kinetic equations derived from the still largely used CNT model will be used to describe some simple nucleation systems. For a complete description of the kinetic models derived from the CNT confer to (Fritz and Noguera 2009) .

Thus, according to the CNT, the nucleation rate ( $J$ ) of a spherical one-solid-phase nucleus is described by Eq.2.55:

$$J = k_n \exp\left(\frac{-\Delta G^*}{k_B T}\right) \quad [2.55]$$

Where  $\Delta G^*$  is the free energy of formation of nuclei of critical radius  $r_c$  or activation energy defined as shown in Eq. 2.56; ,  $k_B$  is the Boltzmann constant, and  $k_n$  is a kinetic prefactor depending on many other parameters but usually empirically determined (Fritz and Noguera 2009).

$$\Delta G_{hom}^* = \frac{4\pi}{3} r_c^2 \sigma \quad [2.56]$$

Where  $\sigma$  is the interfacial tension or surface energy, and  $r_c$  is defined as follows:

$$r_c = \frac{2\sigma v}{k_B T \ln \Omega} \quad [2.57]$$

Where  $v$  accounts for the molar volume of the nucleus.

In heterogeneous nucleation, a correction needs to be applied to the activation energy to account for the reduced surface interactions (at the liquid/nucleus interface) and the new interface interactions between the seed and the nucleus. Such interactions

depend on the contact angle ( $\theta$ ) of the nucleus with the seed surface (or nucleant) (Fig. 2.16), as described in Eq. 2.58.

$$\phi(\theta) = (1 - \cos\theta)^2(2 + \cos\theta)/4 \quad [2.58]$$

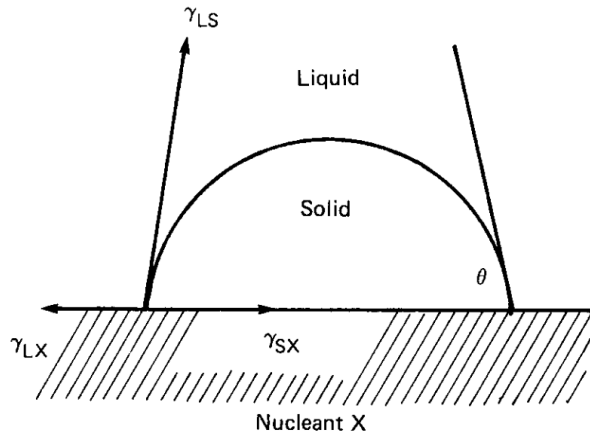


Fig. 2. 16. Spherical or cap-shaped nucleus onto a substrate (or nucleant X) where  $\gamma$  represents the interfacial energy of the different interfaces liquid-solid, nucleant-solid and nucleant-liquid, and  $\vartheta$  is the contact angle (Elliott 1988)

From Eq.2.59, it follows that the activation energy required for heterogeneous nucleation will always be lower than for homogenous nucleation (Fritz and Noguera 2009) because of a reduced surface free energy (Liu 2001) causing an enhancement of the nucleation rate for lower saturation ratios as it is schematically represented in Fig. 2.17.

$$\Delta G_{het}^* = \frac{144\pi}{27} \cdot \frac{\phi(\theta)\sigma^3 v^2}{(k_B T \ln \Omega)^2} \quad [2.59]$$

The major inconvenient of the equations derived from the CNT is the difficulty to determine the energy barrier ( $\Delta G^*$ ) (Liu 2001) and the contact angle (Elliott 1988), in the specific case of heterogeneous nucleation. The little practicality of the previously shown equations in industrial-scale processes has lead to the use of more empirical relationships for both kinds of primary nucleation like the one shown in Eq. 2.60 (Richardson et al. 2002).

$$J = K_N (C - C^*)^n \quad [2.60]$$

Where  $K_N$  is the primary nucleated rate constant and  $n$  is the order of the nucleation process (usually  $>2$ ). Both parameters depend on the physical properties and hydrodynamics of the system.

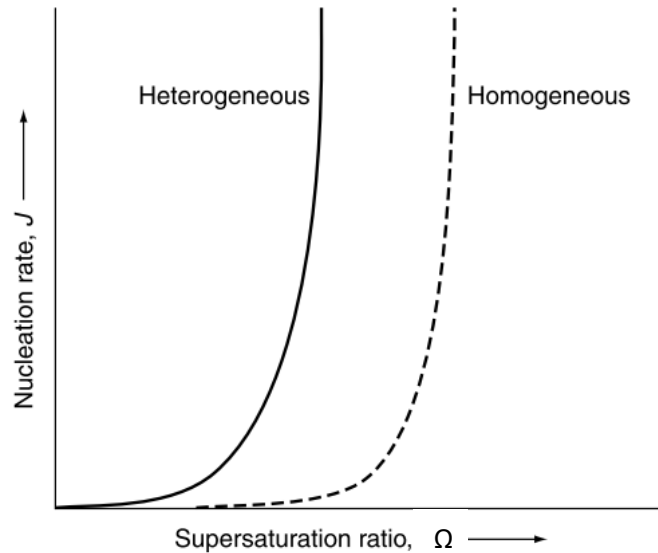


Fig. 2. 17. Effect of supersaturation on the nucleation rates for homogeneous and heterogeneous reactions. (Richardson et al. 2002)

### 2.3.3.2. Crystal growth

Since multiple steps are involved in crystal growth, a first approach would require determining the rate-controlling step of the process. The rate law can be, indeed, diffusion limited or surface-integration limited during both the induction period and after it (Fig. 2.18). When supersaturation and roughness of the surface at the nanoscale (maximum of available sites for growth units) are high, the film resistance is minimum and therefore the process is surface-integration limited (Fritz and Noguera 2009).

An expression for crystal growth of one pure solid phase (not SS) close to the critical radius, and for crystal growth at macroscopic dimensions (size larger than critical radius), is given in Fritz and Noguera (2009) (Eq. 2.61 and 2.62):

$$\frac{dr}{dt} = \kappa \left[ \Omega - \exp\left(\frac{2\sigma v}{k_B T r}\right) \right] \quad [2.61]$$

$$\frac{dr}{dt} = \kappa [\Omega - 1] \quad [2.62]$$

Where  $\kappa$  is the proportionality constant. The same expression is used for diffusion limited crystal growth by replacing  $\kappa$  by  $\kappa/r$ . These equations show the dependency with size and saturation of the rate law. In addition, since the size of the crystal and the saturation, in a batch crystalliser, evolve with time, the expressions describing the growth law would also require to be size and saturation dependant (Fritz and Noguera 2009) among other things (temperature, habit, turbulence... (Richardson et al. 2002)). Such dependency leads to a much more complex expression of the rate law (confer. to Fritz and Noguera (2009)). However, crystal growth in a fixed-bed column where the system is continuously replenished with fresh influent, the saturation conditions stay approximately constant with time. This has two immediate consequences: first, crystal growth is just limited by the physical space available (porosity of the filter bed); second, saturation dependence with time can be neglected. In addition, it is usually more interesting from the process performance perspective, to talk about deposited mass or retained mass rather than size of crystal. Thus, when mass transport governs the rate of the overall reaction, the expression takes the form of the Fick's law for diffusion (Ohlinger et al. 1999). With regards to surface-integration limited crystal growth, the difficulty of assessing the kinetic parameters given that multiple mechanisms can operate in parallel or sequentially (Ohlinger et al. 1999), has prevent the use of classical theories' models and enforced the application of empirical models (Richardson et al. 2002). Such is the case of the expressions in Eq. 2.63 (Richardson et al. 2002) describing the rate for the overall crystal growth process ( $R_G$ , usually given as  $\text{kg}/(\text{m}^2\text{s})$ ) provided that the approximation for ideal solution ( $\gamma = 1$ ) can be applied.

$$R_G = \frac{dm}{dt} = K_G(C - C^*)^s \quad [2.63]$$

Deduced from:

$$\frac{dm}{dt} = k_d A(C - C_i) = k_r(C_i - C^*)^i \quad [2.64]$$

Where  $C$  is the concentration of the specie in the bulk of the solution;  $C^*$  is the concentration of the interface at equilibrium saturation;  $i$  is the order of integration (reaction);  $s$  is the order of the crystal growth process (both  $i$  and  $s$  do not have a mechanistic or kinetic signification associated) which is usually in the range of 1 to 2; and  $K_G$  is the global rate constant, which can be defined as follows when  $i=1$  and  $s = 1$ :

$$\frac{1}{K_G} = \frac{1}{k_d} + \frac{1}{k_r} \quad [2.65]$$

Where  $k_d$  and  $k_r$  account for the diffusion mass transfer coefficient and the reaction mass transfer coefficient, respectively. When  $k_d \approx K_G$  the crystal growth is diffusion controlled, on the opposite case  $k_r \approx K_G$  the deposition step controls the overall rate.

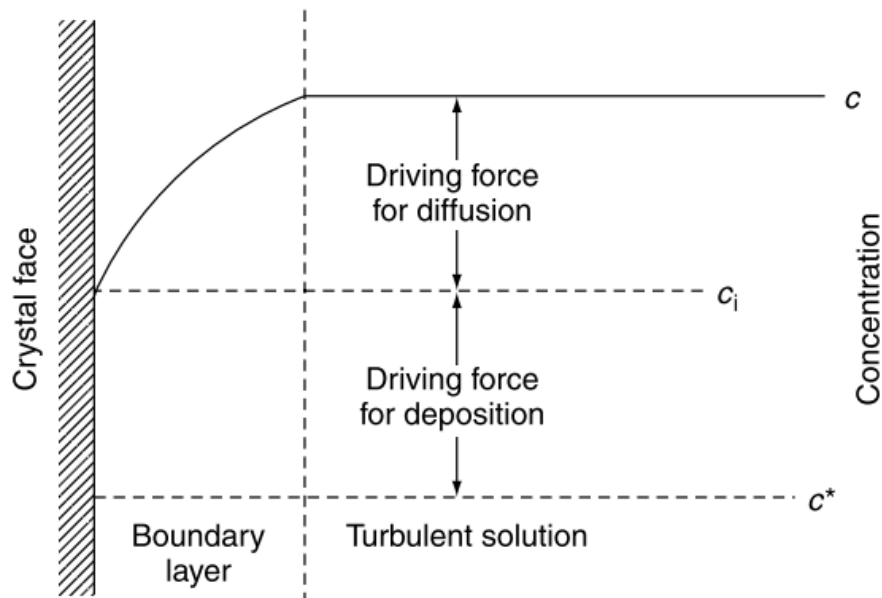


Fig. 2. 18. Scheme of the driving forces for crystal growth, where  $C$  is the concentration at the bulk of the solution,  $C_i$  is the concentration at the interface and  $C^*$  is the concentration at equilibrium. (Richardson et al. 2002).

#### 2.3.4. Calcium phosphate precipitation onto apatite

From reviewing the main concepts about precipitation/dissolution reactions is easy to understand the complexity behind these processes. This is especially true in the case of calcium phosphates with all their polymorphs and their capacity for isomorphous substitutions. In addition, when a complex matrix like wastewater is added to the equation the overall system has become a difficult problem to solve. Precipitation of various minerals in wastewater is likely to occur. The chemical composition and operational conditions of wastewater may allow the precipitation of carbonate minerals, struvite, sulphide minerals, hydroxides of aluminium and iron and phosphate minerals (Mbamba et al. 2015) as calcium phosphates (CaP). The precipitation of CaP solid phases in WWTPs takes place naturally by heterogeneous and secondary nucleation onto the inherently present mineral and organic suspended solids of wastewater (Peng

et al. 2018). Therefore, additional treatment stages in wastewater treatment plants seeking phosphorus removal and recovery may be based on these same mechanisms through the use of seed substrates.

A large variety of substrates have been investigated in order to find a suitable catalyzer for CaP precipitation. Among them, apatite mineral has previously shown to be an efficient crystallization seed to promote calcium phosphate precipitation (Joko 1984, Molle et al. 2005, Bellier et al. 2006). Apatite seeds present the advantage of sharing the same, or at least similar, composition than the precipitate coating the seeds, and therefore the final product would have a single composition (Montastruc et al. 2003), which would facilitate the later phosphorus (P) recovery. On the other hand, the explored processes for P removal and recovery have already include adsorption columns, crystallisers, fluidized beds and fixed-bed systems. This study focus on the use of apatite minerals in fixed-bed columns to promote the precipitation of calcium phosphates from treated wastewater. A technological solution specially adapted for small WWTPs because of its operational simplicity and the theoretically long-term removal capacity.

Calcium phosphate precipitation involves complex equilibria. Thermodynamics of CaP precipitation indicate that the most stable solid phase/polymorph is hydroxyapatite (HAP) (Hermassi et al. 2015) as it can be observed in the solubility product constants values of Table 2.2. However, HAP precipitation is not straightforward. It generally requires the formation of a CaP precursor and the transition trough other metastable solid phases up to its final crystalline HAP structure, according to the Ostwald step rule. The composition of the precursor in CaP formation is governed by the kinetics of the process. Most research carried out in HAP precipitation indicates the formation of amorphous calcium phosphate (ACP) as the phase precursor (Nancollas and Mohan 1970, Meyer and Eanes 1978, Mañas et al. 2012) and the transition up to HAP through the hydrolysis of octocalcium phosphate (OCP) (Nancollas and Mohan 1970, Meyer and Eanes 1978, Castro et al. 2012). This transition may be described as follows (Castro et al. 2012):



As it can be observed in Eq. 2.66, the molecular composition of ACP is usually as that for tricalcium phosphate (TCP) although some hydration molecules may also be present ( $\text{Ca}_3(\text{PO}_4)_2 \cdot x\text{H}_2\text{O}$ ) (Dorozhkin 2010, Hermassi et al. 2015). In an amorphous phase, the composition of the solid is so irregular that a crystal lattice order cannot be recognised, and its structure resembles more of the randomly structure of a liquid phase (Dorozhkin 2010). Because of its chemical composition, some authors have also considered ACP as a microcrystalline TCP (Barone and Nancollas 1977) but this idea is rejected by others (Dorozhkin 2010).

Table 2. 2. Solubility product constant of calcium phosphates found in literature\*

Component	General Equation	pK <sub>ps</sub>	K <sub>ps</sub>	T (°C)	Ca/P	Found in	Original reference	
MCPA	Ca(H <sub>2</sub> PO <sub>4</sub> ) <sub>2</sub>	4H <sup>+</sup> + 2PO <sub>4</sub> <sup>3-</sup> + Ca <sup>2+</sup> <--> Ca(H <sub>2</sub> PO <sub>4</sub> ) <sub>2</sub>	39.1	7.94E-40		0.5	Hermassi et al 2015 from HYDRA-MEDUSA database	
MCPA	Ca(H <sub>2</sub> PO <sub>4</sub> ) <sub>2</sub>		1.14	7.24E-02	25	0.5	Dorozhki, 2010;	Chow 2001
MCPM	Ca(H <sub>2</sub> PO <sub>4</sub> ) <sub>2</sub> ·H <sub>2</sub> O		1.14	7.24E-02	25	0.5	Dorozhki, 2010;	Chow 2001
DCPA	CaHPO <sub>4</sub>	CaHPO <sub>4</sub> (s) → Ca <sup>2+</sup> + HPO <sub>4</sub> <sup>2-</sup>	6.7	1.97E-07	5	1	McDowell et al 1971	McDowell et al 1971,
DCPA	CaHPO <sub>4</sub>	CaHPO <sub>4</sub> (s) → Ca <sup>2+</sup> + HPO <sub>4</sub> <sup>2-</sup>	6.8	1.64E-07	15	1	McDowell et al 1971	McDowell et al 1971,
DCPA	CaHPO <sub>4</sub>	CaHPO <sub>4</sub> (s) → Ca <sup>2+</sup> + HPO <sub>4</sub> <sup>2-</sup>	6.9	1.36E-07	25	1	Han et al	McDowell et al 1971,
DCPA	CaHPO <sub>4</sub>	CaHPO <sub>4</sub> (s) → Ca <sup>2+</sup> + HPO <sub>4</sub> <sup>2-</sup>	7.0	9.20E-08	37	1	McDowell et al 1971	McDowell et al 1971,
DCPA	CaHPO <sub>4</sub>		6.9	1.26E-07	25	1	Chow, 2001 Dorozhki, 2010;Montastruc et al.	McDowell 1968
DCPA	CaHPO <sub>4</sub>		6.9	1.26E-07	25	1	2003	M. Freche, 1989.
DCPA	CaHPO <sub>4</sub>		6.6	2.51E-07	25			
DCPA	CaHPO <sub>4</sub>		-2.7	4.57E+02	25			
DCPD	CaHPO <sub>4</sub> ·2H <sub>2</sub> O	K <sub>sp</sub> = (Ca <sup>2+</sup> )(HPO <sub>4</sub> <sup>2-</sup> ) Ca <sup>2+</sup> + HPO <sub>4</sub> <sup>2-</sup> →	6.6	2.49E-07	25	1	Patel et al., 1974	
DCPD	CaHPO <sub>4</sub> ·2H <sub>2</sub> O	CaHPO <sub>4</sub>	5.7	2.00E-06	25	1	Montastruc et al. 2003	G. Charlot, 1957.
DCPD	CaHPO <sub>4</sub> ·2H <sub>2</sub> O		6.6	2.57E-07	25	1	Chow, 2001	Gregory et al 1970

DCPD	CaHPO <sub>4</sub> ·2H <sub>2</sub> O	Ca <sup>2+</sup> + HPO <sub>4</sub> <sup>2-</sup> → CaHPO <sub>4</sub>	6.6	2.57E-07	25	1	Dorozhki, 2010; Stumm and Morgan 1981	W. Stumm, an J.J. Morgan, 1981.
DCPD	CaHPO <sub>4</sub> ·2H <sub>2</sub> O	Ca <sup>2+</sup> + HPO <sub>4</sub> <sup>2-</sup> → CaHPO <sub>4</sub>	6.7	2.04E-07	25	1	Montastruc et al. 2003	M. Freche, 1989.
DCPD	CaHPO <sub>4</sub> ·2H <sub>2</sub> O	Ca <sup>2+</sup> + HPO <sub>4</sub> <sup>2-</sup> → CaHPO <sub>5</sub>	19.0	1.00E-19			Hermassi et al 2015 from HYDRA-MEDUSA database	
TCP	Ca <sub>3</sub> (PO <sub>4</sub> ) <sub>2</sub>		26.0	1E-26	25	1.5	Stumm and Morgan 1996, Montastruc et al. 2003	A. Ringbom, 1967.
TCP	Ca <sub>3</sub> (PO <sub>4</sub> ) <sub>2</sub>	2PO <sub>4</sub> <sup>3-</sup> + 3Ca <sup>2+</sup> <--> Ca <sub>3</sub> (PO <sub>4</sub> ) <sub>2</sub>	28.9	1.2E-26		1.5	Hermassi et al 2015 from HYDRA-MEDUSA database	
αTCP	α-Ca <sub>3</sub> (PO <sub>4</sub> ) <sub>2</sub>		25.5	1.2E-26	25	1.5	Dorozhki, 2010	
αTCP	α-Ca <sub>3</sub> (PO <sub>4</sub> ) <sub>2</sub>		25.5	3.24E-26	25	1.5	Chow 2001, Fowler and Kuroda 1986	J,L Meyer
βTCP	β-Ca <sub>3</sub> (PO <sub>4</sub> ) <sub>2</sub>	Ca <sub>3</sub> (PO <sub>4</sub> ) <sub>2</sub> <-->3Ca <sup>2+</sup> 2PO <sub>3</sub> <sup>4-</sup>	28.9	1.2E-26	25	1.5	Dorozhki, 2010	
TTCP	Ca <sub>4</sub> (PO <sub>4</sub> ) <sub>2</sub> O		38.0	1.00E-38	25	2	W.E Brown and L.C.Chow	Fowler and Kuroda 1986
TTCP	Ca <sub>4</sub> (PO <sub>4</sub> ) <sub>2</sub> O	Ksp=(Ca <sup>2+</sup> ) <sub>4</sub> (PO <sub>4</sub> <sup>3-</sup> ) <sub>2</sub> (OH <sup>-</sup> ) <sub>2</sub>	38.0	1.00E-38	37	2	Chow, 2001	Matsuya et al 1996
OCP	Ca <sub>4</sub> H(PO <sub>4</sub> ) <sub>3</sub>		46.9	1.26E-47		1.33	Stumm and Morgan, 1996	
OCP	Ca <sub>4</sub> H(PO <sub>4</sub> ) <sub>3</sub>	H <sup>+</sup> +3PO <sub>4</sub> <sup>3-</sup> + 4Ca <sup>2+</sup> <--> Ca <sub>4</sub> H(PO <sub>4</sub> ) <sub>3</sub>	46.9	1.26E-47		1.33	Hermassi et al 2015 from HYDRA-MEDUSA database	
OCP	Ca <sub>3</sub> (HPO <sub>4</sub> ) <sub>2</sub> (PO <sub>4</sub> ) <sub>4</sub> ·5H <sub>2</sub> O	Ksp = (Ca <sup>2+</sup> ) <sub>4</sub> (H <sup>+</sup> )(PO <sub>4</sub> <sup>3-</sup> ) <sub>3</sub>	48.3	5.01E-49	4	1.33	Tung et al 1988	

OCP	$\text{Ca}_8(\text{HPO}_4)_2(\text{PO}_4)_4 \cdot 5\text{H}_2\text{O}$	$\text{Ksp} = (\text{Ca}^{2+})_4(\text{H}^+)(\text{PO}_4^{3-})_3$	48.2	$6.31\text{E-}49$	6	1.33	Tung et al 1988	
OCP	$\text{Ca}_8(\text{HPO}_4)_2(\text{PO}_4)_4 \cdot 5\text{H}_2\text{O}$	$\text{Ksp} = (\text{Ca}^{2+})_4(\text{H}^+)(\text{PO}_4^{3-})_3$	48.4	$3.98\text{E-}49$	23.5	1.33	Tung et al 1988	
OCP	$\text{Ca}_8(\text{HPO}_4)_2(\text{PO}_4)_4 \cdot 5\text{H}_2\text{O}$		48.7	$2.00\text{E-}49$	37	1.33	Tung et al 1988	
OCP	$\text{Ca}_8(\text{HPO}_4)_2(\text{PO}_4)_4 \cdot 5\text{H}_2\text{O}$		96.6	$2.51\text{E-}97$	25	1.33	Dorozhki, 2010	
OCP			49.6	$2.51\text{E-}50$	25	1.33	Tung et al 1988	Nancollas et al. 1985
OCP			46.9	$1.26\text{E-}47$	25	1.33	Tung et al 1988	Moreno et al 1960
OCP	$\text{Ca}_4\text{H}(\text{PO}_4)_3 \cdot 2,5\text{H}_2\text{O}$		49.6	$2.51\text{E-}50$	25	1.33	Montastruc et al. 2003	M. Freche, 1989.
HAP	$\text{Ca}_5(\text{PO}_4)_3(\text{OH})$	$5\text{Ca}^{2+} + 3\text{PO}_4^{3-} + \text{OH}^- \rightarrow \text{Ca}_5(\text{PO}_4)_3\text{OH} (\text{s})$	57.0	$1\text{E-}57$		1.67	Claveau-Mallet 2017	Stumm and Morgan, 1996
HAP	$\text{Ca}_5(\text{PO}_4)_3(\text{OH})$	$10\text{Ca}^{2+} + 6\text{PO}_4^{3-} + 2\text{OH}^- \rightarrow \text{Ca}_{10}(\text{PO}_4)_6(\text{OH})_2 (\text{s})$	114.0	$1\text{E-}114$		1.67	Barca et al 2013 and Blanco et al 2016	Stumm and Morgan, 1996
HAP	$\text{Ca}_{10}(\text{PO}_4)_6(\text{OH})_2$		116.8	$1.58\text{E-}117$	25	1.67	Dorozhki, 2010	
HAP	$\text{Ca}_{10}(\text{PO}_4)_6(\text{OH})_2$		58.3	$4.7\text{E-}59$	25	1.67	Montastruc et al. 2003	M. Freche 1989.
HAP	$\text{Ca}_5(\text{PO}_4)_3(\text{OH})$	$\text{Ksp} = (\text{Ca}^{2+})_5(\text{PO}_4^{3-})_2(\text{OH}^-) + 3\text{PO}_4^{3-} + 4\text{Ca}^{2+} + \text{H}_2\text{O} \leftrightarrow \text{Ca}_5(\text{PO}_4)_3\text{OH} + \text{H}^+$	58.32	$4.7\text{E-}59$	25	1.67	Chow, 2001 --> original source verified Mc Dowell et al 1977	
HAP	$\text{Ca}_5(\text{PO}_4)_3(\text{OH})$		40.5	$3.2\text{E-}41$		1.67	Hermassi et al 2015 from HYDRA-MEDUSA database	
FAP	$\text{Ca}_5(\text{PO}_4)_3(\text{F})$		60.5	$3.2\text{E-}61$	37	1.67	Chow 2001	Moreno et al 1977
FAP	$\text{Ca}_{10}(\text{PO}_4)_6(\text{F})_2$		120	$1.0\text{E-}120$	25	1.67	Dorozhki, 2010	

CIAP	$\text{Ca}_5(\text{PO}_4)_3(\text{Cl})$						
OAP	$\text{Ca}_{10}(\text{PO}_4)_6\text{O}$		69	1.0E-69	25	1.67	Dorozhki, 2010
	$\text{Ca}_x\text{H}_y(\text{PO}_4)_z \cdot n\text{H}_2\text{O}$ , $n=3 - 4,5; 15-20\%$		25,7-			1,0 -	
ACP	$\text{H}_2\text{O}$		32,7			2,2	Dorozhki, 2010
		$3\text{Ca}^{2+} + 2\text{PO}_4^{3-} \rightarrow$					
ACP	$\text{Ca}_3(\text{PO}_4)_2$	$\text{Ca}_3(\text{PO}_4)_2$	26.52	3.01995E-27	25		Montastruc et al. 2003 M.M. Seckler, 1994.
ACP	$\text{Ca}_3(\text{PO}_4)_3$		26.68	2.0893E-27	25	18 -	Montastruc et al. 2003 Dean 1956
ACP	$\text{Ca}_3(\text{PO}_4)_2$		25.2	6.30957E-26	20		Montastruc et al. 2003 Meyer and Eanes 1978
ACP	$\text{Ca}_3(\text{HPO}_4)_2$		Varia ble		25	~ 1.5	
	$\text{Ca}_{10-x}(\text{HPO}_4)_x(\text{PO}_4)_{6-x}$					1,5 -	
CDHA	$x(\text{OH})_{2-x} (0 < x < 1)$		85.1		25	1,67	Dorozhki, 2010

\*Mechanisms of apatite dissolution are not well understood leading to congruent (stoichiometric) and non-congruent (stoichiometric) dissolution. Such different results may depend on the specific composition of this material. All the same, this may also be the cause for the important discrepancies in solubility data, as well as, caused by differences in the experimental setup (Zhu et al. 2009).

The transformation from the precursor to the final stable solid phase (HAP) can take a long solid solution equilibration time (Nancollas and Mohan 1970). However, the transformation from amorphous to a crystalline phase may be fast. The kinetics of the amorphous to crystalline transition depends on the solution composition (Meyer and Eanes 1978) (e.g. slowed down in the presence of  $Mg^{2+}$ , carbonates or silicates and accelerated in the presence of  $Ca^{2+}$ ) as well as pH and temperature (Dorozhkin 2010). Dorozhkin (2010) claimed that depending on environmental conditions, the transformation of ACP to a poorly crystalline form, notably calcium deficient hydroxyapatite (CDHA), can be fast (in the order of hours). An empirical kinetic expression for amorphous to crystalline transition was enunciated by Eanes and Posner (1965) as shown in Eq. 2.68:

$$\frac{dC}{dt} = k_1 + k_2 C \quad [2.68]$$

Where C accounts for the ACP converted fraction into the crystalline phase by time t,  $k_1$  is the nucleation rate constant of the first crystals, and  $k_2$  is an autocatalytic rate constant indicating the proportionality between the transition rate and crystallized mass fraction.

In previous studies, mineral apatite showed to be an efficient crystallization seed to promote calcium phosphate (CaP) precipitation (Joko 1984, Molle et al. 2005, Bellier et al. 2006). It has been claimed that when sufficient apatite seeds are added to stable supersaturated solutions, they will induce the immediate growth of CaP (Barone and Nancollas 1977). However, since most solution conditions will not induced a straightforward HAP crystallization onto apatite seeds, there exist several previous step until HAP formation. Attia and Fuerstenau (1988) described the process in three different steps: chemisorption of constituent ions onto the crystal lattice leading to heterogeneous nucleation of amorphous CaP (also described by Meyer and Eanes (1978)); slow transition from amorphous to a crystalline form; and finally crystal growth of HAP.

In most experimental conditions, surface precipitation of apatite crystals is a surface rate-limited reaction (Nancollas and Mohan 1970) except maybe for precipitation in the pores where diffusion is prone to control the reaction rate (Gebrehiwet et al. 2014). The apatite surface exhibits a different composition from the bulk of the solid

due to interfacial interactions with the solution (Bengtsson 2007). The formation of the electric double layer on apatite surface may be due to the ionization of the surface ions or by adsorption of ionic species dissolved in solution. Attia and Fuerstenau (1988) suggest species like  $\text{Ca}^{2+}$ ,  $\text{F}^-$ ,  $\text{H}_2\text{PO}_4^-$  and  $\text{HCO}_3^-$  or  $\text{Ca}^{2+}$  and  $\text{HCO}_3^-$  as the predominant potential determining ions for FAP and HAP in atmospheric equilibrated solutions. On the other hand, Zhu et al. (2009) suggested  $\equiv\text{CaOH}_2^+$  and  $\equiv\text{PO}^-$  (or its corresponding protonated version  $\equiv\text{POH}$ ) as the predominant species based on FAP structure ( $\equiv$  stands for the surface). Bengtsson (2007) claimed that a simplified model for apatite surface reactive sites would involve  $\equiv\text{CaOH}$  and  $\equiv\text{PO}_3\text{H}_2$  and their protonated and deprotonated species, with the ability to interact with other phosphates, calcium, fluoride and organic ligands present in solution.

Finally, it is worth mentioning that natural minerals (non-synthetic) are rarely found as pure minerals but more or less surrounded by others like calcite and quartz, which have also shown to promote CaP precipitation. In the case of calcite, its presence in the gangue of apatite seeds may act in the overall process retention by two different ways: adsorbing and precipitating calcium phosphates onto their surface (Li et al. 2017); and/or partially dissolving and co-precipitating together with the CaP. The dissolution of calcium carbonates (or other more or less soluble calcium containing minerals that might be present in the gangue) have indeed two main consequences: it increases calcium concentration, becoming a source of  $\text{Ca}^{2+}$ , and increasing supersaturation; it also increases the concentration of carbonates in solution so other carbonate phases may also be supersaturated. When carbonates are present in solution, they most likely coprecipitate with the CaP leading to the formation of a carbonated solid solution whose end-members are HAP and calcite. Typical isomorphic substitutions of carbonates in HAP involve the replacement of  $\text{PO}_4^{3-}$  by  $\text{CO}_3^{2-}$ , the so-called B-type substitution, however, A-type substitutions ( $\text{CO}_3^{2-}$  takes the place of  $\text{Ca}^{2+}$ ) or both (AB-type substitution) are also possible (Lafon et al. 2003). The integration of carbonates in the calcium phosphates structure (e.g. carbonated hydroxyapatite (C-HAP)) lead to more soluble products because of a reduction in the crystallinity of the solid phase (Peng et al. 2018) as shown in Table 2.2. The presence of carbonates in the solid solution crystals is

indicated by higher Ca/P molar ratios than that of stoichiometric HAP (1.67) (Song et al. 2002).

### 2.3.5. Parameters influencing phosphate precipitation onto apatite

The initial precipitation of ACP onto apatite particles is a kinetically driven process. The rate of crystallization and hence, the nature of the phases that may precipitate, also depend on supersaturation (thermodynamic parameter) calcium and phosphate concentrations (relative ratio), seed concentration, ionic strength, temperature, pH, the presence of foreign ions (carbonates, metals) and the time to enable solid-to-solid transformations (Barone and Nancollas 1977, Song et al. 2002, Montastruc et al. 2003). The common factor in the interrelationship between all these parameters (except maybe in the case of the foreign ions impact and solid solution transformations) is, indeed, the supersaturation of the solution.

The precipitation rate is supersaturation dependent. It affects the activation energy of the reaction and so the induction time required for crystallization, which decreases with increasing supersaturation (Anderson and Rubin 1981, Peng et al. 2018). The supersaturation indicates which solid phases are thermodynamically possible. As it was already discussed, the presence of a surface reduces the activation energy required facilitating precipitation. The structural crystal match between seed and the most thermodynamically stable precipitate strongly promotes the reaction (Nancollas and Mohan 1970) by reducing even more the activation energy required and so accelerating the reaction rate. This is, despite in most cases the precipitation reaction takes place producing ACP or any other crystalline phases in first place, which is a heterogeneous nucleated process, the overall process is driven by the most thermodynamically stable solid phase (HAP) which would have the exact same or a pretty close lattice structure as the apatite seed, (in most cases FAP or a carbonated FAP and a gangue).

An important parameter affecting supersaturation is the calcium concentration in solution. The SI of HAP increases logarithmically with calcium concentration and, therefore, increases with increasing Ca/P ratio too (Song et al. 2002). Accordingly,

a high initial Ca/P molar ratio induces more efficient precipitation processes (Karapinar et al. 2006).

The temperature also affects supersaturation. In the typical interval of wastewater temperatures (5 to 30°C), SI increases proportionally to solution temperature (Song et al. 2002).

The supersaturation ratio is also inversely correlated with the ionic strength since it is used to the calculation of activity coefficients (Song et al. 2002). Logically, the more dissolved ions are present in solution the more interactions exists with the constituent solutes being less available for diffusion to the solid surface.

Concerning pH, the amphoteric nature of phosphates makes speciation highly dependent on pH. When pH increases for example because of lime dissolution, pH basifies shifting the protonated phosphates species towards  $\text{PO}_4^{3-}$  production. Thus, increasing hydroxyl concentration increases supersaturation with respect to the more basic species TCP, OCP and HAP/FAP (Zoltek 1976). On the other hand, the formation of TCP, OCP and HAP are base consumption processes so pH decreases as a result (Song et al. 2002, Castro et al. 2012).

Finally, specific adsorption of ions can interfere in CaP deposition by “stealing” the surface sites but also by changing the composition of the surface (Attia and Fuerstenau 1988). Polyphosphates and polyphosphonates have been reported to inhibit crystal growth by adsorbing on the surface and preventing further growth of the crystal (Francis 1969). In the case of polyphosphates the impact is time dependent since they are unstable in water solvents. Carbonates can also inhibit HAP precipitation through the formation of ion pairs with calcium in solution which makes calcium ions less available for HAP precipitation (Song et al. 2002). It can also reduce the point of zero charge of HAP and FAP disturbing their surface chemistry (Attia and Fuerstenau 1988).

## 2.4. Chapter conclusions

Phosphorus retention using specific materials is a physicochemical process based on various interactions at the solid-liquid interface. For natural apatite, such interactions are adsorption and heterogeneous precipitation. The latter becomes the predominant reaction when a long-term retention process is pursued. Mineral apatite was shown to act as a crystallization seed promoting calcium phosphate precipitation such as hydroxyapatite.

Precipitation is a thermodynamically driven process that depends on the solubility of the most stable pure solid phase and the free energy change. The saturation index of a solution determines whether a specific calcium phosphate phase is likely to form in the specific environmental conditions. However, in heterogeneous precipitation the kinetic and mechanistic factors also play a major role in the nucleation and the growth of solid solutions usually involving the precipitation of less thermodynamic stable phases like amorphous calcium phosphate.

The kinetics of precipitation is supersaturation dependent: the induction time for crystallization decreases with increasing supersaturation. In addition, for a particular supersaturation state, precipitation may or may not take place depending on environmental conditions because of the existence of a metastable zone. Therefore, the rate of crystallization and nature of the phases that may precipitate strongly depend on calcium and phosphate concentrations, supersaturation, ionic strength, temperature, pH, the presence of foreign ions and time to enable solid-to-solid transformations.

## Chapter 3. Materials & Methods

---

### 3.1. Introduction

The experimental work conducted within the framework of this PhD thesis can be classified in 4 different strategies: (1) substrate characterisation; (2) full-scale filters campaigns; (3) laboratory pilot column experiments; and (4) a preliminary modelling study. This chapter is dedicated to give an extensive explanation of the experimental methodologies and techniques required for each of these strategies.

#### 3.1.1. Analytical techniques

The fundamentals of the analytical techniques used in this study for the characterisation of solid and liquid samples are here explained.

#### 3.1.2. Analytical techniques for solid sample characterisation

##### 3.1.2.1. Inductively coupled plasma optical emission spectrometry

Inductively coupled plasma optical emission spectrometry (ICP-OES) is an analytical technique that uses the unique emission spectra produced by a particular element when it is exposed to an argon plasma, to identify and quantify it. To be able to execute analyses, the samples must be atomized before entering the plasma. In case of solid samples, as minerals and soils, the atomization can be carried out by fusion and dilution into an acid. The liquid sample is shattered into a fine aerosol using an argon flow at high speed. The fine aerosol enters the plasma and some atoms become ionized, electrons excite jumping from a lower to a higher energy level. Upon relaxation of the electrons, some energy is emitted in the form of photons. The photons are characterized by different wavelengths specific of an element according to the Planck

equation (Eq. 3.1). The emission spectra allows then to identify and quantify the different elements in the sample.

$$\lambda = \frac{hc}{\Delta E} \quad [3.1]$$

Where h is the Planck's constant, c is the speed of light,  $\Delta E$  is the energy difference of the electron between its excited state and its ground or relaxed state.

### 3.1.2.2. Fourier transform infrared spectroscopy

The Fourier-transform infrared (FTIR) spectroscopy is an analytical technique allowing the identification of chemical bonds and functional groups present in a sample by measuring their characteristic vibration frequency. The frequency of vibration of a bond between two atoms is described by Eq.3.2:

$$\bar{\nu} = \frac{1}{2\pi c} \sqrt{k_{AB} \frac{m_A + m_B}{m_A m_B}} \quad [3.2]$$

Where  $\bar{\nu}$  is the vibration frequency, c is the speed of light,  $k_{AB}$  is the bond force constant and  $m_A$  and  $m_B$  are the atomic masses of the atoms involved in the bond (A and B).

The infrared region is comprised in the wavelength range from 12,800 to 10  $\text{cm}^{-1}$ , however, FTIR spectroscopy measurements are usually conducted in the mid-infrared region (4,000 – 200  $\text{cm}^{-1}$ ) since the absorption radiation of a wide variety of organic and inorganic compounds are found in this region. The infrared spectrum is a molecular vibrational spectrum. When a sample is exposed to infrared radiation, the molecules selectively absorb energy of a particular wavelength. The molecules excite causing a change in their dipole moment which is characteristic of a specific chemical structure (molecule); the dipole may stretch, bend or twist when adsorbing the radiation. The energy gap between the ground and excited state is the absorbed energy, which is measured by the detector in the spectrometer. The resulting signal is converted to an interpretable spectrum made of different peaks by the Fourier-transform (transformation of time into wavelength). The generated spectra provides structural information of the sample.

A common sampling technique usually coupled with FTIR measurements is the attenuated total reflectance (ATR). The ATR technique involves a crystal (i.e. the internal reflection element) with a high refractive index and high infrared transmitting properties. When an infrared beam travels from the crystal to the sample, most of the radiation is reflected back to the crystal as shown in Fig.3.1. However, a little fraction of the radiation is able to escape the crystal producing an invisible wave that travels through the sample called the evanescent wave. The penetration of such wave depends of the wavenumber (the smaller is the wavelength the greater the intensity of the peak) and the difference of the refracted index between the sample and the crystal which depends on the crystal material (approximately 2.4 for diamond, the lower the value the greater the penetration). The signal recorded by the detector results from the sum of all the bounces creating the evanescent waves (the more bounces the greater the sensibility). The popularity of such technique come from its high reliability combined with the fact that is a non-destructive method, it does not require sample preparation and it does not depend on the sample thickness

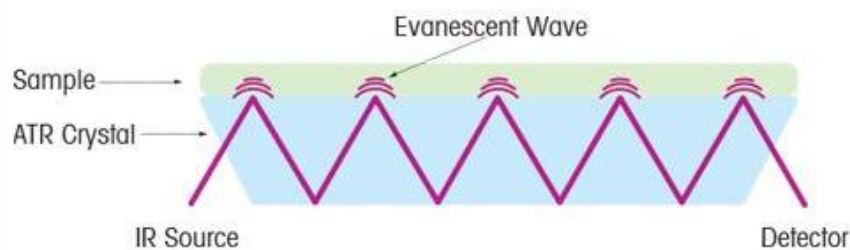


Fig. 3. 1. Scheme of an attenuated total reflection (ATR) cell (Source: <https://www.mt.com>).

### 3.1.2.3. X-ray diffraction

X-ray diffraction (XRD) is a technique used to characterize crystalline materials providing information such as structure, phases, preferred crystal orientations (texture), crystallinity and other structural parameters. The incidence of a monochromatic beam of X-rays on a sample produces a constructive interference and a diffracted X-ray according to the Bragg's law (Eq.3.3) that is recorded by a detector generating spectra or a diffractogram (Bunaciu et al. 2015) (Fig.3.2).

$$n\lambda = 2d \sin\theta \quad [3.3]$$

Where  $n$  is an integer,  $\lambda$  is the wavelength of the X-rays,  $d$  is the interplanar spacing generating the diffraction and  $\theta$  is the diffraction angle. The sample is usually scanned through a range of  $2\theta$  angles.

The peak intensities in a diffractogram are determined by the atomic positions within the lattice planes of the crystal, which has a periodic atomic arrangement. Therefore the peaks of crystalline phases are sharp whereas those on amorphous regions of the sample produced a broad peak (Patel and Parsania 2018). From the relationship between the intensities of amorphous ( $I_a$ ) and crystalline contents ( $I_c$ ) one can determine the degree of crystallinity ( $X_c$ ) of a sample (Eq.3.4).

$$X_c = \frac{I_c}{I_c + I_a} \times 100 \quad [3.4]$$

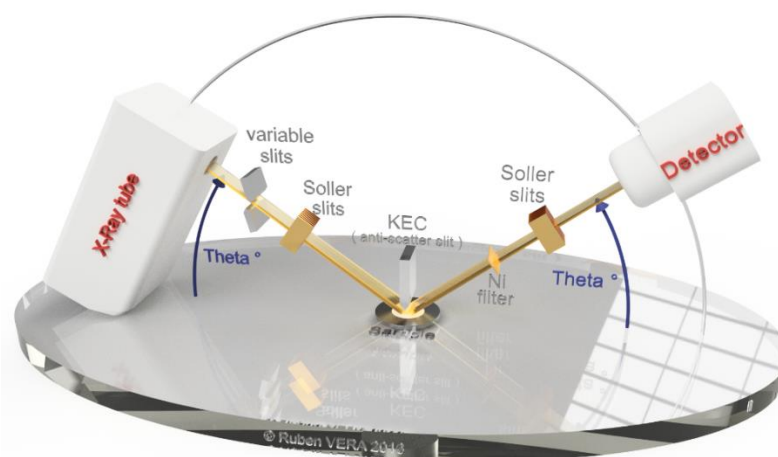


Fig. 3. 2. Scheme of the X-ray Powder diffraction set up used in this study (provided by the Henry Longchambon Diffractometer Center).

When X-rays are applied into a fine powder sample, the technique is then called X-ray powder diffraction. X-ray powder diffraction allows the identification of unknown crystalline materials with multiple crystalline phases by comparing the generated diffractogram with standard reference patterns of pure crystals (mineralogical characterisation).

#### 3.1.2.4. Scanning electron microscopy

The scanning electron microscopy (SEM) uses an electron beam to scan across the surface of the sample. This produces a large numbers of electron signals that can eventually be converted to a visual signal. The interactions between the sample and the electrons are of two major types: elastic and inelastic interactions.

An elastic interaction results from the dispersion by deflection of the incident electron when it gets in contact with the nucleus or outer shell electrons of the sample. The energy loss is negligible and the collision produces a wide-angle directional change of the scattered electrons. If the resulting angle is greater than  $90^\circ$  the incident electrons are called backscattered electrons (BSE).

An inelastic scattering occurs through a variety of interactions between the incident electrons and the atoms of the sample. The sample absorbs a substantial amount of energy in such case. When the electron beam strikes the sample, it causes the ionization of the more superficial atoms of the sample by emitting their loosely bound electrons. These are called secondary electrons (SE).

Both types of electrons BSE and SE can be used to image the sample by converting electrons into photons. SE are commonly used for topographic contrast (visualisation of texture and roughness). The BSE produces topographic information but also compositional information of the sample since the yield of the elastic collision depends on the atomic number of the species present in the sample. The bigger the atomic number, the bigger the nucleus of the atoms, the more electrons are scattered back towards their source. Therefore, the produced signal can be related with the average composition of the sample: the different greys of the image produced can be related to heavier or lighter components. On the other hand, the image from BSE has a lower resolution than SE,  $1.0\mu\text{m}$  against  $10\text{nm}$ , respectively.

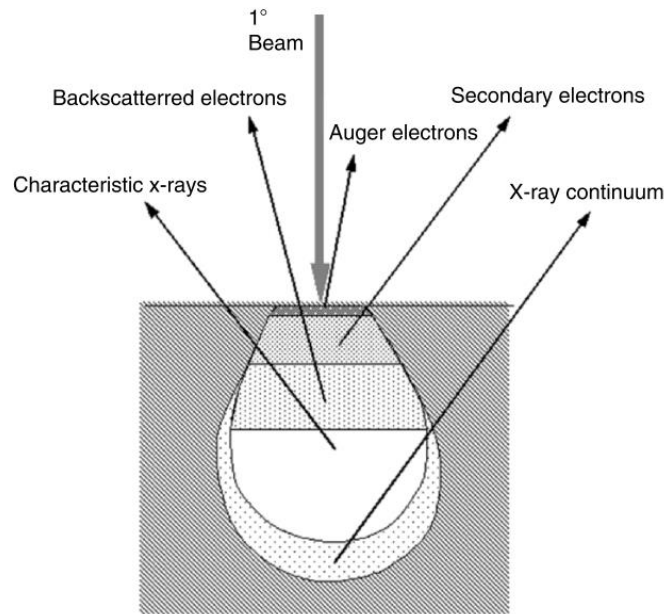


Fig. 3. 3. Interaction of an electron beam with a sample. The shape of the interaction volume is tear drop (Zhou et al. 2006).

Another type of inelastic collision is that producing characteristic X-rays from the sample. The collision of the primary beam electron with an atom of the sample can displace an inner-shell electron. As a result, an outer shell electron of that atom moves to the inner shell to balance the charge in the orbitals emitting an X-ray photon. These X-ray photons produce a spectrum that provides chemical information of the sample, therefore, it can be used as a SEM microanalyses techniques.

### 3.1.2.5. Brunauer Emmett-Teller adsorption isotherm

The theory of Brunauer–Emmett–Teller (BET) describes the physical adsorption of a gas, typically N<sub>2</sub>, at its boiling point on a material's surface. Such adsorption is defined by Eq.3.5.

$$\frac{1}{Q(P_0/P-1)} = \frac{1}{n_m C} + \frac{C-1}{n_m C} (P/P_0) \quad [3.5]$$

Where Q is the specific amount of the adsorbed gas at the relative pressure P/P<sub>0</sub>, n<sub>m</sub> is the monolayer capacity of the adsorbed gas, P is the pressure, P<sub>0</sub> is the saturation pressure of a substance being adsorbed at the adsorption temperature, and C is the BET constant which is exponentially related to the energy of monolayer adsorption. By

representing  $\frac{1}{Q(P_0/P-1)}$  vs  $P/P_0$  the parameter C and the amount of sorbed gas  $n_m$  can be determined from the slope and intercept of the curve which is a linear relationship in the range of  $0.05 < P/P_0 < 0.35$ .

The BET isotherm is applied for the determination of surface areas. The total surface ( $S_{total}$ ) area and the specific surface area (SSA) are calculated following the expressions in Eq.3.6 and 3.7.

$$S_{total} = \frac{m_n N s}{V} \quad [3.6]$$

$$SSA = \frac{S_{total}}{m} \quad [3.7]$$

Where N is the Avogadro number, s is the adsorption cross section of the adsorbing species, V is the molar volume of the gas and m the mass of the sample.

### 3.1.3. Analytical techniques for liquid samples

#### 3.1.3.1. Ionic chromatography

The ionic chromatography analytical technique is based on the affinity of the ions present in a mobile phase (eluent) for the ions of the ion exchange resin column or stationary phase. It is based on the electrostatic interactions between the ions in the solution and the ions of the resin. The strength of the interaction depends on the functional group or ligand of the stationary phase and the size and charge of the ions in the mobile phase. The retention time of the ions in the resin is characteristic of each ionic specie. When the eluent is loaded in the resin column, those ions weakly attaching to the resin are eluted out of the resin column in first place. Those strongly bonding to the stationary phase will be retained for a longer time in the column. The physical separation of the ions allows their identification and quantification by an electrical conductivity detector placed at the outlet of the column. This detector produces a chromatogram (Fig.3.4) which plots conductivity vs. time. Each ion produces a peak on this graph, the height of which is dependent on the relative ion concentration in the injected solution.

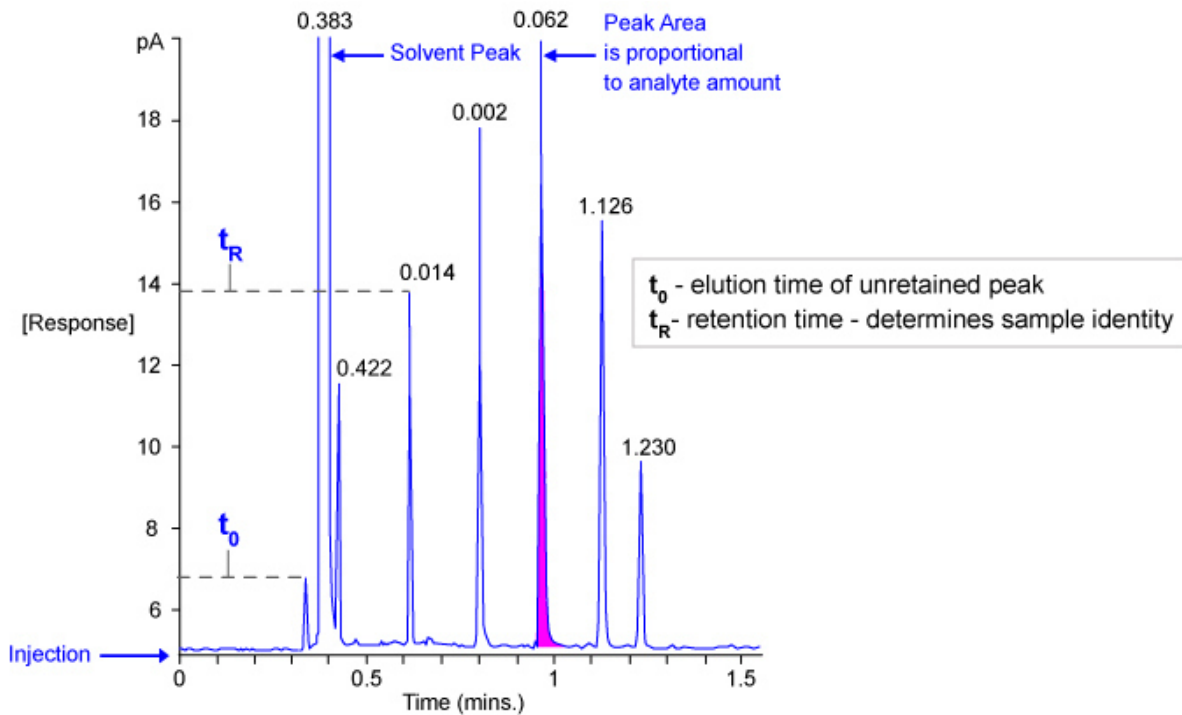


Fig. 3. 4. Example of a chromatogram.

## 3.2. Substrate characterisation

### 3.2.1. Substrates

Three different apatite substrates have been investigated. One concerns a manufactured product (patent: Blandin (2013)) resulting from the pelletization of natural apatite using a cement binder, hereafter called granulated apatite (GA) (Fig.3.5). The GA was assessed in laboratory columns and in full-scale filters. The same production batch was used for all the experiments. The other two products are commercial natural apatites of same origin but different quality that will be called from now on as NA1 (Fig.3.6.a) and NA2 (Fig.3.6.b). Such products have been studied only in laboratory pilot columns.



*Fig. 3. 5. Image of a sample of granulated apatite.*



*Fig. 3. 6. Images of samples of mineral apatite a) NA1 and b) NA2*

### 3.2.1.1. Sampling of solid substrates

Representative samples of the solids were selected by the coning and quartering method (NF EN 932-2). This method allows reducing the sample size of a material without creating a systematic bias. It consist of different steps (Fig.3.7): (1) to form a cone with the material; (2) to flat the cone making a cake; (3) to divide it into quarters and discarding two opposite quarters; (4) to repeat the procedure with a reduced sample until the obtained sample has a suitable size.

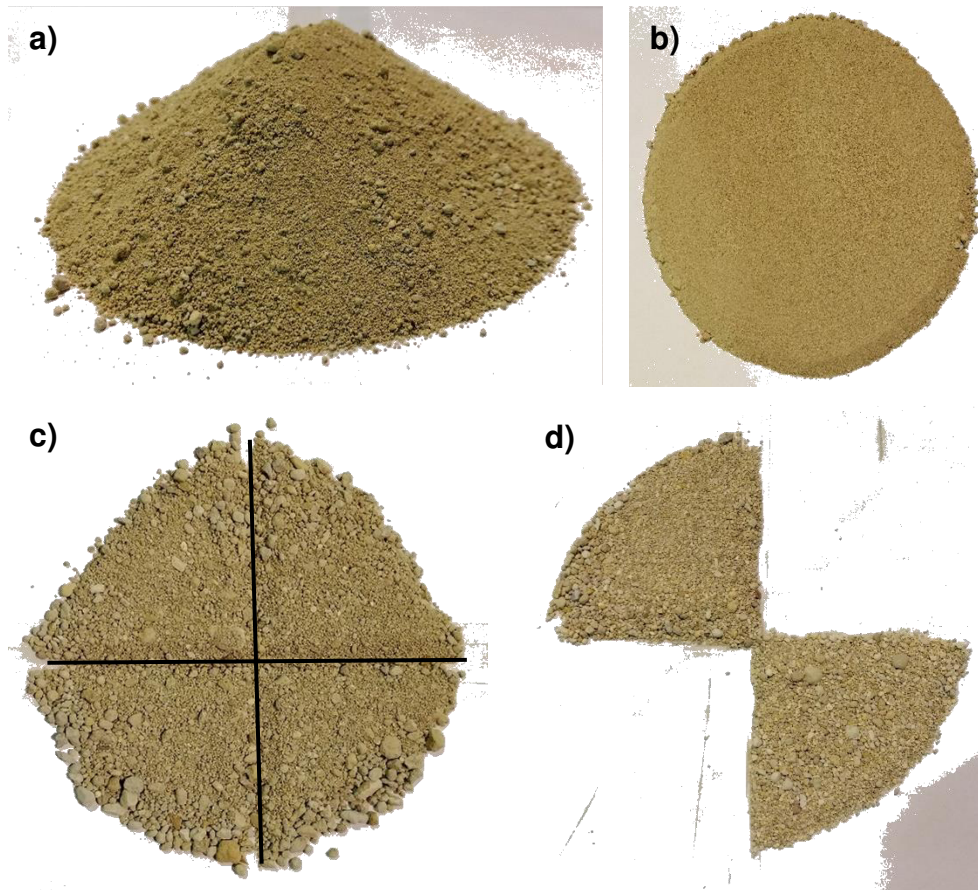


Fig. 3. 7. Steps of the coning and quartering method: a) making a cone; b) flattening; c) quartering; d) discard opposite quarters.

### 3.2.2. Experimental methodology for substrates characterisation

An extensive characterisation of the substrates was required in order to properly describe the phosphorus retention processes. The retention performances have been previously associated with the phosphorus content and/or mineralogical composition of the substrates, thus such analyses were required for the comparison (Bellier et al. 2006, Harouiya et al. 2011, Molle et al. 2011). The identification of the different solid phases involved and their interaction with the solution is also important for mechanistic modelling purposes. The influence of the particle size distribution or the specific surface area on surface reactions is also well known. Such parameters also allow the comparison with substrates of different nature. Some other physical parameters are also needed to allow the calculations of the filters performance. Finally, an insight on the morphology and composition of the substrates and precipitates formed, at the micrometric scale, was crucial to understand the phosphorus retention processes taking place and the different performance results obtained.

Therefore, the characterisation included elemental and mineralogical analyses of the substrates, the determination of several physical properties and the imaging via microscopic techniques. Except when otherwise specified, the measurements were carried out in the facilities of the REVERSAAL Research Unit in INRAE, Lyon-Grenoble-Auvergne-Rhône-Alpes Centre (France).

#### 3.2.2.1. Chemical characterisation

In this study, the elemental composition of GA, NA1, and NA2 was determined by ICP-OES. The raw samples were first grinded with to obtain a powder of approximately 80  $\mu\text{m}$ . The samples were then subjected to alkaline fusion ( $\text{LiBO}_2$ ) followed by acid digestion ( $\text{HNO}_3$ ) to dissolve the sample. To determine the major elements, the solution was subsequently analysed by ICP-OES (iCap6500, Thermo Scientific). The following major elements were analysed (%wt): Na ( $\text{Na}_2\text{O}$ ), Ca ( $\text{CaO}$ ), K ( $\text{K}_2\text{O}$ ), Ti ( $\text{TiO}_2$ ), P ( $\text{P}_2\text{O}_5$ ), Fe ( $\text{Fe}_2\text{O}_3$ ), Al ( $\text{Al}_2\text{O}_3$ ) and Si ( $\text{SiO}_2$ ). The fluorine concentration is analysed using an ion selective electrode (ISE). Chlorine was measured with a UV spectrometry (470nm) (Agilent CARY60). Finally, to analyse total sulphur and total carbon, the samples are heated by induction to approximately 1450°C with and then analysed using an infrared analyser (HORIBA EMIA 320-V2). The analyses were conducted by the *Service d'Analyse des Roches et des Minéraux (SARM)* which is an Analytical Research facility of the *Centre de Recherches Pétrographiques et Géochimiques (CRPG)* in Vandoeuvre-lès-Nancy (France).

The raw grinded samples were also analyzed by ATR-FTIR in the range of 4000-400- $\text{cm}^{-1}$  (NICOLET iS50 FR-IR) with a 4.8  $\text{cm}^{-1}$  resolution using a diamond crystal. The samples were previously dried during 48 hours at 40°C. Data was processed with the Thermo Scientific OMNIC FTIR software. The measurements were carried out at the *Déchets Eaux Environnement Pollutions (DEEP)* laboratory of the National Institute of Applied Science (*Institut National de Science Appliquées, INSA*) in Lyon (France).

The crystallographic microstructure and the chemical composition of the apatite materials (raw samples and after-the-experiment samples) and precipitates formed during the experiments were analyzed by SEM-EDS. The apatite particles were first embedded in an epoxy resin to obtain cylindrical resin blocks (4 cm in diameter), that were abraded and polished in ethanol using successively finer silicon carbide powders.

Finally, an ethanol-based diamond slurry was used to produce a smooth polished finish suitable for recording Electron Backscatter diffraction patterns. The polished sections were carbon coated and examined by SEM (JEOL JSM-7100) equipped with an Electron Backscattered Diffraction pattern detector (EBSD AZtec HKL) and an Energy Dispersive X-ray analyser (EDX Oxford Instruments) for microanalysis (R. Castaing Microcharacterization Centre, France). The measurements were carried out by the laboratory of *Géosciences Environnement Toulouse* at the University of Toulouse III (Paul Sabatier) (France).

Batch pH-dependent leaching tests were conducted following the acid and base neutralization capacity (ANC-BNC) European standard method CENTS/TS 14429. The method was applied in a representative ground sample of the NA1 substrate. The sample was reduced to a fine powder using a ball mill grinder (Retsch S100). The pH was varied from 2 to 12 by adding 2.0M HNO<sub>3</sub> and 5.0M KOH solutions into 150mL centrifuge tubes containing deionized water and approximately 15 g of the sample to reach a final solid-to-liquid ratio of 10 g/mL. The essays were duplicated except for those at pH 6, 7, 8 and 9 (typical pH range in wastewater) that were triplicated. Blanks (no sample addition) were also carried at pH 3, 6 and 12. Once the acid and base solutions were added the tubes were agitated in a rotary shaker (Heidolph REAX 20) set at 10 rpm for 48 h after what the pH was then measured for each suspension (Consort Multiparameter Analyser C3020). The tubes were then centrifuged (Fisher Scientific, SIGMA 4K15C) at 10,000 rpm for 10min. The supernatants were filtered at 0.45 µm (Sartorius Minisart®) and stored at 4 °C before analyses. The leachates were analyzed for:

- a) Total inorganic carbon (TIC).
- b) Anions concentration by ionic chromatography (Thermo Fisher ICS5000+). The following anions were determined: F<sup>-</sup>, Cl<sup>-</sup>, SO<sub>4</sub><sup>2-</sup> and PO<sub>4</sub><sup>3-</sup>. The samples required filtration at 0.22 µm.
- c) Total concentration of major and trace elements by ICP-OES (Ultima 2; Horiba Jobin Yvon SAS): Al, Ca, Cr, Fe, Mg, Na, P, S, Si, Sr and Zn.

The analyses were carried out at the *Déchets Eaux Environnement Pollutions (DEEP)* laboratory of the National Institute of Applied Science (*Institut National de Science Appliquées, INSA*) in Lyon (France).

### 3.2.2.2. Mineralogical characterisation

In this study, the mineralogical characterization was carried out on raw samples of the three substrates by X-ray powder diffraction. The samples were first grounded with a mechanical grinder (Retsch S100) to obtain a grain size of 10-50  $\mu\text{m}$ . The fine grain allows to achieve a good signal-to-noise ration and to minimize preferred orientation of the grains. Approximately 1.0 g of the sample is placed in the sample holder, flatted and spread with a glass piece by successively turning it right to left on the axe, to avoid preferential orientation of the grains.

The samples are then analysed by XRD with a  $\text{CuK}\alpha$  radiation ( $\lambda = 1.54060 \text{ \AA}$ ) on a  $2\theta$  diffractometer (Bruker D8-Advance) in the range of  $5 - 70^\circ$ . Crystalline phases were identified using DIFFRAC EVA software (v.4.1.1) by comparing the registered patterns with the Powder Diffraction Files (PDF). The measurements were conducted at the Henry Longchambon Diffractometer Center of the Claude Bernard University, in Lyon (France).

### 3.2.2.3. Physical characterisation

#### 3.2.2.3.1. Morphology of the surface

SEM-EDS images of the GA surface before and after the experiment were carried out with a SEM-EFG XL30 Philips microscope to observe the morphology of the surface and the changes carried out. The samples were gold coated to avoid surface polarization. The measurements were conducted at the Analytical Science Institute (*Institut de Science Analytiques, ISA*) in Lyon (France).

#### 3.2.2.3.2. Particle size distribution

The particle size distribution of a solid substrate describes each proportion or relative amount of the solid sample that falls in a specific particle size (defined by the diameter if the approximation of spherical particles is considered).

The particle size distribution of all substrates was determined by the standard dry sieving method NF EN ISO 17892-4 (January 2018) where several sieves,

characterized by the size of their mesh (80 $\mu$ m – 12.5mm), are piled up (from the bigger to the smaller mesh) and placed in a mechanical sieve shaker. A representative sample is placed on the first sieve (bigger mesh) and the pile is shaken for 20 min. After that the mass of the sample retained in each sieve is measured.

This procedure was carried out for two representative samples of each substrate. The samples of 500-1000 g were obtained by successively splitting from a bigger sample (25 - 5kg) with a riffle splitter. Such chute splitter repeatedly halves the samples until a sample of the desired size (or mass) is obtained.

#### 3.2.2.3.3. Density

The specific density ( $\rho_s$ ) was determined by the pycnometer method NF EN ISO 11508 (May 2014) (n = 3).

#### 3.2.2.3.4. Dry mass

The dry mass was determined by the gravimetric method described by the standard method ISO 11465:1993 on four representative raw samples.

#### 3.2.2.3.5. Specific surface area

The Specific Surface Area (SSA) was determined by two different methods:

- a) the BET method ( $SSA_{BET}$ ) using N<sub>2</sub> gas with an ASAP 2020M. The measurements were carried out by the Analyze-Texture service of the Institute for Research on Catalysis and the Environment of Lyon (IRCE Lyon) (France).
- b) Considering the particle size distribution ( $SSA_{psd}$ ) of the material and the assumption of spherical particles described by Eq.3.8.

$$SSA \left[ m^2 / kg \right] = \frac{(1-f)}{\rho_s} \sum_{i=1}^{n-1} \frac{12}{d_{i+1} + d_i} \cdot \frac{m_i}{M} \quad [3.8]$$

Where  $f$  is the total porosity of the material,  $\rho_s$  is the specific density ( $\text{kg/m}^3$ ),  $n$  is the total number of sieves used,  $d_i$  is the diameter of the  $i^{\text{th}}$  sieve,  $m_i$  is the recovered mass between the  $i^{\text{th}}$  and the  $i^{\text{th}+1}$  sieve and  $M$  is the total mass of the sample.

### 3.2.3. Characterisation of the filtering bed

Once the substrates are packed forming a filter bed, several properties need to be determined to properly define hydraulic performance of the system.

#### 3.2.3.1. Bulk density

The bulk density ( $\rho_b$ ) was measured by the volume of a dry sample occupied by a known mass of material ( $n = 3$ ).

#### 3.2.3.2. Porosity

The porosity of the media describes the void volume fraction of the total volume of the filter. It was determined using the standard soil science procedure based on estimations of bulk density and particle density (Klute 1986) and calculated as described in Eq.3.9.

$$\text{Porosity} = 1 - \frac{\rho_b}{\rho_s} \quad [3.9]$$

#### 3.2.3.3. Saturated hydraulic conductivity

Hydraulic conductivity refers to the coefficient of proportionality in Darcy's law (Eq.3.10) describing liquid flow through porous media in saturated conditions.

$$k_h = \frac{Q \cdot L}{A \cdot \Delta h} \quad [3.10]$$

Where  $k_h$  (m/s) is the saturated hydraulic conductivity,  $\Delta h$  is the head loss (m),  $A$  is the section area of the column ( $\text{m}^2$ ),  $L$  is the distance between piezometers (m) and  $Q$  is the flow rate ( $\text{m}^3/\text{s}$ ). Also called permeability coefficient, the hydraulic conductivity is a

material property that reflects the relative ease of the liquid flow through porous media (Shackelford 2013).

The hydraulic conductivity of the apatite laboratory columns was measured before and at the end of the experiments using the constant head method (Fig.3.8). The columns used for the laboratory scale experiments on phosphorus retention were the same ones used for the permeability tests allowing the measurements of  $k_h$  at different experimental times without disrupting the filter bed. The test proceeds as follows: a pressure head is set up using the reservoirs fed by a peristaltic pump. The water goes through the bed at a constant flowrate creating a head loss between the sampling points of the column, which are connected with four piezometers. The head loss observed in the piezometers (accuracy  $\pm 1$  mm) is associated to a flowrate, which is determined by measuring the collected water mass (balance accuracy  $\pm 1$  g) during a time interval. The flowrate and head loss were measured three or four times for each pressure head applied (four to six different pressure heads were set up for each test).

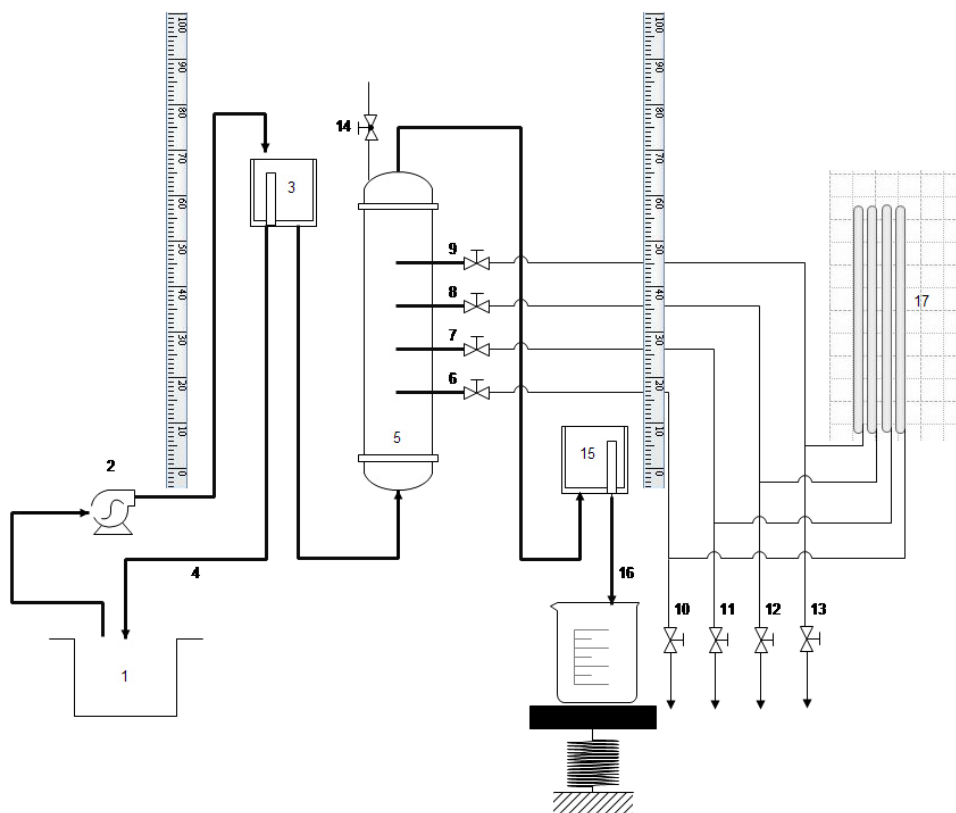


Fig. 3. 8. Scheme of the constant head permeability test setup: 1) feeding tank, 2) peristaltic pump, 3) upper reservoir, 4) Overflow drain for upper reservoir, 5) column, 6-9) sampling points with valves, 10-13) valves for air release, 14) column air purge valve, 15) lower reservoir, 16) Flow measuring point and 17) piezometers.

This test allows the examination of significant changes made in the bulk of the bed due to the accumulation of precipitates or other deposits, the development of a biofilm and/or the changes in the substrate's density due to disaggregation or the compaction of the particles.

#### 3.2.3.4. Flow regime: Tracer test

A tracer tests consists of introducing a tracer into the influent of a reactor to analyse the response observed downstream. The concentration of the tracer at the outlet of the reactor is measured as a function of time drawing a tracer response curve. Tracer tests allow evaluating the hydraulic performance of a system by determining the effluent hydraulic retention time (HRT) and other characteristic parameters of non-ideal flows (dispersion, hydraulic efficiency). The tracer response (Concentration vs time) curve can be normalized and transformed into a retention time distribution curve (RTDC). The retention time distribution function ( $E(t)$ ) is defined as (Kadlec and Wallace 2009):

$$E(t) = \frac{Q(t)C(t)}{\int_0^{\infty} Q(t)C(t)dt} \quad [3.11]$$

Where  $Q(t)$  accounts for the volumetric flowrate ( $m^3/h$ ) at a time  $t$  (h) and  $C(t)$  ( $g/m^3$  of  $mg/L$ ) is the tracer concentration at the outlet of the system at a time  $t$ .  $E(t)$  is, indeed, a probability density function which describes the contact time distribution of the water in a filter. Its most important characteristic is that the air under the curve is equal to the unit.

$$\int_0^{\infty} E(t)dt = 1 \quad [3.12]$$

For non-ideal flows, the mean experimental retention time ( $t_{mean}$ ) or tracer retention time defined by Eq. 3.13 and the theoretical or nominal HRT ( $t_n$ ) defined by Eq.3.14, usually get different values.

$$t_{mean} = \int_{t=0}^{\infty} t E(t)dt \quad [3.13]$$

$$t_n = \frac{V_{total}}{Q} \quad [3.14]$$

$$Q = \frac{\sum Q(t)\Delta t}{t_{total}} \quad [3.15]$$

Where  $V_{total}$  ( $m^3$ ) stands for the total volume of the reactor and  $Q$  is the mean flowrate during the tracer test (Eq.3.15). The flow conditions can be evaluated by the variance ( $\sigma^2$ ) of the RTDC, which measures the dispersion of the tracer in the reactor (Eq. 3.16). Dispersions close to zero suggests near plug flow conditions. Complete mixed conditions are attained when the variance approaches infinite.

$$\sigma^2 = \int_{t=0}^{\infty} (t - t_{mean})^2 E(t) dt \quad [3.16]$$

By interpreting the RTDC one can identify the occurrence of any flow disturbance (e.g. short-circuiting, dead volumes, recirculating zones) and how much the flow approaches an ideal plug flow reactor or an ideal continuous stirred tank reactor (CSTR). In fix-bed systems a good hydraulic efficiency requires near plug flow conditions and a maximum effective utilisation of the filter (Persson J. et al. 1999). For instance, the combination of short-circuits flow paths and recirculating zones may produce a RTDC with a flat peak exhibiting a poor hydraulic efficiency. A poor hydraulic efficiency may be also caused by the presence of dead volumes, which can take the appearance of long RTDC tails. The hydraulic efficiency of a reactor is measured as the relationship between the effective volume and the total volume of the filter (Eq.3.17).

$$e = \frac{V_{effective}}{V_{total}} = \frac{t_{mean}}{t_n} \quad [3.17]$$

And therefore, the fraction of dead zones present in the reactor is obtained from  $1 - e$ .

On the other hand, the generated data of a tracer test can be interpreted to determine the flow conditions of a reactor. In most cases, real flow conditions result from a mix of plug flow and CSTR. The tank-in-series (TIS) hydraulic model which considers the flow as a result of several CSTR in series can be applied. The RTDC of a TIS model produces a gamma distribution curve. The distribution function is defined as the expression in Eq.3.18.

$$E(t) = \frac{N}{t_{mean} \Gamma(N)} \left( \frac{Nt}{t_{mean}} \right)^{N-1} \exp \left( - \frac{Nt}{t_{mean}} \right) \quad [3.18]$$

Where  $N$  is the number of CSTR in series and  $\Gamma(N)$  ( $h^{-1}$ ) is the gamma function. The parameters of the model are then  $t_{mean}$  and  $N$ . When  $N = 1$ , the system behaves as one ideal CSTR, when  $N \geq 50$  the RTDC becomes symmetrical and it can be consider

a Gaussian distribution, therefore the flow conditions approach plug flow (Levenspiel 2012).

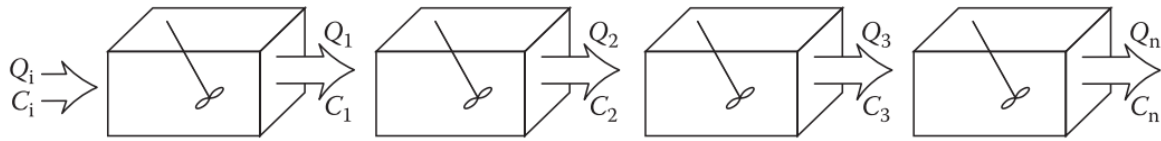


Fig. 3. 9. Tank-in-series hydraulic models assumes equally size completely stirred tank reactors in series ( $t_{mean,1} = \dots = t_{mean,n}$ ) (Kadlec and Wallace 2009).

The gamma distribution is a two-parameter family of continuous probability distributions: the  $\alpha$  parameter or shape parameter, and the  $\beta$  parameter or rate parameter. The probability density function of the gamma distribution is (Croarkin and Tobias 2013):

$$f(t, \alpha, \beta) = \frac{1}{\beta^\alpha \Gamma(\alpha)} t^{\alpha-1} \exp\left(\frac{-t}{\beta}\right) \quad [3.19]$$

The mean of a gamma distribution is  $\alpha\beta$ . In the TIS model  $\alpha = N$ , therefore  $\beta = t_{mean}/N$ . For low values of N, a change in the value causes a significant change in the shape of the curve (Fig.3.10).

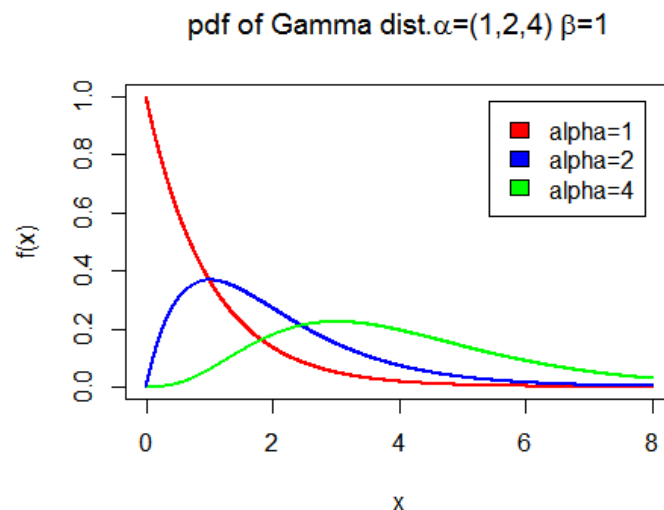


Fig. 3. 10. Representation of the gamma distribution function. The shape of the curve varies significantly when changing the value of alpha for low alpha values.

Two different methods to determine the parameters  $N$  and  $t_{\text{mean}}$  of the TIS model have been proposed: the moment method and the gamma method. The moment method provides an analytical resolution of the parameters based on the calculation of the moment of the RTD function, which is defined as (Metcalf and Eddy 2003):

$$M_n = \int_0^{\infty} t^n E(t) dt \quad [3.20]$$

When  $n = 1$ , the expression becomes Eq.3.13. The first absolute moment is then the mean residence time. When  $n = 2$ , Eq.3.20 becomes Eq.3.16, i.e. the second moment of the RTD function ( $E(t)$ ) is the variance of the distribution ( $\sigma^2$ ). The moment analysis fits the tail of the RTDC, hence it fails to describe RTDC with long tails producing a higher mean retention time and a lower number of tanks in series (Kadlec and Wallace 2009). Although this method is the one proposed in classical literature (Persson J. et al. 1999, Metcalf and Eddy 2003), the fitting of the gamma distribution curve using the  $N$  and  $t_{\text{mean}}$  parameters determined using moments of  $E(t)$  may be poor in some cases.

The gamma method uses a numerical resolution to fit the model to the tracer test data by minimizing the sum of square errors (SSE) between the observed and the predicted data as  $N$  and  $t_{\text{mean}}$  change simultaneously. This can be easily done in a spreadsheet like using the SOLVER tool of Excel™. The SSE fits the data in the peak of the RTDC giving a better fitting of the model specially for curves with long tails.

In this study, tracer tests were conducted at different experimental running times in laboratory columns and full-scale systems. Commonly applied in wastewater treatment facilities because it can be detected at very low concentrations (Metcalf and Eddy 2003), the fluorescein dye ( $C_{20}H_{12}O_5$ ) was used as tracer for all the tests in this study. The tracers were injected as a Dirac injection at the inlet of the filters. A GGUN-FL30 Fluorometer measures the signals (mV) of the effluent which are transformed into concentration values (ppb) through a calibration curve determined for each tracer tests (Concentration, ppb =  $m$  (signal, mV) +  $n$ ). The RTD function was calculated as:

$$E(t) = \frac{Q(t)C(t)}{\sum_0^{t_{\text{final}}} Q(t)C(t)\Delta t} = \frac{M(t)}{M_0} \quad [3.21]$$

Where,  $V(t)$  (L) is the effluent's volume passed through the system at time  $t$  (h) (constant time step),  $C(t)$  ( $\mu\text{g/L}$ ) is the concentration of the effluent at the time  $t$ ,  $M(t)$

(g) is the mass of effluent passed through the system at a time  $t$ , and  $M_0$  (g) is the cumulated tracer mass recovered at the end of the tracer test.

In column experiments, flowrate was measured on a daily basis to keep it constant all along the experiment. It is then considered constant during the tracer tests. In full-scale systems, the flowrate varies during the tracer tests therefore during the test it is measured on a 1 minute time step.

### 3.3. Column experiments

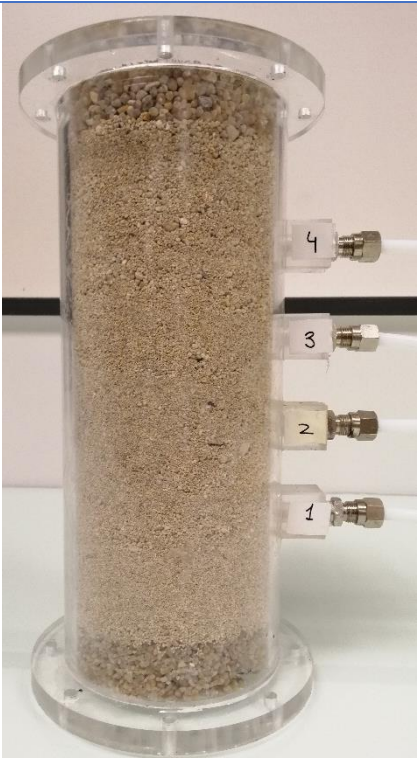
Column experiments aimed the determination of the efficiency and long-term removal capacity of the different substrates under controlled conditions. In the laboratory, a close observation and monitoring allowed focusing on various parameters affecting phosphorus retention (Calcium concentration, biomass development). The phosphorus retention capacity and kinetics, and their evolution with time were assessed through these column experiments. The impact of the influent properties and the evolution of some hydraulic parameters was analysed as well. On the following, a detailed description of the laboratory experiences is given.

#### 3.3.1. Experimental setup

All material were tested in continuous fix-bed columns of  $63.6\text{cm}^2$  section area. From bottom to top, columns composition is presented in Table 3.1.

Table 3. 1. Composition of the experimental laboratory columns for granulated apatite (GA) and natural apatites (NA).

	GA	NA
<b>Bottom transition layer</b>	2.5 cm height of superposed layers of the geo-grid Colblond Enkamal® 7210	2.5 cm height 1/8 mm siliceous gravel (99% quartz, Sibelco)
<b>Filter material</b>	20 cm height of granulated apatite	20 cm height of natural apatite

	GA	NA
<b>Top transition layer</b>	2.5 cm height of superposed layers of the geo-grid Colblond Enkamal® 7210	2.5 cm height 1/8 mm siliceous gravel (99% quartz, Sibelco)
		
	<i>Fig. 3. 11. GA column composition</i>	<i>Fig. 3. 12. NA column composition</i>

The columns had equidistant-depth sampling points to enable solution sampling at various retention times. The pilot-columns were covered with a black opaque plastic coating during the experiments in order to avoid algae development in the media.

All the columns were vertical filters operating in hydraulic saturation. Filters filled with GA operated in a vertical up-flow regime. As it was more difficult to ensure a stable flow in up-flow regime, the filters filled with NA were implemented in a vertical down-flow regime. The flowrate was set by a peristaltic pump or using a gravitational system as shown Fig.3.13.

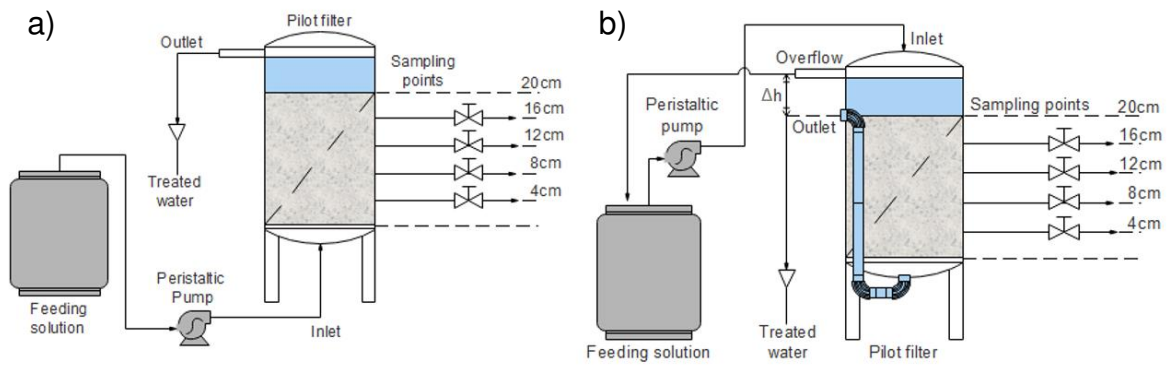


Fig. 3. 13. Schematic representation of the lab-pilots systems for: a) GA filters, the flowrate is set up by the peristaltic pump in the feeding system; b) NA filters, the system is fed by a peristaltic pump but the flowrate is set through an incremental pressure head.

### 3.3.2. Inlet solution

Feeding solutions were manually prepared every two or three days and stored in a 50L tank with no agitation to avoid precipitation inside the tank. The feeding flowrates were set at 5 or 10L/day, depending on the specific column or the experimental time. They were measured every two or three days and adjusted when necessary.

Four different types of feeding solution were prepared:

- (1) Default inlet solution: synthetic solution prepared from tap water and  $\text{KH}_2\text{PO}_4$  (Sigma-Aldrich) to achieve phosphorus inlet concentrations around 15 mg  $\text{PO}_4\text{-P/L}$ . The conductivity was adjusted by adding a NaCl solution (common salt) to approach common values in real wastewater ( $\approx 1000\mu\text{S/cm}$ ).
- (2) High-calcium inlet solution: it consist of the default inlet solution with addition of  $\text{CaCl}_2$  reactant (Supelco) to increase calcium concentration by about 40mg/L respect to tap water calcium concentration.
- (3) Low-calcium inlet solution: tap water is diluted (1/2 dilution) with distilled water to cut in half tap-water calcium concentration. Then,  $\text{KH}_2\text{PO}_4$  and NaCl were added to set phosphorus concentration and conductivity at around 15 mg  $\text{PO}_4\text{-P/L}$  and  $1000\mu\text{S/cm}$ , respectively.
- (4) Treated wastewater inlet solution: this solution was prepared from a biological secondary treatment (activated sludge) effluent with addition of  $\text{KH}_2\text{PO}_4$  in order to adjust phosphate concentration at around 20 mg  $\text{PO}_4\text{-P /L}$ . The adjustment of phosphorus to such concentration aimed to accelerate the saturation of the

filter without increasing the organic load (by increasing flowrate). The phosphorus concentration of the treated wastewater varied from < LQ - 4 mg PO<sub>4</sub>-P /L (min-max) during the experiment. No other reactants were added.

### 3.3.3. Granulated apatite columns

The granulated apatite product was tested in two different columns. The experiment in the first column, called “Column 1”, was divided in two different phases: phase 1, which comprises from day 1 to day 391; and phase 2, which started at day 392 and finished at day 468 (77 days later). During phase 1, the flowrate was set at around 5 L/d; during phase 2, it was set at around 10 L/day in order to accelerate the saturation of the filter. The column is fed by the default solution during the whole experiment and hence the rest of parameters stay constant all along (Table 3.2).

Table 3. 2. Composition of the feeding solutions and operational conditions for both columns filled with GA: Columns 1 and Column 2. Mean value ± Standard deviation (95%) and number of samples analysed in brackets

	Column 1	Column 2
<b>Filled with</b>	GA	GA
<b>Pore volume (L)</b>	0.62	0.64
<b>Flow rate (L/d)</b>	Phase 1: 5.1 ± 0.3 Phase 2: 10.2 ± 0.6	9.6 ± 2
<b>Fed with</b>	Default solution	Phase 1: High calcium sol. Phase 2: Default solution
<b>[P-PO<sub>4</sub>] (mg/L)</b>	14.8 ± 1.2 (46)	12.6 ± 2.9 (33)
<b>[Ca<sup>2+</sup>] (mg/L)</b>	69.8 ± 3.9 (63)	Phase 1: 112.7 ± 7.4 (34) Phase 2: 67.3 ± 3.9 (11)
<b>[HCO<sub>3</sub><sup>-</sup>] (mg/L)</b>	197 ± 14 (63)	182 ± 14 (45)
<b>[NaCl] (mg/L)</b>	323 ± 28 (63)	235 ± 75 (45)
<b>pH</b>	7.5 ± 0.2 (65)	7.7 ± 0.2 (45)
<b>Conductivity (µS/cm)</b>	1 047 ± 63 (65)	1 047 ± 76 (45)
<b>Organic load (g / (m<sup>2</sup> · day)</b>	-	-
<b>P - dosed (kg/m<sup>3</sup> material)</b>	Phase 1: 35.1	Phase 1: 35.8

	Column 1	Column 2
	Phase 2: 50.2	Phase 2: 48.5
<b>Experimental time (d)</b>	Phase 1: 391	Phase 1: 242
	Phase 2: 77	Phase 2: 72

The experiment in the second column, called “Column 2”, was divided in two different phases: phase 1, which comprises from day 1 to day 242; and phase 2 which started at day 243 and finished at day 314 (72 days later). During phase 1, the system was fed with the high-calcium solution in order to increase the supersaturation of the solution to facilitate precipitation. During phase 1, the precipitation on the granules was evident (visual observation). Then, during phase 2, the solution was changed to the default inlet solution to see if precipitation could continue promoted by the precipitate layer despite a lower Ca concentration.

#### 3.3.4. Natural apatite columns

Two different natural apatites were selected for the study: natural apatite 1 (NA1) and natural apatite 2 (NA2). In total, four columns of NA were set up: three columns filled with NA1 and one column filled with NA2. The characteristics of the columns and inflow properties are specified in Table 3.3.

Two reference columns, called NA1\_ref and NA2\_ref, were set with the same operational conditions and inflow characteristics of Column 1 of the GA columns. The NA1 substrate has been chosen, based on economic criteria, for a more extended study to assess the impact of a calcium deficient solution (NA1\_Ca column) and a real treated wastewater solution (NA1\_bio column), on P retention performances.

Flowrate was set at approximately 10L/d for all the systems except for column NA1\_Bio which was set around 5L/d to limit the organic load.

Table 3. 3. Composition of the feeding solutions and operational conditions for the columns filled with NA1 and NA2 (columns NA1\_ref, NA1\_Ca, NA1\_bio and column NA2\_ref). Mean value  $\pm$  Standard deviation (95%) and number of samples analysed in brackets.

Column	NA1_ref	NA1_Ca	NA1_bio	NA2_ref
<b>Filled with</b>	NA1	NA1	NA1	NA2
<b>Pore volume (L)</b>	0.67	0.70	0.69	0.72
<b>Flow rate (L/d)</b>	9.4 $\pm$ 1.9 (85)*	9.9 $\pm$ 1.4 (50)*	5.0 $\pm$ 1.3 (50)*	9.6 $\pm$ 1.9 (85)*
<b>Hydraulic load (m/d)</b>	1.48 $\pm$ 0.3	1.57 $\pm$ 0.22	0.78 $\pm$ 0.20	1.51 $\pm$ 0.3
<b>Fed with</b>	Default solution	Low calcium solution	Treated WW solution	Default solution
<b>[PO<sub>4</sub>-P] (mg/L)</b>	14.6 $\pm$ 1.2	13.8 $\pm$ 0.9	21.0 $\pm$ 2.7	14.6 1.3
<b>[Ca<sup>2+</sup>] (mg/L)</b>	64.4 $\pm$ 11.7	35.2 $\pm$ 2.6 (18)*	65.6 $\pm$ 18.9	66.8 $\pm$ 5.0
<b>Ca/P molar ratio</b>	3.52 $\pm$ 0.42	1.97 $\pm$ 0.20	2.45 $\pm$ 0.75	3.57 $\pm$ 0.35
<b>Organic load (g / (m<sup>2</sup> · day))</b>	-	-	6.7 $\pm$ 4.0 (as TSS) (5)* 40 $\pm$ 46 (as COD) (5)* 3.2 $\pm$ 0.3 (as BOD <sub>5</sub> )** (5)*	-
<b>[NaCl] (mg/L)</b>	319 $\pm$ 52	402 $\pm$ 94	159 $\pm$ 48	311 $\pm$ 33
<b>Conductivity (μS/cm)</b>	992 $\pm$ 102	990 $\pm$ 65	763 $\pm$ 163	1001 $\pm$ 87
<b>pH</b>	7.6 $\pm$ 0.3	7.6 $\pm$ 0.1	7.5 $\pm$ 0.4 (19)*	7.6 $\pm$ 0.2 (33)
<b>Total P-dosed (kg/m<sup>3</sup> material)</b>	49.4	28.9	23.4	54.9
<b>Total P-dosed (g/kg material)</b>	18.1	10.6	8.6	18.5
<b>Experimental time (d)</b>	230	139	133	230
<b>Number of samples</b>	34	20	20	34

\*Number of samples are indicated in brackets in the particular cell when the number of samples is different from the one indicated in the corresponding line of the table.

\*\* Self-monitoring data from the WWTP: mean outlet during the experimental time.

### 3.3.5. Chemical analyses and monitoring

Samples were collected once a week at the inlet and outlet of the systems. The conductivity, pH and temperature of the samples was analyzed *in-situ* using a pHmeter and a conductometer (Mettler Toledo), respectively. To assess the evolution of P concentration inside the bed, samples were also collected at the different sampling points along the column at selected times of the experiment, particularly during the precipitation phase (high phosphorus retention capacities).

The collected samples were stored at 4°C and analyzed within 24 hours after sampling. The cations (sodium, calcium, magnesium, potassium and ammonium) and anions (chloride, sulfate, nitrate, nitrite and phosphate) concentrations were determined on filtered samples (pore size 0.45µm) by ionic chromatography (NF EN ISO 14911 and EN ISO 10304-1, respectively) (Metrohm, IC flex 930). Carbonates and bicarbonates were assessed by the titrimetric analytic method NF EN ISO 9963-1.

Additional measurements were carried out on the samples collected from the column fed with the treated wastewater solution. Such measurements included the chemical oxygen demand (COD) of non-filtered samples according to the norm NF T 90-101; the biological oxygen demand (DBO<sub>5</sub>) according to NF EN 1899-1; total suspended solids (TSS) according to the norm and NF EN 872; and total phosphorus (TP) by ICP-OES.

All the previously described analytic measurements were conducted by the LAMA laboratory of INRAE at Lyon-Grenoble-Auvergne-Rhône-Alpes Centre.

### 3.3.6. Kinetic studies

Several kinetic studies were performed along the experimental time for all the different columns to determine the parameters of the kinetic rate models ( $k$ - $C^*$  model or  $N$ - $k$ - $C^*$  (NTIS) reaction rate models (Kadlec and Wallace 2009)): the volumetric kinetic rate coefficient,  $k_v$  ( $h^{-1}$ ), and the background concentration,  $C^*$  (mg  $PO_4$ -P/L).

A kinetic study consisted in analyzing the evolution of P concentration within the column by sampling at different hydraulic retention times (depths of the column). To address the entire concentration range (from 15 mg  $PO_4$ -P/L to equilibrium), the kinetic

assessment was carried out by reducing progressively the inlet P concentration to simulate longer HRT; i.e., the outlet concentration of the first week was set as the inlet concentration of the following week and so on. This methodology required from one to four or five weeks of measurements until the variation of concentration between two consecutive sampling points were  $\leq 0.1 \text{ mg PO}_4\text{-P/L}$  or the outlet concentration were zero.

This procedure allowed to better define  $k_v$  at high inlet concentration and  $C^*$  when approaching low P inlet concentrations. Generally, both parameters were simultaneously set by minimizing the sum of square errors between the observed and the predicted data. A spreadsheet using the SOLVER tool (Generalized Reduced Gradient nonlinear least square method) of Excel™ was used. Fig.3.14 illustrates an example of the fitting to both reaction rate models.

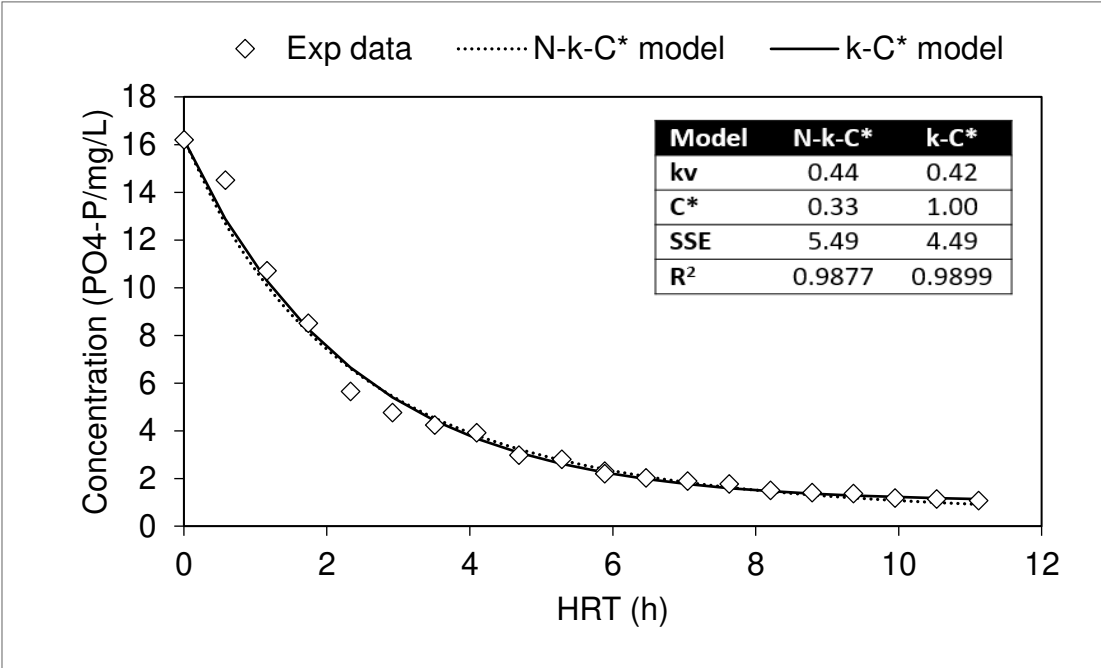


Fig. 3. 14. Example of the fitting method applied in a kinetic study of Column 1 at  $PRC = 5.7 \text{ g PO}_4\text{-P/kg}$  to determine the model parameters  $k_v$  and  $C^*$  of the N-k-C\* model and the k-C\* model. SSE: sum of square errors;  $R^2$ : coefficient of determination.

When no kinetic study was conducted, the calculation of  $k_v$  was carried out by applying the equation of the model based on inlet/outlet phosphorus concentrations and assuming a  $C^*$  value determined in a previous kinetic study. It worth noting, however, that when estimating  $k_v$  values based on average input/output data, an important

uncertainty may occur in particular when outlet concentration is close to  $C^*$ . In addition, the parameter  $C^*$  evolves with time, or more specifically with the phosphorus retention capacity (PRC), therefore when setting  $C^*$ , one assumes it keeps constant during a certain experimental time interval which adds more uncertainty to the results. The kinetic studies must be performed frequently to correct the parameters as they evolve with the PRC.

### 3.3.7. Tracer tests

Fluorescein tracer tests were carried out for all the columns at several times during the experimental time except at initial times (low PRCs) to avoid interferences from fluorescein adsorption on the apatite filter bed. The characteristics of the tracer tests carried out in laboratory columns are shown in Tables 3.4. and 3.5.

Table 3. 4. Tracer tests characteristics on GA filters: mass of tracer used, volume of tracer solution sent to the filter and duration of the tracer tests.

	Column 1	Column 1	Column 1	Column 2
<b>Mass added (<math>\mu\text{g}</math>)</b>	345	184	75	174
<b>Sent volume (<math>\text{cm}^3</math>)</b>	28	7	15	30
<b>Duration (h)</b>	23.4	40.2	17.5	16.4
<b>Exp. time (days)</b>	22	90	468	285
<b>PRC (<math>\text{g PO}_4\text{-P/kg}</math>)</b>	0.83	3.08	10.0	10.5

Table 3. 5. Tracer tests characteristics on NA filters: mass of tracer used, volume of tracer solution sent to the filter and duration of the tracer tests.

	NA1_ref	NA1_Ca	NA1_Ca	NA1_bio	NA2_ref
<b>Mass added (<math>\mu\text{g}</math>)</b>	95	115	76	85	147
<b>Sent volume (<math>\text{cm}^3</math>)</b>	19	23	15	17	29
<b>Duration (h)</b>	20	19	18.5	18.8	42
<b>Exp. time (days)</b>	230	139	110	107	230
<b>PRC (<math>\text{gPO}_4\text{-P/kg}</math>)</b>	16.8	9.75	8.17	7.12	17.5

### 3.4. Field campaigns

Intensive measurement campaigns were carried out in four selected wastewater treatment plants (WWTPs) provided with full-scale granulated apatite filters (GAF) to treat phosphorus (P). The WWTPs treated urban wastewater of small and medium size communities (< 5,000 PE) with treatment wetland systems. Since their commissioning, the WWTPs were monitored by regulatory surveys (inlet/outlet of the WWTP). However, none of them really focused on the performances of the GAF and P treatment revealing the need of conducting intensive campaigns in order to determine their actual performance after several years of operation, and their phosphorus retention capacity (PRC) and kinetics in real conditions.

The selected WWTPs with GAF will be introduced on the following as well as the details of the measurement campaigns conducted.

#### 3.4.1. Full-scale filters

Four over twenty full-scale GAF installed in France were selected based on their age and hydraulic regime. The three oldest filters were: Filter A, Filter B and Filter C. The youngest filter, Filter D, commissioned at the beginning of this study was also monitored. Since GA has a batch production system, the study took care that the three oldest filters selected were produced in the same production batch in order to compare them avoiding potential differences derived from the composition of the GA. The same production batch was also used for the laboratory column experiments previously described.

##### 3.4.1.1. Filter A

Filter A is a vertical up-flow filter placed downstream of a TW plant of 500 PE capacity. The TW plant, commissioned in November 2012, consisted of two stages of non-saturated vertical down-flow filters planted with *Phragmites australis* (typical French system): first stage is a three-cells filter of 200 m<sup>2</sup> of surface area per cell; second stage is a two-cells filter of 200 m<sup>2</sup> of surface area per cell. The WWTP receives municipal and industrial wastewater.

The GAF is fed by a pump with the effluent from second stage of TW. The inflow is distributed at the bottom of the filter by two perforated ramps. The treated wastewater goes its way up to the surface of the filter through 20 cm transition layer (15 cm of 20/40 pebbles + 5 cm of 2/6 gravel) and 1.10 m of GA reactive media. On the surface, there is a water ponding of 10 cm depth. The collecting systems consists of two lateral collector channels. The total volume of the reactive media in the filter is of approximately 45m<sup>3</sup> (12 x 3.4 x 1.1, on site measurements).



*Fig. 3. 15. a) full-scaled granulated apatite filter: Filter A; b) first stage of treatment wetland plant and granulated apatite filter A.*

The regulatory threshold of the station is shown in Table 3.6. The discharge limit of the WWTP concerning total phosphorus (TP) is 2.5 mg/L.

Table 3. 6. Regulatory threshold for major parameters of the WWTP with Filter A.

Parameters	Maximum concentration (mg/L)	Minimum yield (%)
BOD <sub>5</sub>	25	70
COD	90	75
TSS	30	90
TN	-	-
TP	2,5	-

TN: Total nitrogen

#### 3.4.1.2. Filter B

Filter B is a vertical down-flow filter placed downstream of a TW plant of 390PE capacity, commissioned in December 2011 and receiving municipal wastewater. It consisted of two stages of non-saturated vertical down-flow filters (French system) planted with *Phragmites australis*: first stage is a three-cells filter of 218 m<sup>2</sup> of surface area per cell; second stage is a two-cells filter of 168 m<sup>2</sup> of surface area per cell. The TW stages are fed by a gravity system (automatic siphon).

The GAF is continuously fed by gravity with the effluent from second stage of TW. The inflow is distributed at the top of the filter by one-point distribution system to a water ponding of 10 cm depth. The treated wastewater goes down the filter passing a 10 cm depth of calcite gravel layer (10/20) in first place. The water continues then flowing through a 1.3 m depth of GA reactive layer and a 15 cm depth transition layer of gravel 15/25 at the bottom of the filter. The water flows out of the system by three drainage pipes placed at the bottom in front of the inlet point. The total volume of the reactive media in the filter is of approximately 55 m<sup>3</sup> (8.5 x 5 x 1.3, on site measurements).



*Fig. 3. 16.a) Full-scale granulated apatite filter: Filter B; b) second stage of treatment wetland plant and granulated apatite filter.*

The regulatory threshold of the station is shown in Table 3.7. The discharge limit of the WWTP concerning total phosphorus (TP) is 4 mg/L.

Table 3. 7. Regulatory threshold for major parameters of the WWTP with Filter B.

Parameters	Maximum concentration (mg/L)	Minimum yield (%)
BOD <sub>5</sub>	25	90
COD	90	85
TSS	30	90
TKN	10	85
TN	30	45
TP	4	-

TKN: Total Kjeldahl nitrogen

#### 3.4.1.3. Filter C

The WWTP containing filter C is a 4,500 PE capacity TW plant (combined sewer) commissioned in January 2013. It consist of three TW treatment stages: a non-saturated vertical down-flow TW; an horizontal TW partially filled with GAF; and a non-saturated vertical down-flow TW. All of them planted with *Phragmites australis*. The first stage is composed of three filters operating in parallel, each one composed of three cells (600 m<sup>2</sup>/cell). The horizontal filter is a two-basin filter with three cells per basin. Each basin has a surface of 2,700 m<sup>2</sup>. The total surface of the horizontal TW is, therefore, 5,400 m<sup>2</sup>. The inflow is fed by a pump and is distributed with a central ramp to one of the cells of each basin at a time. The water flows horizontally trough a 10 m layer of gravel and a 8 m layer of GA. The total surface of GAF built in the TW is 2400 m<sup>2</sup> (1,200 m<sup>2</sup> /basin). The mean depth of the GAF is 0.65 m. The last stage of treatment is a non-saturated vertical filter TW composed of two filters with three cells per filter (375 m<sup>2</sup>/cell).

The regulatory threshold of the station is shown in Table 3.8. The discharge limit of the WWTP concerning total phosphorus (TP) is 1.5 mg/L.

Table 3. 8. Regulatory threshold for major parameters of the WWTP with Filter C.

Parameters	Maximum concentration (mg/L)	Minimum yield (%)
BOD <sub>5</sub>	25	91
COD	90	85
TSS	35	92
TKN	10	86
NH <sub>4</sub>	4	79
TN	15	92
TP*	1.5	81

NH<sub>4</sub>: ammonium. \* From May to October included.



Fig. 3. 17. Second stage of the treatment wetland plant: horizontal filter + granulated apatite filter C planted with *Phragmites Australis*.

#### 3.4.1.4. Filter D

Filter D is a vertical down-flow filter placed downstream of a TW plant of 1,400 PE capacity and commissioned in December 2016. The WWTP receives domestic wastewater. The TW consists of one aerated filter receiving raw wastewater (Rhizosph'air® - Syntea Company) planted with *Phragmites australis* and divided into 4 cells (375m<sup>2</sup>/cell). The GAF is fed with the effluent of the TW by a pump to a ramp distribution system. The GAF is composed from top to bottom of a 10 cm layer of calcite gravel, a 1.5 m layer of GA and finally a 15 cm gravel transition layer. The total volume of the reactive media is approximately 337.5 m<sup>3</sup> (22.5 x 10 x 1.5).

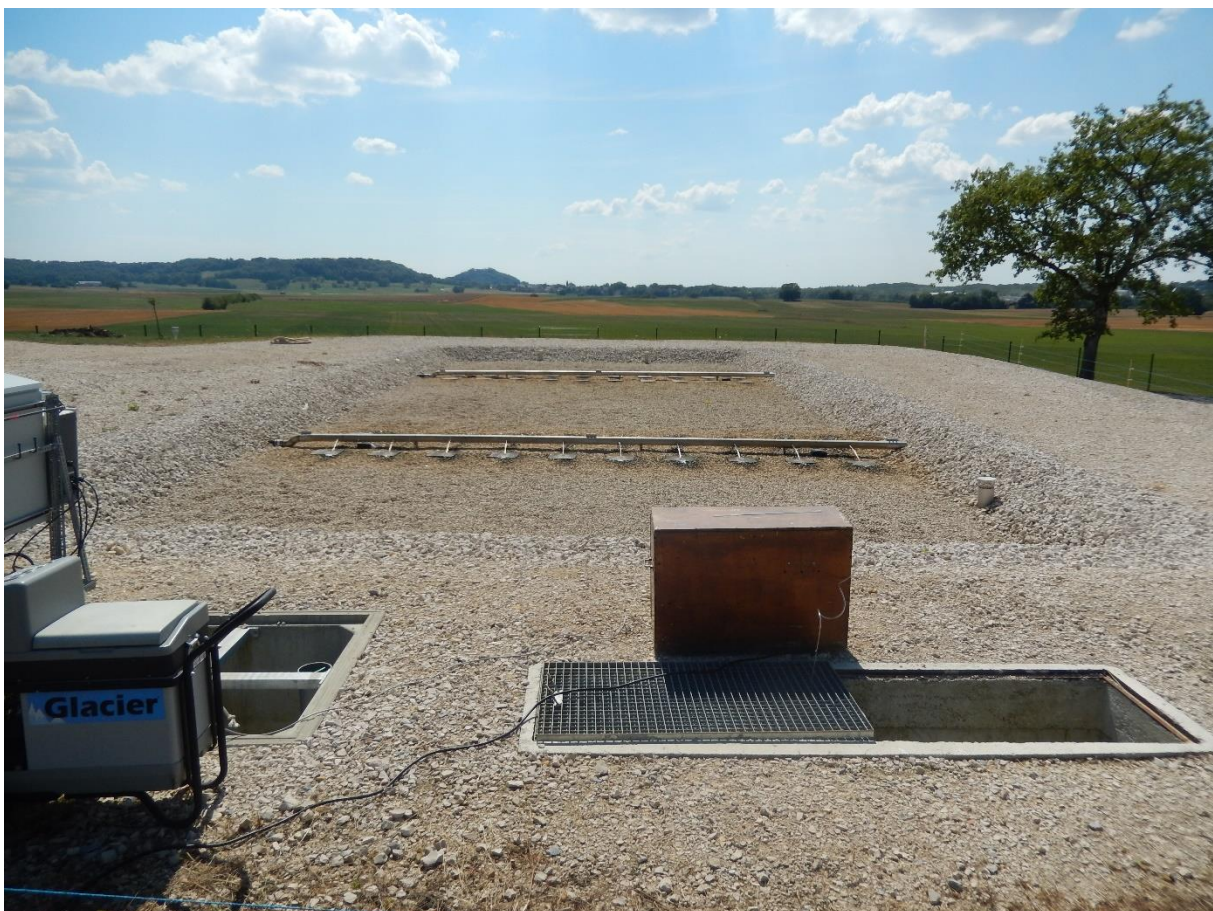


Fig. 3. 18. Full-scale granulated apatite filter: filter D.

The regulatory threshold of the station is shown in Table 3.9. The discharge limit of the WWTP concerning total phosphorus (TP) is 2 mg/L.

Table 3. 9. Regulatory threshold for major parameters of the WWTP with Filter D.

Parameters	Maximum concentration (mg/L)	Minimum yield (%)
BOD <sub>5</sub>	15	95
COD	90	90
TSS	20	90
TKN	15	80
TP	2	80

### 3.4.1.5. Summary of the GAF

Table 3.10 synthetises the main characteristics of the full-scale GAF selected for intensive measurement campaigns.

Table 3. 10. Characteristics of the full-scale granulated apatite filters selected for the study.

	Filter A	Filter B	Filter C	Filter D
<b>WWTP capacity (PE)</b>	500	390	4500	1400
<b>Commissioning date</b>	2012	2012	2013	2016
<b>Treatment stages</b>	VFTW + VFTW + GAF	VFTW + VFTW + GAF	VFTW + HFTW with GAF + VFTW	VATW + GAF
<b>Hydraulic regime of GAF</b>	Vertical up-flow	Vertical down-	Horizontal flow	Vertical down-flow
<b>Water ponding</b>	Yes (10 cm depth)	Yes (10 cm depth)	no	no
<b>Localisation</b>	Downstream the TW	Downstream the TW	Apatite material within the HFTW (2 <sup>nd</sup> treatment stage)	Downstream the TW
<b>Planted</b>	No	No	Yes ( <i>Phragmites australis</i> )	No

	Filter A	Filter B	Filter C	Filter D
<b>Other Characteristics</b>	None	Calcite layer above the filtering material (0.1 m)	None	Calcite layer above the filtering material (0.1 m)
<b>Feeding system</b>	By pump	By gravity	By pump	By pump
<b>GAF dimensions (length x width)</b>	12 x 3.4	8.5 x 5	150 x 8 (TW: 150 x 10 (gravel))	22.5 x 10
<b>GA Depth (m)</b>	1.1	1.3	0.65 (TW: 0.55 (gravel))	1.5
<b>Gravel transition layer depth(m)</b>	0.2	0.15	None	0.15
<b>Hydraulic length in GA (m)</b>	1.1	1.3	8.0	1.5
<b>Regulatory discharge limit in TP (mg P/L)</b>	2.5	4	1.5	2

VFTW: Vertical Flow Treatment Wetland; HFTW: Horizontal Flow Treatment Wetland; VATW: Vertical Aerated Treatment Wetland; GAF: Granulated Apatite Filter; PE: population-equivalent. TP: Total phosphorus.

### 3.4.2. Measurement campaigns

Four-day intensive measurement campaigns were conducted twice a year for each filter during two years. The data was completed with the historical information available from regulatory surveys.

#### 3.4.2.1. Mass balance: 24h proportional sampling

24h-flow proportional samplings were carried out twice per campaigns at the inlet and outlet of the GAF using a refrigerated automatic sampler (Teledyne ISCO 4700). The flowrate was measured using a flowmeter sensor (reference) or a bubble tube (ISCO).

The resulting proportional samples were analyzed *in-situ* for pH and conductivity using a pHmeter and a conductometer (Mettler Toledo), respectively. The samples were then stored in a 2 L flask. An aliquot of the samples was filtered (pore size 0.45µm) and acidified up to pH = 2 with a highly concentrated H<sub>2</sub>SO<sub>4</sub> solution and stored in flasks of 250 mL. The resulting flasks were stored at 4°C and analyzed within the 24-72h hours from their sampling.

The samples were analyzed to determine cations (sodium, calcium, magnesium, potassium and ammonium) and anions (chloride, sulfate, nitrate, nitrite and phosphate) concentration by ionic chromatography (NF EN ISO 14911 and EN ISO 10304-1, respectively). Carbonates and bicarbonates were assessed by the titrimetric analytic method NF EN ISO 9963-1. Analysis of chemical oxygen demand (COD) according to the norm NF T 90-101; total suspended solids (TSS) according to the norm and NF EN 872; and total phosphorus (TP) by ICP-OES were conducted on the filtered samples. Measurements of BOD<sub>5</sub> (NF EN 1899-1) and COD (F T 90-101) were also carried out on un-filtered samples from the last 24h-proportional sampling.

#### 3.4.2.2. Online monitoring

pH, conductivity, temperature and redox potential were measured online at the inlet and outlet of the system with specific sensors and automatically registered with an integrated data logger (VARION® WTW, Secomam). Online PO<sub>4</sub>-P measurements at the outlet of the filter were carried out with a TresCon® WTW on a five-minute time step.

#### 3.4.2.3. pH monitoring during start-up

The evolution of pH in the effluent of Filter D, commissioned in December 2016, was monitored from April 2017 to December 2017 placing pH probes at the inlet/outlet of the filter (VARION® WTW and Secomam). The flowrate was monitored from the start up using the self-monitoring data from the WWTP (SOFREL LT Data logger).

#### 3.4.2.4. Wastewater sampling inside the filter

The evolution of phosphorus concentration inside the filter was determined by sampling the solution inside the filter at different hydraulic retention times. A perforated probe with a tube connected to a peristaltic pump was penetrated into the filter bed with a hammer. For the vertical filter the solution was pumped out at different depths. For the horizontal filter, all measures were carried out at 30 cm from the surface. The concentration of cations, anions was determined for each sample by ionic chromatography (NF EN ISO 14911, EN ISO 10304-1) and titration (NF EN ISO 9963-1). These measurements were repeated at different spots of the filter for each campaigns.

#### 3.4.2.5. Grab-sampling of granulated apatite

Samples of the granulated apatite in the filter were taken at various times with a shovel for all the filters at depths between 10 and 30 cm from the surface. The samples were air dried and stored at room temperature. Eventually some of these samples were analysed by scanning electron microscopy.

#### 3.4.2.6. Dynamic cone penetration tests

Dynamic cone penetration tests were carried out with a PANDA® penetrometer. This tests measures the cone resistance to penetration (shear strength) of the filter bed. This technique allows the determination of density variations of the media with depth.

*Table 3. 11 Number of sampling points at the surface of the filters and date of the penetration tests carried out.*

Filter A	Filter B	Filter C	Filter D
2 points (10-2017)	2 points (05-2017)	16 points (07-2017)	-
-	2 points (06-2017)	16 points (04-2018)	-
-	2 points (10-2017)	-	-

### 3.4.2.7. Tracer tests

Dirac fluorescein-tracer tests were carried out with a GGUN-FL30 Fluorometer once for each filter. The characteristics of the tracer tests are shown in Table 3.12.

Table 3. 12. Tracer tests characteristics of full-scale filters: mass of tracer used, volume of tracer solution sent to the filter and duration of the tracer tests.

	Filter A	Filter B	Filter C	Filter D
<b>Mass added (g)</b>	4.6	2.0	60	0.6
<b>Volume sent (m<sup>3</sup>)</b>	1.4	1.4	37	8.6
<b>Duration (h)</b>	57	73	154	84

### 3.4.2.8. Summary of field campaigns

The set of campaigns and visits carried out for all the selected filters are collected in Table 3.13.

Table 3. 13. Number and date of intensive measurement campaigns and visits (measurements carried out) to the WWTPs.

Campaign	Filter A	Filter B	Filter C	Filter D
<b>1</b>	04-2017	05-2017*	03-2017	03-2018
<b>2</b>	10-2017*	06-2017	07-2017	07-2018
<b>3</b>	02-2018	10-2017	04-2018	-
<b>4</b>	05-2018	04-2018	06-2018	-
<b>5</b>	-	10-2018	-	-

\*one-day visit to the WWTP

# Chapter 4. Results and discussion: Granulated apatite

---

## 4.1. Context and objectives

The experimental work of this study started with the assessment of phosphorus retention capabilities of a manufactured apatite product, the granulated apatite. The granulated apatite was developed and tested for a 3-month period in a laboratory column showing good phosphorus retention performances (results not published) and encouraging its commercialization and use in full-scale filters treating wastewater of rural communities in France. This short study mentioned as well a doubt in the background concentration such material could guarantee on a long term as well as long-term retention kinetics. Therefore, after several years of operation of the full-scale granulated apatite filters, field campaigns were conducted within the framework of this study to evaluate the long-term retention capacity of such systems under real conditions with the ultimate objective of enhancing the filters design and operation vis à vis of a new generation of granulated apatite product. However, first results from field campaigns were less positive than expected. Consequently, the granulated apatite was also tested in laboratory pilot columns in order to determine the long-term phosphorus retention performances and kinetics to identify the causes of the low performances observed in full scale.

In this chapter, results from the experiments conducted in full-scale and laboratory columns filled with granulated apatite are presented under the form of two scientific publications.

## 4.2. Article 1. Field campaigns

*Published journal article: Journal of Water Process Engineering 40 (2021) 101927*

<https://doi.org/10.1016/j.jwpe.2021.101927>

**Granulated apatite filters for phosphorous retention in treatment wetlands: experience from full-scale applications.**

**L., Delgado-González<sup>a,b</sup> S., Prost-Boucle<sup>a</sup>, S., Troesch<sup>b</sup>, P., Molle<sup>a</sup>.**

<sup>a</sup>INRAE, REVERSAAL Research Unit, 5 rue de la Doua, PB 32108, 69100

Villeurbanne Cedex, France. [laura.delgado-gonzalez@inrae.fr](mailto:laura.delgado-gonzalez@inrae.fr); [pascal.molle@inrae.fr](mailto:pascal.molle@inrae.fr)

<sup>b</sup>Syntea, 12 rue Toussaint Fléchaire, 84510, Caumont sur Durance, France.

### Highlights

- The more suitable hydraulic implementation was the vertical filter with water ponding
- Precipitation on the surface of granules was not observed.
- Sorption capacity is exhausted after 5 to 6 years of operation.
- Filter commissioning requires pH correction.

### Abbreviation list

BAM: Bohart-Adams model

BTC: breakthrough curves

Ca: calcium

CaP: calcium phosphate

CHAP: carbonated hydroxyapatite

CSTR: complete stirred tank reactors

DV: dead volume

GA: granulated apatite

GAF: granulated apatite filter

GRG: Generalized Reduced Gradient

HAP: hydroxyapatite

HFTW: Horizontal Flow Treatment Wetland

HRT: hydraulic retention time

MDRM: modified dose-response model

OCP: octocalcium phosphate

P: phosphorus

PE: population-equivalent

PP: particulate phosphorus

PRC: phosphorus retention capacity

SD: standard deviation

SEM: Scanning Electron Microscopy

SI: saturation index

SSA: specific surface area

SSE: sum of square errors

TCP: tricalcium phosphate

TM: Thomas model

TP: total phosphorus

TSS: total suspended solids

TW: treatment wetland

VFTW: Vertical Flow Treatment Wetland

WWTP: wastewater treatment plant

YNM: Yoon and Nelson model

## Abstract

Since natural apatite has shown a great capacity for phosphorus retention from wastewater, a granulated apatite product was developed to control the particle size distribution of the filter material and avoid premature clogging. Since 2012, twenty full-scale granulated apatite filters have been installed in France, with the primary aim to remove phosphorus from domestic wastewater. Measurement campaigns concerning four of these full-scale filters were carried out over two years (2017-2018) to assess their performance, the maximum retention capacity and phosphorus removal kinetics after several years of operation. The filters were selected according to their age and their hydraulic characteristics (horizontal flow, vertical down flow, vertical up flow). The maximum phosphorus retention capacity was found to be approximately 7.4 g PO<sub>4</sub>-P/kg of granulated apatite. The study revealed low kinetic removal rate coefficients. It is believed that phosphorus retention occurred by adsorption and precipitation within the porosity of granules since precipitation on the granules surface was not observed by the Scanning Electron Microscopy images. Therefore, under the specific environmental conditions tested, the substrate behaves exclusively as an adsorptive-like media. The increase in pH due to alkalinity release requires the implementation of pH correction for a significant period after the commissioning of the filter (0.5 to 1.2 years).

**Keywords:** calcium phosphates; constructed wetland; horizontal filter; municipal wastewater; phosphorus adsorption; vertical filter

### 4.2.1. Introduction

One of the objectives of the European Water Framework directive (2000/60/EC, OJ L 327) is to reduce nutrient emissions in order to avoid eutrophication of waterbodies. Wastewater treatment plants (WWTPs) discharging treated wastewater to ecosystems that are prone to eutrophication must implement specific treatment steps for increased phosphorus (P) removal. In small WWTPs, conventional phosphorus removal usually requires chemical dosing and advanced technical maintenance. The use of a filter especially designed to remove phosphorus may be a more appropriate technology for small WWTPs due to the simplicity and low maintenance needs. A wide variety of materials have been tested for this purpose (Vohla et al. 2011, Yang et al. 2018) among

which natural apatite has shown a great retention capacity for long-term removal (Molle et al. 2011). Like treatment wetlands (TWs), in widespread use in France with over 4,000 in operation (Martinez-Carvajal et al. 2019), apatite filters are extensive systems and therefore, they can operate combinedly.

Previous studies on the use of natural apatite for phosphorus removal from domestic wastewater reported that a fine particle size distribution may lead to premature clogging of the filter (Molle et al. 2011, Troesch et al. 2016). Consequently, a granulated apatite (GA) product (Blandin 2013) was developed and manufactured using natural apatite and a binder. For nearly a decade, the granulated apatite was commercialised and used to build 20 full-scale filters downstream of existing TW systems in France.

The operation and retention processes of GAF are based on results obtained in natural apatites on previous works by Molle et al. (Molle et al. 2005) and Harouiya et al. (Harouiya et al. 2011, Harouiya et al. 2011). Phosphorus retention on natural apatite occurs via adsorption and precipitation phenomena. The mineral apatite surface acts as a crystal seed catalysing the precipitation of calcium phosphates (Molle et al. 2005, Molle et al. 2011). Retention kinetics are expected to be high during the commissioning period mostly due to adsorption (Molle et al. 2011). As reactive adsorption sites deplete, precipitation becomes the predominant mechanism, which slows down the kinetic rate until a pseudo-stabilisation phase is reached (Molle et al. 2011).

In a previous work (Delgado-González et al. 2021), lab-scale experiments on GA using synthetic tap water showed that P was retained by means of adsorption and precipitation on the granules. However, the removal process changed depending on the calcium concentration and its impact on the supersaturation of the inlet solution with respect to the calcium phosphate phases: for low calcium concentration conditions (around 70 mg/L), adsorption and precipitation took place within the granule, filling its porosity from a certain depth. For higher calcium concentration (around 110 mg/L), precipitation took place at the granules surface where layers of hydroxyapatite (HAP) and carbonated hydroxyapatite (CHAP) precipitates superposed onto one another (Delgado-González et al. 2021). However, in real conditions, the influence of all the different ions and molecules present in wastewater affect the ionic strength and supersaturation of the solution (Kowacz et al. 2010), which may also cause changes in the retention processes taking place.

This paper presents results from four different TW plants treating P with granulated apatite filters (GAFs) positioned whether as tertiary filter or included in the TW system. This study conducted an assessment of mature phosphorus filters, particularly in terms of P retention capacity (PRC), performance and kinetics, in real conditions. Intensive measurement campaigns were conducted for two years over four selected apatite filters. Filters A, B and C, all commissioned in 2012, were studied to compare performance from different types of filters: vertical up-flow (filter A); vertical down-flow (filter B) and horizontal flow (filter C). A fourth vertical down-flow filter, filter D, was monitored since its commissioning in 2017 to assess the evolution of the effluent's pH due to alkalinity release from the material's binder. The study also used historic data from regulatory surveys and self-monitoring data.

Main objectives of this work include assessing the current performance of the full-scale systems after several years of operation, estimating PRCs and their kinetic removal rates, and assessing the reaction processes taking place in real conditions. The study also compares full-scale GA filter results with laboratory pilot results presented in Delgado-González et al. (Delgado-González et al. 2021).

#### 4.2.2. Materials and Methods

##### 4.2.2.1. Characterisation of granulated apatite

Firstly, a physical, elemental and mineralogical characterisation of the raw granulated apatite was carried out using techniques as the powder X-ray diffraction, inductively coupled plasma mass spectroscopy and optical emission spectroscopy, as well as, by scanning electron microscopy equipped with an Electron Backscattered Diffraction pattern detector. A full description of the characterisation techniques applied on the granulated apatite substrate can be found in Delgado-González et al (Delgado-González et al. 2021).

The specific surface area (SSA) was determined by N<sub>2</sub> adsorption/desorption isotherms (BET method) using an ASAP 2020M. The porosity was determined using the standard soil science procedure based on estimations of bulk density and particle density (Klute 1986) and calculated as described in Eq.4.1. The bulk density ( $\rho_b$ ) was

measured by the volume of a dry sample occupied by a known mass of material ( $n = 3$ ) and the specific density ( $\rho_s$ ) by the pycnometer method NF EN ISO 11508 (May 2014) ( $n = 3$ ).

$$Porosity = 1 - \frac{\rho_b}{\rho_s} \quad [4.1]$$

The mineral composition of the granules was found to be 79.1% (w/w over the crystallized masse, total crystallinity 80%) carbonated fluorapatite, 12.4% calcite, 4.8% quartz and 3.1% dolomite. Elemental content comprises 32.5%Ca (w/w), 11.8%P, 2.4%Si, 2.2%F, 0.8%S and other metals as Na, K, Mg, Al, Fe with a content below 0.5%. The granulated apatite, 2.8/5 ( $d_{10}/d_{60}$ ), has a specific density of 2.9 g/cm<sup>3</sup> and a specific surface area of 32 m<sup>2</sup>/g (BET method). The porosity of the filtering bed is 49%.

#### 4.2.2.2. Full-scale granulated apatite filters

Four granulated apatite filters treating wastewaters of small and medium size communities of France (< 5,000 PE) were selected to carry out intensive measurement campaigns over two years. The GAFs are hydraulically saturated to increase the hydraulic residence time (HRT) and thus, to facilitate a close contact between phosphates and the filtration material (Molle et al. 2011). To avoid clogging by suspended solids and excessive biomass development, the filters can be placed downstream of the treatment wetland or within the wetland in a second or third treatment stage.

Selection of the GAFs was based on the age of the filter and the hydraulic regime. Since long-term retention occurs via precipitation, the three older GAFs in operation, commissioned in 2012, were selected (filters A, B and C). These three filters are filled with the same GA production batch (exact same average composition) to avoid the influence of variations of the granules composition in the results. This would allow to compare the operation of the filters in terms of performance, PRC and retention kinetics while each filter implements a different hydraulic regime (vertical up-flow, vertical down-flow, horizontal flow).

At the commissioning period pH can be high induced by lime dissolution from the granules binder. Therefore, a new GAF (Filter D) was included in the study in order to assess the pH dynamics during the start-up.

Table 4.2.1 and Fig. 4.2.1 collects the main characteristics of the selected filters.

Table 4.2. 1. Characteristics of the granulated apatite filters selected for the study

	Filter A	Filter B	Filter C	Filter D
<b>WWTP capacity (PE)</b>	500	390	4500	1400
<b>Commissioning date</b>	2012	2012	2013	2016
<b>Treatment stages</b>	VFTW + VFTW + GAF	VFTW + VFTW + GAF	VFTW + HFTW with GAF + VFTW	VATW + GAF
<b>Hydraulic regime of GAF</b>	Vertical up-flow	Vertical down-flow	Horizontal flow	Vertical down-flow
<b>Localisation</b>	Downstream the TW	Downstream the TW	Apatite material within the HFTW (2 <sup>nd</sup> treatment stage)	Downstream the TW
<b>Water ponding</b>	Yes (10 cm depth)	Yes (10 cm depth)	no	no
<b>Planted</b>	No	No	Yes ( <i>Phragmites australis</i> )	No
<b>Regulatory discharge limit in TP (mg P/L)</b>	2.5	4	1.5	2

VFTW: Vertical Flow Treatment Wetland; HFTW: Horizontal Flow Treatment Wetland; VATW: Vertical Aerated Treatment Wetland; GAF: Granulated Apatite Filter; PE: population-equivalent. TP: Total phosphorus.

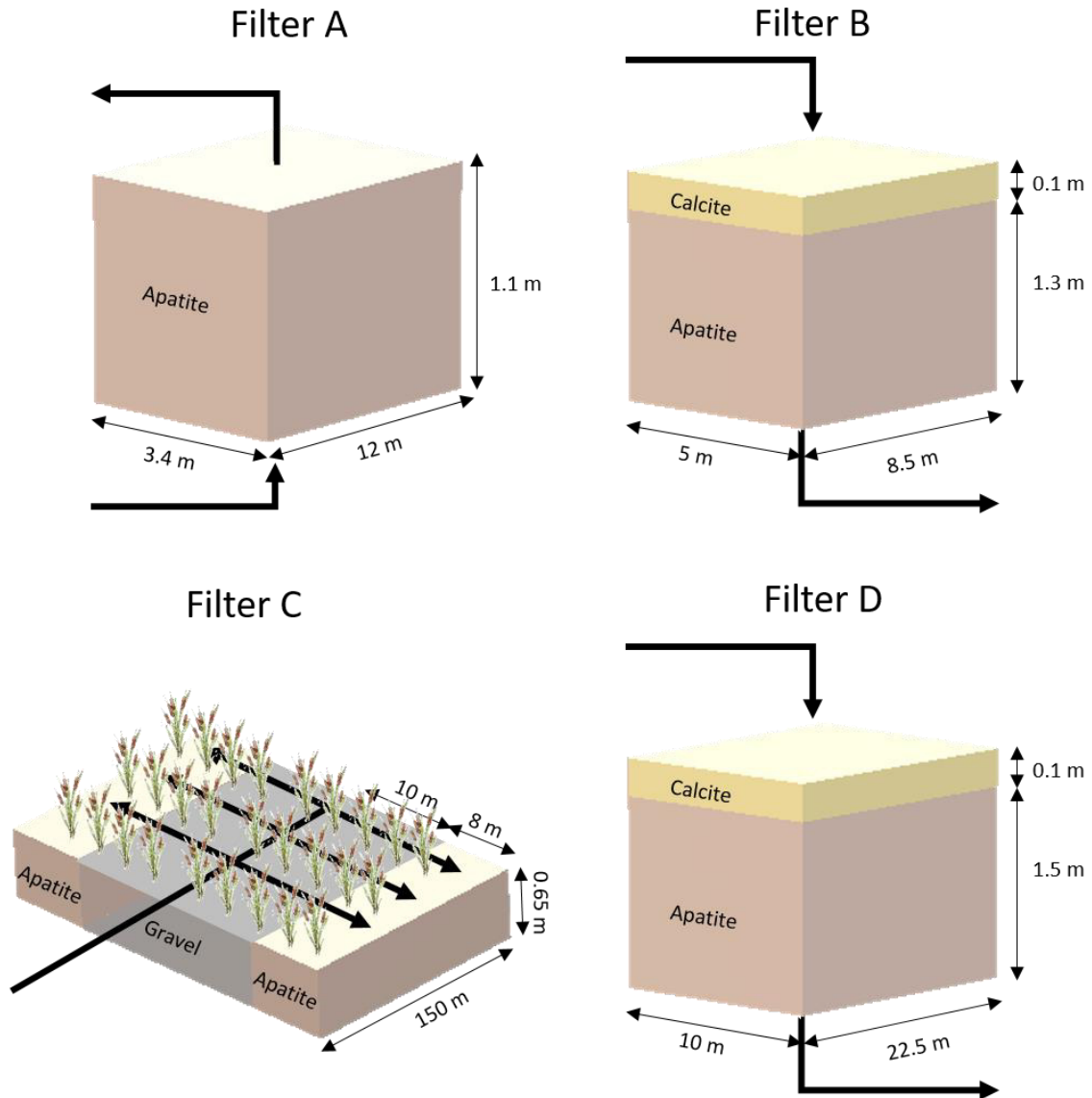


Fig. 4.2. 1. Schemes of the selected granulated apatite filters used in this study

#### 4.2.2.3. Measurement campaigns

The study used data from regulatory surveys carried out from the commissioning of the treatment systems. However, since the treatment plants do not have the same capacity, the number of regulatory surveys was heterogeneous and not enough to perform a precise estimation of saturation levels and retention kinetics. Therefore, intensive measurement campaigns were required to complete the assessment.

Four-day intensive measurement campaigns were conducted twice a year for each filter. These campaigns included 24h-flow proportional sampling at the inlet and outlet of the GAF in order to evaluate P retention. Online  $\text{PO}_4\text{-P}$  measurements at the outlet

of the filter were carried out with a TresCon® WTW analyser to monitor possible dynamics within a day. Sampling was also conducted out at different locations inside the filter, corresponding to different hydraulic retention times (HRTs) in order to estimate P retention kinetics. The analyses of the samples included: pH measurements with a pHmeter (Mettler Toledo); conductivity with a conductometer (Mettler Toledo); redox potential using a probe (Sensolyt 700iq Xylem); TSS, BOD<sub>5</sub> and COD according to the norms NF EN 872, NF EN 1899-1 and NF T 90-101, respectively; TP was measured by ICP-OES and major anions/cations Ca<sup>2+</sup>, Mg<sup>2+</sup>, PO<sub>4</sub>-P by ionic chromatography (NF EN ISO 14911 and EN ISO 10304-1) and HCO<sub>3</sub><sup>-</sup>/CO<sub>3</sub><sup>2-</sup> by the titrimetric analytic method NF EN ISO 9963-1.

For Filter D, the evolution of pH was monitored for several months following the start-up with a flowmeter (bubble tube ISCO) and an online pH sensor (Secomam, WTW VARION®) at the inlet and outlet of the filter.

#### 4.2.2.4. Hydraulic performance

##### 4.2.2.4.1. Tracer Test

To assess hydraulic performance, Dirac fluorescein-tracer tests were carried out with a GGUN-FL30 Fluorometer to precisely determine water retention times and the occurrence of any flow disturbance (short-circuiting, dead volumes, etc.) which would ultimately allow a better evaluation of the kinetic rates. The characteristics of the tracer tests for each filter are given in Table 4.2.2.

*Table 4.2. 2. Tracer tests characteristics: mass of tracer used, volume of tracer solution sent to the filter and duration of the tracer tests.*

	Filter A	Filter B	Filter C	Filter D
<b>Mass added (g)</b>	4.6	2.0	60	0.6
<b>Volume sent (m<sup>3</sup>)</b>	1.4	1.4	37	8.6
<b>Duration (h)</b>	57	73	154	84

A tracer test is characterised by a distribution of hydraulic retention times, defined by the  $E(t)$  function (Eq. 4.2.2). In this study, the retention distribution curve ( $E(t)$  vs  $t$ ) was evaluated using the tank-in-series hydraulic model which produces a gamma distribution (Eq. 4.2.3).

$$E(t) = \frac{Q(t)C(t)}{\int_0^{\infty} Q(t)C(t)dt} \quad [4.2.2]$$

$$E(t) = \frac{N}{t_{exp}\Gamma(N)} \left(\frac{Nt}{t_{exp}}\right)^{N-1} \exp\left(-\frac{Nt}{t_{exp}}\right) \quad [4.2.3]$$

$$t_{exp} = \int_{t=0}^{\infty} t E(t)dt \quad [4.2.4]$$

Where  $Q$  ( $m^3/h$ ) is the flowrate,  $C$  ( $g/m^3$  or  $mg/L$ ) is the tracer concentration at the outlet of the system,  $N$  is the number of complete stirred tanks in series (ad.),  $t$  (h) is time,  $t_{exp}$  (h) is the experimental hydraulic retention time (HRT) which is the mean retention time of the distribution curve. (Eq.4.2.4), and  $\Gamma(N)$  ( $h^{-1}$ ) is the gamma function. The SOLVER tool in Excel™ is used to determine  $t_{exp}$  and  $N$  while minimizing the difference between observed and estimated values of the retention distribution curve (Kadlec and Wallace 2009).

The hydraulic efficiency ( $e$ ) is evaluated using the expression in Eq.4.2.5. Values lower than 1.00 indicate the presence of dead volumes. The spread of the distribution curve with respect to the mean HRT is the variance ( $\sigma^2$  ( $h^2$ )) defined in Eq.4.2.6. The greater the variance, the more different velocities of water are present in the filter.

$$e = \frac{V_{effective}}{V_{total}} = \frac{t_{exp}}{t_n} \quad [4.2.5]$$

$$\sigma^2 = \int_{t=0}^{\infty} (t - t_{exp})^2 E(t)dt \quad [4.2.6]$$

Where  $t_n$  (h) is the nominal (or theoretical) HRT.

#### 4.2.2.4.2. Dynamic cone penetration tests

Finally, dynamic cone penetration tests were carried out (PANDA®) to measure the resistance to penetration (shear strength) of the granulated apatite. This technique allows the determination of density variations of the media due to disaggregation of the

granules or media compaction because of surface precipitation. Its combination with tracer testing gives a more comprehensive overview of the state of the filtration bed, which may eventually identify the occurrence of dead zones and shortcuts.

#### 4.2.2.5. Analytical microscopy

Grab sampling of the filter material was also performed to assess precipitate formation by Scanning Electron Microscopy (SEM). The aim was to observe if precipitation was able to form or not on the surface of the granules, and to compare such observations with those obtained in a previous work with granulated apatite experiments in laboratory columns Delgado-González et al. (Delgado-González et al. 2021). The study also assess the influence of real wastewater in phosphorus retention. SEM micrographs of the surface of apatite granules were performed with a SEM-EFG XL30 Philips microscope.

#### 4.2.2.6. Evaluation of retention capacity by simple modelling

Due to the scattered performance data over the long period of operation for each filter, precise modelling is not feasible. Nevertheless, simple models can be used to estimate and discuss the retention capacity of the granulated apatite in real conditions compared to more accurate data in column experiments of a previous work (Delgado-González et al., 2021). Therefore, two different approaches were explored in this study: sorption models and a first-order kinetic model.

##### 4.2.2.6.1. Sorption models

The first approach considered the evaluation of breakthrough curves (BTCs) through fix-bed sorption models. A BTC represents the evolution of the effluent pollutant concentration with the elapsed time allowing the determination of the maximum sorption capacity of the substrate by using sorption models. Fixed-bed sorption models are based on equilibrium isotherms, axial dispersion, diffusion resistances and reaction kinetics (Patel 2019). Common models include the Thomas model (TM), the Bohart-Adams model (BAM), the Yoon and Nelson model (YNM), the modified dose-response

model (MDRM) and the Clark model (Patel 2019). The TM and BAM usually characterise well systems where the surface reaction is the rate-limiting step of the whole sorption process. However, together with the YNM, the TM and BAM are equivalent models from a mathematical point of view (Chu 2010, Hu et al. 2020) and their parameters are interconnected. Thus, multiple models are not needed for the analysis of a single data set. The sole use of the BAM is recommended by Lee et al. (2014). On the other hand, the application of the Clark model equation requires the use of a parameter from the Freundlich isotherm model, which was not assessed in this study. As a result, the selected models for the analyses of the experimental data of full-scale GAF in real conditions were the BAM and the MDRM (Table 4.2.3).

- BAM (Bohart and Adams 1920): This model assumes a proportional relationship between the adsorption rate and both the remaining capacity of the adsorbent and the solute concentration.
- MDRM (Yan et al. 2001): is an empirical model that reduces the error between the experimental data and the prediction of the Thomas model, especially for very short or very long operation times. The TM combines the Langmuir kinetic model with a second -order reversible reaction and plug-flow hydraulic regime (no axial dispersion).

Table 4.2. 3. Linear and non-linear expressions of the fix-bed sorption models: Bohart and Adams model and modified dose-response model (Lee et al. 2014).

Sorption model	Non-linear	Linear
<b>BAM</b>	$\frac{C_t}{C_0} = \frac{1}{e^{k_{BA}N_0\frac{Z}{U} - k_{BA}C_0t} + 1}$ [4.2.7]	$\ln\left(\frac{C_0}{C_t} - 1\right) = k_{BA}N_0\frac{Z}{U} - k_{BA}C_0t$ [4.2.8]
<b>MDRM</b>	$\frac{C_t}{C_0} = 1 - \frac{1}{\left(\frac{C_0Qt}{q_0X}\right)^a + 1}$ [4.2.9]	$\ln\left(\frac{C_t}{C_0 - C_t}\right) = a \ln t + a \ln\left(\frac{C_0Q}{q_0X}\right)$ [4.2.10]

Where:

- |                       |                                       |
|-----------------------|---------------------------------------|
| a (ad.)               | Modified dose-response model constant |
| C <sub>0</sub> (mg/L) | Influent concentration                |
| C <sub>t</sub> (mg/L) | Effluent concentration at time t      |

$k_{BA}$ (L/ (mg·min))	Bohart and Adams sorption rate constant
$N_0$ (mg/L)	Sorption capacity per unit volume
$q_0$ (mg/g)	Sorption capacity per unit mass of sorbent
$Q$ (mL/min)	Volumetric flow rate
$t$ (min)	Elapsed time
$U$ (cm/min)	Linear flow velocity
$X$ (g)	Mass of sorbent in the column
$Z$ (cm)	Bed depth

This study used the linearized and non-linearized expressions of the selected models to fit the data. The adequacy of the models was evaluated and compared in regards to the sum of square errors (SSE), the coefficient of determination ( $R^2$ ) and the chi-square coefficient ( $X^2$ ) (Foo and Hameed 2010, Lee et al. 2014, Ebelegi et al. 2020).

$$SSE = \sum_{i=1}^m (y_e - y_c)_i^2 \quad [4.2.11]$$

$$R^2 = \frac{\sum_{i=1}^m (y_c - \bar{y}_e)_i^2}{\sum_{i=1}^m (y_c - \bar{y}_e)_i^2 + \sum_{i=1}^m (y_c - y_e)_i^2} \quad [4.2.12]$$

$$X^2 = \sum_{i=1}^m \left[ \frac{(y_e - y_c)^2}{y_c} \right]_i \quad [4.2.13]$$

Where  $y_c$  is the predicted data obtained from the model,  $y_e$  is the experimental data, and  $\bar{y}_e$  is the average of experimental data.

#### 4.2.2.6.2. The N-k-C\* model

Data was also confronted to the N-k-C model (Kadlec and Wallace 2009). The model considers N complete stirred tank reactors (CSTR) in-series with a first-order kinetics. The reaction is described by the  $k_v$  parameter (the kinetic rate coefficient, k) which does not depend on the hydraulic loading rate or the inlet concentration (Gajewska et al. 2013). The model also uses the concept of a background or residual concentration ( $C^*$ ) which, applied to P retention onto apatites, could account for an equilibrium

concentration derived from adsorption and precipitation processes. Thus, the evolution of P concentration at the outlet of the system (C) with the HRT (t) is obtained by the expression in Eq. 4.2.14 according to the N-k-C\* model:

$$C = (C_0 - C^*) \left(1 + \frac{k_v t}{N}\right)^{-N} + C^* \quad [4.2.14]$$

where  $C_0$  is the inlet concentration of phosphorus, N is the number of CSTR in series,  $k_v$  the volumetric kinetic rate coefficient and  $C^*$  the P equilibrium concentration (background concentration). The parameters of the model ( $k_v$  and  $C^*$ ) are estimated from kinetic studies by fitting the evolution of P concentration inside the filter at different HRTs. The N parameter is determined from tracer tests.

### 4.2.3. Results and discussion

#### 4.2.3.1. Hydraulic performance

In order to identify flow heterogeneities and dead zones, tracer tests were carried out for all the filters. Data was analysed using a TIS hydraulic model with a gamma distribution of retention times. Table 4.2.4 shows a summary of the tracer test results. The associated tracer curves can be found in the Supplementary Information (Fig. S.4.2.1).

Table 4.2. 4. Tracer tests results for filter A – D: tank in series hydraulic model solved by the gamma method. (Kadlec and Wallace 2009).

	Filter A	Filter B	Filter C	Filter D
<b>Nominal flow (m<sup>3</sup>/d)</b>	75	57	935	293
<b>Mean hydraulic load during tracer test</b>	126 %	45 %	71 %	22%
<b>Mass % of tracer recovered</b>	59 %	100 %	65 %	73%
<b>Theoretical HRT (h) using (Q<sub>mean</sub>)</b>	7.5	33	50	70
<b>Tracer retention time (h)</b>	4.1	27	56	17
<b>N (number of CSTR in series)</b>	6.2	2.7	4.8	4.6
<b>Coefficient of determination (R<sup>2</sup>)</b>	0.9014	0.0919	0.7565	0.7824
<b>Dead volume</b>	45 %	17%	0%	76%
<b>Variance (σ<sup>2</sup>) (h<sup>2</sup>)</b>	2.7	273	662	63

The filters are in agreement with TIS hydraulic model with N going from 4.6 to 6.2 reactors, the latter belonging to filter A (highest N value). For filter B, the goodness of the fitting is extremely low because the influent is highly scattered in time (several hours) and a bell shape distribution curve cannot be obtained. This must be taken into account on the following when interpreting the kinetic parameters and the phosphorus retention capacity based on N and the dead zones here determined. Dispersion values are quite moderate except for the horizontal filter (filter C). The analysis of the hydraulic performance leads to other observations according to the hydraulic regime:

- Vertical filters

The presence of high to moderate dead zones was identified by tracer test regardless of flow direction (up-flow or down-flow). Since the mass of tracer recovered was lower than 80% for filters A and D, the results must be interpreted with care; however, visual observations corroborated the presence of some hydraulic anomalies and pointed out the importance of the even hydraulic distribution in vertical granulated apatite filters. Water distribution and recovery systems must be well-designed in order to limit dead zones. In Filter D (down-flow), the lack of a superficial ponding water and insufficient distribution ramps do not allow a good water distribution over the entire surface of the filter. Water infiltrates close to the distribution pipes and moves vertically to the outlet resulting in an important short-circuit in the tracer curve (Fig. S.4.2.1.d). For Filter A (up-flow vertical filter) which has a ponding zone, the dead zone can be attributed to heterogeneities in the water flow due to deficiencies in the collector systems. Filter B showed some heterogeneity in the cross-section of the bed during penetrometry tests which may have led to the appearance of dead volumes. The material density increased progressively with the depth of the filter as shown in Fig. 4.2.2.b. Since the filter is by-passed and drained during the winter period, crystallization phenomena onto the apatite surface can be exacerbated, effectively gluing the granules to one another.

This compaction at some levels of the filtering bed may have led to water flow disruptions and bed heterogeneities.

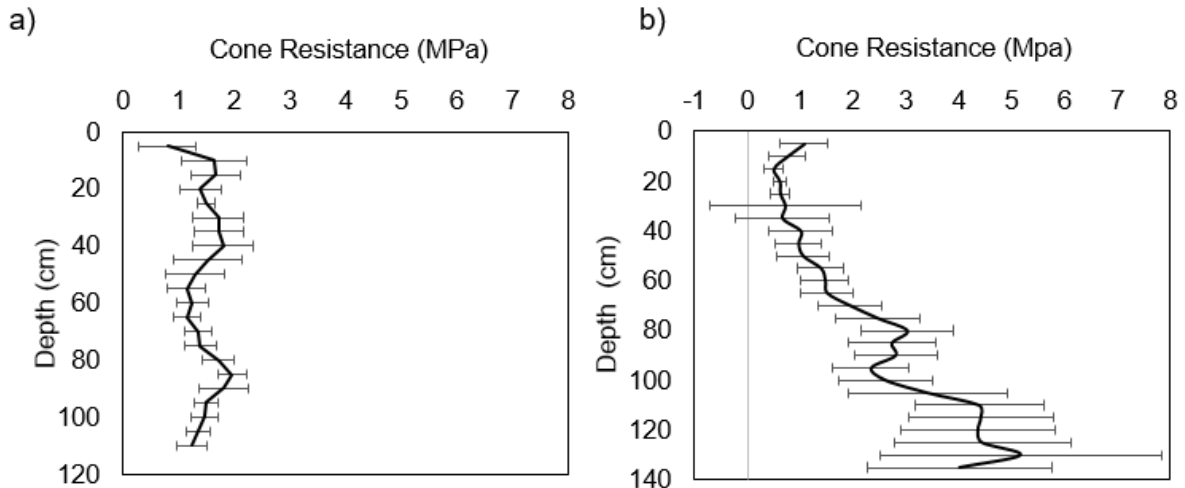


Fig. 4.2. 2. Dynamic cone penetration test results: Evolution of cone resistance with the depth of the reactor for: a) Filter A showing a normal cross section density profile (median of 4 profiles), and b) for Filter B showing anomalies in the bed density which increases progressively with the depth of the filter (median of 7 profiles).

- Horizontal filter planted with *Phragmites australis*:

For Filter C, no dead volume was identified but a short-circuit at the beginning of the tracer test was observed (See Fig.S.4.2.1.c, Supplementary Information). Visual observation confirmed surface flow at different locations. It is thus possible that hydraulic conductivity decreased with time due to organic matter accumulation, development of *Phragmites*, or the evolution of the GA density (compaction/degradation). Such flow heterogeneity within the media was as well confirmed by internal spot-samplings, which revealed important differences in P concentrations at locations of the filter with the same theoretical HRT. Due to the large surface of the filter and the distribution-system implemented (large central distribution ramps with not enough maintenance), flow distribution and flow-pathways inside the filter bed are highly heterogeneous leading to high performance variations inside the filter. The lack of a homogeneous flow distribution is also caused by heterogeneities in the material density. Penetrometer measurements together with direct observation revealed compaction, solidification and disaggregation of the granules at different locations within the filter. Those disturbances of the media density (at depths in

between -10 and -30 cm from surface, see Fig. S.4.2.2, Supplementary Information) might be attributed to variably hydraulic saturation conditions that could have dried the more superficial layers and favoured crystallisation. Indeed, despite the filter was supposed to operate hydraulically saturated it was often found to be partially unsaturated during the campaigns.

#### 4.2.3.2. Evolution of pH

Monitoring of Filter D, from its commissioning, showed a dramatic increase of the effluent pH. Such pH increase is mostly due to lime dissolution from the cement binder of the granulated apatite in contact with water, which releases hydroxyl ions into the effluent as represented in Eq. 4.15 (Yang et al. 2018):



The calcite layer above the apatite may also help keeping a basic pH for a longer time. Fig.4.2.3 shows the evolution of pH with the amount of effluent passed per volume of filter. pH drops below the upper regulatory threshold of 8.5 pH units after 100 m<sup>3</sup> of water per m<sup>3</sup> of filter or 420 m<sup>3</sup>/m<sup>3</sup> when dead zones are considered. Since high pH values in WWTPs effluents can endanger aquatic ecosystems, a pH correction of the plant's effluent must be implemented during significant periods after the commissioning of the filter (from months to around a year according to the design of the filter).

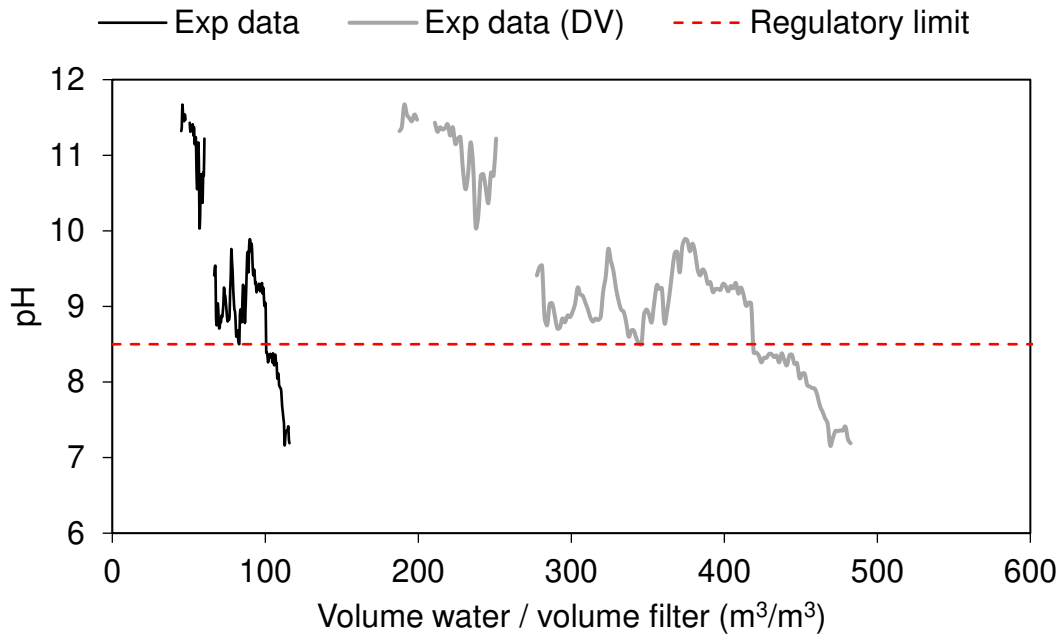


Fig. 4.2. 3. Evolution of pH measured at the outlet of filter D with pore volume with and without considering dead volumes (DV) after the commissioning of filter D

Lime dissolution also affects supersaturation of the solution by increasing the  $\text{Ca}^{2+}$  concentration. High pH and supersaturation levels should promote the precipitation of calcium phosphates and calcium carbonates. Calcium dissolution and pH increase can be also responsible for high kinetic rates in GAF right after the commissioning. There may be some counterproductive effects. The formation of a carbonated layer on the surface of the GA may prevent CaP retention and may accelerate the compaction of the material, leading to a decrease of the hydraulic conductivity.

#### 4.2.3.3. Phosphorus retention performances: PRC

Phosphorus retention efficiency depends on the cumulated P load retained by a particular filter. Performance results can be represented in terms of PRC. To calculate the saturation level, data from the historical performance of regulatory surveys and data from measurement campaigns was used. Since regulatory data often concerned just inlet and outlet concentrations of the WWTP, and not from GA filter specifically, an estimation of the performance evolution was carried out. These estimations were based on several criteria:

- Phosphate ( $\text{PO}_4\text{-P}$ ) concentration at the outlet of the filter is determined from total phosphorus (TP) measurements by applying an average particulate phosphorus (PP) to total suspended solids (TSS) ratio obtained during measurement campaigns ( $\text{PP/TSS} = 0.01$ ). When the filter is on second stage (Filter C) P concentration at the outlet of the filter is assimilated to the P concentration at the outlet of the WWTP (as  $\text{PO}_4\text{-P}$ ), since no significant retention of P is expected to occur on the third stage of treatment.
- The mean inlet  $\text{PO}_4\text{-P}$  concentration of measurement campaigns for a particular filter is used when no data are available.
- Finally, estimations are carried out considering a constant mean flow rate based on all available data.

The application of these criteria entails, indeed, a high level of uncertainty resulting in a high variability of the estimations that must be considered for results interpretation. The characteristics of the inflow for the three Filters A, B and C are presented in Table S.4.2.1 of the Supplementary Information.

By representing the evolution of the retained P as a function of the cumulative load received by the filters, the maximum retention capacity of GA in real conditions can be discussed. Fig. 4.2.4 shows similar initial retention trends for low cumulative P loads in all filters. Nevertheless, the evolution of the performance of the filter with increasing cumulative load can only be seen for Filter A. A reduction of the filter efficiency is observed at around 3.5 g  $\text{PO}_4\text{-P}$  retained / kg material, attaining an asymptotic trend at 4.0 g  $\text{PO}_4\text{-P}$ / kg material. When the estimated dead volume (DV) is considered, the maximum PRC is attained at 7.4 g  $\text{PO}_4\text{-P}$  / kg material P in a reduced reactor volume (Fig. 4.2.4.a). Several factors may significantly affect PRC estimations like the presence of dead zones, as well as the uncertainties associated with flow rates and the inlet concentrations. For instance, to consider the impact of inlet concentration assumptions, the standard deviation of the mean inlet concentration can be used, as shown in Fig. 4.2.4.b for Filter A. This highlights the great variability of PRC estimations due to the uncertainty associated with the low regulatory surveys frequency.

The evolution of PRC is also compared with the results of the experiment conducted in a laboratory-scale filter with synthetic water under controlled conditions (Column 1 from Delgado-González et al. (Delgado-González et al. 2021)). The drop in P retention

yield is observed at PRC values higher than those obtained under real conditions. The differences may be due to the uncertainties associated with the hypothesis applied for the estimations in full-scale systems, but also the consequences of the impact of real wastewater characteristics on chemical reaction. In this sense, two major aspects may negatively affect P retention in full-scale systems: the biomass development onto the surface of the filter material (Harouiya et al. 2011) and the influence of several different ions present in the effluent, on the chemical reaction. It has been reported that the concentration and type of organic molecules and inorganics salts present in the effluent produce different aqueous solvation environments which may affect differently the precipitation processes and kinetics even when comparing solutions with the same ionic strength (Kowacz et al. 2010). It is worth noting that when considering the dead volume and the uncertainty on the input concentration, the estimation can bring the saturation curve close to the one obtained in laboratory conditions (Fig. 4.2.3.b).

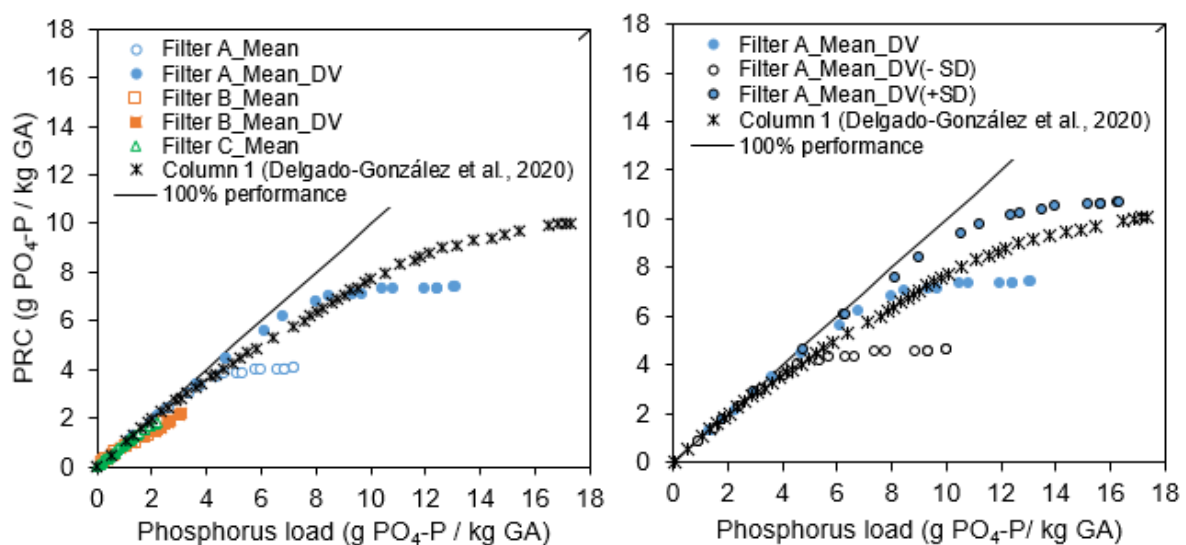


Fig. 4.2. 4. a) Evolution of the phosphorus retention capacity of granulated apatite. Estimations just based in mean inlet P concentrations are here considered. DV: dead volume; b) Evolution of PRC of filter A considering dead volumes (45%). SD: Standard deviation; DV: dead volume.

#### 4.2.3.4. Kinetic rates of P retention in full-scale systems

The calculation of the reaction kinetics can be assessed based on input/output concentrations or by internal sampling along the hydraulic retention time. The calibration of model parameters for both types of sampling data implies, however,

different issues. When defining  $k_v$  values on average input/output data, a strong uncertainty in  $k_v$  is observed for outlet concentrations close to  $C^*$ . On the other hand, when the outlet concentration is high,  $C^*$  cannot be estimated correctly. A more precise estimation of the model parameters is possible by monitoring the evolution of P concentration at the bulk of the filter by internal sampling. Nevertheless, heterogeneous flows within the media can induce uncertainties as well. Consequently, the model parameters are here discussed only as an order of magnitude and compared to the experiments done in controlled conditions (Delgado-González et al., 2021).

Fig. 4.2.5 shows kinetic rate coefficients estimated by internal sampling during the intensive campaigns. The evolution of  $k_v$  with the PRC obtained in a laboratory column with synthetic water is also plotted for comparison. Fig. 5 provides an example of how the model was fitted to the experimental data to determine the model parameters  $k_v$  and  $C^*$ . The nonlinear GRG (Generalized Reduced Gradient) solver method was used for the calculations. The hydraulic efficiency of the filters was taken into consideration for the estimations. All filters showed low kinetic rate coefficients, in most cases, below the ones determined for the laboratory column, although it can be assumed that results remain in the same order of magnitude ( $k_v$  from lab-column experiments  $\pm 1\text{h}^{-1}$ ). The differences are likely related with the uncertainties associated to the historical data and the flow heterogeneities in the bulk of the filter that cannot be taken into consideration (a mean flowrate is used but the measurements are localized in a specific point of the filter). In addition, the implementation of the reactions in real conditions (wastewater instead of synthetic water) can also affect the kinetic rates differently from laboratory experiments with synthetic solutions (Kowacz et al. 2010, Molle et al. 2011).

The model parameters evolve with the PRC, which is not homogeneous in the bulk of the filter. The media layers close to the feeding would normally have greater amounts of P retained than those layers close to the outlet of the filter. This may result in differences in  $k_v$  and  $C^*$  values as a function of HRT inside the filter. This was indeed the case of Filter A (up-flow) during the first campaign, where the first 50 cm of the filter were hardly reactive with a  $k_v$  of approximately  $0.09\text{h}^{-1}$ . The last 50 cm of the filter was still actively retaining P at relatively high kinetic rates ( $k_v = 1.3\text{h}^{-1}$ ). An average  $k_v$  value was calculated for the entire filter.

Localised flow heterogeneities inside the filter can also lead to differences in the estimated parameters. For instance, variations of  $k_v$  were observed in Filters A or D for

the same PRC. On the other hand, the extremely low values of Filter C are derived from a large HRT, since a significant reduction in P concentration is still observed (See Table S.4.2.2. of Supplementary Information).

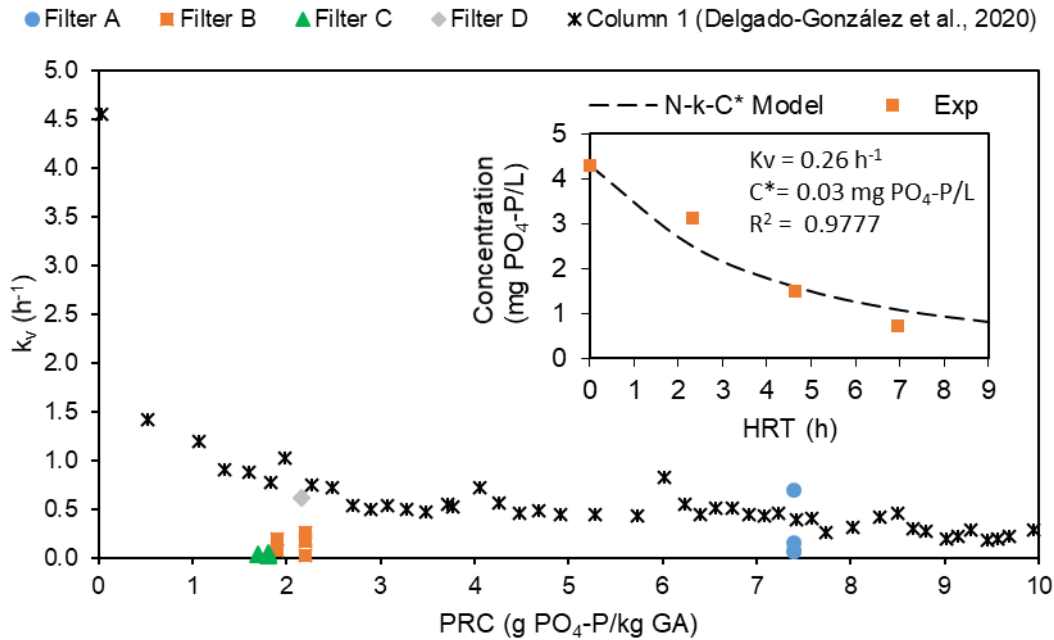


Fig. 4.2. 5. Estimated kinetic rate constants from data collected during intensive campaigns as a function of the PRC for all filters and comparison with laboratory column study (Column 1) from Delgado-González et al, (2021). The insight shows an example from filter B of the adjustment of experimental data to the TIS reaction model in order to determine the model parameters  $k_v$  and  $C^*$ . The adequacy of the adjustment was analysed by the calculation of the coefficient of determination ( $R^2$ ).

#### 4.2.3.5. Adsorption Models

Previous results have showed a relatively rapid loss of performance of the GAF, leading to the supposition that the material may behaved more as an adsorptive substrate than a seed to promote precipitation. The precipitates filling the internal porosity of the granules may behave as an adsorptive-like process where the filling indicates the end of the sorption capacity. Consequently, fixed-bed adsorption models were used to assess the evolution of output concentrations with time. Due to limited data concerning the other filters and their lower PRC attained, estimations using the adsorption models were only possible for Filter A. The calculations considered

constant flow rate (53 m<sup>3</sup>/day), constant inlet concentration (mean value = 4.4 mg PO<sub>4</sub>-P/L) and 45% of dead zones.

The Bohart-Adams model (BAM) and the modified dose-response model (MSRM) were used and compared with experimental data (Fig. 4.2.6). In both cases, the non-linear regressions of the models showed to be in better agreement with experimental data than linear regressions (Table 4.2.5). Among the non-linear expressions, the goodness of the fitting is slightly better for the MDRM. Despite previous results on the hydraulics performance showed that the system does not behave as a plug flow reactor, the MDRM is an empirical model especially adapted for very long experimental times as the case of this study.

By using fixed-bed models, one can also predict the maximum phosphorus retention capacity of the system. This was 8.0 and 7.0 g PO<sub>4</sub>-P /kg GA according to the non-linear regressions of the MDRM and BAM, respectively. The predictions are in agreement with results shown in Fig. 4.2.4.b.

The objective of this analysis was not to give an in-depth assessment of sorption mechanisms but to be able to correlate the behaviour of the GAF with those associated with sorption systems. In this sense, based on the given results, it can be assumed that Filter A behaved as an adsorptive media under the particular solution conditions of the system.

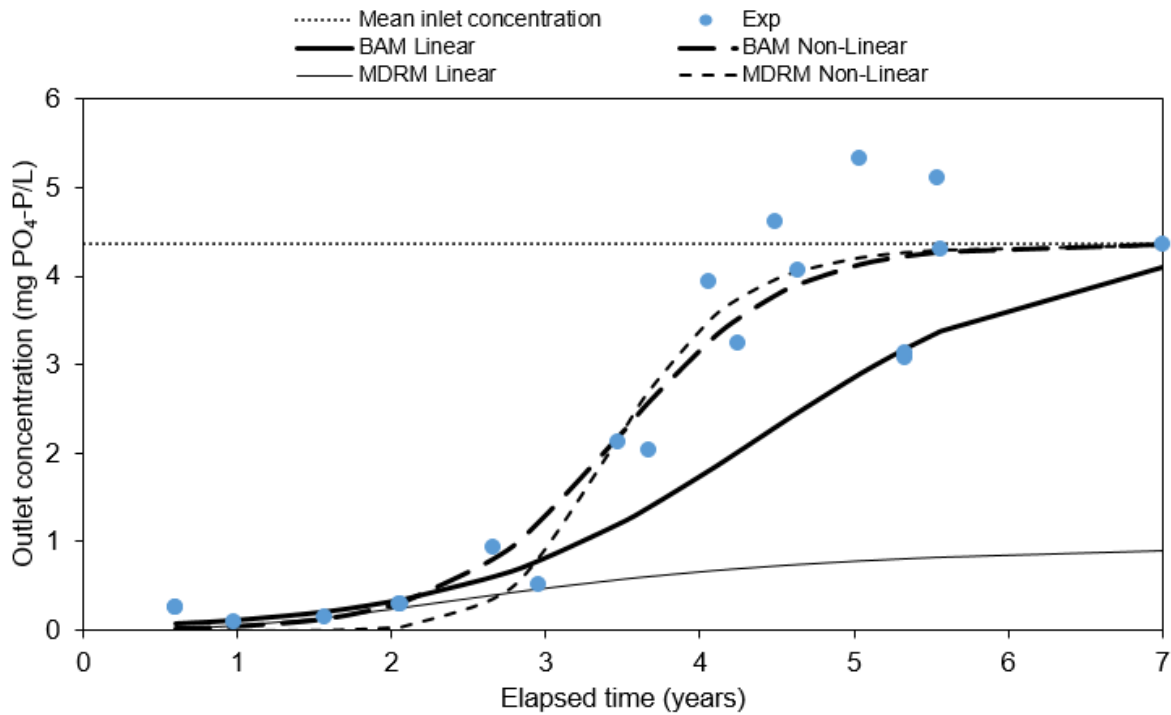


Fig. 4.2. 6. Evolution of the estimated phosphorus outlet concentration of filter A with time considering a mean inlet concentration of 4.4 mg  $PO_4$ -P/L and simulation of phosphorus outlet concentration as a function of time according to the BAM and MDRM.

Table 4.2. 5. Fitting parameters of the Bohart and Adams model and the modified dose-response model and results of the fitting analyses using the sum of square errors (SSE), the coefficient of determination ( $R^2$ ) and the chi coefficient ( $X^2$ ).

	Non-linear					Linear				
	Fitting parameters		SSE	$R^2$	$X^2$	Fitting parameters		SSE	$R^2$	$X^2$
<b>BAM</b>	$K_{BA} = 8.0E-7$	$N_0 = 6,500$	0.36	0.902	1.0	$K_{BA} = 4.59E-7$	$N_0 = 8,248$	29.3	0.809	0.9
<b>MDRM</b>	$a = 9.00$	$q_0 = 8.0$	0.35	0.910	0.0	$a = 2.65$	$q_0 = 7.24$	31.7	0.647	0.0

#### 4.2.3.6. Retention processes

In Delgado-González et al. (2021), it was found that P retention occurred in two different ways depending on calcium concentration and its impact on the supersaturation of the solution with respect to CaP solid phases (hydroxyapatite (HAP) as the referent precipitate). For low Ca concentrations (around 70 mg/L), the ions were able to diffuse through the internal porosity of the granules adsorbing and then precipitating within the pores. This would eventually clog their internal porosity from a

depth of 100-300  $\mu\text{m}$  from the surface. Once precipitates reach the surface of the granule, the reaction would not occur at a sufficient rate (lower specific surface area) leading to a decrease of the retention performance. For solutions with higher Ca concentration (around 110mg/L) supersaturation allowed heterogeneous precipitation onto the surface of the granules, leading to superposed layers of carbonated HAP precipitates that can theoretically grow until the porosity of the GAF clogs. The supersaturation of a solution with respect to a particular solid phase can be assessed through the saturation index (SI) defined by the expression in Eq.4.2.16. It depends in temperature, the ionic strength of the solution and the concentration of the constitutive elements of the solid phase in solution.

$$SI = \log \frac{IAP}{K_{sp}} = \log \frac{\prod_i a_i^{v_i}}{(\prod_i a_i^{v_i})_{eq}} \quad [4.2.16]$$

Where IAP is the ionic activity product,  $K_{sp}$  is the solubility product constant,  $a_i$  is the activity of the  $i^{\text{th}}$  constitutive element of the solid in solution,  $v_i$  is the stoichiometric number for the  $i^{\text{th}}$  element and “eq” indicates chemical equilibrium.

The supersaturation conditions of full-scale GAF were assessed to help identifying the process involved in P retention with real wastewater. The saturation indexes (SI) of the influent were calculated using Phreeqc (Parkhurst and Appelo 2013) (See Tables S.4.2.3 - 6 of the Supplementary Information). Table 4.2.6 shows the supersaturation characteristics of the influent in filter A revealing supersaturated conditions with respect to CaP phases as tricalcium phosphate (TCP), octocalcium phosphate (OCP) and hydroxyapatite (HAP), but also with carbonated compounds as calcite and dolomite. The SIs, in particular for HAP are lower but closer to the influent characteristics of Column 1 of Delgado-González et. al (2021) where the adsorption and precipitation occurred inside the granules. Such results would explain the low kinetic rates observed in Fig. 4.2.5.

Table 4.2. 6. Saturation indexes with respect to different solid phases of the inlet solution of filter A during the different campaigns compared with the mean saturation indexes of the inlet solution of columns 1 and 2 from Delgado-González et al. (2021). Simulation carried out with Phreeqc using a modified LLNL database (Song et al. 2002, Parkhurst and Appelo 2013).

		SI HAP	SI OCP	SI TCP	SI DCPD	SI Calcite
<b>Column 1</b>	Phase 1 and 2	10.4	4.90	2.29	-13.3	-0.06

		SI HAP	SI OCP	SI TCP	SI DCPD	SI Calcite
<b>Column 2</b>	Phase 1	12.2	5.87	3.18	-13.3	0.38
<b>Filter A</b>	Campaign 1- sample 1	9.7	4.22	1.87	-13.6	0.09
	Campaign 1- sample 2	9.9	4.03	2.22	-13.8	0.31
	Campaign 2- sample 1	9.9	4.09	2.31	-13.7	0.43
	Campaign 2- sample 2	7.4	2.78	0.61	-13.8	-0.45

In order to assess the similarity of the retention processes in full-scale systems with those observed in the laboratory columns, scanning electron microscopy (SEM) images were carried out on samples of the filtration bed for Filters A, B and C. The micrographs revealed a porous surface with a morphology close to that of a raw granule in all the cases. Some traces of crystalline particles were also observed on the surface of the granules but a precipitate layer wrapping the granules was not present as it was observed in Delgado-González et al. (2021).

The mentioned difference can be understood from the comparison of both images of Fig. 4.2.7. The Fig. 4.2.7.a shows a porous surface with some residues and crystalline particles from a granule in Filter B. The appearance of the surface of the granules from the other filters was also similar to that of Fig. 4.2.7.a (See Fig. S.4.2.4 of Supplementary information). In Fig. 4.2.7.b, a micrograph of a sample taken from the laboratory column fed with a high calcium concentration is shown (Delgado-González et al., 2021). A completely different morphology of the surface is clearly observed; a deposit layer formed onto the granule, which was identified as a carbonated HAP in Delgado et al. (2021). Therefore, concerning samples from the full-scale filters, there are no elements indicating an effective precipitation of calcium phosphates at the surface of the granules.

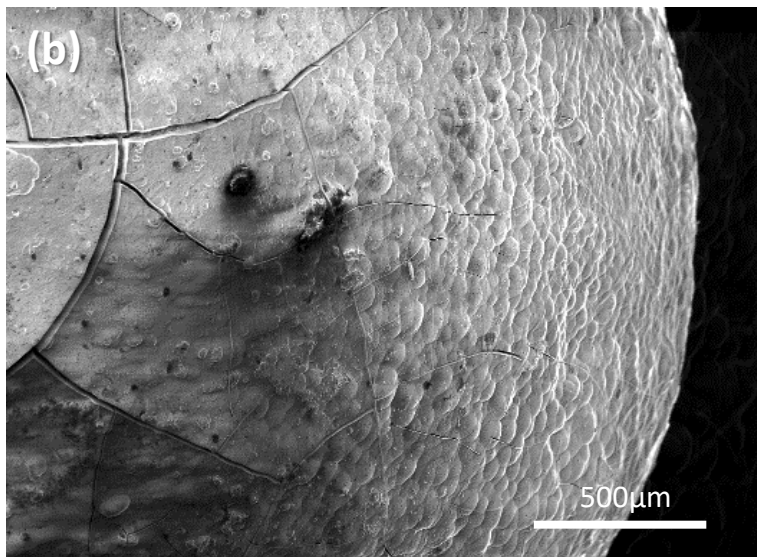
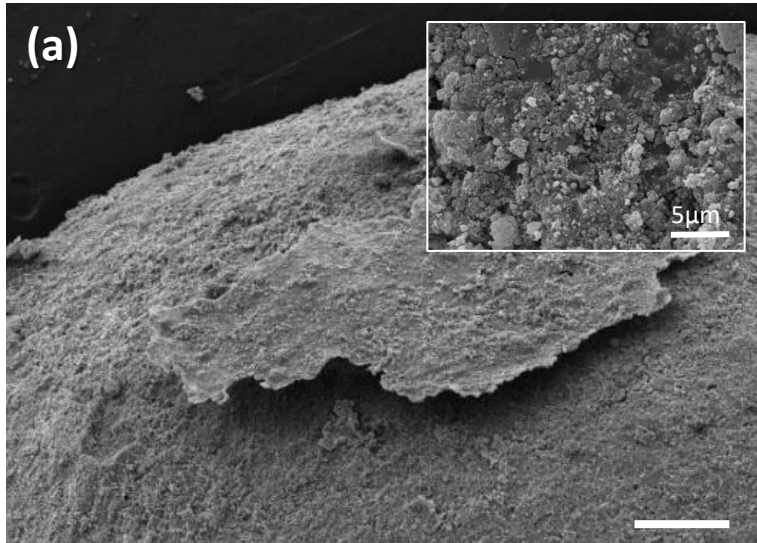


*Fig. 4.2. 7. SEM micrographs of the surface of the granules. Samples from: (a) filter B at a mean PRC of approximately 2.5 g  $PO_4$ -P/kg GA, the insight is an amplified micrograph of the surface of the granule; (b) Column 2 of Delgado-Gonzalez et al. (2020) fed with a high calcium concentration solution, at a mean PRC of the column of 6.2 g  $PO_4$ -P/kg GA showing a carbonated hydroxyapatite formed onto the surface of the granule.*

In conclusion, it appears that P retention is carried out in a similar way as in the low-supersaturated solutions of the laboratory-scale filters. The retention dynamics could be then assimilated to a sorption process rather than a precipitation process, reason why data correlates relatively well with adsorption models. The major differences in P retention performance and kinetics with respect to column experiments are: (1) the scaling-up effect which would account for a reduction in the hydraulic performance; (2) the impact of the ion concentration and organic and inorganic molecules on the supersaturation of the solution; (3) the reduction of the available surface area due to

the adsorption of organic molecules and/or the development of biomass on the granules.

#### 4.2.4. Conclusions

The assessment of full-scale GAF has highlighted some critical issues that should be considered in the design and implementation of these systems. In terms of the hydraulic performance, the use of several different measures and techniques (tracer tests, penetrometer measurements and spot-samplings) has determined the presence of dead volumes in all the four filters in this study. Since the horizontal configuration led to important heterogeneities in the media and in the water flow, a vertical filter with a permanent water ponding appears to be a better configuration ensuring the hydraulic saturation of the filter. Nevertheless, special attention should be paid in the conception and installation of the hydraulic distribution and collection system to avoid the presence of dead zones.

The maximum PRC of a full-scale GAF under real conditions was estimated in 7.4 g PO<sub>4</sub>-P /kg based on the evolution of the PRC of Filter A and considering the presence of dead zones. Depending on the specific characteristics of the filter and the wastewater, this translates into an effective filter life of five to six years. However, the lack of historical data has introduced important uncertainties to the estimations, thus maximum PRC may vary from 4.6 to 10.7 g PO<sub>4</sub>-P /kg of GA. The PRC determined for full-scale apatite filters is consistent with results from laboratory columns (PRC approximately 10g PO<sub>4</sub>-P/kg).

The  $k_v$  values for full-scale GAF are generally lower but close to those obtained for the lab-scale experiments in Delgado-González et al. (Delgado-González et al. 2021). The flow heterogeneities and the influence of wastewater can be responsible of such differences. The uncertainties associated with the determination of the PRC can also play a significant role in the results obtained. The simulation of SI and the observation of SEM micrographs of the surface of the granules has allows to say that P retention takes places by adsorption and precipitation within the porosity of granule any sustainable precipitation does initiate at the surface. As a result, the behaviour of the system can be estimated with a sorption process.

Finally, the monitoring of the pH for Filter D, has shown a significant increase of the pH of the effluent. Approximately 420 m<sup>3</sup> of water per cubic meter of filter were needed to reduce pH to the regulatory limits when considering dead zones.

#### 4.2.5. Supplementary information

##### Comments on Table S.4.2.2.

Table S.4.2.2 provides a summary of the calculated values for the volumetric kinetic rate coefficients and the background concentrations ( $C^*$ ) according to the tank-in-series (TIS) reaction model. Calculations were carried out using the SOLVER tool from Excel™ using a A Generalized Reduced Gradient (GRG) nonlinear least square method. The sum of square errors between predicted and experimental data was minimized to determine  $k_v$  and  $C^*$ .

It is also worth noting the differences in the  $k_v$  value as a function of the location of the sampling (sampling points 1 or 2) within the filter due to the possible heterogeneities of the media. Either these heterogeneities may reflect areas where the mechanisms are potentially different, or the flows are locally different.

The evolution of phosphorus (P) concentration inside the filter A during the October-2017 campaign, showed two distinct retention rates as a function of the depth of the filter, for the same sampling point. Indeed, in a vertical up-flow regime, the quantity of P retained is higher at the bottom of the filter, close to the inlet, implying that this part of the filter would reach its maximum retention capacity faster than other regions. Results showed that the first 50 cm of the filter were, indeed, hardly reactive with a  $k_v$  around 0.08 h<sup>-1</sup>. It is then likely that the lower part of the filter had already reached its maximum retention capacity at that moment. Instead, the last 50cm of the filter were still active retaining P at relatively high kinetic rates with a  $k_v = 0.68$  h<sup>-1</sup>. The  $k_v$  and  $C^*$  parameters presented in Table S.4.2.2. are the mean value of both these regions.

In February 2018, the reaction rates determined were not significant enough to allow the phosphorus concentration of the effluent to be reduced perceptibly. Filter A showed indeed, a dramatic decrease of the retention constant between October 2017 and February 2018 indicating the depletion of the reactivity of the filter. This was also confirmed during the last visits and campaigns conducted on the WWTP (no internal

samplings carried out) where inlet and outlet solutions had almost the same concentrations.

For filter B, the  $k_v$  values were in average  $0.15 \pm 0.09 \text{ h}^{-1}$ , with a  $C^*$  parameter close to zero. The different samplings points show heterogeneities in the evolution of P concentrations with depth.

In filter C, the compaction of the material in certain places made it difficult to carry out the samplings. For the three samplings conducted (one in July 2017 and two in June 2018), the calculated kinetic rate constants were very low even when phosphorus retention was still significant (difference in concentration between the inlet and outlet of the filter). This is due to the very long residence times that smooth the values of the kinetic constant. Here again, some heterogeneities in the evolution of the concentrations in the filter were observed, which can be used to criticize the absence of the dead volumes found by the tracer tests. For example, the outlet concentration of the sampling point (1) during the June-2018 campaign was  $0.74 \text{ mg PO}_4\text{-P/L}$  while the concentration of the effluent from the filter was  $1.58 \text{ mg PO}_4\text{-P/L}$ .

The sampling carried out next to the feed ramp in filter D (sampling point 2) showed a relatively good kinetic coefficient. However, for the sampling point placed in between feed ramps (sampling point 1), P concentrations were close to zero leading to an overestimated  $k_v$  value which cannot be taken into consideration. This fact is associated with the presence of a dead volume as it was determined by the tracer test.

#### Comments on Table S.4.2.4

Filter B shows little supersaturation with respect to hydroxyapatite (HAP) for the ionic conditions of the effluent before entering the filter. The water of the community arriving to this TW is characterised for a low concentration of calcium ions (soft water). A calcite layer above the granulated apatite material compensates this low concentration of calcium by dissolving inside the filter. Thus, calcium and carbonates concentration increases from  $37 \pm 14$  (6)  $\text{mg Ca}^{2+}/\text{L}$  and  $33 \pm 11$  (4)  $\text{mg HCO}_3^-/\text{L}$  to approximately 60 and 130  $\text{mg/L}$ , respectively. Consequently, the appearance of supersaturation with respect to calcium phosphates (other than HAP) and carbonate phases, as calcite and dolomite, can be expected after this layer. However, as the proportional-flow samplings are carried out before the calcite layer, not enough data are available for the simulation.

#### Comments on Table S.4.2.5.

Saturation indices (SI) simulations for filter C have resulted in supersaturation for a great variety of compounds containing sulphates, calcium, magnesium and carbonates as for example gypsum, dolomite, magnesite, calcite and aragonite, in addition to calcium phosphate phases. The reason behind such SI lies in the fact that, the proportional-flow sampling is carried out on a primary effluent, where a great concentration of dissolved compounds is still present. Once again, the samples are not fully representatives of the influent feeding the granulated apatite filter (GAF) since it is preceded by a HTW (HTW and GAF shared the same basin, no physical separation). Thus, the SI of GAF influent is expected to be lower than SIs showed in Table S.4.2.5 and S.4.2.6.

Table S.4.2. 1. Inflow characteristics for all filters (Mean value  $\pm$  Std. deviation, median (number of samples)). All measurements available considered (campaigns + regulatory surveys + self-monitoring)

Filter	Flow rate (m <sup>3</sup> /day)	Mean hydraulic load	pH	Conductivity ( $\mu$ S/cm)	Redox (mV)	Concentration (mg/L)					
						PO <sub>4</sub> -P	Ca <sup>2+</sup>	HCO <sub>3</sub> <sup>-</sup>	DCO <sup>*</sup>	DBO <sub>5</sub>	TSS
<b>A</b>	53 $\pm$ 40, 38 (7)	71%	7.6 $\pm$ 0.4, 7.5 (6)	993 $\pm$ 302, 972 (4)	371 $\pm$ 128, 353 (4)	4.4 $\pm$ 1.4, 4.4 (5)	122 $\pm$ 31, 127 (4)	245 $\pm$ 52, 225 (4)	31 $\pm$ 20, 25 (7)	4 $\pm$ 1 (5)	7 $\pm$ 8, 4 (6)
<b>B**</b>	44 $\pm$ 18, 45 (9)	77%	6.6 $\pm$ 0.3, 6.7 (9)	703 $\pm$ 177, 691 (9)	278 $\pm$ 259, 396 (7)	3.4 $\pm$ 0.9, 3.1 (8)	38 $\pm$ 15, 39 (6)	33 $\pm$ 11, 33 (4)	40 $\pm$ 31, 22 (9)	8 $\pm$ 9, 3.2 (6)	10 $\pm$ 11, 4 (10)
<b>C***</b>	664 $\pm$ 194, 618 (6)	71%	7.5 $\pm$ 0.4, 7.5 (6)	1398 $\pm$ 158, 1344 (6)	247 $\pm$ 158, 261 (6)	4.2 $\pm$ 1.7, 3.6 (6)	136 $\pm$ 4, 136 (6)	349 $\pm$ 28, 350 (3)	66 $\pm$ 28, 61 (6)	26 $\pm$ 18, 25 (4)	25 $\pm$ 11, 27 (6)

\*Non-filtered; \*\* Measures carried out before the calcite layer; \*\*\*Measures carried out at the inlet of the constructed wetland.

Table S.4.2. 2. Comparison of volumetric kinetic reactions coefficients (kv) and background concentrations (C\*) calculated from internal samples taken in the bulk of the filters studied.

Campaign	Filter A				Filter B				Filter C				Filter D		
	Oct-17		Feb-18		Jun-17		Oct-17		Apr-18		Jul-17		Jun-18		Mar-18
Sampling point	1	2	1	2	1	2	1	2	1	2	1	1	2	1	2
<b>C* (mg/L)</b>	1.3	0.52	1	1	0.03	0.03	0.03	0.03	0.03	0.03	0.03	0.03	0.03	0.03	0.46
<b>kv (h<sup>-1</sup>)</b>	0.69	0.15	0.08	0.06	0.02	0.19	0.26	0.17	0.19	0.07	0.04	0.02	0.04	1.36	0.62
<b>C_in (mg/L)</b>	7.50	7.60	4.25	4.23	3.04	2.96	4.29	4.63	2.67	2.68	5.92	3.58	4.24	0.63	2.95
<b>C_out (mg/L)</b>	1.90	3.79	3.26	3.30	2.58	0.74	0.45	0.87	0.47	1.50	0.18	0.74	0.12	0.07	0.47
<b>Q (m<sup>3</sup>/j)</b>	60	60	60	60	40	40	65	65	53	53	350	464	464	113	113
<b>HRT (h)</b>	5	5	5	5	10	10	6	6	8	8	40	30	30	8	8
<b>Estimated PRC*</b>	7.4	7.4	7.4	7.4	2.2	2.2	2.2	2.2	1.9	1.9	1.7	1.8	1.8	2.2	2.2
<b>R<sup>2</sup></b>	0.968	0.933	0.994	0.987	0.494	0.907	0.956	0.967	0.888	0.967	0.820	0.660	0.869	0.983	0.945

\*Dead volumes considered

Table S.4.2. 3. Saturation indexes of the influent in filter A during the measurement campaigns (proportional-flow samples). Green values show supersaturation, red values show undersaturation.

	Ca <sub>3</sub> (PO <sub>4</sub> ) <sub>2</sub>	Ca <sub>3</sub> (PO <sub>4</sub> ) <sub>2</sub>	CaHPO <sub>4</sub> :2H <sub>2</sub> O	CaCO <sub>3</sub>	CaMg(CO <sub>3</sub> ) <sub>2</sub>	Ca <sub>5</sub> (PO <sub>4</sub> ) <sub>3</sub> OH	Ca <sub>4</sub> H(PO <sub>4</sub> ) <sub>3</sub> :3H <sub>2</sub> O
	ACP	TCP	Brushite	Calcite	Dolomite	HAP	OCP
Solution 1	-0.4	1.87	-13.57	0.09	0.17	9.7	4.22
Solution 2	-0.3	2.22	-13.76	0.31	0.49	9.89	4.03
Solution 3	-0.27	2.31	-13.71	0.43	0.74	9.88	4.09
Solution 4	-1.64	0.61	-13.77	-0.45	-0.94	7.45	2.78

Table S.4.2. 4. Saturation indexes of the influent in filter B during the measurement campaigns (proportional-flow samples). Green values show supersaturation, red values show undersaturation.

	Ca <sub>3</sub> (PO <sub>4</sub> ) <sub>2</sub>	Ca <sub>3</sub> (PO <sub>4</sub> ) <sub>2</sub>	CaHPO <sub>4</sub> :2H <sub>2</sub> O	CaCO <sub>3</sub>	CaMg(CO <sub>3</sub> ) <sub>2</sub>	Ca <sub>5</sub> (PO <sub>4</sub> ) <sub>3</sub> OH	Ca <sub>4</sub> H(PO <sub>4</sub> ) <sub>3</sub> :3H <sub>2</sub> O
	ACP	TCP	Brushite	Calcite	Dolomite	HAP	OCP
Solution 1	-4.92	-2.67	-14.71			1.86	-1.41
Solution 2	-5.89	-3.64	-14.89	-2.93	-4.89	0.11	-2.57
Solution 3	-4	-1.73	-14.47			3.39	-0.28
Solution 4	-3.8	-1.54	-14.46	-1.78	-2.56	3.82	-0.07
Solution 5	-4.31	-14.6	-14.6			2.81	-0.77
Solution 6	-4.6	-2.26	-14.67	-2.18	-3.45	2.32	-1.12
Solution 7	-5.28	-3.02	-14.7	-2.56	-4.2	1.09	-1.79

Table S.4.2. 5. Saturation indexes of the influent in filter C during the measurement campaigns (proportional-flow samples). The table continuous in Table S.4.2.6. Green values show supersaturation, red values show undersaturation.

	Ca <sub>3</sub> (PO <sub>4</sub> ) <sub>2</sub>	CaSO <sub>4</sub>	CaCO <sub>3</sub>	CaSO <sub>4</sub> :0.5H <sub>2</sub> O	Ca <sub>3</sub> (PO <sub>4</sub> ) <sub>2</sub>	CaHPO <sub>4</sub> :2H <sub>2</sub> O	CaCO <sub>3</sub>	CaMg(CO <sub>3</sub> ) <sub>2</sub>	CaSO <sub>4</sub> :2H <sub>2</sub> O
	ACP	Anhydrite	Aragonite	Bassanite	TCP	Brushite	Calcite	Dolomite	Gypsum
Solution 1	3.75	0.74		0.09	6	-12.03			1.01
Solution 2	3.16	0.52	2.63	-0.13	5.41	-12.19	2.78	5.91	0.79
Solution 3	5.3	0.34		-0.3	7.64	-11.75			0.54
Solution 4	5.29	0.32		-0.32	7.63	-11.76			0.52
Solution 5	4.28	0.61	3.24	-0.04	6.54	-12.31	3.38	7.15	0.88
Solution 6	2.54	0.59	2.18	-0.06	4.83	-12.07	2.32	5	0.8

Table S.4.2. 6. Saturation indexes of the influent in filter C during the measurement campaigns (proportional-flow samples). Green values show supersaturation, red values show undersaturation.

	Ca <sub>5</sub> (PO <sub>4</sub> ) <sub>3</sub> OH	CaMg <sub>3</sub> (CO <sub>3</sub> ) <sub>4</sub>	MgCO <sub>3</sub>	CaCO <sub>3</sub> :H <sub>2</sub> O	Ca <sub>4</sub> H(PO <sub>4</sub> ) <sub>3</sub> :3H <sub>2</sub> O	Ca <sub>3</sub> (PO <sub>4</sub> ) <sub>2</sub>		
	HAP	Huntite	Magnesite	Monohydrocalcite	OCP	Whitlockite	CO <sub>2</sub> (g)	NO (g)
Solution 1	16.5				9.92	5.73		
Solution 2	15.47	5.46	1.44	1.95	9.16	5.13		
Solution 3	19.53				11.82	7.67		
Solution 4	19.52				11.8	7.67		
Solution 5	17.83	7.96	2.08	2.56	10.16	6.21		
Solution 6	14.26	3.78	1.02	1.48	8.72	4.78	0.22	0.14

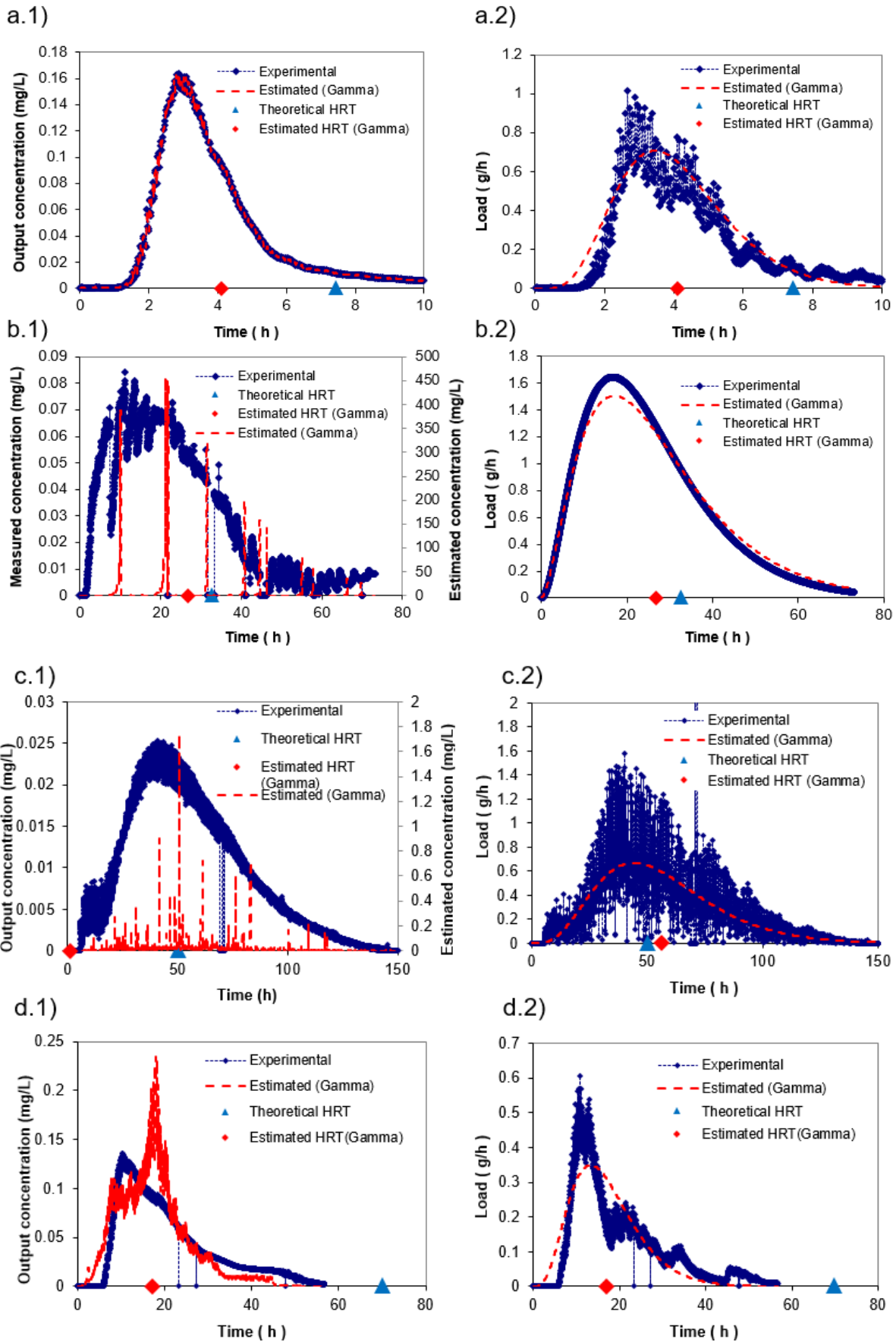


Fig.S.4.2. 1. Fluorescein tracer tests results carried out during campaigns (data analysis by gamma method): a) Filter A; b) Filter B, c) Filter C, d) Filter D.

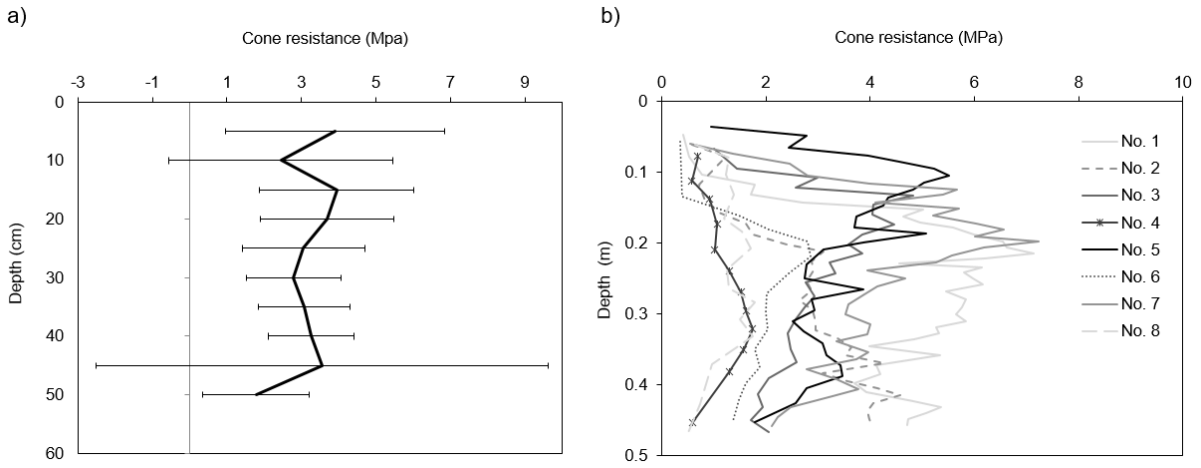


Fig.S.4.2. 2. Results of dynamic cone penetration tests in filter C: a) Median value and standard deviation of 16 probes at different spots of the filter, b) evolution of the cone resistance with depth at 8 different spots (the 16 dynamic cone penetration tests are not shown for a better comprehension of the plot).

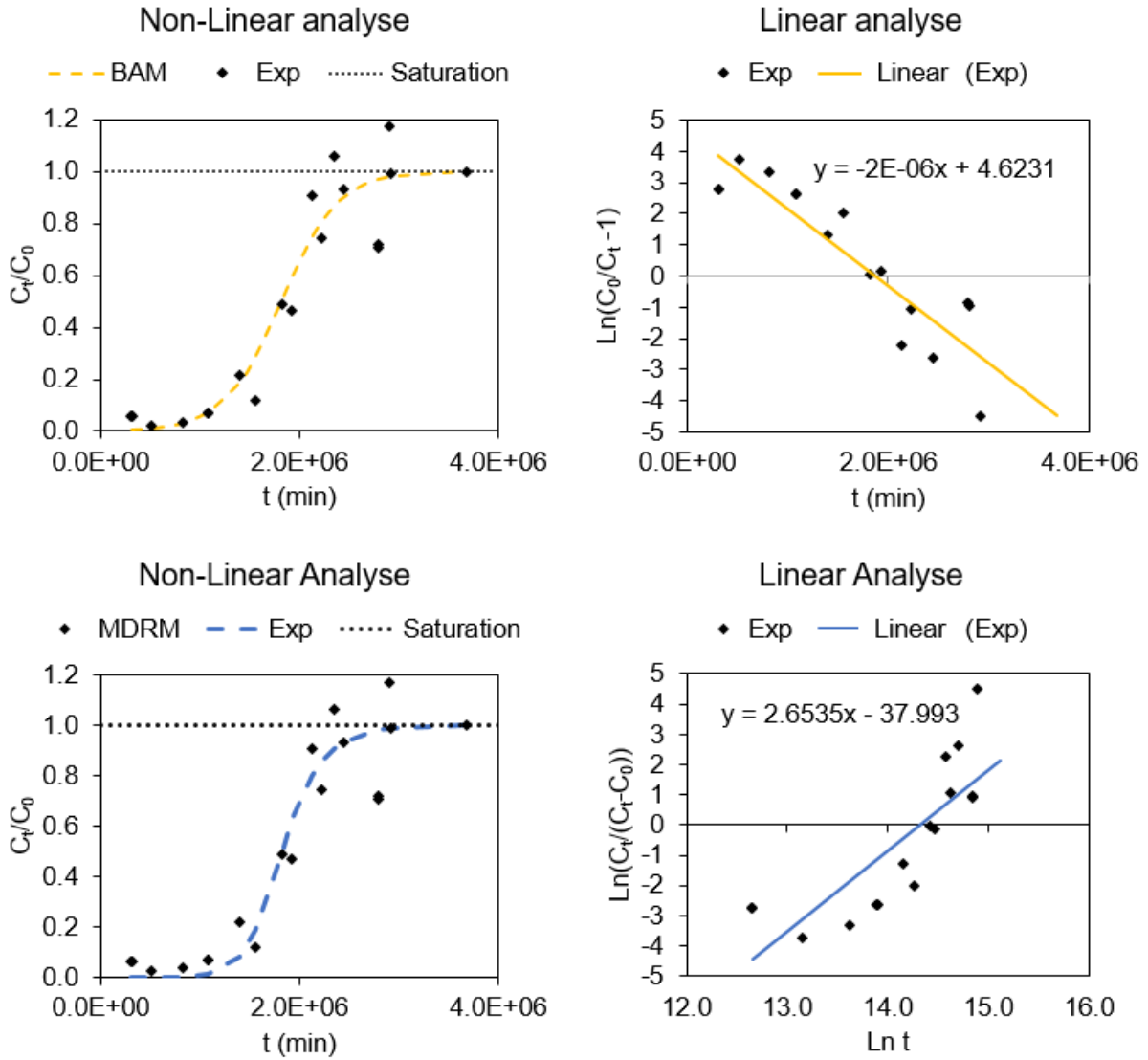


Fig.S.4.2. 3 Non-linear and linear analyses of experimental data of filter A by Bohart-Adam Model (up) and Modified dose response model (down).

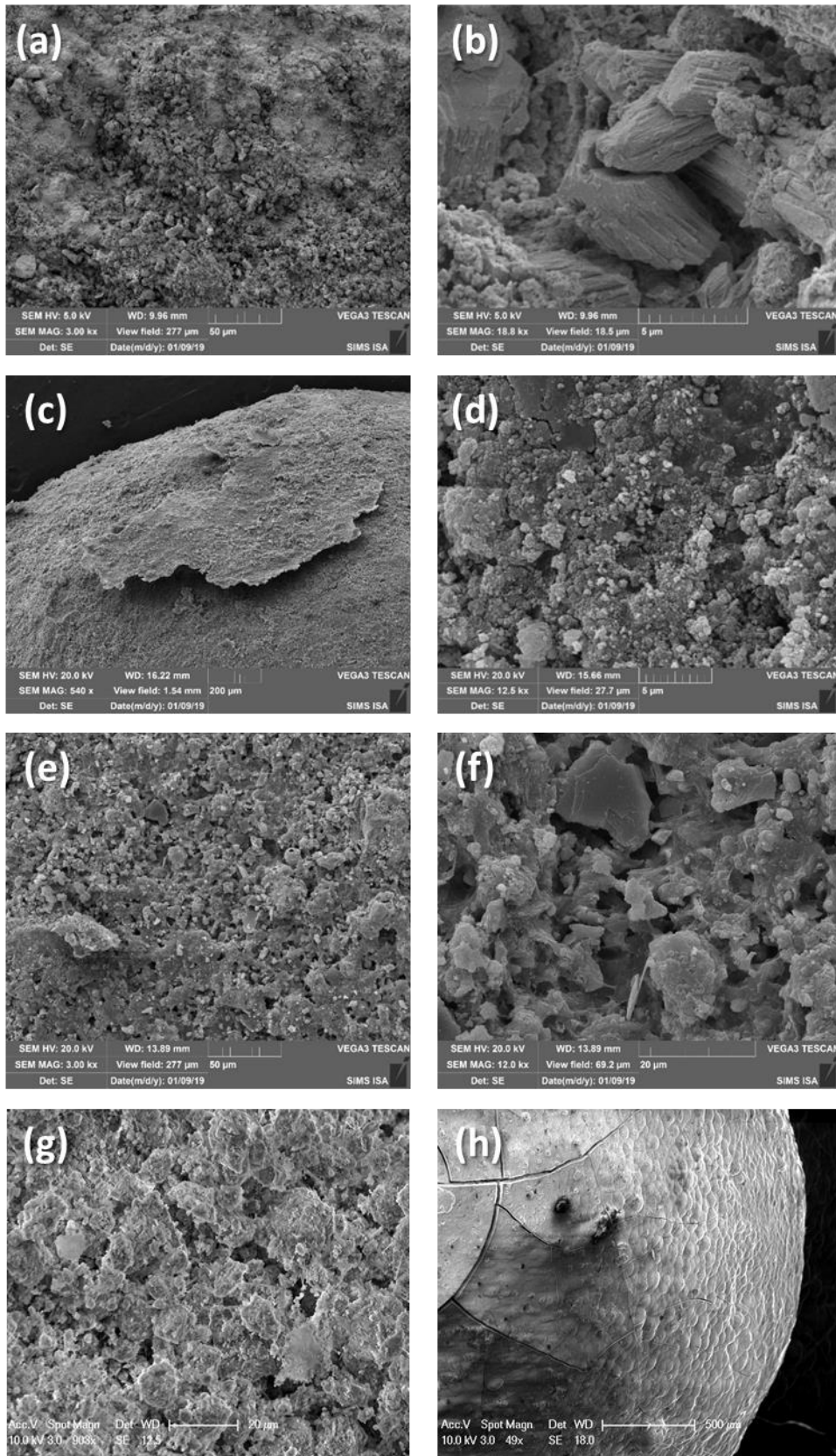


Fig.S.4.2. 4. SEM micrographs of the surface of the granules. Samples from: filter A (a and b); filter B (c and d); filter C (e and f); a raw apatite granule (g); Column 2 of Delgado-Gonzalez et al., 2021 at the end of the experiment where a carbonated hydroxyapatite formed onto the surface of the granule (h).



### 4.3. Article 2. Granulated Apatite laboratory columns

*In press: Water Science and Technology 2021.*

*doi: 10.2166/wst.2021.010*

#### **Phosphorous Retention by Granulated Apatite: Assessing Maximum Retention Capacity, Kinetics and retention processes.**

**Laura Delgado-González<sup>a,d</sup> \*, Bruno Lartiges<sup>b</sup>, Mathieu Gautier<sup>c</sup>, Stéphane Troesch<sup>d</sup>, Pascal Molle<sup>a</sup>**

<sup>a</sup> Inrae, REVERSAAL Research Unit, 5 rue de la Doua, 69100 Villeurbanne, France ;

<sup>b</sup> University of Toulouse III (Paul Sabatier), Géosciences Environnement Toulouse, 14 av. Edouard Belin, F-31400 Toulouse, France

<sup>c</sup> Univ Lyon, INSA Lyon, DEEP Laboratory, 69621 Villeurbanne France

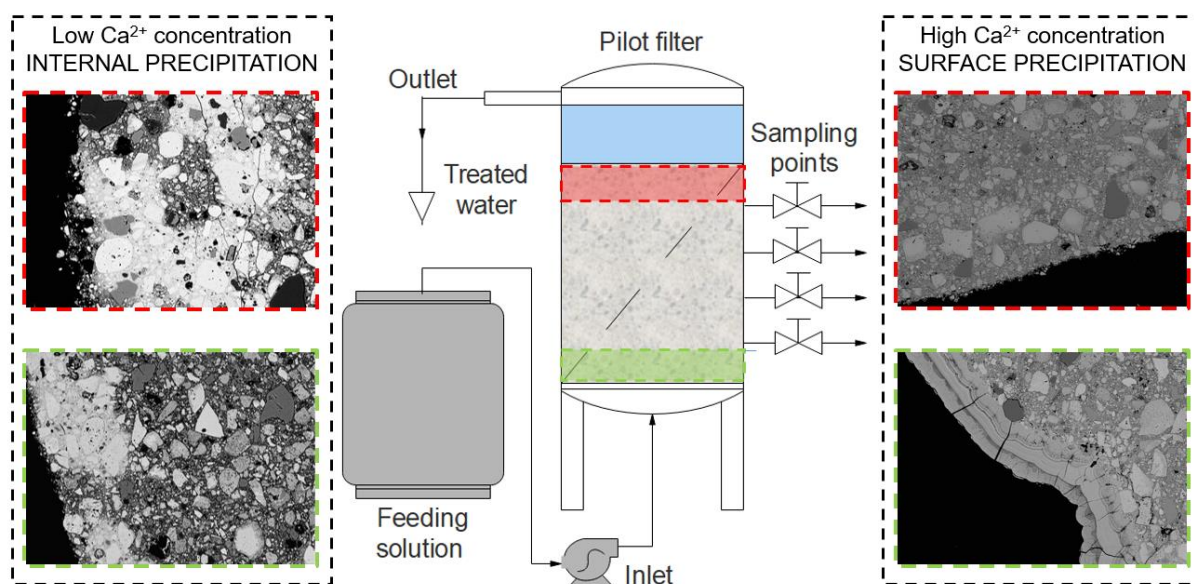
<sup>d</sup> SYNTEA, Lieu-dit Belle-Croix, 33 490 Le Pian sur Garonne, France

\*Corresponding author: [laura.delgado-gonzalez@inrae.fr](mailto:laura.delgado-gonzalez@inrae.fr); (+33) 644 935 247

#### **Highlights**

- The kinetics and phosphorus retention capacity of granulated apatite are low and do not ensure long-term removal
- The access to apatite surface in the granule is hindered by the binder matrix
- Hydroxyapatite and carbonated-hydroxyapatite precipitate within the granule onto the binder matrix at low calcium concentration
- Hydroxyapatite and carbonated-hydroxyapatite precipitate onto the granule surface at high calcium concentration

## Graphical Abstract



## Abstract

Natural apatites have previously shown a great capacity for phosphate retention from wastewater. However, its fine particle size distribution may lead to a premature clogging of the filter. Accordingly, a granulated apatite product was developed and manufactured in order to control the particle size distribution of the media. Experiments were conducted on laboratory columns to assess their phosphorus retention capacity, to identify the processes involved in phosphorus retention and to evaluate their kinetic rates. The results showed phosphorus retention capacities of 10.5 and 12.4 g PO<sub>4</sub>-P·kg<sup>-1</sup> and kinetic rate coefficients in the range of 0.63 and 0.23 h<sup>-1</sup> involving lower values than those found for natural apatites in previous studies. Scanning Electron Microscopy images showed that apatite particles in the granules were embedded in the binder and were not readily accessible to act as seeds for calcium phosphate precipitation. The retention processes differ depending on the supersaturation of the solution with respect to calcium phosphate phases: at low calcium concentrations (69.8 ± 3.9 mg·L<sup>-1</sup>), hydroxyapatite precipitates fill up the porosity of the binder up to a depth of 100 - 300 μm from the granule surface; at higher calcium concentrations (112.7 ± 7.4 mg·L<sup>-1</sup>), precipitation occurs at the granule surface forming successive layers of hydroxyapatite and carbonated calcium phosphates.

**Keywords:** granulated apatite filter, phosphorus retention; small WWTPs.

#### 4.3.1. Introduction

Phosphorus (P) is a key nutrient involved in eutrophication of surface waters (Prochaska and Zouboulis 2006). The major cause leading to the deterioration of water quality originates from anthropogenic sources such as municipal wastewater and runoff from agricultural areas (Bouwman et al. 2005). In all possible futures scenarios, this pressure will continue to increase globally demanding at least the implementation of additional treatments for phosphorus removal in Wastewater Treatment Plants (WWTPs) (van Puijenbroek et al. 2019).

In small WWTPs, the addition of iron or aluminum salts to treat phosphorus is commonly used. Nevertheless, P removal remains a critical issue demanding the implementation of a supplementary treatment with simpler and more suitable technologies that can potentially meet P recovery purposes. Filtration through specific materials with an affinity for P binding appears to be an appropriate solution to reach these objectives. It also allows to maintain the extensive feature of Treatment Wetlands (TWs) (Molle et al. 2005) which represent more than 4,000 small WWTPs in France (Martinez-Carvajal et al. 2019). A large variety of filter substrates, from natural materials through man-made products to industrial coproducts, have been tested in laboratory, pilot and/or full-scale experiments in order to assess their P removal performance and retention capacities (Vohla et al. 2011, Yang et al. 2018). The adequacy of a given material for P retention is assessed from its Phosphorus Retention Capacity (PRC) that depends on various physicochemical characteristics of the material (Blanco et al. 2016).

Previous studies have already demonstrated the validity of natural apatite as a specific filtering material for P retention (Molle et al. 2005, Bellier et al. 2006, Harouiya et al. 2011). Two different groups of natural apatite have been identified according to their fluorapatite content (FAP,  $\text{Ca}_5(\text{PO}_4)_3\text{F}$ ): poor quality (40 - 60% apatite content) and rich quality (90% apatite content). The latter substrate showed a great compromise in terms of performance, long term removal and potential capacity for P recovery (Molle et al. 2011). The main drawback of such material is its fine particle size distribution (Molle et al. 2011) which may cause hydraulic limitations for its applicability in wastewater treatments. Accordingly, a granulated apatite product was developed, patented and manufactured in a similar way as fertilizers pellets, by using a cement binder (10%

w/w) and a natural source of apatite from phosphate rocks. The granulation allows to control the particle size distribution of the filtration bed and, thus, to ensure a safer filtration operation regarding the filter hydraulics.

P retention using specific materials is a physicochemical process based on various interactions at the solid-liquid interface. For natural apatite, the surface reactions previously identified were adsorption and precipitation (Molle et al. 2005). The adsorption takes place at the beginning of the filter's lifespan onto Ca oxides specific sites of phosphate minerals (Molle et al. 2005). As those sites become saturated, precipitation takes over as the long term mechanism governing the P retention process (Molle et al. 2011). Mineral apatite was shown to act as a crystallization seed promoting calcium phosphate (CaP) precipitation such as hydroxyapatite (HAP,  $\text{Ca}_5(\text{PO}_4)_3\text{OH}$ ) (Molle et al. 2005, Bellier et al. 2006).

Precipitation is a thermodynamically driven process that depends on the solubility of the most stable pure solid phase and the free energy change. In a CaP system, the most stable solid phase is hydroxyapatite (HAP,  $\text{Ca}_5(\text{PO}_4)_3\text{OH}$ ) followed by octocalcium phosphate (OCP), tricalcium phosphate (TCP) and dicalcium phosphate (DCP) among the most common CaP, depending on their solubility product ( $K_{sp}$ ) (Song et al. 2002). The saturation index (SI) of a solution determines whether a specific CaP phase may precipitate ( $\text{SI} > 0$ ).

However, kinetic and mechanistic factors also play a major role in the nucleation and the growth of solid solutions and may determine their crystal composition (Prieto et al. 2016). The kinetics of precipitation is supersaturation dependent: the induction time for crystallization decreases with increasing supersaturation (Anderson and Rubin 1981). In addition, for a particular supersaturation state, precipitation may or may not take place depending on environmental conditions because of the existence of a metastable zone (Song et al. 2002). Therefore, the rate of crystallization and nature of the phases that may precipitate strongly depend on calcium and phosphate concentrations, supersaturation, ionic strength, temperature, pH, the presence of foreign ions and time to enable solid-to-solid transformations (Barone and Nancollas 1977, Montastruc et al. 2003).

In this work, a transformed apatite-based product is analyzed in laboratory columns for P retention for the first time. The study intends to assess the suitability of the granulated

apatite for phosphorus removal from wastewaters of small WWTPs, which would provide the advantages of extensive systems, requiring simple management and offering a final product that can be revalorized in the fertilizer industry. Therefore, the objectives of this work are (1) to assess the PRC of a granulated apatite product using long-term column experiments; (2) to evaluate the kinetic rate of the reactions and its evolution with PRC using a simplified reaction rate model; (3) to identify the reaction processes taking place under various solution conditions and their impact in the PRC and the reaction rate; (4) to assess the adequacy of the granulated apatite filter for a long-term P retention.

#### 4.3.2. Material & Methods

##### 4.3.2.1. Characteristics of granulated apatite

The granulated apatite product was specifically designed to be used as a filtering material for P retention in wastewater. It was developed, patented (Blandin 2013) and manufactured by a French fertilizer company, which provided the product for this study.

A physicochemical and mineralogical characterization of the raw granulated apatite was carried out. Elemental analyses were carried out by alkaline fusion ( $\text{LiBO}_2$ ) followed by acid digestion ( $\text{HNO}_3$ ) and subsequent analyses of the solutions by inductively coupled plasma optic emission spectrometry (ICP-OES) (iCap6500, Thermo Scientific). The mineralogical characterization was carried out on raw dried grounded ( $80 < \mu\text{m}$ ) samples by X-ray diffraction (XRD) with a  $\text{CuK}\alpha$  radiation ( $\lambda = 1.54060 \text{ \AA}$ ) on a  $2\theta$  diffractometer (Bruker D8-Advance) in the  $5 - 70^\circ$  range. Crystalline phases were identified using DIFFRAC EVA software (v.4.1.1) by comparing the registered patterns with the Powder Diffraction Files (PDF).

The crystallographic microstructure and the chemical composition of the raw granulated material and of the precipitates after experiment were also investigated. The apatite granules were first embedded in an epoxy resin to obtain cylindrical resin blocks (4 cm in diameter), that were abraded and polished in ethanol using successively finer silicon carbide powders. Finally, an ethanol-based diamond slurry was used to produce a smooth polished finish suitable for recording Electron Backscatter diffraction patterns. The polished sections were carbon coated and

examined by Scanning Electron Microscopy (SEM JEOL JSM-7100) equipped with an Electron Backscattered Diffraction pattern detector (EBSD AZtec HKL) and an Energy Dispersive X-ray analyser (EDS Oxford Instruments) for microanalysis (R. Castaing Microcharacterization Centre, France).

SEM-EDS images of the granule surface before and after the experiment were also carried out with a SEM-EFG XL30 Philips microscope. In that case, samples were gold coated to avoid surface polarization.

The Specific Surface Area (SSA) was determined by N<sub>2</sub> adsorption/desorption isotherms (BET method) using an ASAP 2020M.

#### 4.3.2.2. Column experiments setup

The granulated apatite material was tested in two columns of 9 cm diameter and 20 cm of filter media depth (void volume of 0.62 L). The columns have equidistant depth sampling points, which enable solution sampling at various retention times. The system operated hydraulically saturated in a vertical and controlled up-flow regime (peristaltic pump). The columns were covered with a black opaque plastic coating in order to avoid algae development in the media. A schematic representation of the laboratory columns used for the experiments is presented in Fig 4.3.1.

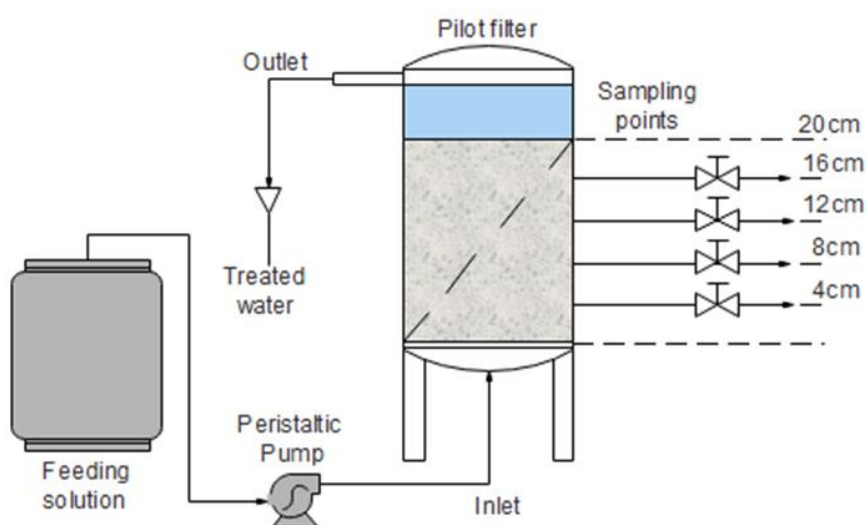


Fig. 4.3. 1. Schematic representation of laboratory columns.

#### 4.3.2.3. Feeding and analyses protocol

Several-month-experiments were carried out in two columns: Column 1 and Column 2 (Table 4.3.1). Both filters were fed with a synthetic solution prepared from tap water and  $\text{KH}_2\text{PO}_4$  (Sigma-Aldrich) to achieve phosphorus inlet concentrations around  $15 \text{ mg P-PO}_4\text{-L}^{-1}$ . The conductivity was also adjusted by adding a  $\text{NaCl}$  solution (common salt,  $300 \text{ mg}\cdot\text{L}^{-1}$ ) to approach common values in real wastewater ( $\approx 1000 \text{ }\mu\text{S}\cdot\text{cm}^{-1}$ ). To investigate the influence of various parameters, the experiments were conducted in two different stages. For Column 1, flow rate was set approximately at  $5 \text{ L}\cdot\text{d}^{-1}$  during Stage 1 and  $10 \text{ L}\cdot\text{d}^{-1}$  during Stage 2 in order to reach the maximum PRC within the experimental time. The corresponding hydraulic loads used, also presented in Table 1, are in the range of hydraulic loads for full-scale systems. For Column 2, the flow rate was kept constant approximately at  $10 \text{ L}\cdot\text{d}^{-1}$  along the whole experiment. However, the calcium concentration was adjusted to  $113 \pm 7 \text{ mg}\cdot\text{L}^{-1}$  by the addition of  $\text{CaCl}_2$  (Sigma-Aldrich) during stage 1 of Column 2. This allowed to study the influence of calcium concentration in the reaction processes and kinetics. During Stage 2 of Column 2, the calcium concentration was kept equal to  $70 \pm 4 \text{ mg}\cdot\text{L}^{-1}$ , as for both stages of Column 1. Therefore, at stage 2, the experimental conditions of both columns were the same.

Table 4.3. 1. Composition of the feeding solutions and operational conditions for both Columns 1 and 2. Mean value  $\pm$  Standard deviation (95%) and number of samples analysed in brackets

	Column 1 (Low $\text{Ca}^{2+}$ concentration)	Column 2 (High $\text{Ca}^{2+}$ concentration)
<b>[P-<math>\text{PO}_4^{3-}</math>] (<math>\text{mg}\cdot\text{L}^{-1}</math>)</b>	$14.8 \pm 1.2$ (46)	$12.6 \pm 2.9$ (33)
<b>[<math>\text{HCO}_3^-</math>] (<math>\text{mg}\cdot\text{L}^{-1}</math>)</b>	$197 \pm 14$ (63)	$182 \pm 14$ (45)
<b>[<math>\text{Ca}^{2+}</math>] Stage 1 (<math>\text{mg}\cdot\text{L}^{-1}</math>)</b>	$69.8 \pm 3.9$ (63)	$112.7 \pm 7.4$ (34)
<b>[<math>\text{Ca}^{2+}</math>] Stage 2 (<math>\text{mg}\cdot\text{L}^{-1}</math>)</b>	$69.8 \pm 3.9$ (63)	$67.3 \pm 3.9$ (11)
<b>Conductivity (<math>\mu\text{S}\cdot\text{cm}^{-1}</math>)</b>	$1\ 047 \pm 63$ (65)	$1\ 047 \pm 76$ (45)
<b>pH</b>	$7.5 \pm 0.2$ (65)	$7.7 \pm 0.2$ (45)
<b>Flow-rate Stage 1 (<math>\text{L}\cdot\text{day}^{-1}</math>)</b>	$5.1 \pm 0.3$ (391)	$9.6 \pm 2$ (304)
<b>Flow-rate Stage 2 (<math>\text{L}\cdot\text{day}^{-1}</math>)</b>	$10.2 \pm 0.6$ (76)	$9.6 \pm 2$ (304)
<b>Hydraulic load Stage 1 (<math>\text{m}^3\cdot\text{m}^{-2}\cdot\text{day}^{-1}</math>)</b>	$0.80 \pm 0.05$ (391)	$1.51 \pm 0.31$ (304)

<b>Hydraulic load Stage 2 (m<sup>3</sup>·m<sup>-2</sup>· day<sup>-1</sup>)</b>	1.6 ± 0.09 (76)	1.51 ± 0.31(304)
<b>Hydraulic retention time Stage 1 (h)</b>	2.9 ± 0.2 (391)	1.6 ± 0.7 (304)
<b>Hydraulic retention time Stage 2 (h)</b>	1.5 ± 0.1(76)	1.6 ± 0.7 (304)
<b>Experimental time_Stage 1 (days)</b>	391	242
<b>Experimental time_Stage 2 (days)</b>	77	72
<b>P- dosed_Stage 1 (kg·m<sup>-3</sup> material)</b>	35.1	35.8
<b>P- dosed_Stage 2 (kg·m<sup>-3</sup> material)</b>	50.2	48.2

Samples were collected once a week at the inlet and outlet of the systems. To assess the evolution of P concentration inside the filtering media, samples were also collected at the different sampling points of the column, spaced 4 cm from each other, at selected times of the experiment. Calcium and phosphate concentrations were analyzed on filtered samples (pore size 0.45 µm) by ionic chromatography (NF EN ISO 14911 and EN ISO 10304-1). Both conductivity and pH were measured for each sample. The flow rate was checked every two days and adjusted when necessary.

The saturation indexes (SI) of the inlet solution for the minerals considered were calculated using the geochemical software PHREEQC v.3 (Parkhurst and Appelo 2013) using the LLNL database modified to take into account the  $K_{sp}$  of the different minerals according to Song et al. (2002)

#### 4.3.2.4. The k-C\* Model

The results were adjusted to the slightly modified k-C\* model (Eq. 4.3.1) (Kadlec and Wallace 2009).

$$C = (C_0 - C^*)exp(-k_v t) + C^* \quad [4.3.1]$$

Where C is the P concentration at time t, or hydraulic retention time (HRT),  $C_0$  is the inlet concentration of phosphorus,  $k_v$  the volumetric kinetic rate coefficient and  $C^*$  the P equilibrium concentration.

Several kinetic studies were performed along the experiment at different PRC at both Columns 1 and 2. The evolution of P concentration was then analyzed within the column by sampling at different hydraulic retention times (HRT) to determine the

parameters of the k-C\* model (Kadlec and Wallace 2009). Consecutive kinetics studies were carried out by reducing progressively the inlet P concentration to reproduce several piston reactors in series. This allows to better define  $k_v$  at high inlet concentration and  $C^*$  when approaching low P inlet concentrations.

### 4.3.3. Results and discussion

#### 4.3.3.1. Material characterization

The granulated apatite was found to contain about 12%wt of P and 79%wt of apatite content. Such content falls between poor and rich quality in the classification of natural apatites for filtering media proposed by Molle et al. (2011). The XRD analyses revealed that the apatite phase present in the granulated apatite is a carbonate fluorapatite (CFAP) (Table S.4.3.1).

The initial granulated apatite also contained high amounts of Ca (32.6%wt) that may be present in the CFAP, in calcite (12.4%wt), and to a lesser extent in dolomite (3.1%wt) (Table S.4.3.2). Some quartz particles were also present at low concentrations (4.8%wt). The amorphous phases were not identified; however, their composition is likely derived from the cement binder used for granulation whose elemental composition was determined by ICP spectrometry Table S.4.3.2).

SEM images and EDXS microanalyses further confirm the presence of various mineral phases previously identified by XRD analyses, and provide a description of the granule morphology. Fig.4.3.2.a reveals particles of 20 to 100  $\mu\text{m}$  in size embedded in a binder matrix with micrometric to sub-micrometric particles and the presence of a highly porous network. The brightness of particles is related to their average atomic number, thus identifying a vast majority of apatite particles (light grey to white) with minor occurrences of calcite (grey), quartz (dark grey) and dolomite.

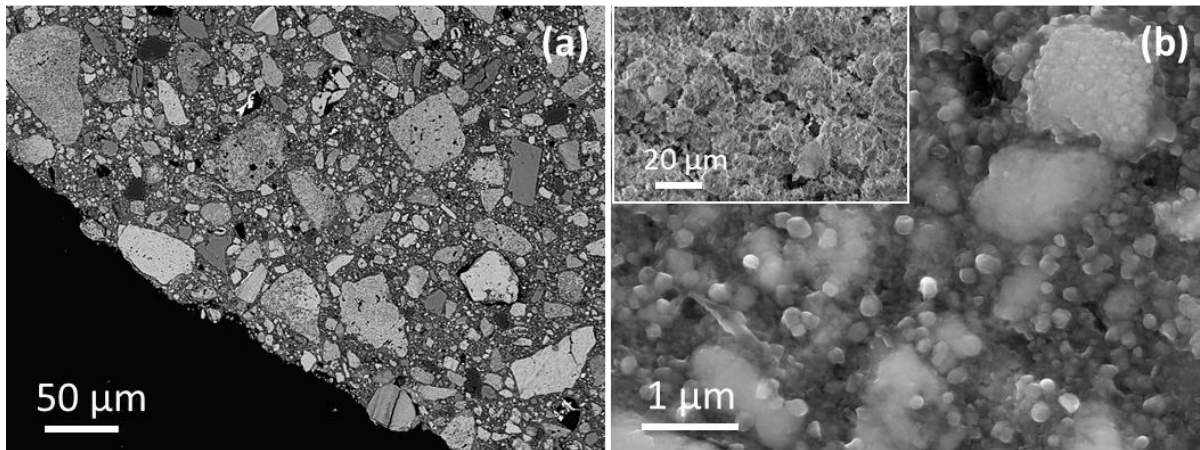


*Fig. 4.3. 2. SEM micrographs of polished cross-section of a raw granulated apatite pellet (left): (a) Edge of a granule in backscatter electron mode revealing mostly apatite particles embedded in a composite matrix. (c) Micrograph of the matrix in the secondary electron mode showing that the binder is formed of nanoparticles; the inset shows the external surface of the pellet.*

Enlarged micrographs of the composite matrix (Fig. 4.3.2.b) reveal that the binder matrix is formed of nanoparticles, 30-200 nm in diameter, partially covering the apatite particles. The inset in Fig. 4.3.2.b shows the porosity of the external surface of the granulated apatite. In the following, the interconnected pore space developed by the binder and the particles within the granules is called the internal porosity of the granules or granules porosity. It differentiates from the pore space developed by a bed of granules or bed porosity.

The BET measurement indicates a relatively high specific surface area (SSA) of about 32 m<sup>2</sup>/g (See Table S.4.3.3). for a detailed comparison with other filtering materials used for P retention). The sorption capacity is strongly correlated with SSA and particle size distribution: high SSA and fine particles normally lead to a high PRC. The particle size distribution of the granulated apatite product does not show the presence of fine particles. Hence, the large SSA likely results from both the highly porous network of the granulated apatite pellets and the nanoparticles of the binder matrix observed from SEM micrographs (Fig. 4.3.2.b).

### 4.3.3.2. Column experiments

#### 4.3.3.2.1. Maximal retention capacity

The amount of P retained per amount of phosphorus entering the filter for both columns 1 and 2 is shown in Fig. 4.3.2. P retention performances seem to reach an asymptotic trend, with Column 2 showing a slight improvement on P retention performance compared to Column 1. Data showed performances decreasing under 90% from just 2.3 and 2.8 g P-PO<sub>4</sub>·kg<sup>-1</sup> material and estimated maximum PRCs at 10.5 g P-PO<sub>4</sub>·kg<sup>-1</sup> material and 12.4 g P-PO<sub>4</sub>·kg<sup>-1</sup> material for Columns 1 and 2, respectively (Table S.4.3.4).

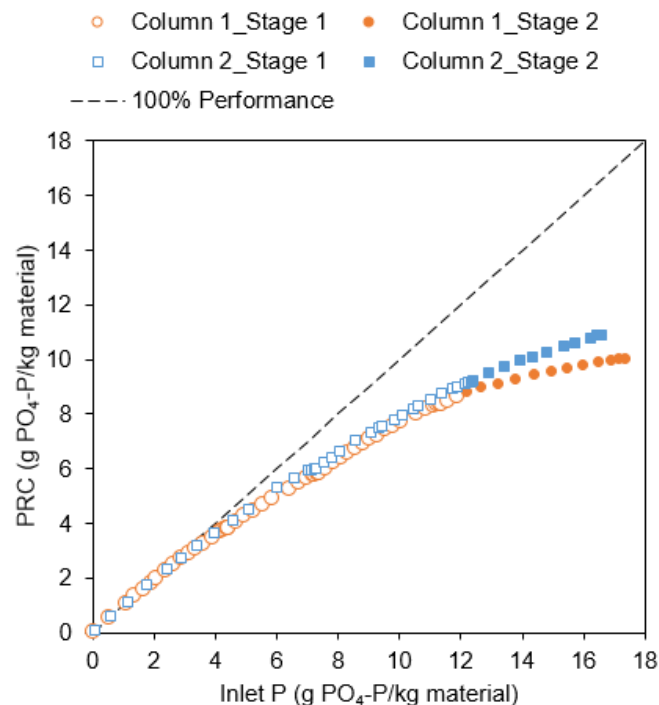


Fig. 4.3. 3. Evolution of phosphorus retention performance for columns 1 and 2. The plot compared their performance to the line of 100% and shows the correlation equations for the estimation of their maximum PRC.

Molle et al. (2005) carried out long-term experiments with rich quality natural apatite attaining a retention capacity of 13.9 g PO<sub>4</sub>-P /kg whereas the material performance for P retention was still greater than 90% at the end of the experiment. Therefore, the maximal retention capacity of granulated apatite appears relatively low compared to that of natural apatite.

#### 4.3.3.2.2. Estimation of kinetic parameters

Similarly to natural apatite, the evolution of kinetic rate constant with P retention capacity in granulated apatite (Fig. 4.3.4) reveals the presence of two different processes for phosphorus retention (Molle et al. 2005). High kinetic rate coefficients at the beginning of the filter's lifespan is attributed to the presence of adsorption reactions (Molle et al. 2005). As precipitation becomes the predominant mechanism, the kinetic rate coefficient decreases to attain a pseudo stabilization. For dimensioning purposes based on a long-term retention, the mean  $k_v$  value during the precipitation phase is therefore an important parameter. Thus, a substrate with a high stabilized kinetic coefficient (for high PRC) should be favored in order to have high P retention rates.

Previous studies have pointed out that the apatite content in the filtering material significantly affects the kinetic rate and hence the removal efficiency (Molle et al. 2011). The evolution of the kinetic rate coefficient with P retention capacity of the two columns was compared with natural substrates of rich and poor apatite content. Fig. 4.3.4 indicates that  $k_v$  of Column 1 evolves similarly to what is observed for a natural apatite material of poor quality. On the other hand, the calcium addition in Column 2 leads to higher  $k_v$  values characterizing a trend half way between poor and rich-quality natural apatites. The mean  $k_v$  value during precipitation is  $0.63 \text{ h}^{-1}$  for Stage 1 and  $0.41 \text{ h}^{-1}$  for Stage 2. For Column 1, the mean  $k_v$  values determined are  $0.48 \text{ h}^{-1}$  and  $0.23 \text{ h}^{-1}$  for Stages 1 and 2, respectively.

The impact of calcium addition in Column 2 during Stage 1 leads to an improved retention rate with regards to Column 1 in spite of the more demanding hydraulic conditions. This evidences that calcium concentration may be a limiting factor in CaP retention rates even when enough Ca concentration is provided ( $\text{Ca/P} > 1.67$  in both cases). A higher calcium concentration increases supersaturation resulting in an increase of the crystal growth rate (Peng et al. 2018). During Stage 2, on the other hand, both columns share the same operational conditions but  $k_v$  for Column 2 is almost twice as that of Column 1. This may indicate that different processes occurred during the preceding stage leading to significantly different kinetic rates. These aspects will be discussed more precisely from the examination of the SEM images.

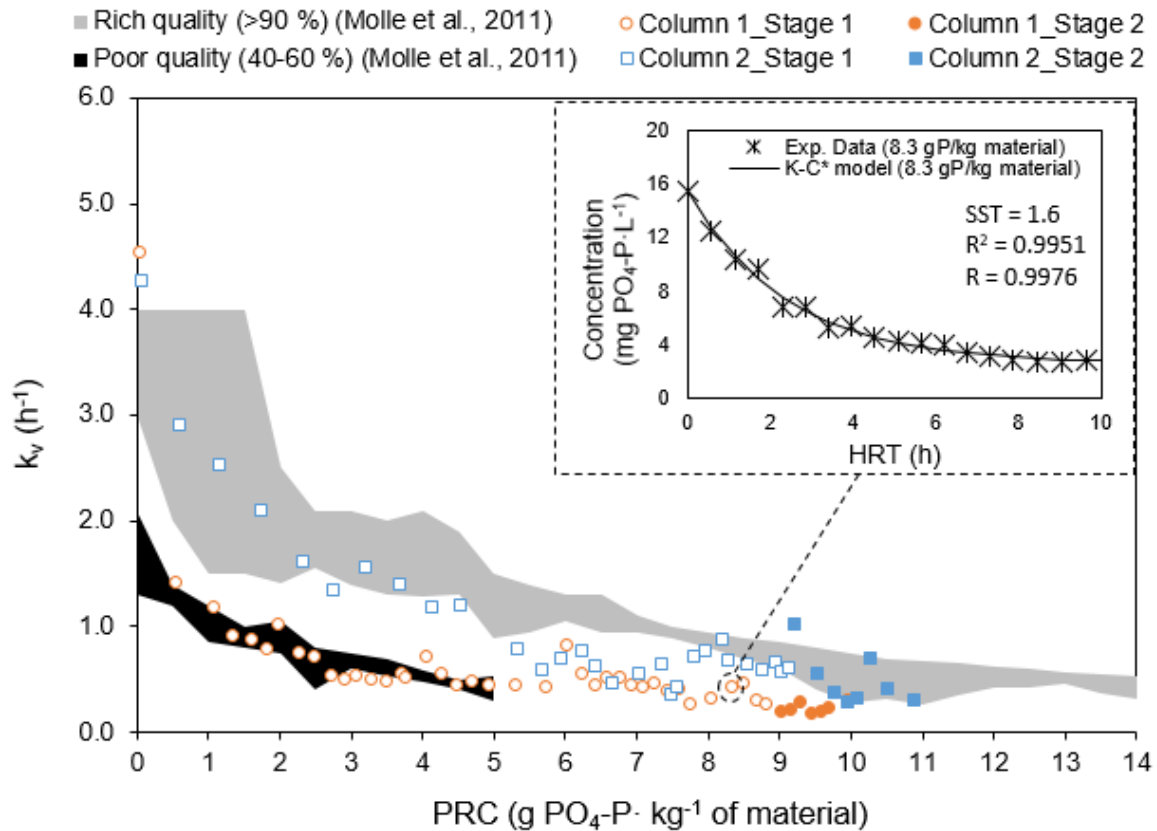


Fig. 4.3.4. Evolution of kinetic constants with media PRC for both columns and comparison to natural apatite from Molle et al. (2011) (shaded area) showing lower  $k_v$  values than rich quality apatite. The insight shows an example of the adjustment of experimental data to  $k$ - $C^*$  model to determine  $k_v$  and  $C^*$ . The adjustment of the data was verified by the calculation of the sum of square errors (SSE), the coefficient of determination ( $R^2$ ) and the correlation coefficient ( $R$ ).

#### 4.3.3.2.3. Estimation of background concentration

The evolution of  $C^*$  with PRC is also an important parameter to assess, since it determines the lowest P concentration achievable for a given filtering material under given solution conditions. Fig. 4.3.5.a shows how  $C^*$  strongly increases with the retention capacity of the media, under the operational conditions of Column 1. Using the correlation it can be estimated that outlet concentrations will exceed 1 and 2 mg P- $\text{PO}_4\cdot\text{L}^{-1}$  for PRCs around 4 and 10 g P- $\text{PO}_4\cdot\text{kg}^{-1}$  of material, respectively. Therefore, the substrate may not ensure low concentration discharge restrictions over a long-term retention. Instead for Column 2 (Fig. 4.3.5.b),  $C^*$  evolves with a logarithmic trend which stabilizes close to 1 mg P- $\text{PO}_4\cdot\text{L}^{-1}$  once the adsorption phase is over. Therefore, P retention for such particular feeding conditions appears to have a weak dependence on the PRC of the media for the range considered. This might be explained by the

increment in supersaturation due to calcium addition that makes precipitation less dependent on the catalytic properties of the material but on the solution properties.

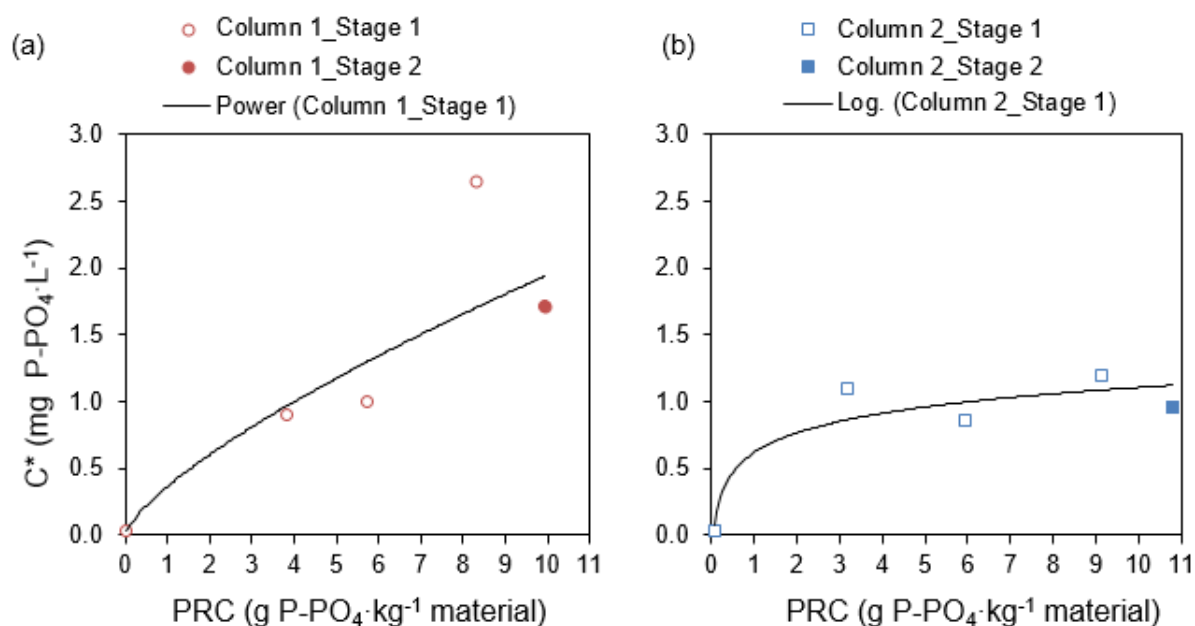


Fig. 4.3. 5. Evolution of  $C^*$  parameter with PRC for Column 1 (a) showing a power-like correlation and for Column 2 (b) showing a logarithmic evolution.

#### 4.3.3.2.4. Factors affecting CaP precipitation

The level of supersaturation in solution may have played a key role on the experimental results. Some aspects like pH or Ca/P molar ratio affect the supersaturation ratio and hence the kinetics of the process.

Precipitation of HAP should imply a pH decrease in solution (Blanco et al. 2016). However, no pH decrease could be observed during the whole experiment for the system in Column 1. In contrast, for Column 2, a pH decrease occurs several times during the experiment. Such discrepancy may be explained by the occurrence of distinct P retention processes for the two systems.

On the other hand, the initial Ca/P molar ratio in solution plays an important role on the crystallization since it affects the efficiency of precipitation and the elemental composition of the crystal product (Peng et al. 2018). Mean inlet Ca/P ratio is  $3.7 \pm 0.4$  for Column 1 during Stages 1 and 2, and  $7.9 \pm 3.6$  and  $3.9 \pm 0.5$  for Column 2 during Stage 1 and Stage 2, respectively. This resulted in a lower Ca/P ratio retained (Eq.

4.3.2) on average for Column 1 than for Column 2 Stage 1 (Fig. 4.3.6). The Ca/P ratio retained was compared with the CaP phases more likely to precipitate. For Column 1, the average Ca/P molar ratio retained in the column is lower than any of the possible stoichiometric CaP phases. On the contrary, higher Ca/P ratios were achieved for Column 2 during both Stages 1 and 2.

$$\left(\frac{Ca}{P}\right)_{retained} = \frac{[Ca^{2+}]_{in} - [Ca^{2+}]_{out}}{[P-PO_4^{3-}]_{in} - [P-PO_4^{3-}]_{out}} \quad [4.3.2]$$

A mean retained Ca/P ratio may give an idea on how much impact inlet conditions have on P retention. However, as Ca and P are being consumed, supersaturation and Ca/P ratio in solution evolve in the bulk of the column (Fig S.4.3.1). CaP precipitation along the column induces an increase in Ca/P ratio of the solution with the HRT. On the contrary, supersaturation is greater close to the system's inlet and therefore, most of the P precipitation will take place there. The mean Ca/P ratio retained will neither account for dissolution nor re-precipitation processes that may take place inside the column. Therefore, the speciation of CaP phases and its evolution (solid to solid transformations) may vary in time and space as a function of the media depth (Montastruc et al. 2003).

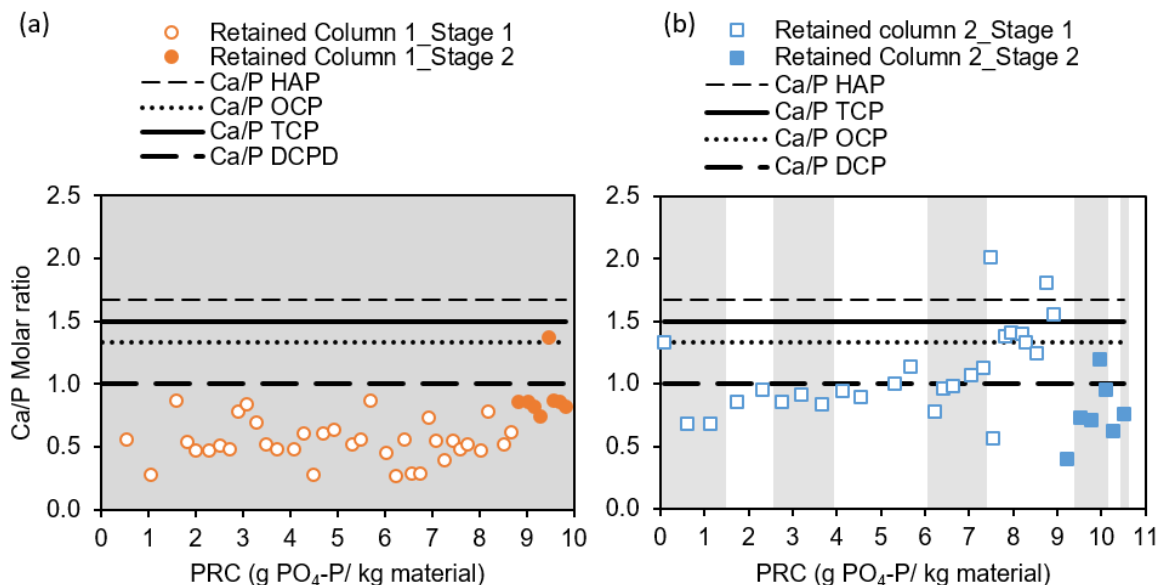


Fig. 4.3. 6. Evolution of the average Ca/P molar ratio of the column with media saturation for Column 1 (a) and Column 2 (b). The grey shaded areas indicate the regions where acidification did not occur during the process.

The saturation indexes for several calcium phosphates and calcite were determined for the three different inlet solution conditions (Table S.4.3.5). Results indicated supersaturation with respect to HAP, OCP and TCP for all inlet solutions and undersaturation for DCP, while calcite shows SI values close to equilibrium ( $SI=0$ ) (Table S.4.3.6). Several authors have already reported that some species such as TCP or OCP may act as precursors or metastable phases for HAP precipitation (Montastruc et al. 2003, Blanco et al. 2016). Following the Ostwald step rule (Van Santen 1984), the sequence for Ca/P precipitation starts with the more soluble species, which then undergoes several dissolution/recrystallization processes until the most stable phase is formed (Montastruc et al. 2003, Han et al. 2016, Prieto et al. 2016). Thus, in the systems being considered the theoretical sequence for Ca/P precipitation would be: TCP, OCP and HAP for both columns. Actually, slightly greater SI values were found for Column 2, which may explain the higher kinetic rates observed.

#### 4.3.3.3. Identification of retention processes

Results concerning the retention performance and the kinetic aspects have shown a media with low PRC and low kinetic rates. SEM observations coupled with EDS analyses allow to unveil the P retention processes associated with these features and to compare with those determined for mineral apatite, as well as the influence of Ca addition on them.

Fig. 4.3.7.a-d shows SEM micrographs of polished cross-sections of granules collected at the end of the experiment either at the bottom (a, c) or at the top (b, d) of Column 1. Micrographs (Fig. 4.3.7.a-b) reveal that part of the porosity in the vicinity of the granule edge has been irregularly clogged to a depth of 100 to 300  $\mu\text{m}$  (Fig. S.4.3.2.b). The clogged region viewed in the backscattered electron mode (Fig. 4.3.7.c-d), appears in a light grey shade close to that of apatite particles, which suggests an equivalent chemical composition. EDXS microanalyses lead to a Ca/P elemental ratio of about 1.7, which confirms a precipitation of hydroxyapatite in the internal porosity of the granule. Close examination of clogged regions showed that the binder matrix is evenly coated with the precipitate, whereas unclogged regions look similar to the initial raw material with Ca/P ratio remaining in the 1.8 - 2.2 range (Fig. S.4.3.2.a and Fig.

S.4.3.3). Thus, it appears that adsorption and precipitation phenomena are not carried out at the interface of the large apatite particles present in the granule, but within the binder matrix itself. Indeed, the apatite particles are almost completely surrounded by other particles and the binder, which prevent ions to have an easy access to the apatite mineral surface. As a consequence, the precipitate essentially fills up the binder porosity.

Two hypotheses may account for the phosphorus retention under the operational conditions of Column 1. First, the presence of micrometric to sub-micrometric apatite particles in the binder matrix which may act as seeds for CaP precipitation. Then, local increases in supersaturation at the pore scale due to the dissolution of calcium containing minerals present in the binder which would facilitate precipitation by increasing the reaction rates. In both cases, the diffusion rates within the pore are expected to be lower than adsorption and precipitation rates, which added to the tortuosity of the pores, results in a restricted penetration of phosphate ions in solution along the pores into the granule. A reduction of the binder porosity of the granule as precipitates grow would also explain the kinetic evolution of the system with PRC. A decrease in porosity implies a reduction of the specific surface area, which would achieve its minimal value at the granule surface. Therefore, as the porosity is clogged up the kinetic rate drops.

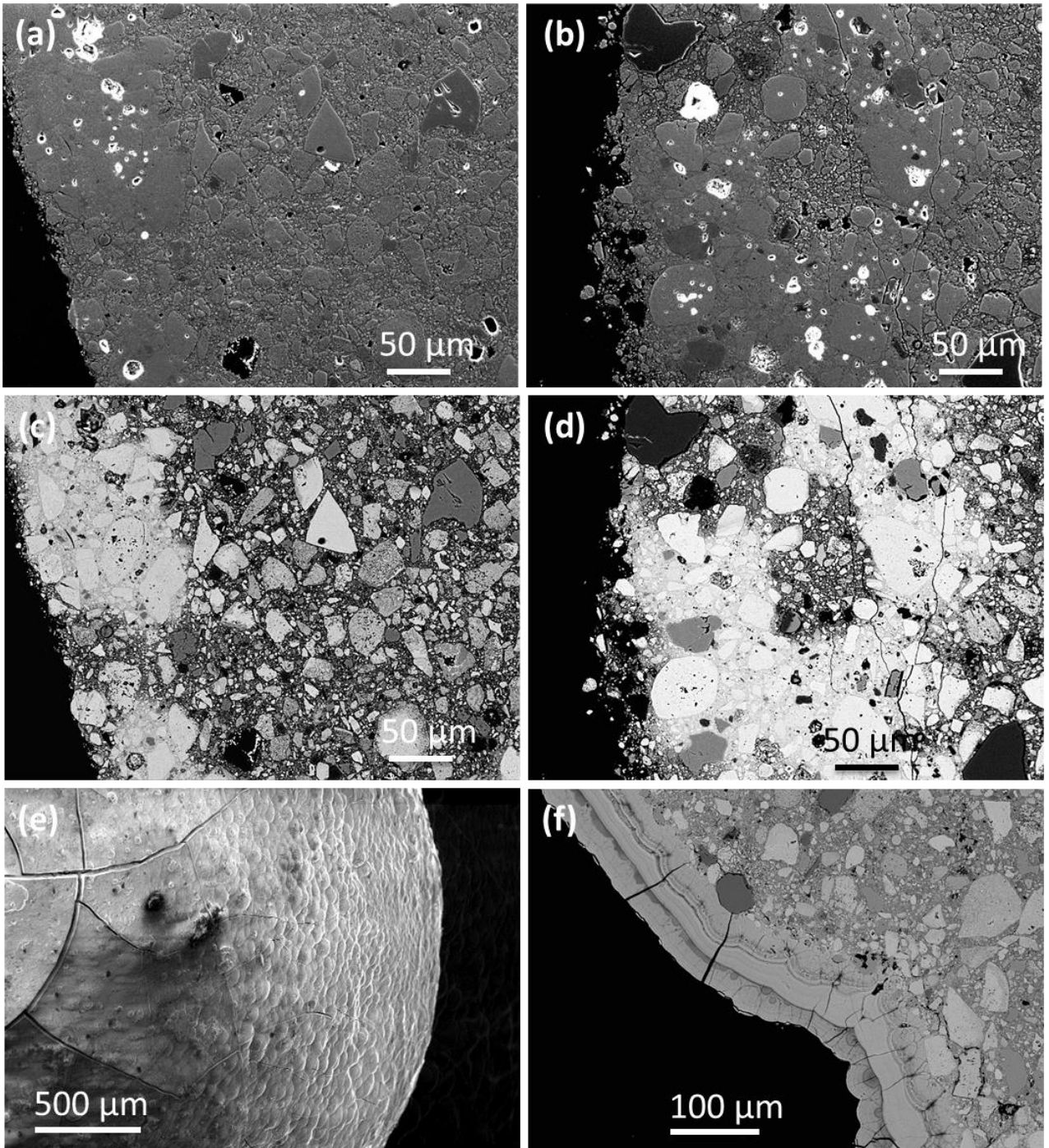


Fig. 4.3. 7. SEM micrographs of polished cross-sections of the granules in Column 1 (mean PRC=10 g PO<sub>4</sub>-P /kg) (a-b) Clogged regions close to the edge of granules examined in the secondary electron mode at (a) the bottom of the column (b) the top of the column; (c-d) corresponding micrographs in the backscattered electron mode, the regions in light grey colour identifying the clogged porosity at (c) the bottom of the column (d) the top of the column; SEM images of a pellet from the bottom of Column 2 showing a deposit of CaP (e-f): detail of the surface of the granule at a mean PRC = 6.2 g PO<sub>4</sub>-P/kg (e); detail of a polished cross-section enlarged at the edge of the pellet at a mean PRC=10.9 g PO<sub>4</sub>-P /kg.

In contrast, SEM examination of granules collected at the inlet (bottom) of Column 2 evidences entirely different processes (Fig. 4.3.7.d-e). A deposit of about 140 μm thick

has coated the external surface of granules. Furthermore, the clogging of the internal porosity that was previously observed for Column 1 is not present here (Fig. S.4.3.4). EDX line graphs of the deposit indicate that the average Ca/P molar ratio is  $1.64 \pm 0.14$ , which is consistent with a HAP precipitate. However, the obvious growth lines in the deposit associated with variations of Ca/P ratio in the 1.4 - 1.8 range, suggest that other forms of CaP phase might precipitate such as TCP, OCP and carbonated apatite. In particular, carbonation of apatite seems to occur and is represented by each dark growth line (Fig. 4.3.7.e). Slight changes in solution conditions may affect the continuity of the growing crystal leading to changes in composition of the solid solution. Presumably the most recent precipitation layer (external) corresponds to Stage 2 where Ca concentration is reduced and thus the molar ratio C/Ca increases leading to a more carbonated precipitate. Nevertheless, further experiments would be necessary to establish relationships between solution conditions and the evolution of the precipitates.

Unlike samples taken near the inlet of the system, no precipitation process could be observed in the samples collected from the media layers close to the outlet of the filter in Column 2 (Fig. S.4.3.5.b), although the occurrence of adsorption cannot be dismissed. For the middle media layers, no SEM analyses were conducted, however, it would be likely that retention processes as those seen for Column 1 occurred at some levels in the column with decreasing supersaturation. This results in a sharper PRC gradient with HRT where the major P retention occurred in the first centimeters of the filter. Indeed, crystal growth requires a lower energy barrier to be exceeded than the formation of new nuclei. As supersaturation becomes lower with increasing HRT, the energy barrier to form new nuclei is higher. Therefore the decline in the kinetic rate with PRC may be related to a reduction of the media porosity (or SSA) close to the inlet of the system.

#### 4.3.4. Conclusions

Two long-term column experiments for phosphorus retention with granulated apatite filters were conducted and assessed using the  $k-C^*$  model. The results showed unexpected low  $k_v$  values during precipitation (in the range of  $0.63 \text{ h}^{-1}$  to  $0.23 \text{ h}^{-1}$ ) and low estimated values of maximum PRC ( $10.5$  and  $12.4 \text{ g P-PO}_4\text{-kg}^{-1}$  of material)

compared with those of natural apatite. Such result would prevent the granulated apatite filters to ensure an appropriate long-term performance. The  $k-C^*$  model presents some limitations and is not capable of representing processes variations (depending on environmental conditions) and their associated kinetics. A mechanistic model would be necessary in such a case.

Mechanistic differences with respect to natural apatite were identified by the examination of SEM micrographs coupled with EDXS microanalyses. The binder matrix used for granulation hinders the access to the surface of apatite particles, which are then less likely to act as seeds for precipitation. As a consequence, calcium concentration, which affects the supersaturation of the inlet solution, appears to be the predominant parameter affecting the retention processes. For calcium concentrations around  $70 \text{ mg}\cdot\text{L}^{-1}$ , a lower supersaturation was attained enabling diffusion of ions through the granule porosity which adsorb and precipitate at the binder matrix, all along the filter. The precipitation of hydroxyapatite may result in this case from two different processes: (1) seeded precipitation onto micrometric apatite particles; (2) precipitation promoted by local increases in supersaturation caused by the dissolution of calcium from the binder. In contrast, for calcium concentrations around  $113 \text{ mg}\cdot\text{L}^{-1}$ , the supersaturation of the solution close to the inlet of the system appeared to be high enough to promote heterogeneous nucleation onto the granules surface. The deposit showed different layers of precipitates as hydroxyapatite and carbonated hydroxyapatite. The samples close to the outlet of the system did not show the formation of any deposit although adsorption into the matrix is suspected to occur.

Finally, it appeared that two major causes were responsible for the decrease in the kinetic rate of phosphorus retention: (1) the reduction of the SSA available with increasing PRC; (2) the decrease of supersaturation either along the column due to ions retention or inside the granules due to less Ca dissolution from the binder.

In conclusion, this work used laboratory column experiments conducted for more than a year to evaluate the capacity of this new material for phosphorus retention from wastewater. Despite granulated apatite has potentially the capacity for phosphorus retention, results showed worse performances and kinetics than natural apatites derived from its own configuration and the way they are manufactured. This will inevitably result in a high frequency of bed renewal which may not be interesting from an economical point of view. The authors recommend to address future research

efforts to enhance the comprehension of phosphorus retention processes on natural apatites and their hydraulic limitations for wastewater treatment applications.

#### 4.3.5. Supplementary Information

Table S.4.3. 1. Mineralogical composition %wt and crystallinity %wt of the granulated apatite determined by XRD analyses.

Material	Apatite	Calcite	Quartz	Dolomite	Clay	Ankerite	Cryst. <sup>c</sup>
<b>Granulated apatite</b> <sup>a</sup>	79.1 <sup>b</sup>	12.4	4.8	3.1	-	-	79.95

<sup>a</sup>Mean mineral composition based on XRD analyses of four granulated apatite samples. <sup>b</sup>Apatite as carbonate fluorapatite (C-FAP). <sup>c</sup>Crystallinity Mass percentage of the sample with crystalline structure. XRD measurements analyse solely the crystalline part of the sample.

Table S.4.3. 2. . Elementary composition %wt based on ICP-MS and ICP-OES analyses of the granulated apatite

Material (%wt)	Ca	P	Mg	Si	Al	Fe	Na	K	F	S total
<b>Granulated apatite</b>	32.6	11.8	0.4	2.4	0.5	0.3	0.53	0.29	2.17	0.76

Table S.4.3. 3. Grain size distribution, particle specific density and SSA (BET method) of some substrates studied for phosphorus retention from wastewater.

Material type	Particle size (mm)	Specific density (g/cm <sup>3</sup> )	SSA (m <sup>2</sup> /g)	References
<b>Steel Slag</b>	5 - 10	3.8	0.308	(Claveau-Mallet et al. 2017)
<b>Oyster shell</b>	2	2.56	9.94	(Wang et al. 2013)
<b>Broken briks</b>	2	2.37	10.78	
<b>Volcanics</b>	2	1.82	18.72	
<b>Zeolite</b>	2	2.07	8.81	
<b>Sand</b>	0.21(d <sub>10</sub> ) - 0.49	NA	0.08	(Prochaska and Zouboulis 2006)
<b>Dolomite</b>	(d <sub>60</sub> ) 1.2	NA	1.4	
<b>Bauxite</b>	< 2.8 - >12.7	NA	6.8	(Drizo et al. 1999)
<b>Zeolite</b>	4.1 - >12.7	NA	31.4	
<b>Shale</b>	< 2.8 - >12.7	NA	19.9	

Material type	Particle size (mm)	Specific density (g/cm <sup>3</sup> )	SSA (m <sup>2</sup> /g)	References
<b>Granulated apatite</b>	2.8(d <sub>10</sub> ) – 5 (d <sub>60</sub> )	2.89	32	This study

Table S.4.3. 4. Fitting equations applied on phosphorus performance curves and maximal retention capacity estimations for columns 1 and 2. Data were correlated with two different functions: a second-degree polynomial and an exponential function. First correlation would allow estimation of a feasible maximum retention capacity after which P retention by granulated apatite is no longer interesting in terms of performance (< 20% P retention). Instead, the exponential function would allow the assessment of a theoretical maximum retention capacity at infinite time.

	f(x)		Maximal PRC (g PO <sub>4</sub> -P/kg material)	R <sup>2</sup>
<b>Column 1</b>	$f(x) = ax^2+bx+c$	$-0.0236x^2+0.9994x-0.0408$	10.5	0.9987
	$f(x) = a - be^{-mx}$	$13.8 - 13.8e^{-0.079x}$	13.8	0.9971
<b>Column 2</b>	$f(x) = ax^2+bx+c$	$-0.0196x^2+0.9828x+0.0355$	12.4	0.9997
	$f(x) = a - be^{-mx}$	$17.0 - 17.0e^{-0.0625x}$	17.0	0.9994

Table S.4.3. 5. General equation, solubility product and Ca/P molar ratio for different calcium phosphates used in Phreeqc calculations.

		pK <sub>sp</sub> (25°C)	Ca/P	Reference
<b>Hydroxyapatite (HAP)</b>	$\text{Ca}_5(\text{PO}_4)_3\text{OH} \leftrightarrow 5\text{Ca}^{2+} + 3\text{PO}_4^{3-} + \text{OH}^-$	58.4	1.67	(Song et al. 2002)
<b>Octacalcium phosphate (OCP)</b>	$\text{Ca}_8\text{H}(\text{PO}_4)_6 \cdot 3\text{H}_2\text{O} \leftrightarrow 4\text{Ca}^{2+} + 3\text{PO}_4^{3-} + \text{H}^+ + 3\text{H}_2\text{O}$	50.61	1.33	(Song et al. 2002)
<b>Tricalcium phosphate (TCP)</b>	$\text{Ca}_3(\text{PO}_4)_2 \leftrightarrow 3\text{Ca}^{2+} + 2\text{PO}_4^{3-}$	28.92	1.5	(Song et al. 2002)
<b>Dicalcium phosphate dihydrated (DCPD)</b>	$\text{CaHPO}_4 \cdot 2\text{H}_2\text{O} \leftrightarrow \text{Ca}^{2+} + \text{HPO}_4^{2-} + 2\text{H}_2\text{O}$	-6.55	1.0	(Parkhurst and Appelo 2013)
<b>Calcite</b>	$\text{CaCO}_3 + \text{H}^+ \leftrightarrow \text{Ca}^{2+} + \text{HCO}_3^-$	-1.85		(Parkhurst and Appelo 2013)

Table S.4.3. 6. Mean saturation index with respect to different solid phases at the inlet solution (values during the kinetic study excluded) calculated with Phreeqc using a modified LLNL database (Song et al. 2002, Parkhurst and Appelo 2013).

		SI HAP	SI OCP	SI TCP	SI DCPD	SI Calcite
<b>Column 1</b>	Stage 1 and 2	10.4	4.90	2.29	-13.3	-0.06
<b>Column 2</b>	Stage 1	12.2	5.87	3.18	-13.3	0.38
	Stage 2	11.2	5.24	2.65	-13.4	0.14

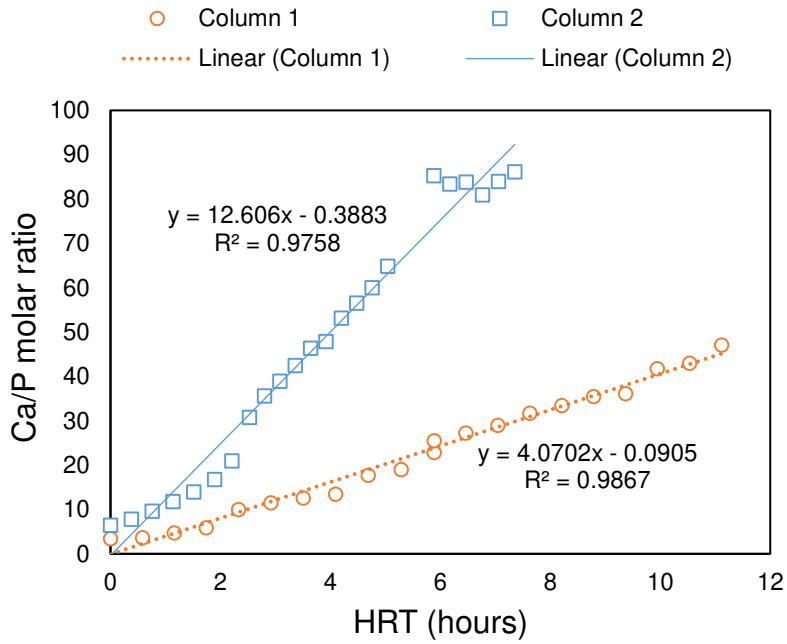


Fig. S.4.3. 1. Evolution of Ca/P molar ratio in solution with HRT during a kinetic study at a PRC of 5.7g PO<sub>4</sub>-P/kg material for Column 1 (Stage 1) and at 5.9 g PO<sub>4</sub>-P/kg material for Column 2 (Stage 1).

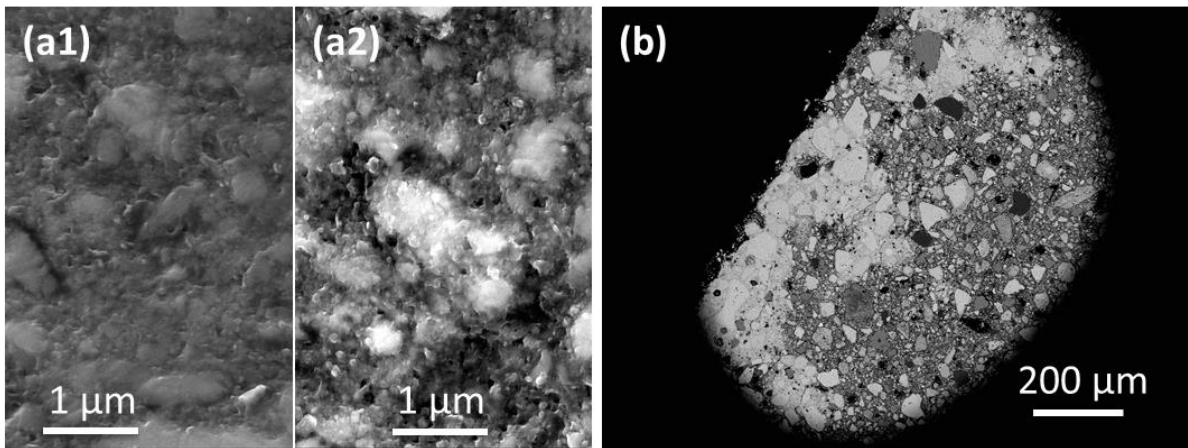


Fig. S.4.3. 2. Typical SEM micrographs of polished cross-sections of the granule in Column 1 (mean retention capacity = 10 g PO<sub>4</sub>-P/kg of granulated apatite)s; (a1-a2) comparison of the aspect of the binder matrix within clogged and unclogged regions (secondary electron mode); (b) .Edge of a granule at low magnification showing the irregular clogging of the internal porosity.

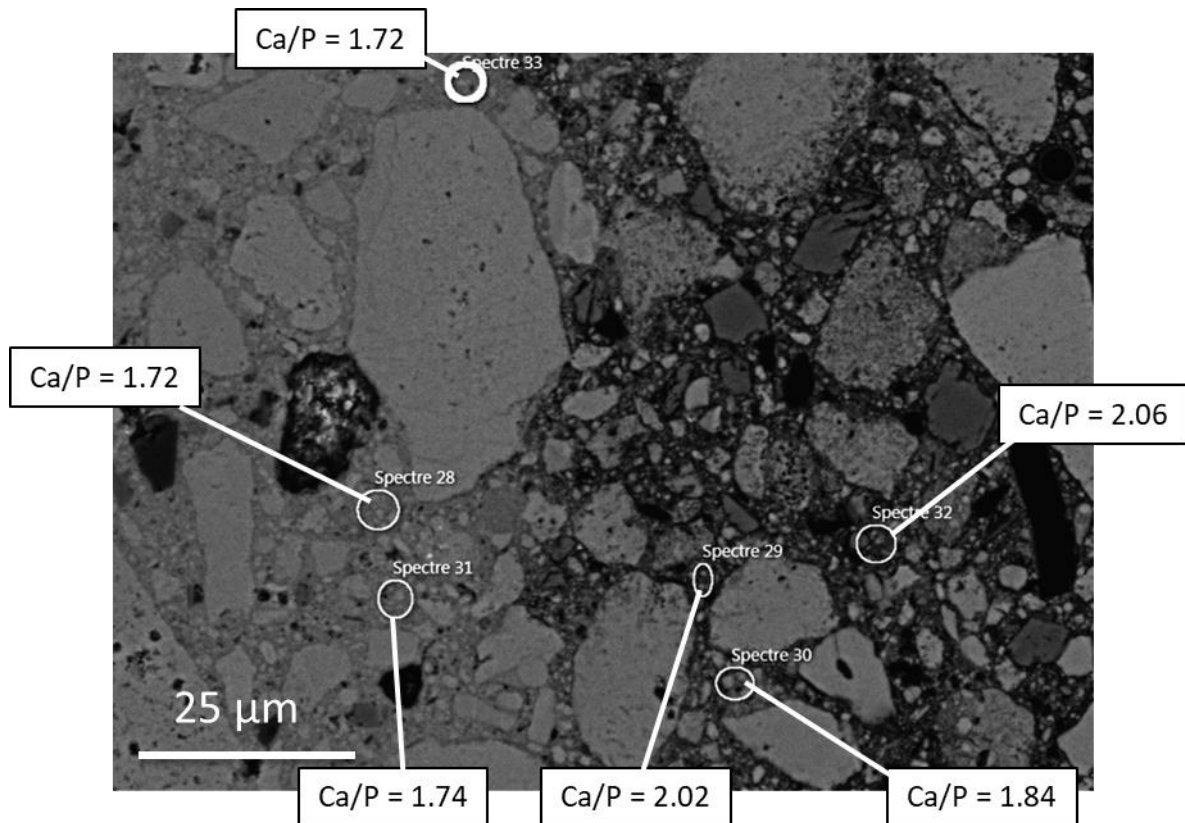


Fig. S.4.3. 3. EDX microanalyses of the polish cross-section of a granule sample from Column 1 and Ca/P molar ratio showing values around 1.7, close to stoichiometric HAP, in the light grey shade region at the binder level (Specters 28, 31, 33) and values around 1.8 -2.0 for the dark grey shade region at the binder (Specters 29, 30, 32).

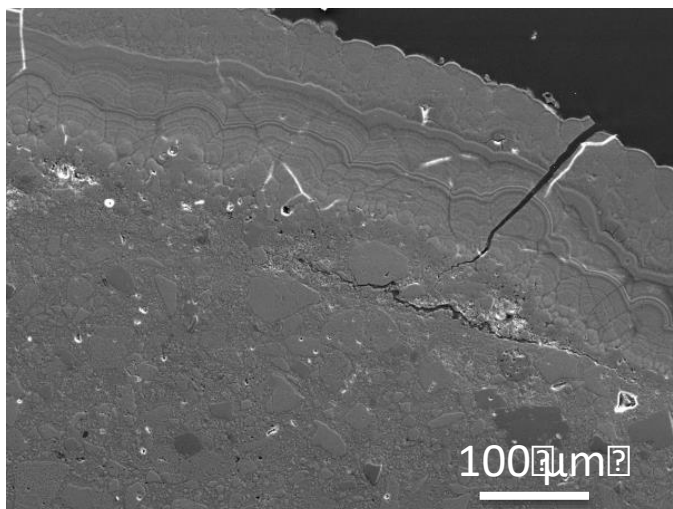


Fig. S.4.3. 4. Micrograph of a polished cross-section of a granule in secondary electron mode of a sample taken from the bottom of Column 2 (close to the inlet of the system). No loss of porosity is observed inside the granule but a deposit on its surface. Image equivalent to Fig. S.4.3.5.a. in secondary electron mode.

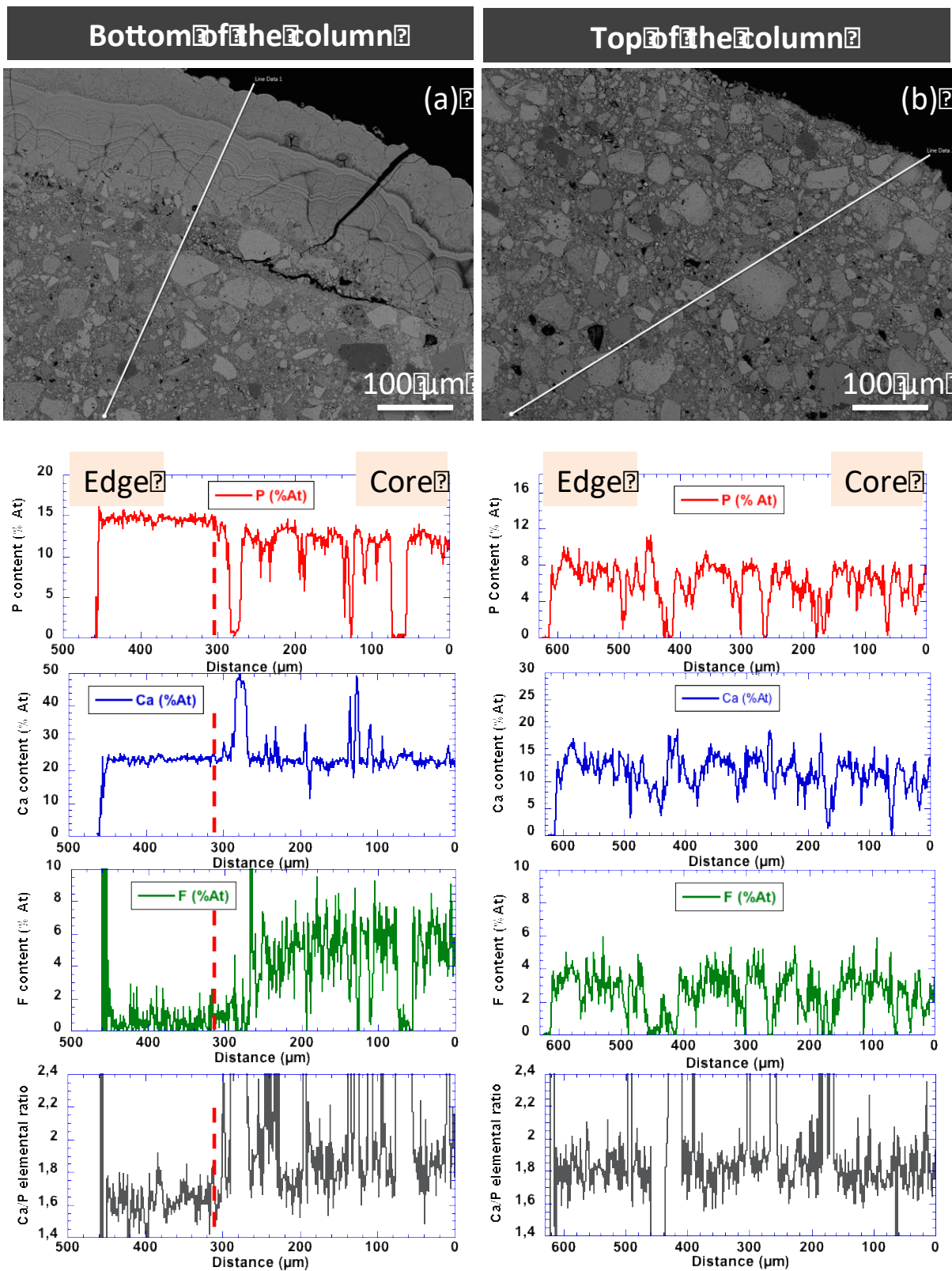


Fig. S.4.3. 5. Typical SEM micrographs in secondary electron mode of cross-polished sections of the granules samples taken at the bottom (a) and at the top (b) of Column 2 and the line-scan spectrum associated of main elements of apatite (HAP and FAP).

#### 4.4. Chapter Conclusions

Results from field campaigns on full-scale granulated apatite filters revealed some dysfunctions in the systems resulting in a lower lifespan for which they were designed (~ 10 years). Although partially derived from hydraulic issues, the low hydraulic efficiencies did not fully explain the low phosphorus retention performances. Instead it was suspected to be related with the nature of the substrate and the retention processes taking place. Under the environmental conditions of real effluents, the substrate did not form a calcium phosphate precipitate on its surface. The laboratory column experiments validated the assumptions made showing that the apatite particles inside the granules were not readily accessible to the ions in the solution but they were embedded in the binder of the granules. Hence, the substrate did not work as natural apatites reducing the supersaturation level of the solution with respect to the calcium phosphates phases (the more similar composition between seed and precipitate the lower the supersaturation required) but, like other more traditional adsorbing substrate. Granulated apatite provides a surface for heterogeneous precipitation effective in forming precipitates only with higher concentrations of calcium and phosphates. When such conditions were not reached, phosphorus retention occurred within the porosity of the granules attaining its maximum phosphorus retention capacity with the clogging of the internal porosity.

Consequently, the new generation of granulated apatites tested (results not shown in this document) was never pursued, and the attention turned back to natural apatites.

## Chapter 5. Results and discussion: Natural apatite

---

### 5.1. Context and objectives

Previous studies on natural apatite showed the interesting capability of natural apatites for phosphorus retention from wastewater. Phosphorus retention capacity and kinetic was shown to be specific to the particular composition of the apatite, which depended at the same time on the origin of the phosphate rock. However, previous studies used sieved natural apatite to fulfil hydraulic needs of classical treatment wetlands design. The sieving involved using just the coarser part of the material, representing less than 5 % of the commercial product, which made the process economically difficult to implement. In addition, natural apatite was evaluated until a phosphorus retention capacity that would be useful to overpass to better assess long-term performance of such systems. Hence, a full study on apatite commercial products was necessary to validate its adequacy for its application in phosphorus retention from wastewater.

Two new commercial natural apatite materials were selected to be studied in laboratory columns. Since major concerns on the use of natural apatite filters derived from its fine particle size distribution, the commercial products were slightly sieved to eliminate the finest particles, thus reducing the risk of a premature clogging. The study on laboratory columns aimed to determine the maximum phosphorus retention capacity of the natural apatites, the evolution of their kinetics with time and the impact of more restrictive environmental conditions (low calcium concentration and real wastewater effluent) on the efficiency of the process. The evaluation of the substrates was carried out using engineering reaction models to be able to provide a design assessment based on simple models easily handled by designers. However, such engineering reaction models are not able to fully describe complex systems, eg. calcium phosphate precipitation in a complex matrix like wastewater, and just provide a simple representation of the system. Thus, the ultimate objective of the study was to explore

the use of a mechanistic model for a better understanding of the processes involved. Such model would be an optimizing tool for the design of the filters based on the particular effluent conditions. This exploration provided the basic elements required to allow the later development of a complete and validated mechanistic model. In this study, the description of the solid matrix and hydraulics of the apatite filters were achieved using the Phreeqc and Hydrus-1D softwares.

In this chapter, results from the study of apatite filters in laboratory columns and the preliminary study for the development of a mechanistic model are presented in the form of two scientific publications.

## 5.2. Article 3. Natural Apatite laboratory columns

*Submitted to peer reviewed journal*

### **Seeded phosphorus retention in fixed-bed laboratory columns by apatites**

**Laura Delgado-González<sup>a,c</sup> \***, **Bruno Lartiges<sup>b</sup>**, **Stéphane Troesch<sup>c</sup>**, **Arnaud Proietti<sup>d</sup>**, **Pascal Molle<sup>a</sup>**

<sup>a</sup> Inrae, REVERSAAL Research Unit, 5 rue de la Doua, 69100 Villeurbanne, France ;

<sup>b</sup> Université de Toulouse III (Paul Sabatier), Géosciences Environnement Toulouse, 14 av. Edouard Belin, F-31400 Toulouse, France

<sup>c</sup> SYNTEA, Lieu-dit Belle-Croix, 33 490 Le Pian sur Garonne, France

<sup>d</sup> Université de Toulouse III (Paul Sabatier), Centre de Microcaractérisation R. Castaing, 3 Rue Caroline Aigle, 31400 Toulouse, France

\*Corresponding author: [laura.delgado-gonzalez@inrae.fr](mailto:laura.delgado-gonzalez@inrae.fr); (+33) 644 935 247

### **Highlights**

- High phosphorus retention capacity
- High kinetic rates
- No significant loss of permeability
- Precipitation of amorphous calcium phosphate

### **Abstract**

Phosphorus retention in small wastewater treatment plants is crucial to prevent eutrophication of downstream catchments. In this paper, two different apatite materials, NA1 and NA2, were studied in four fixed-bed laboratory columns to assess their phosphorus retention capacity. Different inflow conditions were set for the NA1 substrate to assess the impact of calcium and biomass development on performances. The substrates showed high phosphorus retention (>16.8 g PO<sub>4</sub>-P/kg for NA1 and >

17.5 g PO<sub>4</sub>-P/kg for NA2) and high kinetic rate coefficients (1.45 and 1.70 h<sup>-1</sup> for NA1 and NA2, respectively) with performances above 80% for both substrates. The maximum phosphorus retention capacity was not attained at the end of experiments. The NA1 column fed with a calcium deficient synthetic solution, showed just slightly reduced kinetic rates probably due to calcite and dolomite dissolution from the media. The column fed with treated wastewater did not show any significant reduction in hydraulic conductivity due to biomass development. No loss of permeability due to chemical clogging was observed in the other columns, neither. For both natural apatites, phosphorus retention occurred by precipitation of amorphous calcium phosphate. Such retention process is sustainable suggesting that it may proceed over higher retention capacities.

**Keywords:** phosphates recovery; reactive filter; surface reaction; amorphous calcium phosphate; wastewater.

### 5.2.1. Introduction

Phosphorus removal in small wastewater treatment plants (WWTP) is a technological issue not yet fully solved (Vohla et al. 2011). The use of filters with reactive substrates such as apatites (Ca<sub>5</sub>(PO<sub>4</sub>)<sub>3</sub>(OH,F,Cl)) can be a suitable solution to retain phosphorus because of their low maintenance requirements and long-term removal capacity (Molle et al. 2005, Molle et al. 2011). Used as a tertiary treatment in small WWTP, to avoid excessive biomass development, apatite can promote seeded precipitation of calcium phosphates (CaP) (Nancollas and Mohan 1970). Seeded precipitation operates in the metastable zone between the solubility and the super solubility curve. The more the seed crystals and the precipitates are close in composition the lower the supersaturation of the solution required to promote such precipitation (Jang and Kang 2002).

The precipitation of calcium phosphate phases involves complex equilibria. From a thermodynamic perspective, the most stable solid phase is hydroxyapatite (HAP) (Hermassi et al. 2015). However, HAP precipitation is not straightforward. According to the Ostwald step rule (Ostwald 1897, Chung et al. 2008), it generally requires the formation of a CaP precursor and the transition through other metastable solid phases up to the final crystalline HAP structure. The composition of the precursor is governed by precipitation kinetics. Most research carried out on HAP precipitation indicates the formation of amorphous calcium phosphate (ACP) as the phase precursor (Nancollas and Mohan 1970, Meyer and Eanes 1978, Mañas et al. 2012) and the transition up to HAP through crystallisation of tricalcium phosphate (TCP, Ca/P = 1.5), calcium deficient hydroxyapatite (CDHA, Ca/P = 1.5 - 1.6 (Dorozhkin 2010)) or octocalcium phosphate (OCP, Ca/P = 1.33) (Nancollas and Mohan 1970, Meyer and Eanes 1978, Castro et al. 2012).

Calcium availability is an important parameter to promote CaP precipitation. It may be provided by the wastewater and/or supplied by an additional soluble phase (e.g. calcite). The dissolution of Ca-containing minerals increases calcium availability and the supersaturation of the solution with respect to CaP phases. The role of dissolved Ca on P retention was pointed out in previous works on Ca-containing substrates such as shellsand (Ádám et al. 2007), oil shale ash (Kõiv et al. 2010) or steel slags (Barca et al. 2014).

Apatite mineral has previously shown to be an efficient crystallization seed to promote calcium phosphate precipitation (Joko 1984, Molle et al. 2005) from wastewater. However, such efficiency varies with apatite composition, nature of phosphate rock and origin (igneous/sedimentary) (Bellier et al. 2006, Harouiya et al. 2011, Harouiya et al. 2011, Molle et al. 2011). When considering wastewater treatment applications, another important aspect related to the filter efficiency is the particle size distribution of the substrate. A fine particle-size-distribution exposes more surface area for the reactions to take place improving the kinetic rates and performances of the system. On the other hand, fine particles increase the risk of a premature chemical or biological clogging of fixed bed reactors.

In this work, two different natural apatite materials available on the market are assessed to determine their capabilities to retain phosphates. The paper examines and compares their phosphorus retention capacity, performances and kinetics by using

simplified models suitable for design purposes. One of these materials was selected to evaluate their performance under alternative environmental conditions: a calcium deficient influent and a treated wastewater influent. The loss in hydraulic efficiency due to chemical and/or biological clogging is also investigated.

## 5.2.2. Materials and methods

### 5.2.2.1. Characterisation of apatite materials

Two different natural apatite materials are used in this study, hereafter called natural apatite 1 (NA1) and natural apatite 2 (NA2). A physical, chemical and mineralogical characterisation of both raw apatite products was carried out. Representative samples of both substrates were selected using the coning and quartering method (NF EN 932-2).

Elemental analysis of Ca, P, Si, Al, Fe, K, Mg and Na were carried out by alkaline fusion ( $\text{LiBO}_2$ ) followed by acid digestion ( $\text{HNO}_3$ ) and subsequent analyses of the solutions by inductively coupled plasma optic emission spectrometry (ICP-OES) (iCap6500, Thermo Scientific). Fluorine concentration was analysed using an ion selective electrode (ISE). Finally, total sulphur and total carbon were analysed using an infrared analyser (HORIBA EMIA 320-V2) after heating the samples by induction to approximately  $1450^\circ\text{C}$ .

The mineralogical characterization was carried out on dry ground ( $80 < \mu\text{m}$ ) raw samples by X-ray diffraction (XRD) with a  $\text{CuK}\alpha$  radiation ( $\lambda = 1.54060 \text{ \AA}$ ) on a  $2\theta$  diffractometer (Bruker D8-Advance) in the  $5 - 70^\circ$  range. Crystalline phases were identified using DIFFRAC EVA software (v.4.1.1) by comparing the registered patterns with the Powder Diffraction Files (PDF).

The crystallographic microstructure and the chemical composition of the apatite materials were also analyzed using imaging techniques. The apatite particles were first embedded in an epoxy resin to obtain cylindrical resin blocks (4 cm in diameter), that were abraded and polished in ethanol using successively finer silicon carbide powders. Finally, an ethanol-based diamond slurry was used to produce a smooth polished finish

suitable for recording Electron Backscatter diffraction patterns. The polished sections were carbon coated and examined by Scanning Electron Microscopy (SEM JEOL JSM-7100) equipped with an Electron Backscattered Diffraction pattern detector (EBSD AZtec HKL) and an Energy Dispersive X-ray Spectroscopy analyser (EDXS Oxford Instruments) for microanalysis (R. Castaing Microcharacterization Centre, France). This technique was also applied after the experiment to examine the chemical composition of the precipitates formed.

Particle size distribution was determined by the standard dry sieving method NF EN ISO 17892-4 (January 2018). The porosity of the media was determined using the standard soil science procedure based on estimations of bulk density and particle density (Klute 1986). Particle density was determined by the pycnometer method NF EN ISO 11508 (May 2014) ( $n = 3$ ), and the bulk density was measured by the volume occupied by a known mass of material ( $n = 3$ ).

The Specific Surface Area (SSA) was determined by considering the particle size distribution of the material with the assumption of spherical particles (McCabe et al. 2005).

$$SSA \left[ m^2/kg \right] = \frac{(1-f)}{\rho_s} \sum_{i=1}^{n-1} \frac{12}{d_{i+1}+d_i} \cdot \frac{m_i}{M} \quad [5.2.1]$$

Where  $f$  is the total porosity of the material,  $\rho_s$  ( $kg/m^3$ ) is the specific density,  $n$  is the total number of sieves used,  $d_i$  (m) is the diameter of the  $i^{th}$  sieve,  $m_i$  (kg) is the recovered mass between the  $i^{th}$  and the  $i^{th} + 1$  sieve and  $M$  (kg) is the total mass of the sample.

#### 5.2.2.2. Column experiments setup

Long-term tests in four fix-bed laboratory columns were conducted. The columns were filled with 20 cm high and  $63.6 \text{ cm}^2$  of section area of apatite filtering material. Three of the four columns (NA1\_Ref, NA1\_Ca and NA1\_bio) contained the NA1 apatite product to investigate various aspects related to P retention such as calcium content and biomass development. The fourth column, referred to as NA2\_Ref, contained NA2 material for the comparison with the NA1 substrate.

The experiments were carried out in hydraulically saturated systems in a vertical down-flow regime (See Fig. S.5.2.1 of Supplementary Information for more details). All columns present equidistant internal sampling points to allow solution sampling at various retention times. Two gravel transition layers (2-6 mm siliceous gravel, Sibelco) were placed at the inlet and outlet of the filters to prevent the loss of the apatite material. The columns were also wrapped with black opaque plastic sheet to avoid algae development.

### 5.2.2.3. Feeding and analyses protocol

Except for column NA1\_bio, the pilot columns were fed with a synthetic solution prepared from tap water and  $\text{KH}_2\text{PO}_4$  (Sigma-Aldrich) to achieve phosphorus inlet concentrations around 15 mg  $\text{PO}_4\text{-P/L}$ . The conductivity was also adjusted by adding a NaCl solution (common salt) to approach common values in real wastewater ( $\approx 1000\mu\text{S/cm}$ ). The aim of the experiment in column NA1\_Ca was to analyze the effectiveness and kinetic rate of P retention at low calcium concentrations. Therefore, the inlet solution is diluted with distilled water to halve the tap water calcium concentration. The feeding solution of NA1\_bio column is the outlet effluent of a biological secondary treatment where phosphate concentration is adjusted with  $\text{KH}_2\text{PO}_4$  addition to attain concentrations around 20 mg  $\text{PO}_4\text{-P/L}$ .

Flow rates of all columns were set around 10L/day except for column NA1\_bio which was set around 5L/day to limit the P load on the filter. Table 5.2.1 summarizes the feeding characteristics of the columns and the duration of the experiments.

Table 5.2. 1. Inlet solution characteristics of the laboratory column experiments and duration of the tests. Mean value  $\pm$  Standard deviation (95%).

Column	NA1_Ref	NA1_Ca	NA1_bio	NA2_Ref
<b>Filled with</b>	NA1	NA1	NA1	NA2
<b>Pore volume (L)</b>	0.67	0.70	0.69	0.72
<b>Flow rate (L/d)</b>	9.4 $\pm$ 1.9 (85)*	9.9 $\pm$ 1.4 (50)*	5.0 $\pm$ 1.3 (50)*	9.6 $\pm$ 1.9 (85)*
<b>Hydraulic load (m/d)</b>	1.48 $\pm$ 0.3	1.57 $\pm$ 0.22	0.78 $\pm$ 0.20	1.51 $\pm$ 0.3

Column	NA1_Ref	NA1_Ca	NA1_bio	NA2_Ref
<b>Fed with</b>	Synthetic solution	Synthetic solution	2nd stage treated wastewater	Synthetic solution
<b>[PO<sub>4</sub>-P] (mg/L)</b>	14.6 ± 1.2	13.8 ± 0.9	21.0 ± 2.7	14.6 ± 1.3
<b>[Ca<sup>2+</sup>] (mg/L)</b>	64.4 ± 11.7	35.2 ± 2.6 (18)*	65.6 ± 18.9	66.8 ± 5.0
<b>Ca/P molar ratio</b>	3.52 ± 0.42	1.97 ± 0.20	2.45 ± 0.75	3.57 ± 0.35
<b>Organic load (g / (m<sup>2</sup> · day))</b>	-	-	6.7 ± 4.0 (as TSS) (5)* 40 ± 46 (as COD) (5)* 3.2 ± 0.3 (as BOD <sub>5</sub> )** (5)*	-
<b>[NaCl] (mg/L)</b>	319 ± 52	402 ± 94	159 ± 48	311 ± 33
<b>Conductivity (μS/cm)</b>	992 ± 102	990 ± 65	763 ± 163	1001 ± 87
<b>pH</b>	7.6 ± 0.3	7.6 ± 0.1	7.5 ± 0.4 (19)*	7.6 ± 0.2 (33)
<b>Experimental time (d)</b>	230	139	133	230
<b>Number of samples</b>	34	20	20	34

\*Number of samples are indicated in brackets in the particular cell when such number is different from those indicated in the corresponding line of the table.

\*\* Self-monitoring data from the WWTP: mean outlet during the experimental time.

Samples were collected once a week at the inlet and outlet of the systems. To assess the evolution of P concentration inside the column, samples were also collected at the different sampling points along the column at selected times of the experiment, particularly during the precipitation phase (high phosphorus retention capacity (PRC)). Calcium, phosphate, carbonates and other ions concentrations were analyzed in filtered samples (pore size 0.45μm) by ionic chromatography (NF EN ISO 14911 and EN ISO 10304-1). Measurements of the chemical oxygen demand (COD) and total suspended solids (TSS) were also conducted for some samples of NA1\_bio according to the norms NF T 90-101 and NF EN 872, respectively. The biochemical oxygen demand (BOD<sub>5</sub>) analytical results (NF EN 1899-1) were taken from the monitoring data of the wastewater treatment plant. The conductivity and the pH were also measured for each sample. Finally, the flow rate was checked every two days and adjusted when necessary.

#### 5.2.2.4. Reaction rate models

The evolution of phosphorus concentration along the column was fitted with two different reaction rate models: the k-C\* model and the N-k-C\* model (Kadlec and Wallace 2009).

The k-C\* model is a simplified kinetic model that assumes first order kinetics for P retention, an ideal plug flow reactor and a background concentration. The evolution of P concentration (C) with hydraulic retention time (HRT) represented by t (h) can be obtained by the following expression:

$$C = (C_0 - C^*)exp(-k_v t) + C^* \quad [5.2.2]$$

where C<sub>0</sub> is the inlet concentration of phosphorus (mg/L), k<sub>v</sub> the volumetric kinetic rate constant (h<sup>-1</sup>) and C\* the P equilibrium concentration (mg/L). The k-C\* model has been traditionally used to describe pollutant retention in porous systems such as treatment wetlands (Merriman et al., 2017) and more particularly in the case of phosphorus retention by apatite filters (Harouiya et al. 2011, Harouiya et al. 2011, Molle et al. 2011). Even though the plug flow may not be strictly accurate describing the hydrodynamics of such systems, it provides a reasonable estimation of the treatment performances when background concentrations must be considered (Merriman et al., 2017).

The N-k-C\* model is a combination of the k-C\* model with the hydrodynamics of a tank-in-series (TIS) model. The number of tanks-in-series (N) introduced in the equation (Eq. 5.2.3) must be determined by tracer tests.

$$C = (C_0 - C^*) \left(1 + \frac{k_v t}{N}\right)^{-N} + C^* \quad [5.2.3]$$

The parameters of both models, k<sub>v</sub> and C\*, are determined by kinetic studies.

#### 5.2.2.5. Assessment of model parameters

To estimate the parameters of the models several kinetic studies were performed at different PRC along the experiment. A kinetic study analyses the evolution of P concentration within the columns at different hydraulic retention times (HRT). To

address the entire concentration range (from 15 mg PO<sub>4</sub>-P/L to equilibrium), the kinetic assessment was carried out by reducing progressively the inlet P concentration to simulate longer HRT; i.e., the outlet concentration of the first week was set as the inlet concentration of the following week and so on. Such methodology requires from one to four or five weeks of measurements, until the variation of concentration between consecutive sampling points is  $\leq 0.1$  mg PO<sub>4</sub>-P/L or the outlet concentration is zero.

Both models were adjusted to the data resulting from these kinetic studies using a Generalized Reduced Gradient (GRG) nonlinear least square method. While the  $k_v$  parameter is better defined at high inlet concentrations,  $C^*$  requires approaching low P outlet concentrations (equilibrium). When no kinetic study was conducted, the  $C^*$  was set at the value defined in a previous kinetic study and  $k_v$  was then determined based on inlet/outlet concentrations. Such calculation involve some fair uncertainties as  $C^*$  evolves slowly between two kinetic experiments (kinetic studies were performed frequently for this purpose).

#### 5.2.2.6. Tracer tests

Direct tracer tests were conducted to determine the parameter N of the TIS hydraulic model, which describes the number of completely stirred tank reactors (CSTR) of equal volume in series. The retention distribution curve (E(t) vs t) of a TIS hydraulic model is defined by the gamma distribution curve shown in Eq. 5.2.4.

$$E(t) = \frac{N}{t_{exp}\Gamma(N)} \left(\frac{Nt}{t_{exp}}\right)^{N-1} \exp\left(-\frac{Nt}{t_{exp}}\right) \quad [5.2.4]$$

$$t_{exp} = \int_{t=0}^{\infty} t E(t) dt \quad [5.2.5]$$

Where E(t) is the retention time distribution function, t (h) is time,  $t_{exp}$  (h) is the experimental hydraulic retention time (HRT) which is also the mean retention time of the distribution curve (Eq. 5.2.5) and  $\Gamma(N)$  ( $h^{-1}$ ) is the gamma function.

A GGUN-FL30 Fluorometer was used to analyse the evolution with time of the concentration of the fluorescein-tracer at the outlet of the columns of the NA1 substrate. The characteristics of the tracer tests for each filter are described in Table 5.2.2.

Table 5.2. 2. Tracer tests characteristics: mass of tracer used, volume of tracer solution sent to the filter and duration of the tracer tests.

	NA1_Ref	NA1_Ca	NA1_bio
<b>Mass added (<math>\mu\text{g}</math> fluorescein)</b>	95.3	114.8	85.1
<b>Sent volume (<math>\text{cm}^3</math>)</b>	19	23	17
<b>Duration (h)</b>	20	19	18.8

The experimental data from the tracer test is then used to determine  $E(t)$  using the following expression:

$$E(t) = \frac{Q(t)C(t)}{\int_0^{\infty} Q(t)C(t)dt} \quad [5.2.6]$$

Where  $Q$  ( $\text{m}^3/\text{h}$ ) is the flowrate,  $C$  ( $\text{g}/\text{m}^3$  or  $\text{mg}/\text{L}$ ) is the tracer concentration at the outlet of the system. The model is used to fit the data by a simultaneous determination of  $t_{\text{exp}}$  and  $N$  (SOLVER (Excel™) tool by minimization of the sum of square errors). For values of  $N = 1$ , the system behaves as an ideal CSTR. For  $N$  values above or equal to 50 (Levenspiel 2012), the retention distribution curve produces the Gaussian distribution of a plug flow reactor.

#### 5.2.2.7. Study of hydraulic conductivity

A constant head permeability test was carried out at the beginning and at the end of the experiments to assess changes in the hydraulic conductivity ( $k_h$ ) of the system (See Fig. S.5.2.2 and S.5.2.3 of Supplementary Information for a scheme of the experimental setup). The Darcy's equation (Eq. 5.2.7) is used to determine  $k_h$  ( $\text{m}/\text{s}$ ), where  $\Delta h$  is the head loss ( $\text{m}$ ),  $A$  is the section area of the column ( $\text{m}^2$ ),  $L$  is the distance between piezometers ( $\text{m}$ ) and  $Q$  is the flow rate ( $\text{m}^3/\text{s}$ ).

$$k_h = \frac{Q \cdot L}{A \cdot \Delta h} \quad [5.2.7]$$

### 5.2.3. Results and discussion

#### 5.2.3.1. Characterisation of apatite materials

Results from XRD are presented in Table 5.2.3. NA1 and NA2 contain 51 and 78%(wt) of apatite as carbonated fluorapatite (C-FAP), respectively. Other crystalline phases present in both apatites NA1 and NA2 are calcite, dolomite and quartz. Amorphous phases were also present in the samples with 21% and 18% (wt) for NA1 and NA2, respectively.

Natural apatite rock suppliers provide the quality of the material in terms of elemental composition (Table 5.2.4). Since the most abundant phosphate rock is apatite, it can be admitted that the apatite content is proportional to the P content. However, as XRD measurements can only analyse crystalline phases, it cannot be directly related with the results in Table 5.2.1. In this study, the P content of NA1 and NA2 is 11.0 and 13.8% (wt), respectively.

Table 5.2. 3. Mineralogical composition % (wt) and crystallinity % (wt) of the apatite substrates NA1 and NA2.

Material	Apatite	Calcite	Quartz	Dolomite	Clay	Cryst. <sup>b</sup>
<b>NA1</b>	51.0 <sup>a</sup>	22.4	9.7	16.4	-	78.6
<b>NA2</b>	77.5 <sup>a</sup>	13.3	6.4	2.8	-	81.6

<sup>a</sup>Apatite as carbonate fluorapatite (C-FAP). <sup>b</sup>Crystallinity Mass percentage of the sample with crystalline structure. XRD measurements analyse solely the crystalline part of the sample.

Table 5.2. 4. Elementary composition on weight percentage based on ICP-MS and ICP-OES analyses of the apatite substrates NA1 and NA2.

Material (%wt)	Ca	P	Mg	Si	Al	Fe	Na	K	F	C	S total
<b>NA1</b>	33.2	11.0	1.2	3.7	0.7	0.4	3.3	0.1	2.6	3.3	0.46
<b>NA2</b>	36.7	13.8	0.4	1.7	0.2	0.2	3.4	0.1	3.3	2.3	0.50

Table 5.2.5 presents physical characteristics of apatite substrates used in this study. The apatite material NA2 shows a smaller particle size distribution than NA1 resulting in a slightly greater SSA for NA2 according to method 1.

Table 5.2. 5. Grain size, porosity, particle specific density and SSA obtain from the particle size distribution method (method 1) and the BET method (method 2) for natural apatites NA1 and NA2.

Material	Particle size* d <sub>10</sub> -d <sub>60</sub> (mm)	Porosity (%)	Specific density (g/cm <sup>3</sup> )	SSA (m <sup>2</sup> /kg)
<b>NA1</b>	0.6 – 2.0	54	2.7	0.83
<b>NA2</b>	0.6 – 1.0	57	2.9	0.96

\*d<sub>10</sub> and d<sub>60</sub> mesh diameter allowing 10 and 60% of the material to pass through

The micrographs and SEM-EDXS analyses on the raw substrates have revealed interesting aspects about the morphology and composition of both products. The NA1 material often shows a gangue substrate coating the apatite particles (Fig. 5.2.1.a). The coating is mainly composed of clays as montmorillonite ((Na, Ca)<sub>0.33</sub>(Al, Mg)<sub>2</sub>(Si<sub>4</sub>O<sub>10</sub>)(OH)<sub>2</sub>·nH<sub>2</sub>O) which usually contains Fe as a common cation substitution (Anthony et al. 1995). In apatite NA2, the occurrence and amount of gangue observed are lower leading to a “cleaner” apatite product (Fig. 5.2.1.b), which may explain the differences in terms of Al and Fe composition with respect to NA1. The Ca/P molar ratio of apatite particles was typical of carbonated apatites, i.e.  $1.78 \pm 0.8$  for NA1 and  $1.80 \pm 0.7$  for NA2.

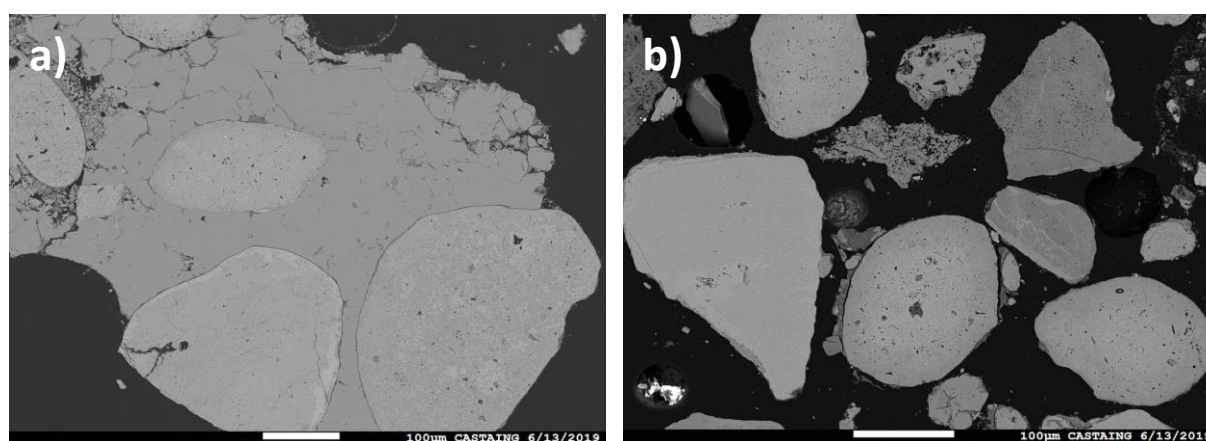


Fig. 5.2. 1. SEM micrographs of polished cross sections of the raw material products in the back-scattered mode: a) NA1 apatite particles appeared embedded in a gangue of different nature (darker grey), and b) NA2 substrate particles, the sample present a much less concentration of clay gangue.

### 5.2.3.2. P retention performances

The performance of the system is expressed in Fig. 5.2.2 as the amount of P retained per amount of P entering the filter. A 100% performance is represented by the straight-line  $y = x$ . Fig. 5.2.2.a) shows that NA1 and NA2 have a similar evolution of their retention capacity until they attained 8 g PO<sub>4</sub>-P/kg material. At this point, the performance of NA1 starts to decrease and it shows slight differences with NA2. For the latter, the separation from the 100% line starts at 10 g PO<sub>4</sub>-P/kg. After 230 days of experiment, the columns NA1 and NA2 have cumulated 16.8 and 17.5 g PO<sub>4</sub>-P/kg material with removal performances still reaching 80% and 83%, respectively, for hydraulic retention times of 1.8 hours. The experimental time was not large enough to attain the maximum PRC of the materials yet high enough to reach interesting values from an operational point of view.

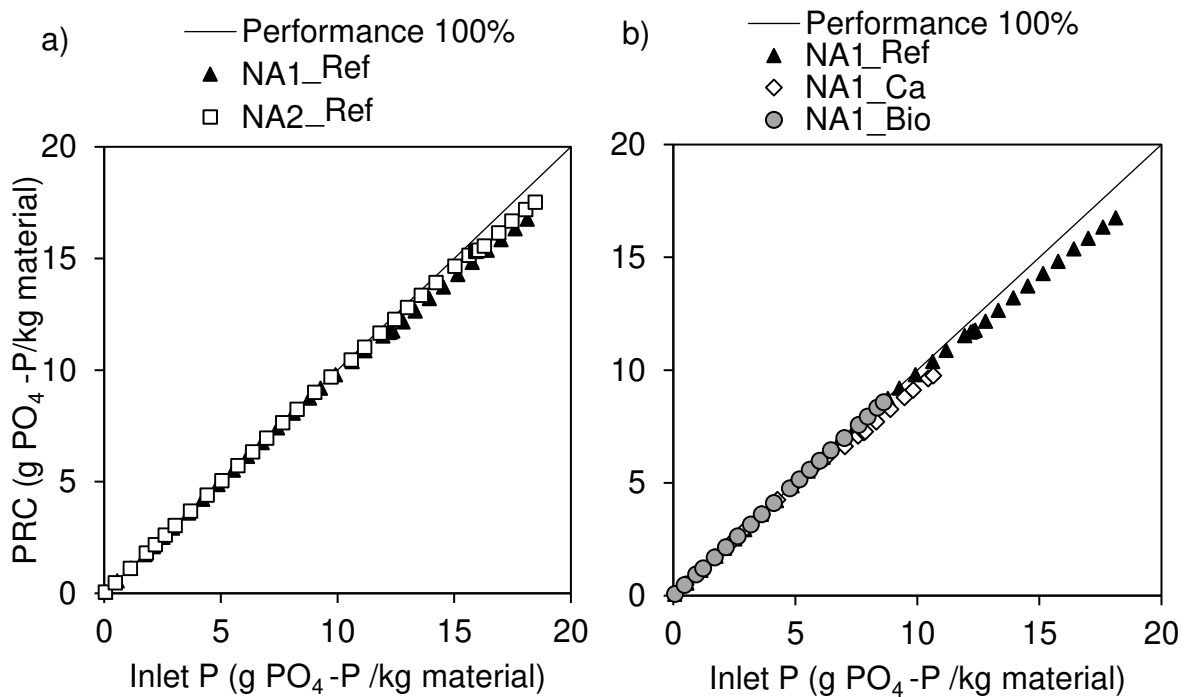


Fig. 5.2. 2. Evolution of phosphorus retention performance for a) NA1\_Ref and NA2\_Ref columns and b) NA1\_Ref, NA1\_Ca, NA1\_bio columns. The plots show the maximum PRC attained during the experiments and compare their performances against the 100% performance line.

Fig. 5.2.2.b) shows the results of the experiments using NA1 for different operating conditions (lack of Ca, biofilm growth). For the column NA1-Bio the performance remained close to 99% at the end of experiment, following the same trend as NA1\_Ref. Thus, up to a PRC equal to 8.6 g PO<sub>4</sub>-P/kg NA1, the experiment showed that the effect

of a biofilm development is limited. It can also result from biological assimilation; however, as the organic load is low ( $3.2 \text{ g DBO}_5/\text{m}^2/\text{d}$ ), biomass assimilation may not be significant.

Instead, the lack of calcium affects P retention performance more significantly. It starts to reduce at  $3.0 \text{ g PO}_4\text{-P}/\text{kg NA1}$  and it is below 80% from a PRC of around  $9.6 \text{ g PO}_4\text{-P}/\text{kg NA1}$ . The reduction of calcium concentration does affect, indeed, the supersaturation of the solution with respect to the CaP solid phases, thus, reducing the reaction rate and the performance of the process.

#### 5.2.3.3. Tracer tests

The N parameter was determined from fluorescein-tracer tests using the gamma distribution expression of Eq. 5.2.4. This leads to an N value of 5.5, 13.0 and 19.0 for the NA1\_Ref column, the NA1\_Ca column and the NA1-bio column, respectively. As the hydrodynamics of the NA1\_Ref column is the furthest from the plug flow regime, it will be selected in the following to assess the limits of the application of the k-C\* model to laboratory columns.

A full description of the tracer test results can be found in the Supplementary Information section.

#### 5.2.3.4. Assessment of the kinetics

The evolution of the kinetic rate coefficient with the phosphorus retention capacity starts from high values that gradually decrease until a pseudo stabilisation is attained (Molle et al. 2011). This behaviour would account for an initial stage where adsorption and a rapid precipitation of calcium phosphates occur; then the kinetic rate gradually reduces and the retention is mainly associated with the crystal growth of calcium phosphates.

In Fig. 5.2.3 the kinetic rate coefficient is evaluated using the k-C\* model to compare both substrates, NA1 and NA2. It reveals a longer initial stage for NA2 than for NA1. The mean  $k_v$  value of NA2\_Ref during this period is of  $4.34 \text{ h}^{-1}$  lasting up to  $9 \text{ g PO}_4\text{-P}/\text{kg}$ . For NA1\_Ref, the first high kinetic coefficient stage attains around  $6.5 \text{ g PO}_4\text{-P}/\text{kg}$ .

P/kg, with a mean value of  $4.26 \text{ h}^{-1}$ . Despite the longer initial stage for NA2\_Ref with respect to NA1\_Ref, the  $k_v$  values during the pseudo-stabilisation stage appear to attain a similar range for both columns. The average  $k_v$  values in the pseudo-stabilisation stage are  $1.45 \text{ h}^{-1}$  and  $1.70 \text{ h}^{-1}$  for NA1\_Ref and NA2\_Ref, respectively.

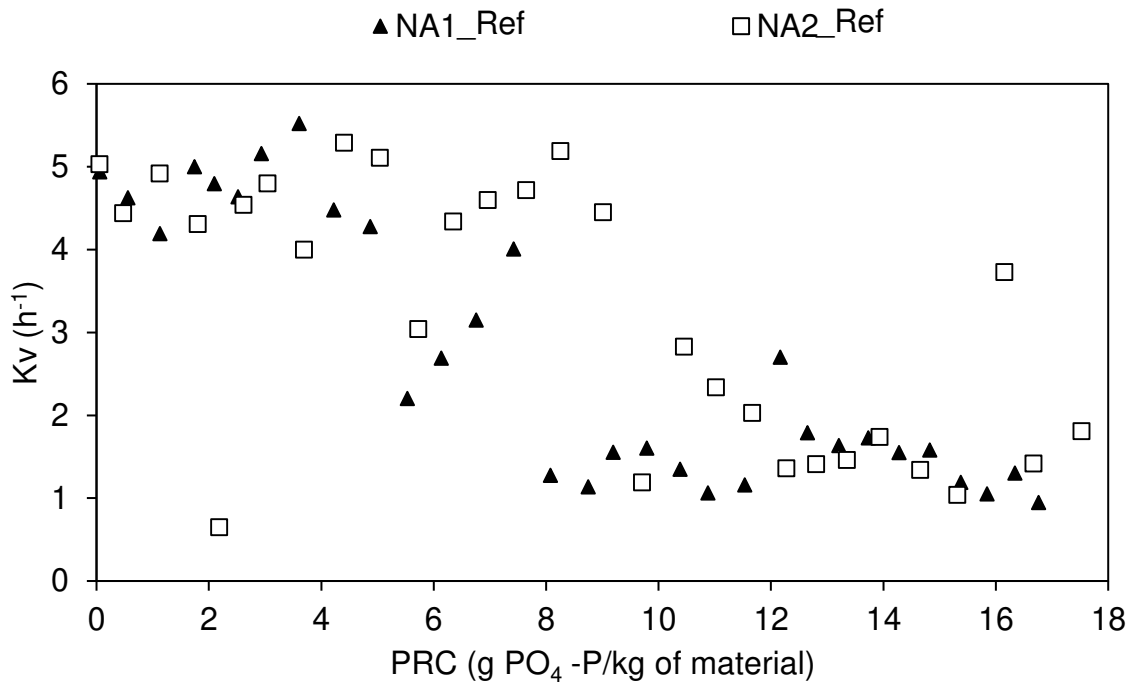


Fig. 5.2. 3. Evolution of the kinetic rate constant (according to the  $k\text{-}C^*$  model) with the media PRC for columns NA1\_Ref and NA2\_Ref.

In Fig. 5.2.4, both models,  $k\text{-}C^*$  and  $N\text{-}k\text{-}C^*$ , are compared in the case of the NA1\_Ref column. A significant difference of  $k_v$  parameters can be seen between the models for low PRC values ( $C^*$  close to zero). The  $N\text{-}k\text{-}C^*$  model presents a mean  $k_v$  of  $9.03 \text{ h}^{-1}$  compared to  $4.26 \text{ h}^{-1}$  for the  $k\text{-}C^*$  model. Such difference appears to be overcome in the pseudo-stabilisation stage where similar mean  $k_v$  values are obtained ( $1.64 \text{ h}^{-1}$  for  $N\text{-}k\text{-}C^*$  model and  $1.45 \text{ h}^{-1}$  for the  $k\text{-}C^*$  model). From both Fig. 5.2.4 and Table 5.2.6 one can see that the  $k\text{-}C^*$  model leads to a more conservative evolution of the model parameters than the  $N\text{-}k\text{-}C^*$  model.

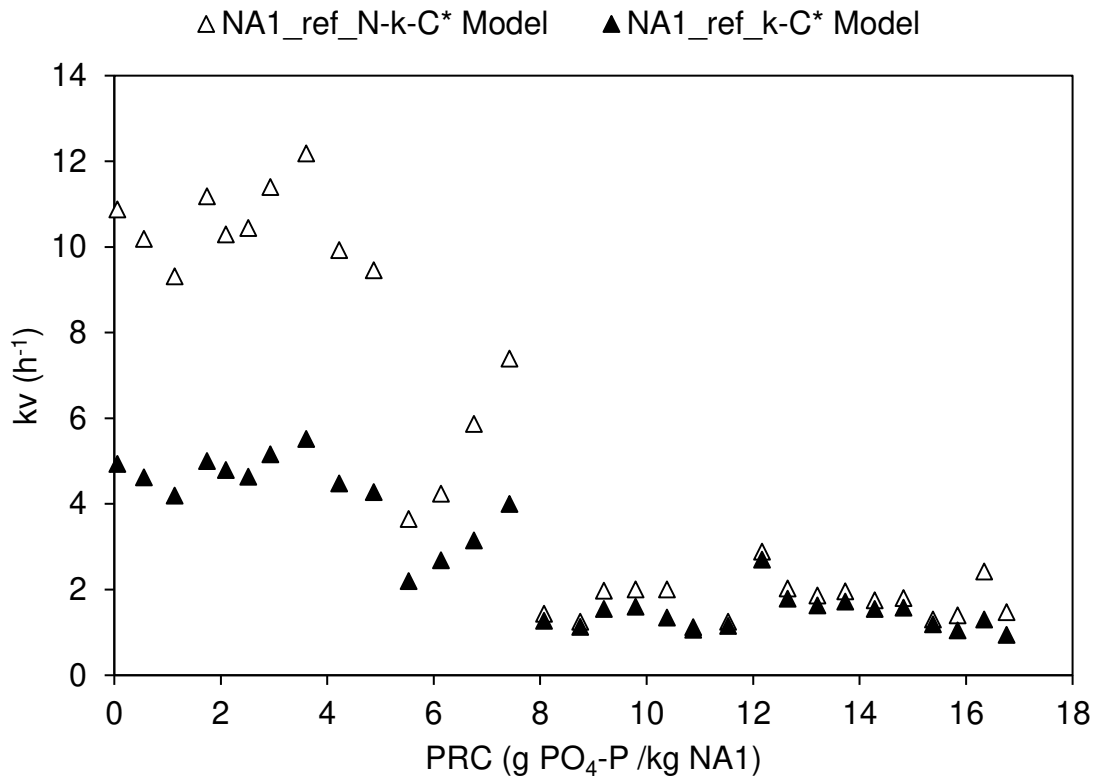


Fig. 5.2. 4. Evolution of the kinetic rate constant according to the N-k-C\* model and the k-C\* model with the media PRC for column NA1\_Ref.

Regarding C\*, Table 5.2.6 presents the background concentrations adjusted to the N-k-C\* and/or the k-C\* models for columns NA1\_Ref and NA2\_Ref. It appears that outlet concentrations below 1 mg PO<sub>4</sub> -P/L up to a PRC of approximately 11 and 15 g PO<sub>4</sub>-P/kg material for NA1\_Ref and NA2\_Ref, respectively. However, for higher PRC values C\* above 2 mg PO<sub>4</sub>-P/L are possible. Nevertheless, due to the short retention time in the columns (around 2 h) it is not easy to transpose such results for full-scale systems where higher hydraulic retention times may lead to different retention mechanisms (formation of different CaP phases and/or different rate-limiting steps). It is a specific and important aspect that would need to be precise in the future to better define design and guarantee low outlet P concentrations.

Table 5.2. 6. Estimation of the  $C^*$  value from experimental data from laboratory columns NA1\_Ref and NA2\_Ref according to N-k- $C^*$  model and/or k- $C^*$  model.

NA1_Ref			NA2_Ref	
N-k- $C^*$ Model (N = 5.5)		k- $C^*$ Model	k- $C^*$ Model	
PRC (g PO <sub>4</sub> -P /kg )	C* (mg PO <sub>4</sub> -P/L)	C* (mg PO <sub>4</sub> -P/L)	PRC (g PO <sub>4</sub> -P /kg)	C* (mg PO <sub>4</sub> -P/L)
0.05	0	0	0.05	0
10.9	0	0.33	15.3	0.80
11.5	0.45	0.75	17.5	2.00
15.8	1.9(*)	1.21(*)		

(\*) Poor estimation.

Fig. 5.2.5 presents the evolution of the kinetic coefficient for NA1 according to the different environmental conditions set (Ca concentration and biomass growth). For the NA1\_Ca column, the lower inlet calcium concentrations led to a more gradual reduction of the kinetic rate coefficient from the beginning of the experiment (low PRC values) unlike the NA1\_Ref column which remained relatively stable at high values up to around 6.5 g PO<sub>4</sub>-P/kg NA1. As a result, the pseudo-stable stage of NA1\_Ca is attained at a lower PRC than NA1\_Ref (approximately at 6 g PO<sub>4</sub>-P/kg NA1 against 8 g PO<sub>4</sub>-P/kg NA1 for the NA1\_Ref column), however,  $k_v$  appears to stabilize at similar values.

Inlet calcium concentrations of the NA1\_Ca column were high enough to allow HAP precipitation (Ca/P = 1.67). However, a reduced calcium concentration affects the supersaturation of the solution, which in turn reduces the kinetic rate of the reaction. The mean inlet Ca/P molar ratios were, indeed,  $3.5 \pm 0.7$  for NA1 and  $2.0 \pm 0.2$  for NA1\_Ca as shown in table 5.2.1. Nevertheless, the actual Ca/P ratio affecting the precipitation can increase inside the column due to the dissolution of the calcareous material from the gangue. Such dissolution-reprecipitation of calcium as calcium phosphates could have smoothed the impact of a calcium deficient solution on the kinetic rates, especially during the initial stage when most of Ca-containing phases dissolve. The effect of a calcium deficient solution in precipitation during the stabilization phase could not be evaluated.

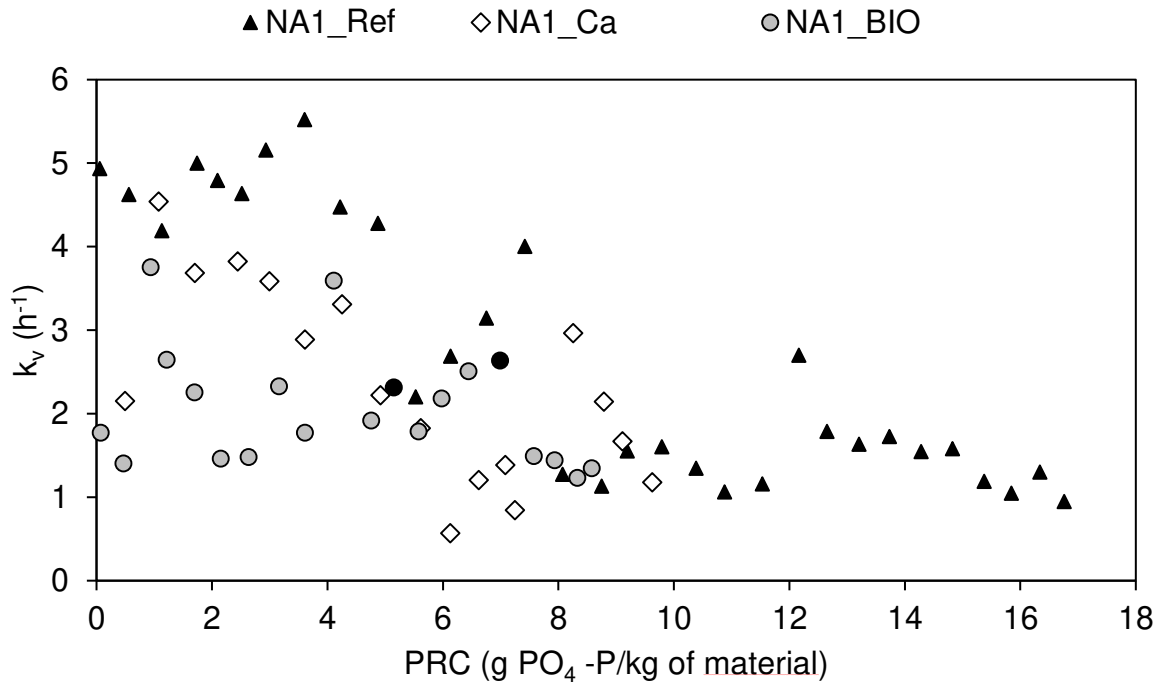


Fig. 5.2. 5. Evolution of the kinetic rate constant (according to the  $k-C^*$  model) with the media PRC for columns NA1\_Ref, NA1\_Ca, NA1\_Bio.

In the case of the column using treated wastewater, NA1\_bio, the evolution of  $k_v$  with PRC appears to be lower than under NA1\_Ref conditions contrasting to close to zero outlet concentrations for the NA1\_Bio column along the whole PRC range of the experiment (See Fig.S.5.2.6 of Supplementary Information). To limit the organic load (from values up to 130 to 40 g DCO/m<sup>2</sup>/d), the flow rate of this column was reduced to 5 L/day instead of 10 L/day thus increasing the retention time. When determining kinetic rate coefficients based on inlet/outlet concentrations, the HRT affects the calculation of  $k_v$ . It is not possible to know whether the column retained phosphorus on the first column layers, which would result in high kinetic rate coefficients, or whether P concentration gradually decreased with the HRT (lower  $k_v$  values). Two kinetic measurements were carried out by internal sampling on the NA1-Bio column revealing kinetic rate coefficients in the same range as the NA1\_Ref column (black dots in Fig. 5.2.5). Such results, in addition to the similar  $k_v$  values to NA1-Ref in the stabilization region, suggest that the effect of wastewater and biomass development is limited in the PRC range and operational conditions considered.

#### 5.2.3.5. SEM observation of calcium phosphate precipitates

At the end of the experiments, solid samples were taken close to the top (inlet) and close to the bottom (outlet) from columns NA1\_Ref and NA2\_Ref. The samples were observed and analysed by SEM-EDXS in order to identify the precipitates formed. The micrographs revealed the presence of a deposit formed on the surface of both substrates for those samples taken close to the inlet of the system (lines-scans of EDXS analyses are available in Supplementary Information).

In NA1 (Fig. 5.2.6.a), the more superficial layer is constituted of a structured precipitate with a Ca/P molar ratio of approximately 1.5, characteristic of amorphous calcium phosphate (ACP) and tricalcium phosphate (TCP). However, the precipitate is more likely to be ACP since the Kikuchi lines characteristics of crystallised phases could not be observed in the backscattered SEM images. The ACP layer formed at the surface of apatite particles directly exposed to the solution and onto the clay gangue. In the presence of the clay gangue, phosphorus was first retained inside the clay: P ions diffuse into the clay where the oxides and hydroxides of aluminium and iron, as well as small embedded particles of apatite, would likely act as specific sorption sites leading to further precipitation of phosphates as ACP (Ca/P =1.5).

A comprehensive micrograph of this phenomenon is shown in Fig. 5.2.6.b). The particles in light grey represent the apatite particles and, surrounding them, a darker grey edge signals the presence of the clay gangue. The layers of the structured precipitate can be seen on the right of the image in a grey level close to that of the FAP particles. Below the structured ACP layers, the clay gangue is lighter but it turns to a darker grey level to the left of the image, thus illustrating the diffusive phenomenon into the clay. One can also observe that the particles on the left, wrapped in the clay gangue, were not in contact with the solution and therefore no precipitate was formed, i.e. the precipitation onto the apatite particles is limited by the presence of the clay gangue.

In NA2 samples, only the structured layer was identified also corresponding to ACP precipitates (Fig. 5.2.7). Since clay concentration in the NA2 substrate is much less significant, the precipitate is directly formed onto the surface of the apatite particles. Therefore, the presence of the gangue in the NA1 substrate may be the reason of lower performances and kinetic rates than in NA2.

The mean thickness of the structured ACP layer in the samples close to the inlet for both substrates is approximately 30 $\mu$ m.

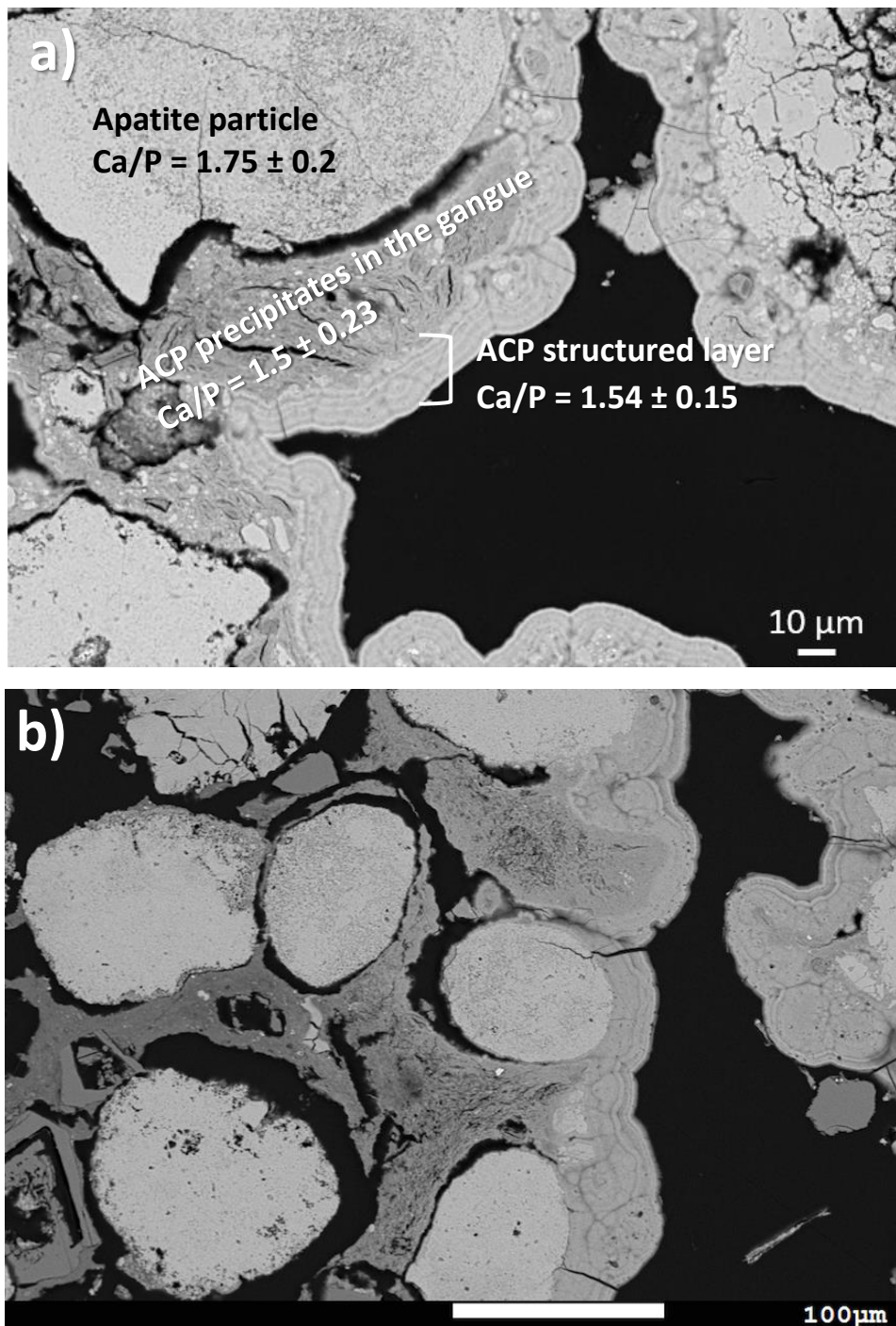


Fig. 5.2. 6. Typical SEM micrographs in the back-scattered mode of the samples taken from column NA1\_Ref close to the inlet of the system. Image a) shows the different layers above the carbonated fluorapatite ( $\text{Ca/P} = 1.75$ ), where phosphorus is retained: one corresponding to the clay part where ACP is formed ( $\text{Ca/P} = 1.5$ ) and the layer above it corresponding to a structured ACP precipitate ( $\text{Ca/P} = 1.54$ ). Image b) illustrates the diffusion of phosphorus in the clay and the isolation of apatite particles surrounded by the gangue. The different solid phases and layers are identified in the image by the different levels of grey.

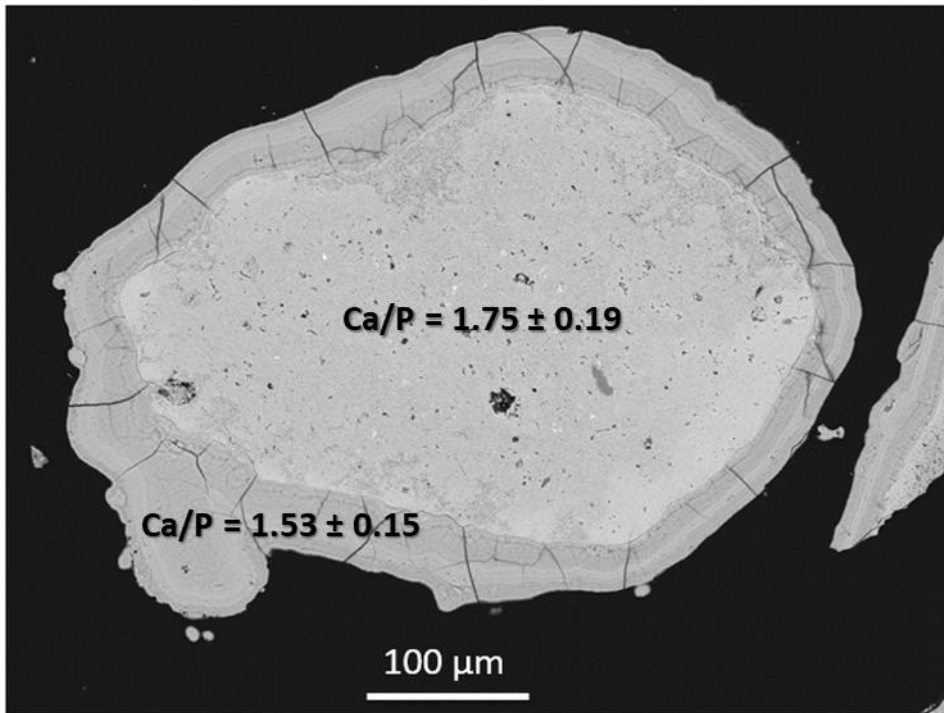


Fig. 5.2. 7. Typical SEM micrographs in the back-scattered mode of the samples taken from column NA2 showing a precipitate formed directly onto the surface of the carbonated fluorapatite with a Ca/P ratio of 1.53 corresponding to ACP. The different solid phases and layers are identified in the image by the different levels of grey.

Neither the NA1\_Ref nor the NA2\_Ref samples taken from the bottom of the columns and analysed by SEM-EDXS showed the formation of precipitates.

To analyse the evolution of phosphorus retention with the HRT one can observe the evolution of the solution Ca/P molar ratio retained between two consecutive sampling points in the column (Table 5.2.7), calculated as shown in Eq. 5.2.8.

$$\left(\frac{Ca}{P}\right)_{retained} = \frac{[Ca^{2+}]_i - [Ca^{2+}]_{i+1}}{[PO_4-P]_i - [PO_4-P]_{i+1}} \quad [5.2.8]$$

Where  $[Ca^{2+}]_i$  and  $[PO_4-P]_i$  are the calcium and phosphorus molar concentrations at the  $i^{th}$  sampling point and  $[Ca^{2+}]_{i+1}$  and  $[PO_4-P]_{i+1}$  are the calcium and phosphorus molar concentrations at the consecutive ( $i^{th}+1$ ) sampling point.

It can be seen that the retained Ca/P molar ratio shows a general tendency to evolve from higher to lower values along both the NA1\_Ref and NA2\_Ref columns with increasing HRT. This can be related to a decreasing supersaturation of the solution with HRT as calcium phosphates are being retained. Such supersaturation reduction causes in turn less calcium phosphate precipitation. In addition, it seems that a front of

calcium phosphates retention travels from the surface of the column to lower depths, as the PRC increases (values in bold in Table 5.2.7). Such evolution suggests that the kinetic rate of the calcium phosphate retention is decreasing in the first sections where the PRC is higher, allowing more calcium and phosphate ions to reach lower sections of the column with enough supersaturation to precipitate.

At high PRCs, as shown in the NA2\_Ref column (Table 5.2.7) the first two sections of the column are still active with retained Ca/P ratios relatively high. However, from the third section (from 8 cm deep to the bottom), results show Ca/P molar ratios higher than those of the previous section or even negative Ca/P accounting for some dissolution. Even though the phosphorus concentration along the column always decreases with the HRT, the calcium concentration varies along the column, sometimes retaining and sometimes releasing the ions (Fig. S.5.2.9 of Supplementary Information). Such behaviour also involves calcite and dolomite equilibria, showing unsaturated conditions at certain depths of the column and at different PRC. Indeed, the evolution of Ca, Mg and bicarbonates concentration with the HRT shows the occurrence of dissolution and reprecipitation processes inside the bed (Fig. S.5.2.7). Finally, the absence of precipitates in the bottom samples analysed by SEM-EDXS, may be explained by the formation of little amounts of amorphous calcium phosphates that re-dissolve with unstable solution conditions (supersaturation - unsaturation).

Table 5.2. 7. Evolution of the retained Ca/P molar ratio in solution with increasing hydraulic retention time (phosphorus inlet concentration around 15 mg PO<sub>4</sub>-P/L). The retained Ca/P ratio is calculated as the calcium concentration difference between two sampling points divided by the phosphorus concentration difference between the same two sampling points. The shaded values indicate calcium phosphate retention.

	NA1_Ref Column			NA2_Ref Column		
<b>PRC (g PO<sub>4</sub>-P/kg material)</b>	8.1	8.8	10.9	9.7	15.1	17.2
<b>0 – 4 cm depth</b>	<b>1.22</b>	<b>2.53</b>	<b>2.42</b>	<b>1.65</b>	<b>1.38</b>	<b>2.01</b>
<b>4 – 8 cm depth</b>	<b>0.27</b>	<b>1.16</b>	<b>1.71</b>	<b>0.81</b>	<b>1.54</b>	<b>2.37</b>
<b>8 – 12 cm depth</b>	0.00	<b>0.64</b>	<b>1.12</b>	<b>1.13</b>	0.00	-4.31
<b>12 – 16 cm depth</b>	-0.36	-0.05	<b>0.07</b>	<b>0.35</b>	<b>1.15</b>	<b>6.21</b>
<b>16 – 20 cm depth</b>	-0.84	-0.68	0.00	-1.05	<b>0.40</b>	<b>1.06</b>

### 5.2.3.6. Hydraulic performance

The use of natural apatite with a fine particle size distribution may induce a premature clogging. In order to measure the loss of hydraulic performance, permeability tests were conducted in the columns before and after the experiments. Results can be seen in Table 5.2.8. It shows no significant variations of the hydraulic conductivity since the values before and after the experiment remain of the same order of magnitude. Indeed, the diminution of the hydraulic conductivity over the time of the experiment is less important than the experimental uncertainty. The variation of the permeability between the different sections of the columns (Table 5.2.9) is not significant either. One can conclude that the deposit cumulated (thickness of precipitates ~ 30µm) or the biomass development (NA1\_bio), considering the PRC achieved for each column, did not cause any significant loss of hydraulic conductivity.

Table 5.2. 8. Hydraulic conductivity of the filtering bed determined by the constant head permeability test before and after the experiment for all the columns of the study.

Hydraulic conductivity (m/s)	NA1_Ref	NA1_Ca	NA1_Bio	NA2_Ref
<b>Before experiment</b>	$1.2 \cdot 10^{-4}$	$1.2 \cdot 10^{-4}$	$1.2 \cdot 10^{-4}$	$4.2 \cdot 10^{-4}$
<b>After experiment</b>	$2.0 \cdot 10^{-4}$	$4.1 \cdot 10^{-4}$	$4.0 \cdot 10^{-4}$	$7.6 \cdot 10^{-4}$

Table 5.2. 9. Evolution of the hydraulic conductivity inside the filter at different depths. Measures are taken at the piezometers and therefore the conductivity is measured for the column section between piezometers at the end of the experiments.

Hydraulic conductivity (m/s)	NA1_Ref	NA1_Ca	NA1_Bio	NA2_Ref
<b>4 cm – 8 cm</b>	$1.5 \cdot 10^{-4}$	$5.2 \cdot 10^{-4}$	$4.7 \cdot 10^{-4}$	$6.1 \cdot 10^{-4}$
<b>8 cm – 12 cm</b>	$2.9 \cdot 10^{-4}$	$3.8 \cdot 10^{-4}$	$4.0 \cdot 10^{-4}$	$8.6 \cdot 10^{-4}$
<b>12 cm – 16 cm</b>	$2.7 \cdot 10^{-4}$	$5.4 \cdot 10^{-4}$	$5.6 \cdot 10^{-4}$	$8.1 \cdot 10^{-4}$

### 5.2.4. Conclusions

The natural apatites NA1 and NA2 have shown great potential for phosphorus retention from wastewater. The retention capacity attained at the end of the experimental time was 16.8 and 17.5 g PO<sub>4</sub> -P/kg for the NA1\_Ref and NA2\_Ref columns, respectively.

However, the maximum phosphorus retention capacity was not achieved in both cases. High kinetic rate coefficients are observed for the columns both during the initial stage and the pseudo-stabilisation stage. For the latter, the attained values were 1.45 and  $1.70\text{h}^{-1}$  for NA1\_Ref and NA2\_Ref, respectively, when they were evaluated through the  $k\text{-}C^*$  model (more conservative results). The kinetic rate is slightly affected by calcium deficient solutions during the initial stage most probably because of calcium dissolution from the substrate. The impact of low calcium inlet concentrations during the precipitates growth could not be assessed. Regarding the column fed by real treated wastewater effluent, NA1\_Bio, the phosphorus retention performance is  $\geq 99\%$  for the whole PRC range of study. The kinetic rate coefficients determined by internal samplings are in the same range as those for NA1\_Ref and the evolution of  $k_v$  appears to stabilize at similar values as well. Hence, biomass development appears to have little impact on P retention for the PRC range considered. Regarding  $C^*$ , the parameter increases with time but it remains below  $1\text{ mg PO}_4\text{-P/L}$  up to 11 and  $15\text{ g PO}_4\text{-P/kg}$  for NA1 and NA2, respectively. However, defining the evolution of  $C^*$  with increasing PRCs and with longer HRTs would be necessary to better precise design and guaranteed outlet concentrations.

SEM images showed the formation of a precipitate in the samples taken close to the inlet of the columns. The presence of a clay gangue in NA1 substrate allowed some CaP retention within the clay layer, too. Then a structured layer of amorphous calcium phosphate was able to grow onto the clay gangue and the surface of apatite particles. For the NA2 substrate, with very little amount of clay gangue, phosphorus retention was achieved by the precipitation of amorphous calcium phosphate directly on the apatite surface. Finally, neither chemical nor biological clogging was observed considering the PRCs attained. Besides, the loss of hydraulic conductivity was not significant in any column.

In conclusion, the retention of phosphorus from wastewater by apatite filters seems to be a promising solution for small wastewater treatment plants. However, scaled up experiences with real wastewater are required to ensure the design.

## 5.2.5. Supplementary information

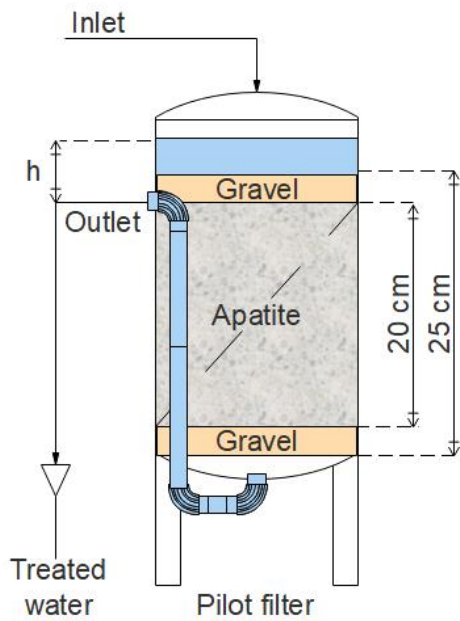


Fig. S.5.2. 1. Experimental column setup

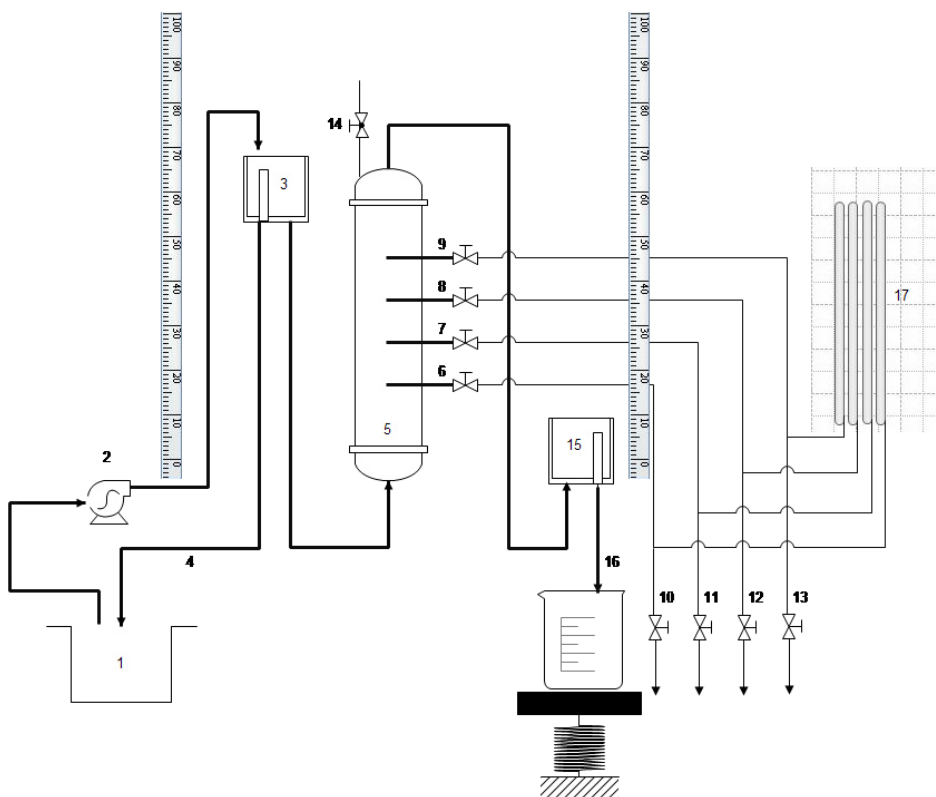
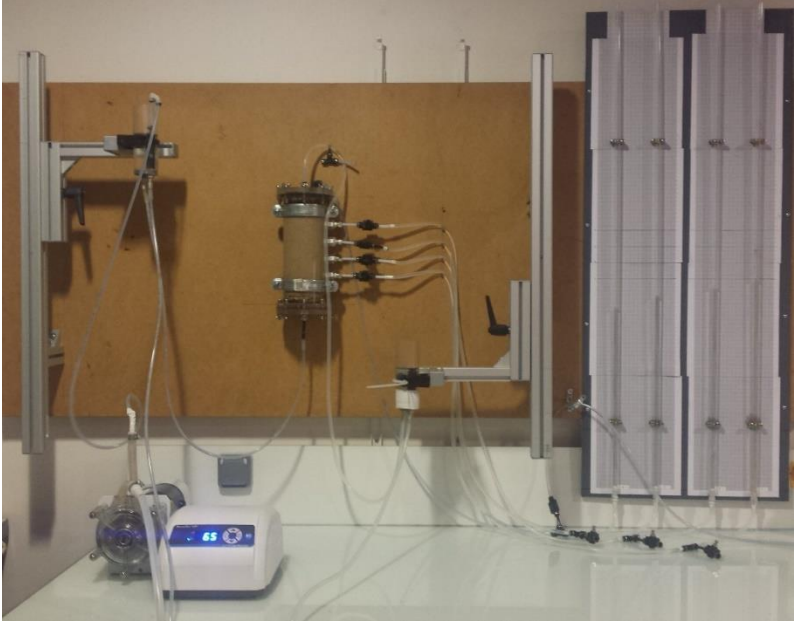


Fig. S.5.2. 2. Scheme of the constant head permeability test setup: 1) feeding tank, 2) peristaltic pump, 3) upper reservoir, 4) Overflow drain for upper reservoir, 5) column, 6-9) sampling points with valves, 10-13) valves for air release, 14) column air purge valve, 15) lower reservoir, 16) Flow measuring point and 17) piezometers.



*Fig. S.5.2. 3. Photograph of the experimental setup used for the constant head permeability test.*

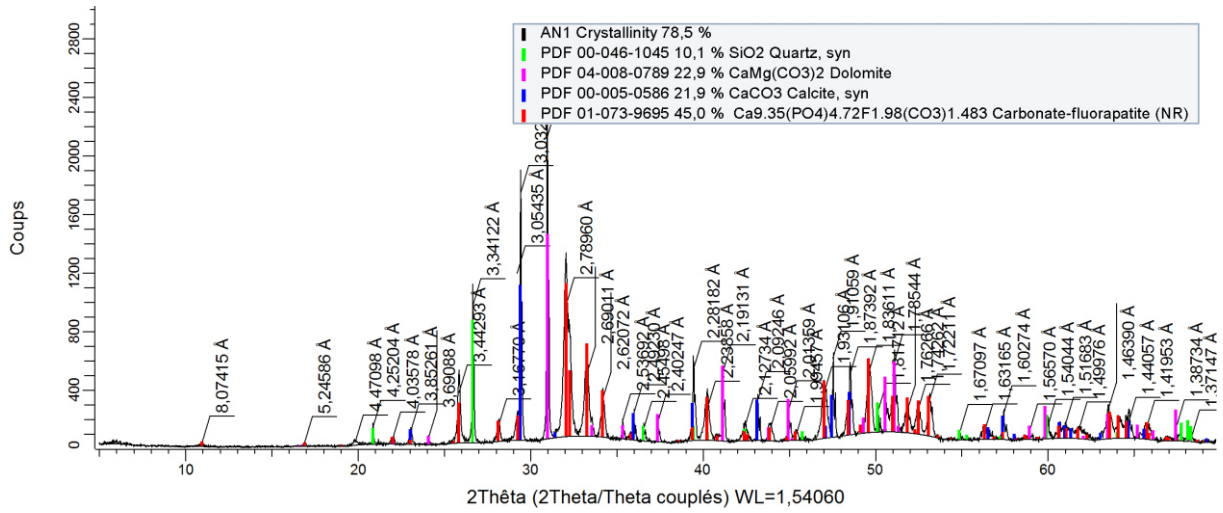


Fig. S.5.2. 4. XRD spectrum of the NA1 substrate

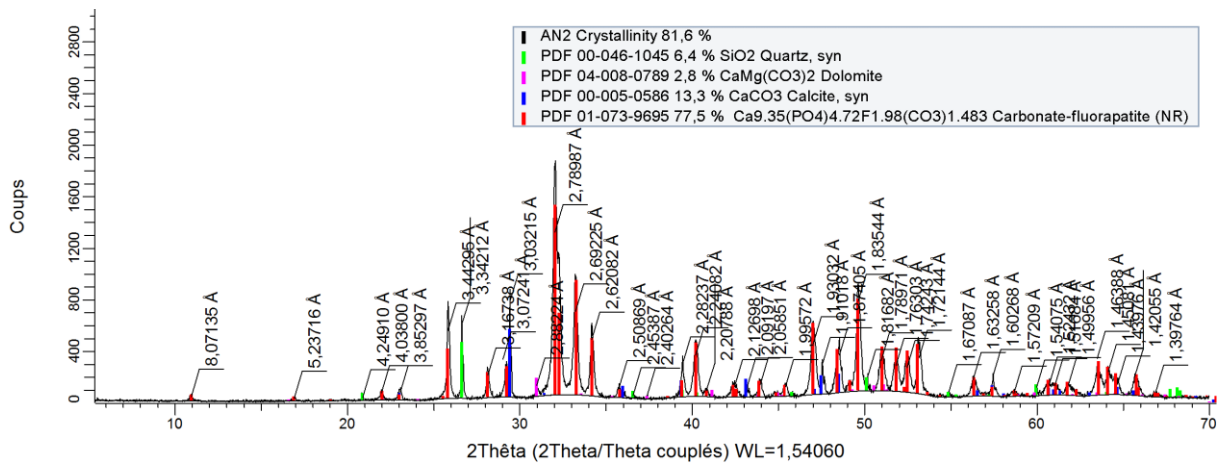


Fig. S.5.2. 5. XRD spectrum of the NA1 substrate

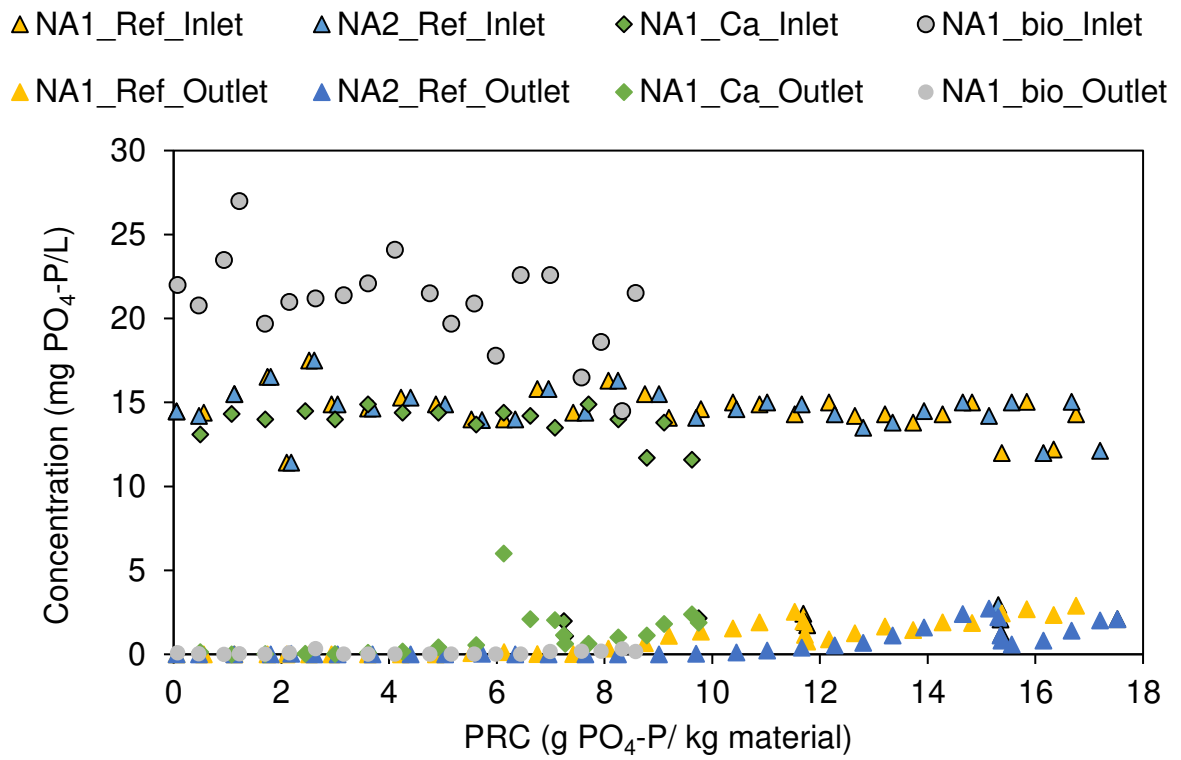


Fig. S.5.2. 6. Inlet and outlet phosphorous concentration for all the columns of the study.

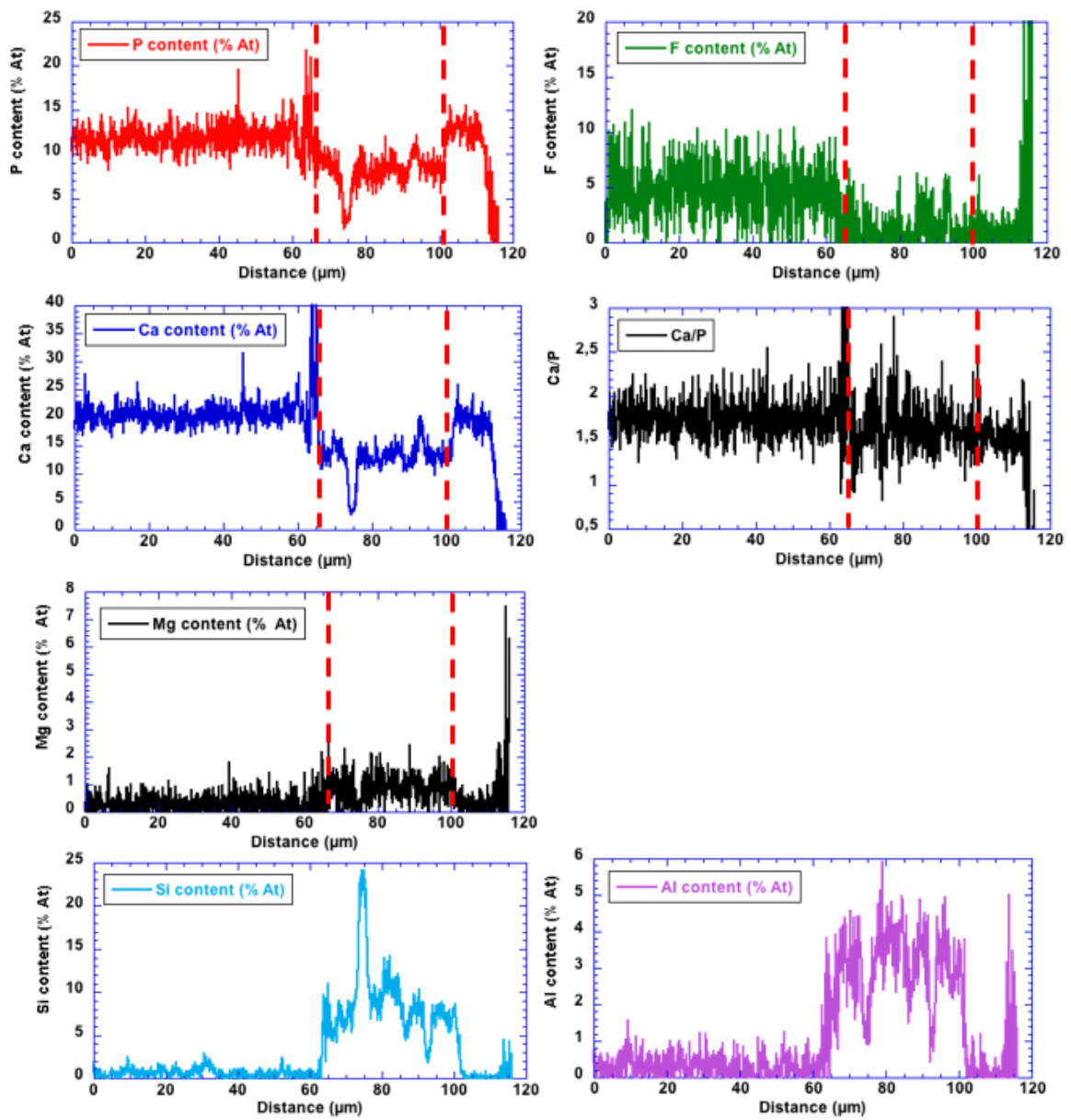
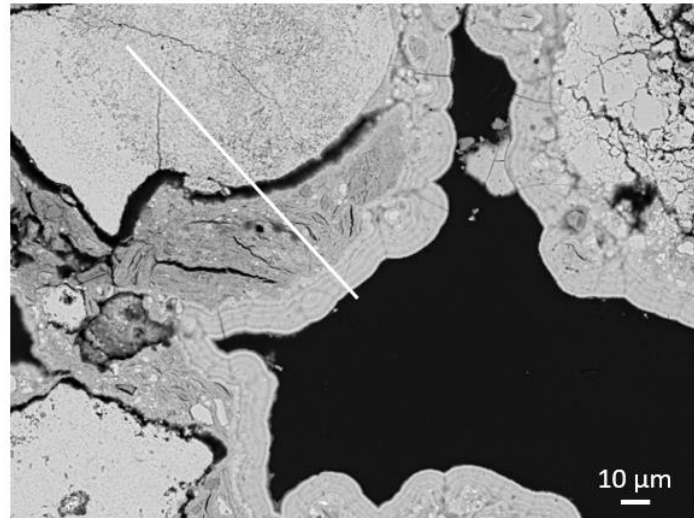


Fig. S.5.2. 7. Line-scan of the different elements analysed by EDS for the sample taken at the top of the NA1\_Ref column (close to the inlet).

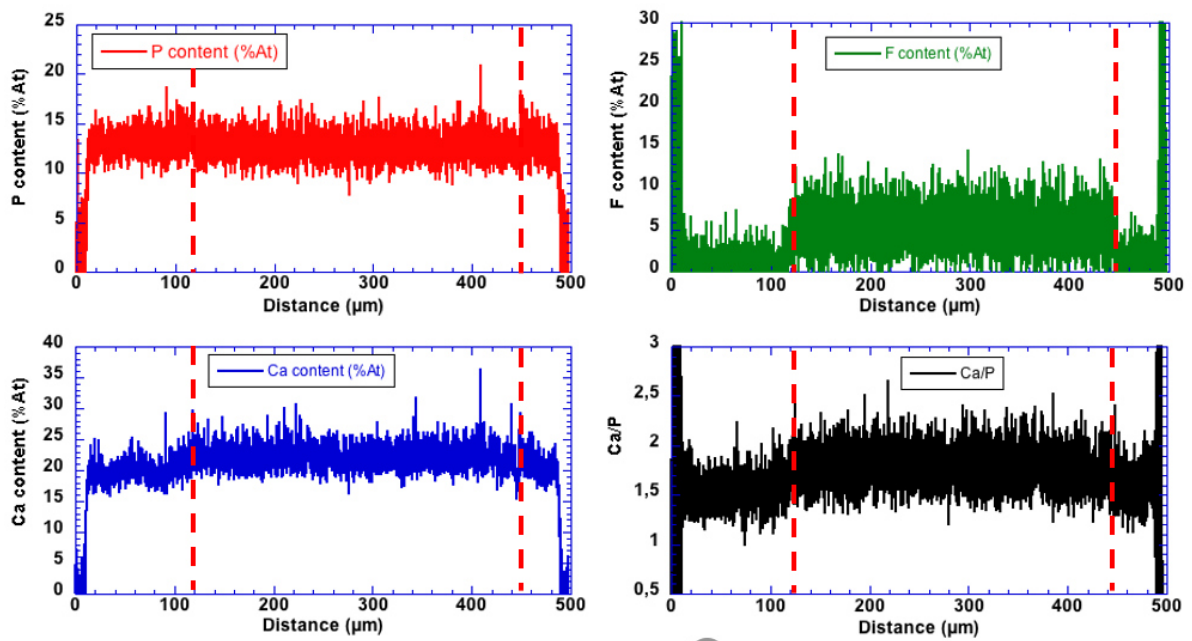
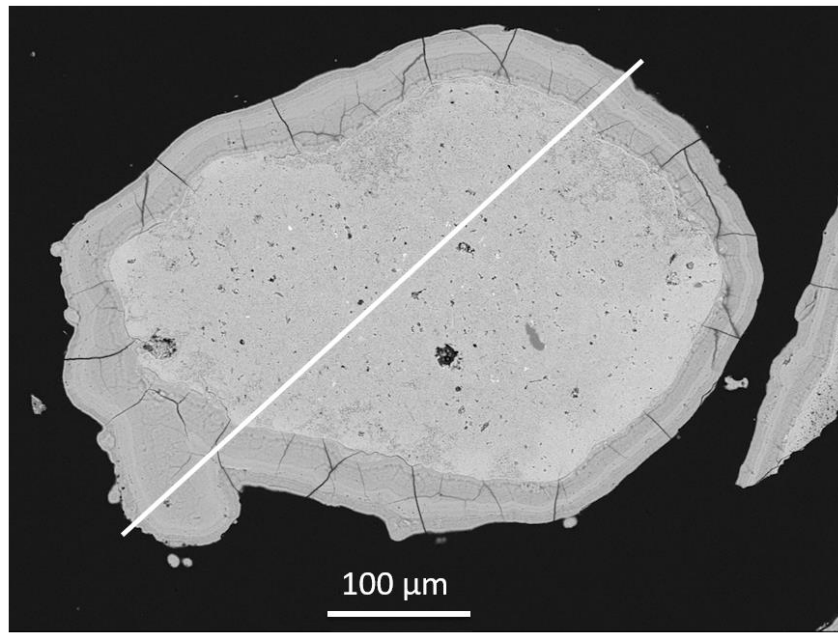


Fig. S.5.2. 8. Line-scan of the different elements analysed by EDS for the sample taken at the top of the NA2\_Ref column (close to the inlet).

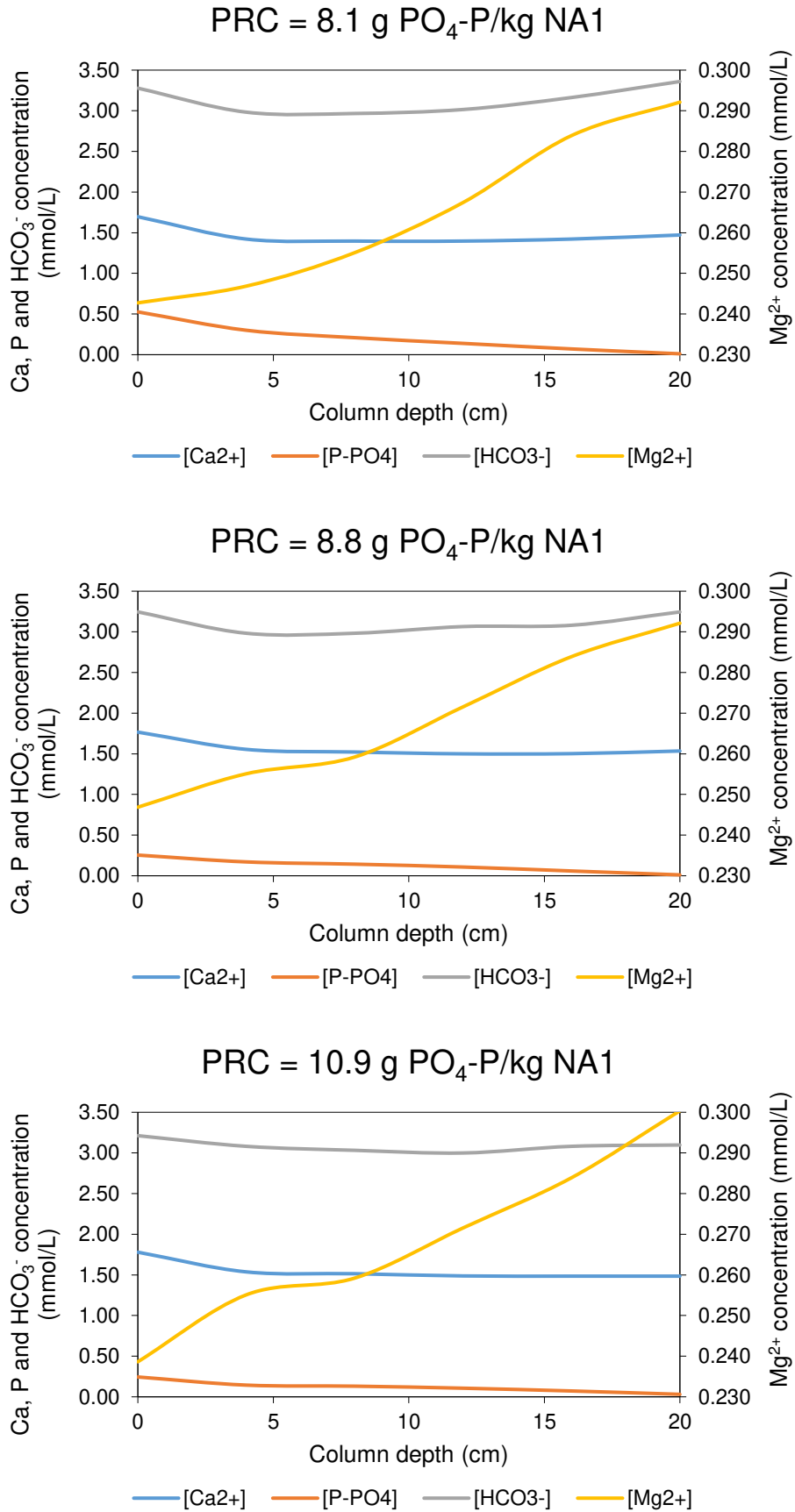


Fig. S.5.2. 9. Evolution of some anions and cations concentration along the column NA1\_Ref at different specific average PRCs. The plots manifest the dissolution and reprecipitation processes involving calcite, dolomite and calcium phosphates

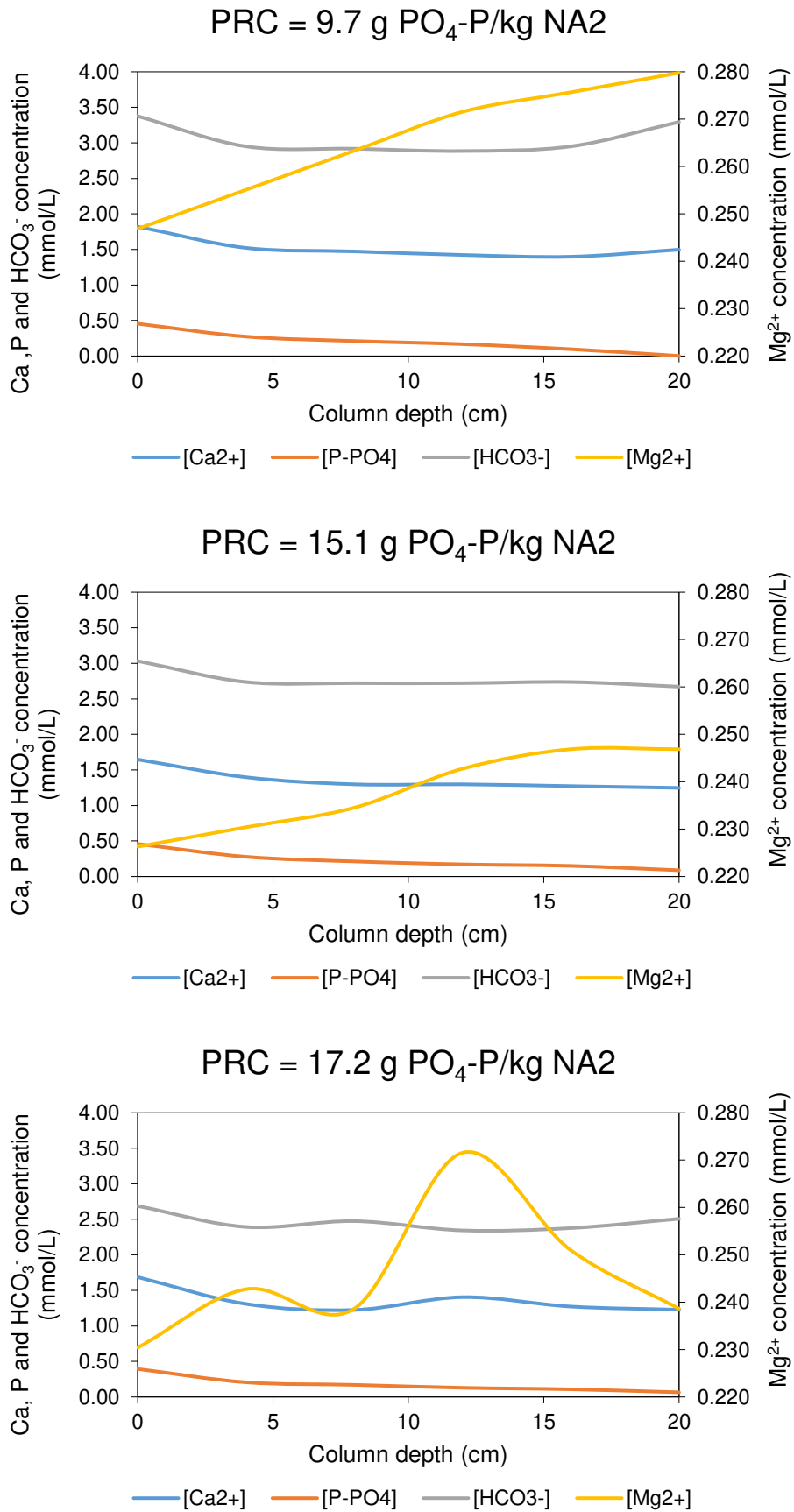


Fig. S.5.2. 10. Evolution of some anions and cations concentration along the column NA2\_Ref at different specific average PRCs. The plots manifest the dissolution and reprecipitation processes involving calcite, dolomite and calcium phosphates

### 5.3. Article 4. Modelling

## **Geochemical and hydrodynamic characterisation of fixed-bed apatite columns for phosphorus retention modelling**

**L. Delgado<sup>a,b</sup>, N. Forquet<sup>a</sup>, D. Blanc<sup>c</sup>, M. Gautier<sup>c</sup>, P. Molle<sup>a</sup>**

<sup>a</sup>INRAE, REVERSAAL Research Unit, 5 rue de la Doua, 69100 Villeurbanne, France

<sup>b</sup>Synteia, 12 rue Toussaint Fléchaire, 84510, Caumont sur Durance, France

<sup>c</sup>Univ Lyon, INSA Lyon, Laboratoire DEEP, 69621 Villeurbanne France

**Corresponding author:** [laura.delgado-gonzalez@inrae.fr](mailto:laura.delgado-gonzalez@inrae.fr)

### **Abstract**

A geochemical and hydrodynamic characterisation of a fixed-bed apatite column is presented in order to provide the basis for the development of a mechanistic model of phosphorus retention from wastewater using the HP1 module of Hydrus-1D software. The mineralogical assemblage was properly modelled using batch pH leaching tests. The estimation of the dispersion was carried out by inverse modelling based on experimental data from tracer test experiments. An exploratory test was carried out to determine the modelling capabilities solely of based on the thermodynamics of dissolution/precipitation reactions. Simulations showed that a pure thermodynamic model could not properly describe the process indeed. Phosphorus retention on apatite filters requires the development of a more complex mechanistic model involving kinetic reactions like amorphous calcium phosphate precipitation.

**Keywords:** hydraulics, mineral assemblage, phosphates removal, PHREEQC, porous media, reactive filter

### 5.3.1. Introduction

The use of natural apatite filters for phosphorus retention from treated wastewater has shown to be a promising technology for small wastewater treatment plants (WWTPs) (Chapter 5.2). The use of laboratory column experiments for the assessment of performances and retention capacities of a material allows to define the kinetics of the process and the removal potential under the environmental conditions tested. However, when scaling-up the process, results may differ from those of laboratory columns mostly due to the differences in flow conditions and in the particular chemistry of the effluent. The development of a mechanistic model could be a tool to explore and predict the effects of different operating conditions we can find in real environment, as well as an optimization tool for the design of the full-scale filters based on the specific chemistry of the effluent. The most common issues of mechanistic models derive from the use of too many or immeasurable fitting parameters. Reducing the number of fitting parameters and using easily measurable ones will help to avoid uncertainties in predicting new operating conditions.

In this work, a geochemical and hydrodynamic characterisation of a fixed-bed apatite column is presented in order to provide the basis for the development of a mechanistic model using the HP1 module of Hydrus-1D software (Šimůnek et al. 2013). The HP1 module couples Hydrus-1D capability for simulation of convective, dispersive and diffusive transport in porous media with the capacity of PHREEQC (Parkhurst and Appelo 1999 ) for modelling geochemical reactions. To our knowledge the HP1 has never been used for the modelling of phosphorus retention in fix-bed columns.

For this a preliminary characterisation of the filter bed matrix and the hydrodynamics of the process is required. A geochemical characterisation of the substrate involves the modelling of a simplified mineralogical assemblage of the solid matrix. Such mineralogical assemblage is carried out by the simulation of batch leaching tests based on aqueous solution/mineral equilibrium using the PHREEQC program. Hydraulic is fitted with Hydrus-1D software under hydraulic saturated conditions. The data from an experimental tracer test carried out on the laboratory columns is used to determine the model parameters describing the hydrodynamics of the system.

In a previous work (Chapter 5.2), experiments conducted in laboratory columns filled with natural apatites and fed with a synthetic phosphate solution showed that phosphorus retention occurred via the formation of amorphous calcium phosphate (ACP) on the surface of the material. The apatite acts as a catalyser reducing the activation energy of the reaction (Joko 1984). The more alike are the composition of the seed and the precipitate the greater is the catalysing effect. The thermodynamics of the process are governed by the most stable calcium phosphate, which is the hydroxyapatite (HAP). However, the precipitation of HAP is not straightforward and involves the formation of more soluble precursor phases like ACP (Nancollas and Mohan 1970, Meyer and Eanes 1978, Mañas et al. 2012). The formation of such precursors is governed by the kinetics of the process. In the laboratory columns, the low hydraulic retention times used (1.8 hours) would not allow the transformation of the amorphous calcium phosphate into HAP. Montastruc et al. (2003) determined that retention times between 225 and 400 min would be necessary at neutral pH (7 - 8) for such transformation.

Calcium phosphate heterogeneous precipitation in a complex liquid matrix as wastewater entails, indeed, a system of great complexity (Montastruc et al. 2003). The calcium-phosphates have many polymorphs (Hermassi et al. 2015), phosphates react with a great variety of metals, precipitating and/or co-precipitating and admitting isomorphous substitutions. Indeed, phosphorus retention mechanisms are not yet fully understood (Herrmann et al. 2013).

The experimental data provided by previous work on laboratory columns could not provide the kinetic information required for the modelling of the process. Therefore, a pure thermodynamic modelling based on dissolution/precipitation reactions is here explored, in order to identify some of the issues and limits of the HP1 tool for the modelling of phosphate retention in apatite filters.

### 5.3.2. Material and methods

#### 5.3.2.1. Substrate

A natural apatite product referred to as NA1 was selected to conduct a preliminary modelling study. The physical and mineralogical characterisation of the substrate has already been presented in a previous work (Chapter 5.2) where a full description of the characterisation methods applied can also be found. The particle size distribution and specific density of the NA1 substrates are  $0.6/2$  ( $d_{10}/d_{60}$ ), and  $2.7 \text{ g/cm}^3$ , respectively. The resulting porosity and saturated hydraulic conductivity of the filtering bed are 54% and  $2 \cdot 10^{-4} \text{ m/s}$  respectively. The major mineral phases present in the substrate are fluorapatite, calcite, dolomite, quartz and montmorillonite.

Elemental analysis of major species was carried out by alkaline fusion ( $\text{LiBO}_2$ ) followed by acid digestion ( $\text{HNO}_3$ ) and subsequent analyses of the solutions by inductively coupled plasma optic emission spectrometry (ICP-OES) (iCap6500, Thermo Scientific). Tracer elements were also analyzed by inductively coupled plasma mass spectrometry (ICP-MS) (CP-MS iCapQ, Thermo Scientific). The fluorine concentration is analysed using an ion selective electrode (ISE). Chlorine was measured with a UV spectrometry (470nm) (Agilent CARY60). Finally, to analyse total sulphur and total carbon, the samples were heated by induction to approximately  $1450^\circ\text{C}$  and then analysed using an infrared analyser (HORIBA EMIA 320-V2).

#### 5.3.2.2. Experimental leaching protocol

Batch pH-dependent leaching tests were conducted following the acid and base neutralization capacity (ANC-BNC) European standard method NF EN 14429. The method was applied in a representative ground sample of the substrate. The sample was reduced to a fine powder using a ball mill grinder (Retsch S100). The pH was varied from 2 to 12 by adding 2.0 M  $\text{HNO}_3$  and 5.0 M KOH solutions into 150 mL centrifuge tubes containing deionized water and approximately 15 g of sample to reach a final solid-to-liquid ratio of 10 g/mL. The essays were duplicated except for those at pH 6, 7, 8 and 9 (typical pH range in wastewater) which were triplicated. Blanks (no solid sample addition) were also carried at pH 3, 6 and 12. Once the acid and base solutions were added the tubes were agitated in a rotary shaker (Heidolph REAX 20)

set at 10 rpm for 48 h after what the pH was then measured for each suspension (Consort Multiparameter Analyser C3020). The tubes were then centrifuged (Fisher Scientific, SIGMA 4K15C) at 10,000 rpm for 10min. The supernatants were filtered at 0.45  $\mu\text{m}$  (Sartorius Minisart®) and stored at 4 °C before analyses.

#### 5.3.2.3. Leachates analyses

The leachates were analysed for anions concentration of F<sup>-</sup>, Cl<sup>-</sup>, SO<sub>4</sub><sup>2-</sup> and PO<sub>4</sub><sup>3-</sup> on filtered samples (0.22  $\mu\text{m}$ ) by ionic chromatography (Thermo Fisher ICS5000+) according to the standard method EN ISO 10304-1. Total inorganic carbon (TIC) was also measured. Finally, the total concentration of major and trace elements (Al, Ca, Cr, Fe, Mg, Na, P, S, Si, Sr and Zn) was determined by inductively coupled plasma optical emission spectroscopy (ICP-OES) (Ultima 2; Horiba Jobin Yvon SAS).

#### 5.3.2.4. Mineralogical Assemblage

The numerical simulation of batch leaching experiments was performed using the U.S. Geological Survey (USGS) computer program PHREEQC Interactive 3.0.6. The model developed is based on the precipitation-dissolution of mineral phases and the calculation of saturation index of the leaching solutions. The assemblage was optimized by comparing simulated curves to experimental data reiteratively. The Lawrence Livermore National Library (llnl) thermodynamic database supplied with PHREEQC was used for solubility products and dissolution reactions of mineral phases. A previous identification of the mineral phases present was carried out by X-ray diffraction (XRD) and by scanning electron microscopy energy dispersive X-ray spectroscopy (SEM-EDXS). The methodology applied and the results of these measurements can be found in a previous work (Chapter 5.2). This multi-technique approach should enhance the geochemical representation of the substrate for modelling purposes (Bisone et al., 2016).

### 5.3.2.5. Experimental column

The experimental column set up is illustrated in Fig. 5.3.1. The column has a section area of 63.6 cm<sup>2</sup> and is filled (from top to bottom) with a transition gravel layer of 2.5 cm high (1/8, 99% quartz, Sibelco), 20 cm of the reactive substrate NA1 and then again 2.5 cm of the gravel transition layer.

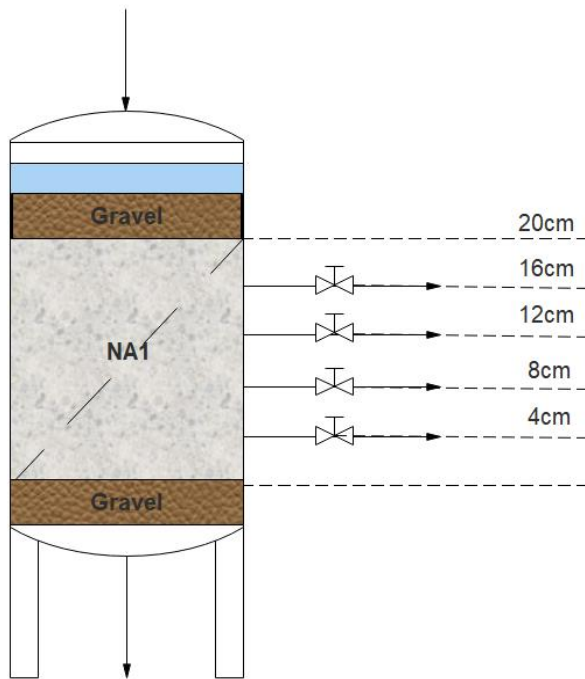


Fig. 5.3. 1. Experimental setup of laboratory columns filled with natural apatite NA1.

The column operates hydraulically saturated and is fed at  $9.4 \pm 1.9$  L/d with a synthetic solution ( $14.6 \pm 1.2$  PO<sub>4</sub>-P/L,  $64.4 \pm 11.7$  mg Ca/L). It was monitored for 230 days where cations (Ca<sup>2+</sup>, Mg<sup>2+</sup>, Na<sup>+</sup>, K<sup>+</sup>) and anions (Cl<sup>-</sup>, SO<sub>4</sub><sup>2-</sup>, PO<sub>4</sub><sup>3-</sup>) concentration were measured on a weekly basis at the inlet and outlet of the column by ionic chromatography (NF EN ISO 14911 and EN ISO 10304-1) (Metrohm, IC flex 930). Bicarbonates were also analysed by the titrimetric analytic method NF EN ISO 9963-1. Samples were also taken using the internal sampling points of the column at different moments of the experiment to follow the evolution of phosphorus concentration with the hydraulic retention time.

### 5.3.2.6. Tracer tests

A tracer test was carried out in the laboratory column: 10 cm<sup>3</sup> of a 5 mg/L fluorescein-tracer solution was introduced as a Dirac injection in the column measuring the tracer outlet concentration for 20 h with a GGUN-FL30 Fluorometer. The experimental data was used to fit the dispersion of the system in the hydraulic model.

#### 5.3.2.7. Hydraulic model

The hydraulic model is implemented by the Hydrus -1D program according to the Richards equation (Eq.5.3.1).

$$\frac{\partial \theta(h)}{\partial t} = \frac{\partial}{\partial x} \left[ K(h) \left( \frac{\partial h}{\partial x} + \cos \alpha \right) \right] - S(h) \quad [5.3.1]$$

where h is the water pressure head [L],  $\theta$  is the volumetric water content [L<sup>3</sup>L<sup>-3</sup>], t time [T], x is the spatial coordinate [L], S is the sink term [L<sup>3</sup>L<sup>-3</sup>T<sup>-1</sup>],  $\alpha$  is the angle between the flow direction and the vertical axis, and K is the unsaturated hydraulic conductivity [LT<sup>-1</sup>]. In hydraulically saturated conditions, the water content does not vary with pressure head but is equal to the bed porosity and the Darcy's equation can be derived from (Eq. 5.3.1).

#### 5.3.2.8. Solute transport model in 1D.

When using the HP1 model the solute transport is handled by the PHREEQC module and in HYDRUS the solute is transported as if they were inert tracers (i.e., no interaction with the solid phase, and no solute sink terms). The reactions are, therefore, considered in the PHREEQC module using equilibrium or kinetic reactions. The transport equation is described by Eq. 5.3.2.

$$\frac{\partial \theta c_i}{\partial t} = \frac{\partial}{\partial x} \left( \theta D_i^w \frac{\partial c_i}{\partial x} \right) - \frac{\partial q c_i}{\partial x} - S c_{r,i} + R_i \quad [5.3.2]$$

where  $i$  ( $= 1, \dots, N_m$ ) is the aqueous species number ( $N_m$  is the total number of aqueous species),  $c_i$  is the aqueous concentration of the  $i$ th species [ $ML^{-3}$ ],  $q$  is the volumetric flux density [ $LT^{-1}$ ],  $S$  the sink term in the water flow equation  $c_r$  the concentration of the sink term [ $ML^{-3}$ ],  $D_w$  is the dispersion coefficient in the liquid phase [ $L^2T^{-1}$ ], and  $R_i$  is the general source/sink term due to geochemical reactions [ $ML^{-3}T^{-1}$ ]. This sink/source term accounts for heterogeneous equilibrium reactions, and homogeneous and heterogeneous kinetic reactions.

The equation for the equilibrium precipitation/dissolution reactions of a mineral can be written as:

$$\sum_{j=1}^{N_m} \nu_{ji}^p A_j^m = A_i^p \quad [5.3.3]$$

where  $i = 1, \dots, N_p$  ( $N_p$  is the number of minerals), and  $A_i^p$  is the formula of the mineral, while the superscript  $p$  refers to pure phases (minerals). For equilibrium conditions, the mass-action equation is therefore described by Eq.5.3.4.

$$K_i^p = \prod_{j=1}^{N_m} (\gamma_j^m c_j^m)^{-\nu_{ji}^p} \quad [5.3.4]$$

since the activity of a pure phase (mineral) is assumed to be 1. The activity coefficients are defined with the Davies equation or the extended Debye-Hückel equation.

### 5.3.3. Results and discussion

#### 5.3.3.1. Mineral Assemblage

The concentration of major elements present in the substrate is shown in Table 5.3.1. Analysis by ICP-EOS has allowed the identification and quantification of important amounts of calcium, phosphorus, magnesium, silicon, fluorine, sodium and carbon. Lower amounts of aluminium, iron, potassium and sulphur are also present. Among the trace elements, Zn was the one element present in a significant concentration (388

µg/g) and therefore is the only trace specie considered in the mineral assemblage (Table S.5.3.2).

Table 5.3. 1. Concentration of major elements present in the NA1.

Material (%wt)	Ca	P	Mg	Si	Al	Fe	Na	K	F	C	S total
<b>NA1</b>	33.2	11.0	1.2	3.7	0.7	0.4	3.3	0.1	2.6	3.3	0.46

According to the phases identified by XRD and SEM-EDXS and considering the species determined by the elemental analyses, the resulting mineral assemblage better compiling with the experimental results of the leaching tests is presented in Table 5.3.2.

Table 5.3. 2. Mineral phases considered in the assemblage: general equation of the dissolution/precipitation reaction; solubility product and initial concentration of the phase in the assemblage (log  $K_{sp}$  values come from the Lawrence Livermore National Laboratory (Llnl) database supplied with PHREEQC).

Phase	General Equation	Log $K_{sp}$	Concentration (mol/L NA1)
<b>Calcite</b>	$\text{CaCO}_3 + \text{H}^+ = \text{Ca}^{2+} + \text{HCO}_3^-$	1.8487	4.28
<b>Dolomite</b>	$\text{CaMg}(\text{CO}_3)_2 + 2\text{H}^+ = \text{Ca}^{2+} + \text{Mg}^{2+} + 2\text{HCO}_3^-$	4.0579	5.56
<b>Fluorapatite</b>	$\text{Ca}_5(\text{PO}_4)_3\text{F} + 3\text{H}^+ = \text{F}^- + 3\text{HPO}_4^{2-} + 5\text{Ca}^{2+}$	-24.99	6.85
<b>Quartz</b>	$\text{SiO}_2 = \text{SiO}_2$	-3.999	4.3E-3
<b>Fluorite</b>	$\text{CaF}_2 = \text{Ca}^{2+} + 2\text{F}^-$	-10.04	5.19
<b>ZnCO<sub>3</sub>:H<sub>2</sub>O</b>	$\text{ZnCO}_3:\text{H}_2\text{O} + \text{H}^+ = \text{H}_2\text{O} + \text{HCO}_3^- + \text{Zn}^{2+}$	0.1398	1.97E-1
<b>Gypsum</b>	$\text{CaSO}_4:2\text{H}_2\text{O} = \text{Ca}^{2+} + \text{SO}_4^{2-} + 2\text{H}_2\text{O}$	-4.482	4.3E-3
<b>Montmor.Mg</b>	$\text{Mg}_{0.495}\text{Al}_{1.67}\text{Si}_4\text{O}_{10}(\text{OH})_2 + 6\text{H}^+ = 0.495\text{Mg}^{2+} + 1.67\text{Al}^{3+} + 4\text{H}_2\text{O} + 4\text{SiO}_2$	2.388	3.42
<b>Whitlockite</b>	$\text{Ca}_3(\text{PO}_4)_2 + 2\text{H}^+ = + 2\text{HPO}_4^{2-} + 3\text{Ca}^{2+}$	-4.225	15.45
<b>MgSO<sub>4</sub></b>	$\text{SO}_4^{2-} + \text{Mg}^{2+} = \text{MgSO}_4$	2.412	2.6E-2

The initial choice of mineral phases was made on the basis of XRD analysis, literature data, and elemental composition. Trials were conducted reiteratively, adjusting the

mineral phase concentrations to better represent experimental results. Results in Fig.5.3.2 indicate that the substrate is mostly dominated by basic minerals that dissolve in the presence of acid. Therefore, great amounts of acid are required to reduce the pH to acidic values accounting for the buffering effect of phosphates and carbonates in solution. This is coherent with the presence of phases as calcite, dolomite or fluorapatite. The modelled mineral assemblage is in relatively good agreement with experimental results.

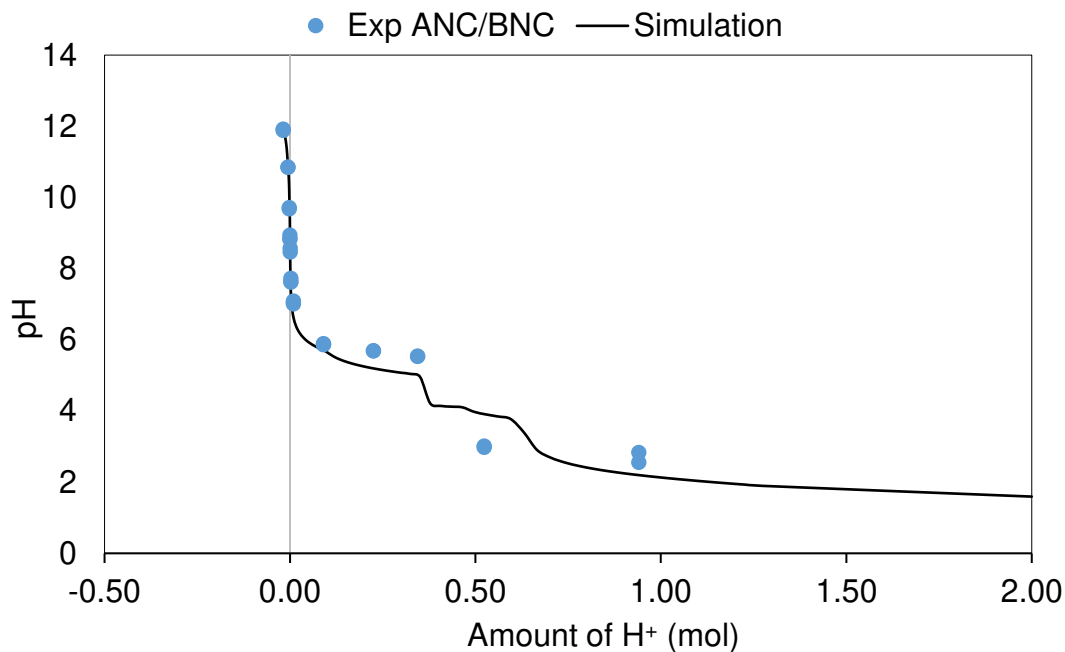


Fig. 5.3. 2. Acid/alkaline titration curve of the natural apatite substrate

The same conclusion can be derived from the observation of the leaching behaviour of major elements shown in Fig.5.3.3. The goodness of the model must be judged in terms of order of magnitude and tendency of the set of species considered. When adding a mineral phase or changing its concentration the resulting behaviour will affect all the species present in the assemblage. One should find the model that better fits the data sets from a global point of view. From Fig.5.3.3 one can see that the most important elements present in the substrate are well represented by the final mineral assemblage modelled. One can also noticed that the resulting mineral assemblage depends in the accessibility and solubility of the solid phases, their sensitivity to pH, as well as, the solubility of the considered element depending upon the pH and ionic

composition of the aqueous phase (Kania et al., 2019). This may imply that concentration of phases and elements resulting from analytical results cannot be directly transposed to the mineral assemblage but they must be seen as guidelines.

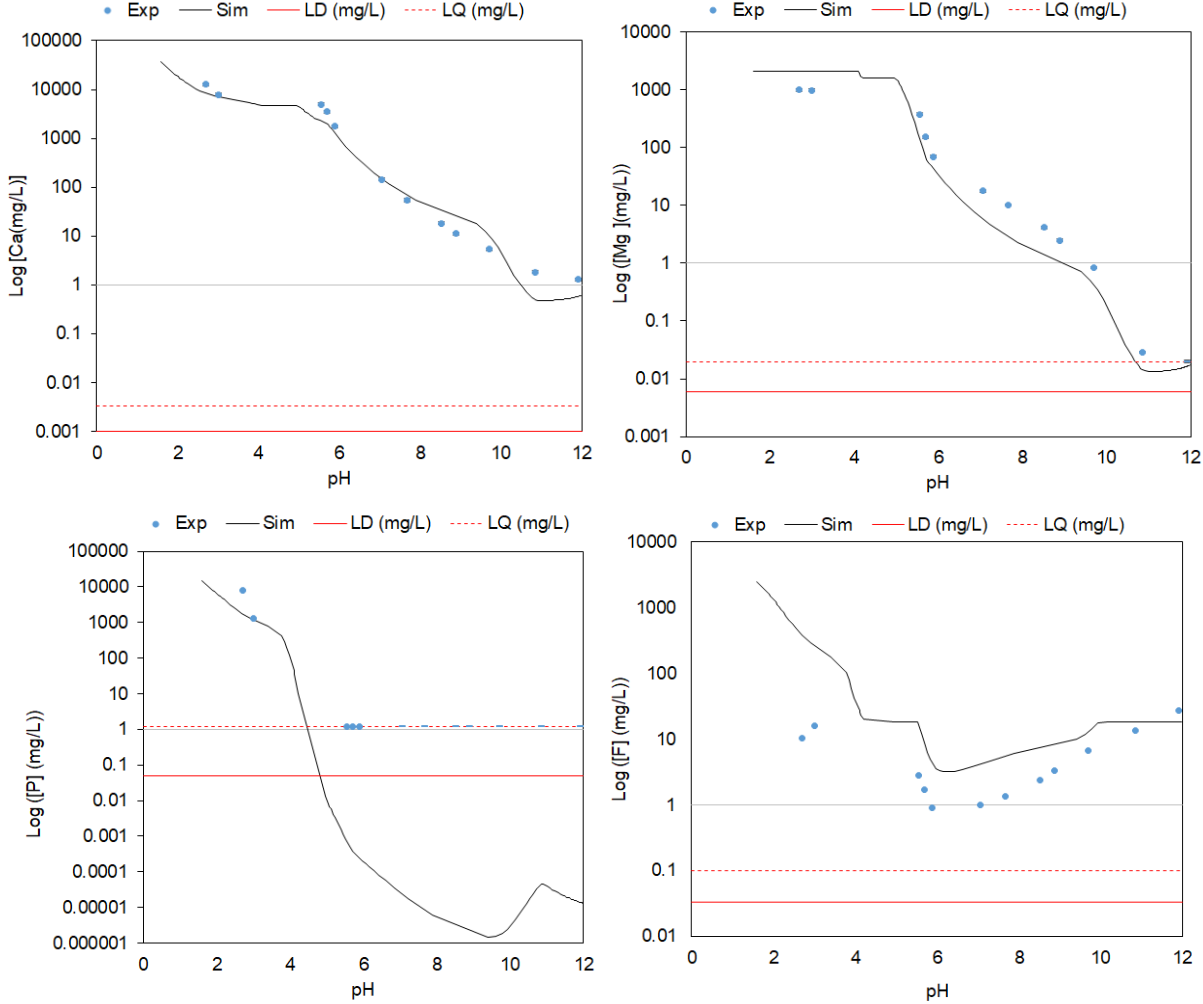


Fig. 5.3. 1. Leaching of target major elements ( $Ca^{2+}$ ,  $Mg^{2+}$ ,  $PO_4^{3-}$ ,  $F^-$ ) from the apatite sample at equilibrium with water at room temperature and different pH values.

### 5.3.3.2. Hydraulic Model

Hydrus-1D was used to simulate the tracer test carried out in the experimental column in order to determine solute dispersion. The molecular dispersion was estimated by inverse modelling using a minimization of the sum of squared errors as a local optimization method. The calculations were initiated with a dispersion value of 2.5 cm (min = 1.0, max = 100) and required 4 iterations to determine the final value. The solute

dispersion was found to be 2.1 cm. The goodness of the fitting was evaluated by the coefficient of determination ( $R^2 = 0.9975$ ).

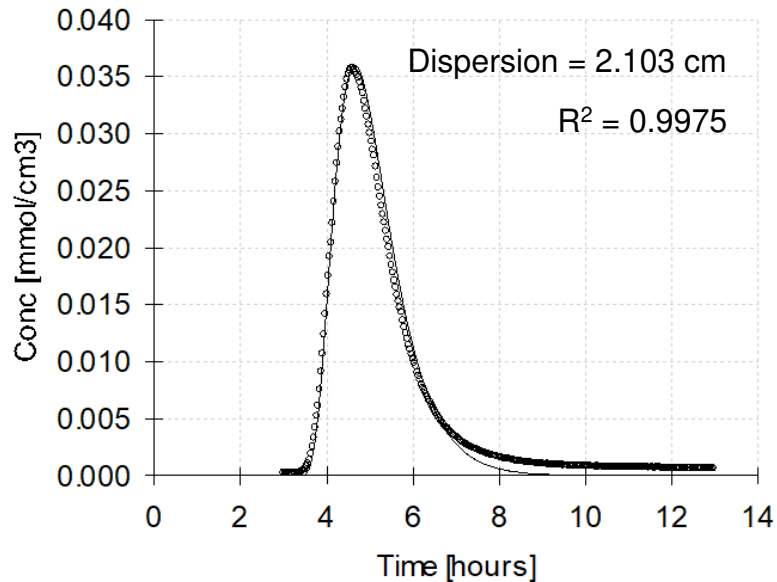


Fig. 5.3. 4. Simulation of tracer test with Hydrus-1D. Determination of solute molecular dispersion by inverse modelling.

#### 5.3.3.3. Thermodynamic model

This study explores the possibility of using a pure thermodynamic model based on precipitation/dissolution reactions to describe phosphate precipitation in a fixed-bed column filled with natural apatite material. Although a kinetic model would be a more realistic representation of the actual reactions taking place in such a system, the great amount of parameters needed makes the modelling of phosphate adsorption and heterogeneous precipitation of calcium phosphates on apatite from a treated wastewater liquid matrix a really complex problem. In addition, when a high number of fitting parameters that are difficult to measure intervene in the models, there is an increasing probability of having numerous fitting parameters dataset that compile with the experimental data without being possible to determine which one is the best to represent correctly the real process.

The simulation assumed the precipitation of amorphous phosphate (ACP). Since ACP is not the most stable calcium phosphate phase the system does not represent real

equilibrium situations. In addition, to account for the catalytic effect of the apatite surface, the solubility product constant was changed in a reiterative process until the phosphorus outlet concentrations in the solution were of the same order of magnitude as experimental data. The precipitation of ACP is therefore forced to occur to see if it could account for the global process taking place in the column. The model involves the mass balances for calcium and for phosphate as a function of ACP conversion. The equation describing the precipitation of ACP is written as:



From the iterative process, it results that the Log  $K_{ps}$  value for ACP giving the closer results to the experimental data was Log  $K_{ps} = -9$ . Results of this thermodynamic exploratory approach are shown in Fig. 5.3.5. However, the model did not produce a gradual increase of the phosphorus outlet concentration as the results from column experiments, but instead a sudden increase of the model is produced at 156 days of operation. Such increase seems to be produced by the complete dissolution and exhaustion of an important calcium-containing solid phase. This would result in a reduction of dissolved calcium ions affecting further precipitation of calcium phosphates.

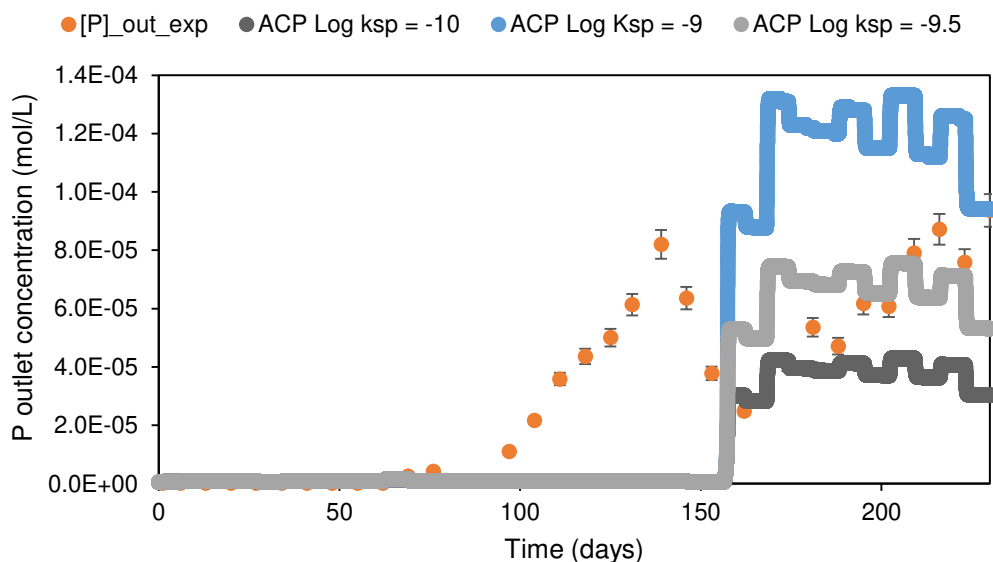


Fig. 5.3. 5 Evolution of phosphorus concentration at the outlet of the filter with the operating time of the system: simulation and experimental data.

When comparing the evolution of phosphorus concentration within the column (Fig. 5.3.6) a difference is also observed in the prediction between an operating time before and after the day 156. At  $t = 162$  days the simulation predicts an evolution with values in the same order of magnitude as the experimental values. For  $t = 131$  days, the phosphorus concentration decreases abruptly to concentrations much lower than the experimental ones.

The simulated precipitation of the ACP is limited to the first 4 cm of the column (Fig. 5.3.7). In the experimental column, although phosphorus concentration was gradually reduced along the column as it can be observed in Fig. 5.3.6., the model represents a precipitation that take place close to the inlet of the system where the supersaturation is higher. If this phenomena is optically visible in that layers close to the inlet and confirmed by SEM images (samples taken from the bottom of the column confirmed that no precipitate was formed there), the evolution of P concentration within the column cannot be well represented by the thermodynamic model.

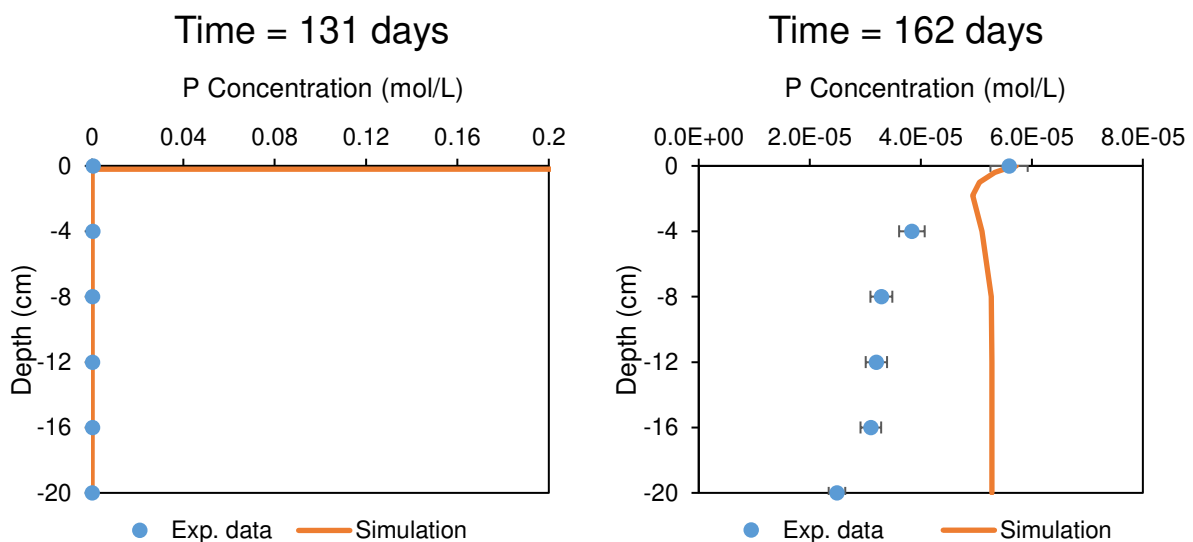


Fig. 5.3. 6. Phosphorus concentration evolution in the column with increasing hydraulic retention time (internal samplings). A comparison between the simulation and experimental data is shown at different operating times during the stabilisation phase of the column where precipitation must be the predominant process taking place.  $\text{Log } K_{sp} (\text{ACP}) = -9.5$ .

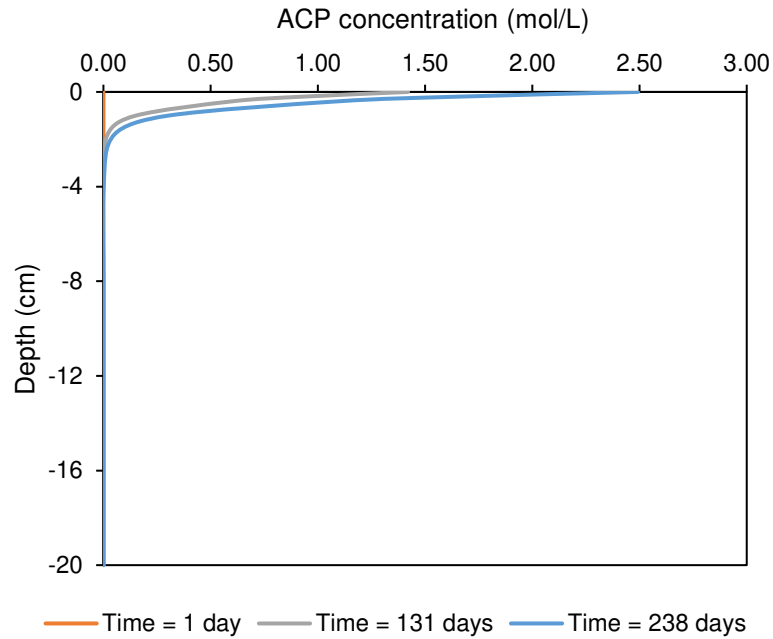


Fig. 5.3. 7. Evolution of the simulated amount of ACP precipitated with the depth of the column. Log  $K_{sp}$  (ACP) = -9.5.

The results showed that the thermodynamic approach applied involves an extreme simplification of the process and could not reproduce correctly the results from laboratory columns. A better representation of the system's dissolution/precipitation reactions would require a kinetic approach or a more complex thermodynamic approach. In addition, it will need to account for the evolution with time of the phases in contact with the solution and for the creation of new sorption sites as the precipitate forms. The hydraulic model would also need to account for the reduction in porosity due to calcium phosphates precipitation.

#### 5.3.4. Conclusions

The exploratory approach to model the processes taking place in the column has evidenced the incapability of a simplistic model based on pure thermodynamic approach to describe the phosphorus retention by apatite filters in a fixed-bed column. On the other hand, the mineralogical assemblage and the hydrodynamics of the system properly described experimental results. The solid matrix and solute transport

defined in this work can be used for future studies of mechanistic models for such systems.

### 5.3.5. Supplementary Information

Table S.5.3 1. Result of tracer analysis by ICP-MS of the apatite material.

As	Ba	Be	Bi	Cd	Co	Cr	Cs	Cu	Ga	Ge	Hf	In
$\mu\text{g/g}$												
15.9	77.6	1.47	0.05	22.1	1.41	205	0.59	44.3	2.91	0.61	1.16	< L.D.

Mo	Nb	Ni	Pb	Rb	Sb	Sc	Sn	Sr	Ta	Th	U	V
$\mu\text{g/g}$												
3.58	1.42	78.2	6.33	6.68	2.23	9.74	< L.D.	852	0.13	5.41	128	177

W	Y	Zn	Zr	La	Ce	Pr	Nd	Sm	Eu	Gd	Tb	Dy	Ho
$\mu\text{g/g}$													
< L.D.	175	388	54.7	70.8	52.2	12.3	53.7	11.4	3.05	13.6	2.10	14.3	3.52

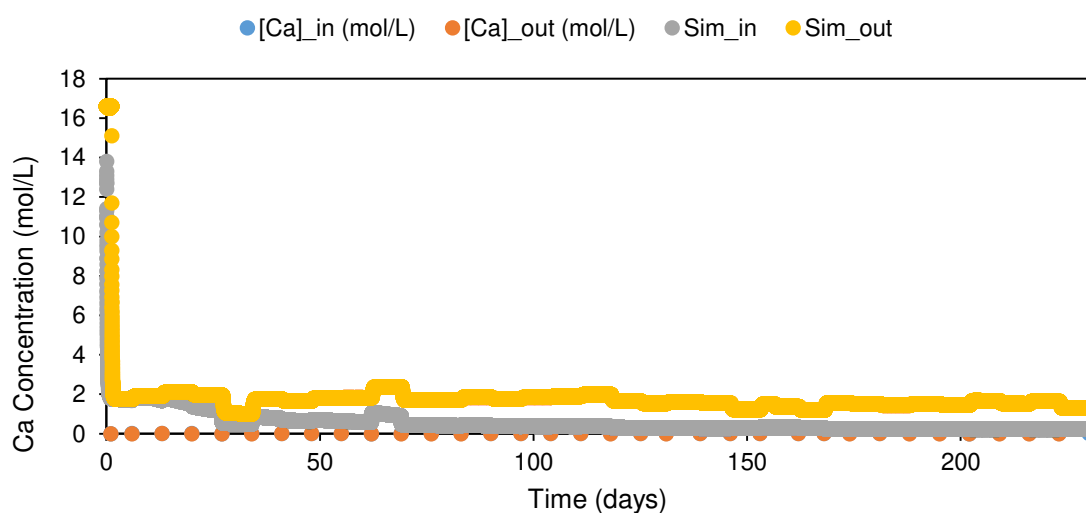


Fig. S.5.3 1. Evolution of calcium concentration at the inlet and outlet of the filter with the operating time of the system: simulation and experimental data.

## 5.4. Chapter conclusions

The results previously presented have underlying the high capability of natural apatite for phosphorus retention. The two substrates tested showed high performances and kinetic rates. The phosphorus retention capacity (PRC) attained within the duration of this work was higher than those reached in previous studies (Fig.1.10) for both substrates, showing a great potential for long-term operation. In addition, no significant loss of hydraulic conductivity was measured within the PRC range of study, which secures the system from the hydraulic point of view. In conclusion, the natural apatite materials here tested exhibited an interesting potential for phosphorus retention from wastewater.

The use of engineering reaction rate models has shown, however, some limitations for the description of complex processes as calcium phosphate precipitation. An interesting approach to solve such limitations would be the development of a mechanistic model. First steps in such direction were explored in this work by modelling the geochemical and hydrodynamic characterisation of the apatite column. The mineralogical assemblage and the hydrodynamic model of the system developed in this study were satisfactory and could be used for modelling work. However, if the thermodynamic approach used to represent P evolution allows to reproduce P tendency evolution at the outlet of the column, the precise P evolution within the column is not satisfactory. Indeed, a more complete study of the mechanistic model using a kinetic approach would be necessary to properly simulate chemical reaction processes in order to develop a useful tool for filter's design and optimization.

## Final discussion, conclusions and perspectives

---

In this study, two different types of apatite substrate for phosphorus retention from pre-treated wastewater were investigated: a manufactured granulated apatite and two different natural apatites. The granulated apatite, although capable of retaining phosphorus, cannot allowed long-term phosphorus retention. Results from field campaigns on full-scale granulated apatite filters revealed some dysfunctions in the systems resulting in a lower lifespan for which they were designed (~ 10 years). Although some hydraulic inefficiencies were identified at full scale, the most important cause leading to low performances and kinetics was explained by the morphology and composition characteristics of the product. Such results were first observed in full-scale systems and then validated in laboratory columns: the granulated apatite could not formed a sustainable precipitation of calcium phosphate on the surface of the granules except if high supersaturation levels in the solution were provided, conditions for which other more unreactive or non-selective substrates may could also promote heterogeneous nucleation. The reason behind such behaviour was found to be the morphology of the granules since the actual apatite particles were embedded in the binder of the granules. Then, for lower calcium and phosphates concentration, typical values of wastewater effluents, the material behaved more as an adsorption-like substrate rather than a surface for crystal growth of calcium phosphates.

Regarding natural apatites, the laboratory experiments showed great phosphorus retention capacities and high kinetics rates without any hydraulic issues detected for the retention capacities attained. The low retention times applied in the laboratory did not prevent the retention of calcium phosphates by seeded precipitation on the apatite surface. The precipitation of calcium phosphates formed a structured layer identified as amorphous calcium phosphate likely capable of sustaining the precipitation process to higher saturation levels of the filter bed. Therefore, natural apatite filters would represent a competitive solution for phosphorus retention and recovery from wastewater. The use of reaction rates models for the evaluation of these processes entails however some limitations mostly concerning the environmental interactions that

participate in a calcium phosphate system. Being aware of the complexity of such processes and the limitations of the engineering models to predict their behaviour, a mechanistic modelling approach would be necessary in order to overcome such issues. First steps in such direction were explored in this work by modelling the geochemical and hydrodynamic characterisation of the apatite column. The mineralogical assemblage and the hydrodynamics models of the system developed in this study were satisfactory and could be used for a modelling work in future investigations.

Design guidelines for natural apatite filters cannot be based, however, on the mechanistic approach but simple engineering reaction rates models, like the  $k-C^*$  and the  $N-k C^*$  models, could be used to discussed preliminary design approaches. Such models require little amount of parameters to be defined providing a simple tool to compare the adequacy of the materials for P retention in WWTPs and for design purposes. However, the use of such models entails a simplification of the processes taking place and, thus, they present some limitations (e.g. pH, competitions, anions/cations influence are not taken into consideration). In addition, it cannot be distinguished if  $k_v$  represents one mechanism or an average of several mechanisms and it cannot explain the variations of a  $k_v$  and  $C^*$  with the PRC. However, discussion on design configurations can bring interesting information to better precise future research needs. Such discussion is based on NA1 product results in order to identify the possibilities and limits of the different configurations proposed.

As a first design discussion, we proposed the following assumptions:

- 1) The filter (a vertical down-flow system) is set to be a tertiary treatment to limit biomass growth and suspended solids accumulation within the media.
- 2) The filter is assumed to achieve a lifespan of 30 years. When possible the designs were optimized to exhaust the filters at the end of the system's lifespan.
- 3) The simulations are carried out considering a P production of 2.1 g/PE/d and wastewater volume of 150 L/PE/d as well as a maximum admissible outlet concentration of 2 mg TP/L.
- 4) The design assumed a maximum phosphorus retention capacity of 20 g TP/ kg of NA1 material.

- 5) Design is tested for combined sewer making difference between dry weather conditions and storm events (double the hydraulic load)
- 6) Design limitations include the organic load (OL) and the hydraulic load (HL) on the filter(s):
  - a. Mean organic concentration entering the filter is fixed at 10 mg O<sub>2</sub>/L DBO<sub>5</sub> and maximum organic load is set to 30 g BOD<sub>5</sub>/m<sup>2</sup>/d in relation to the hydraulic section.
  - b. Maximum hydraulic load is set at 0.8 m/d for dry weather conditions and peak hydraulic load until 1.6 m/d during rain events. This last value corresponds to the measurement of the hydraulic conductivity at the end of the experiment (Chapter 5.1) taking into account a security factor of 10. The saturated hydraulic conductivity used for the design of a full-scale filter is, therefore, 2·10<sup>-5</sup> m/s. In addition, to avoid the appearance of shortcuts and other hydraulic disturbances, the minimum depth of the filter is set at 30 cm. Finally, a maximum freeboard is set at 50 cm to allow water ponding on the top surface.
- 7) Two reaction rate models are used: the k-C\* model and the N-k-C\* model. Tracer tests conducted on full-scale granulated apatite filters showed that the hydrodynamics of full-scale filters is likely to behave as several completely stirred tank reactors in series. For the discussion the design was implemented using N = 5.5. On the other hand, experiments carried out on laboratory columns on natural apatites showed that the k-C\* model could be applied leading to lower k<sub>v</sub> values and higher C\*. Therefore, it is also used to observe if such fitting parameters could be more conservative for the design compared to N-k-C\* model. The evolution of the parameters with the PRC is estimated as follows:
  - a. A sigmoidal correlation is used to determine the evolution of the C\* parameter with the phosphorus retention capacity (PRC). C\* represents the equilibrium concentration of phosphates in solution and so the minimum concentration attainable at the outlet of the filter. Fig.D.C.1 shows the evolution of C\* with the k-C\* and N-k-C\* models. The k-C\* models attains the discharge limit little before attaining its maximum

phosphorus retention capacity. For the N-k-C\* model, outlet concentrations above 2 mg TP/L are reached from approximately 16 g TP/ kg NA1.

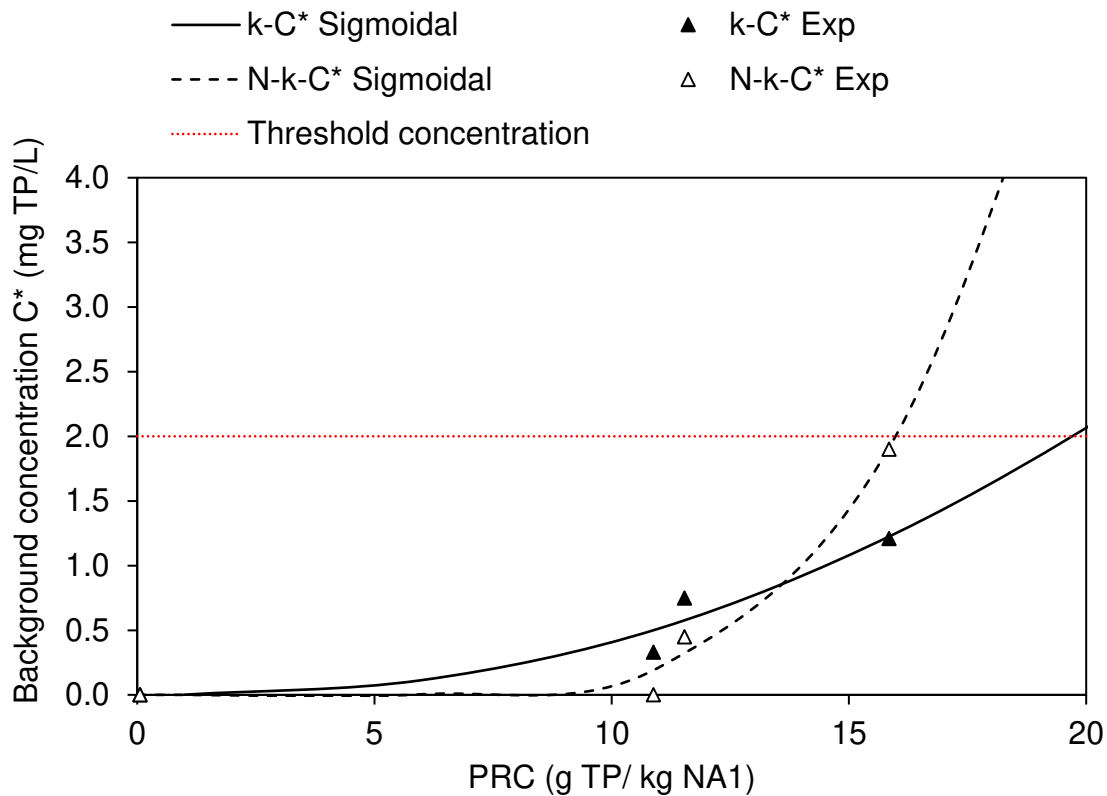


Fig. D.C. 1 Sigmoidal evolution of background concentration with the phosphorus retention capacity using a sigmoidal curve adjusted to the  $C^*$  values estimated from experimental data of laboratory columns (column NA1).

- b. The evolution of kinetic constant for NA1 apatite is close to a quadratic regression for  $k_v$  values below  $1.2 \text{ h}^{-1}$  and  $1.4 \text{ h}^{-1}$  for the k-C\* and N-k-C\* model, respectively. From these  $k_v$  values (at around PRCs of 15 and 17 g TP/kg NA1 for k-C\* model and N-k-C\* model, respectively), the simulation considers that systems achieve the pseudo-stabilization and the evolution follows a straight line.

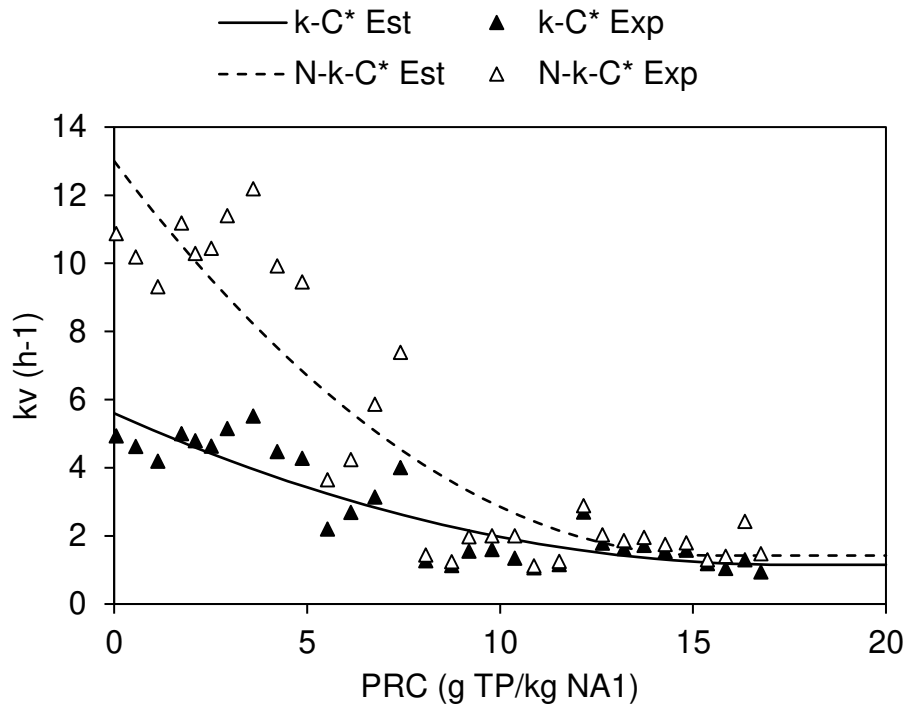


Fig. D.C. 2. Evolution of predicted  $k_v$  with phosphorus retention performance considering the  $k-C^*$  model and the  $N-k-C^*$  model.

Design simulations are done assuming the following hypothesis:

Wastewater treatment plant capacity = 1000 PE (population-equivalent)

Flowrate (dry weather flow) =  $Q_d = 150 \text{ m}^3/\text{d}$

Flowrate (rain event) =  $Q_w = 2 Q_d = 300 \text{ m}^3/\text{d}$

Inlet phosphorus concentration (dry weather flow) =  $C_{d\_in} = 14 \text{ mg TP/L}$

Diluted inlet phosphorus concentration (storm event) =  $C_{s\_in} = 7 \text{ mgTP/L}$

Design is discussed according to two different configurations whether a unique filter is implemented for a 30 year-period functioning without any material replacement, or two filters in series where the first filter material can be replaced on a regular basis. The second solution allows being more compact but includes additional cost from the material replacement. Both configurations are designed based on dry weather or storm event as well as using both models  $k-C^*$  and  $N-k-C^*$  model.

### One-Filter Configuration

The design of a one-filter configuration system involves finding the volumetric capacity that allows a complete use of its phosphorus retention capacity while respecting the outlet concentration threshold, as shown in Fig. D.C.3. When considering a design based on dry weather conditions, the volumetric capacity that complies with the imposed criteria according to the k-C\* and N-k-C\* model is 870 and 1094 m<sup>3</sup> (Table D.C.1), respectively. Taking volumetric capacities below or above the specified volume, will lead to a lower lifespan or to a system badly optimized, respectively.

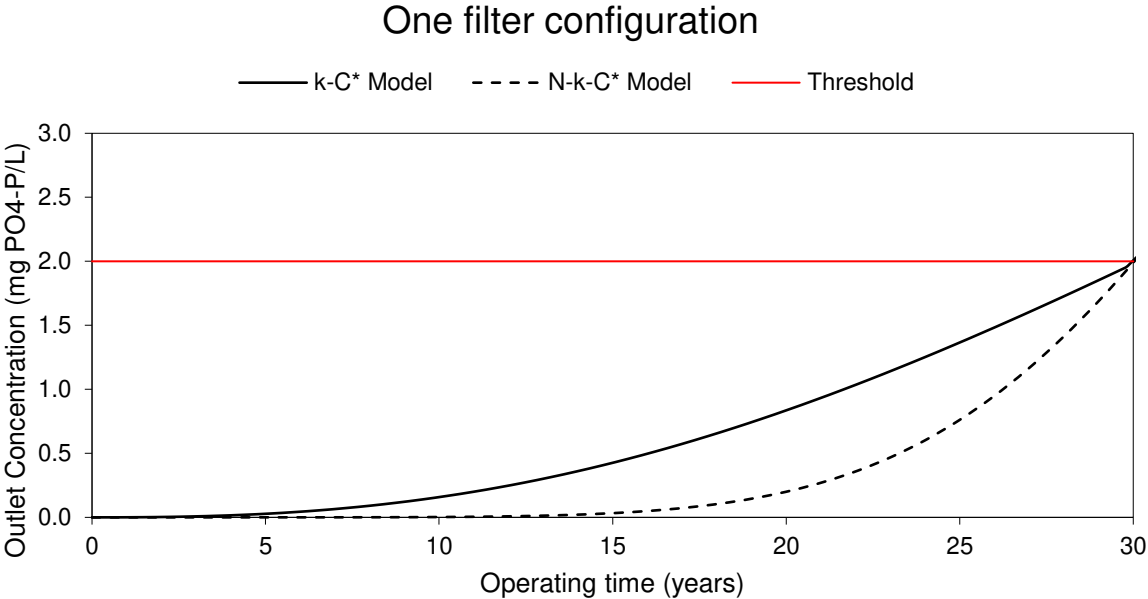


Fig. D.C. 3. Evolution of outlet concentration from a one-filter configuration designed based on the k-C\* and the N-k-C\* model for dry weather conditions.

When considering a design based on storm event conditions (assuming a double hydraulic load), the volumetric capacity, although limited by the higher HL, is reduced because of a reduced inlet phosphorus load. Consequently, with such hypothesis, the dry weather flow appears to be the limiting factor. Finally, as it can be seen in Table D.C.1, in a one-filter configuration, that both models lead to similar volume of apatite and N-k-C\* seems to be more conservative.

Table D.C. 1. Design characteristics of a one-filter configuration

	k-C* Model		N-k-C* Model	
	Dry weather	Storm Events	Dry weather	Storm Events
<b>Volume F1 (L/PE)</b>	870	412	1094	531
<b>Depth max F1 (m)</b>	0.76	0.52	0.85	0.59
<b>Surface F1 (m<sup>2</sup>)</b>	1145	792	1287	900
<b>Total footprint (m<sup>2</sup>)</b>	1145	792	1287	900
<b>Total Vol (m<sup>3</sup>)</b>	870	412	1094	531
<b>Total mass (ton)</b>	1117	529	1405	682

## Two-Filter Configuration

In a two - filter configuration in series, the total volume of material required for the 30-year period (full lifespan of the system) and the frequency of replacements of the first filter's material volume, are new factors to be considered. Although the discussion here proposed is not about economic criteria but just operational criteria, two different types of design are suggested to illustrate the impact of the number of replacements: type 1, minimum volume for both filters F1 and F2; type 2, a replacement of F1 every 10 years approximately.

When seeking for low volumes of the filter, the HL is usually the limiting factor. Fig. D.C.4 it shows the results for dry weather conditions according to both reaction rate models. The minimum volume capacity when using the k-C\* model allows to attain outlet concentrations below 1 mg TP/L during the whole operating time of the system with six replacements of the F1 bed. However, there is the possibility to avoid the sixth replacement of F1 allowing F2 to exhaust its retention capacity for the last years of the lifespan of the system in order to optimize it. For the N-k-C\* model, a lower number of replacements is required which reduces the total volume and mass of material that needs to be replaced compared to the k-C\* model design. On the other hand, the footprint requirements are higher for the N-k-C\* model design (Table D.C.2). In a 2 filter configuration with a filter bed replacement every 10 years, a greater surface is

also required for N-k -C\* but since the replacement is set to 10 years for both designs, the total volume and mass required in both systems are the same.

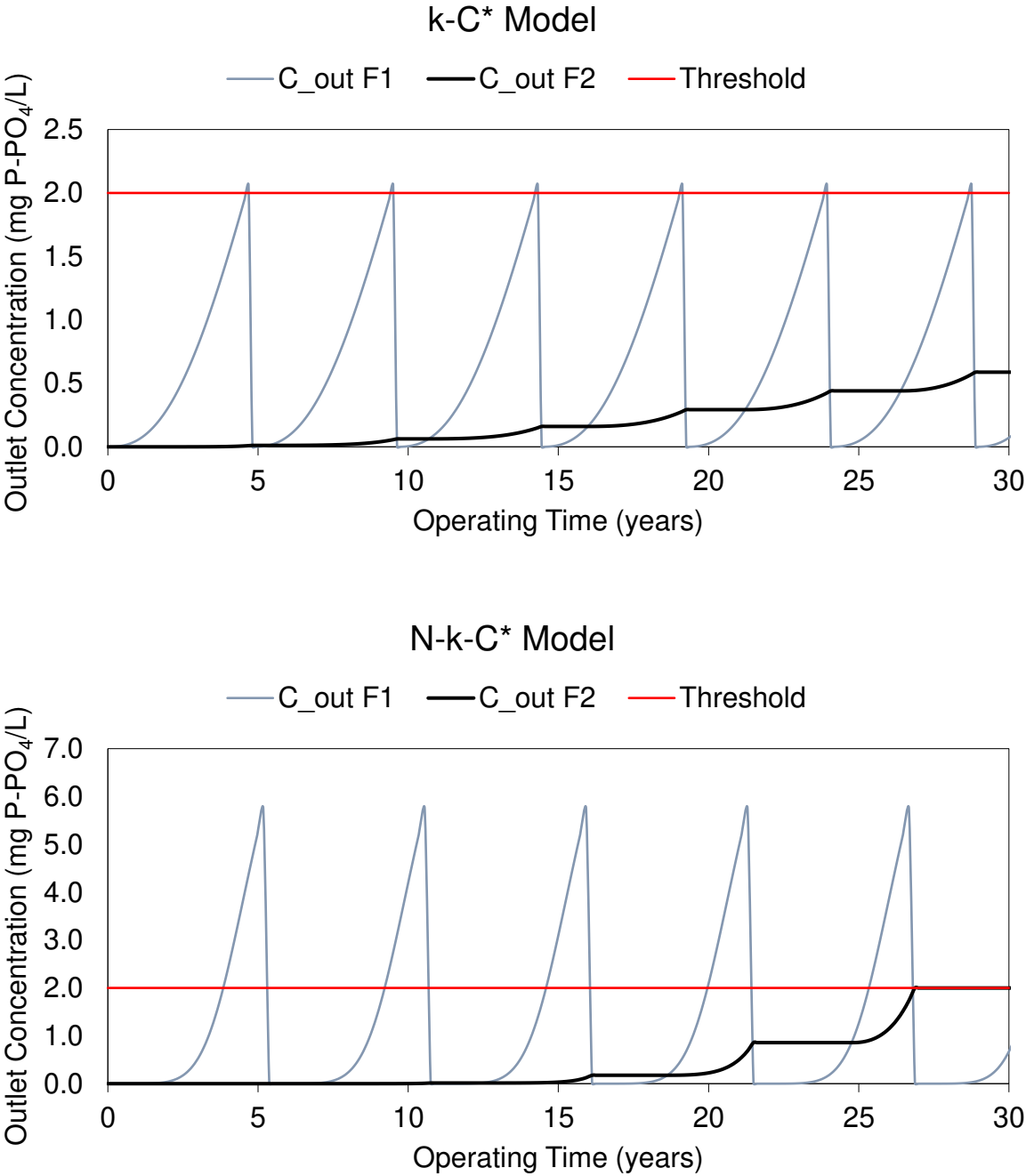


Fig. D.C. 4. Design of a two-filter system based on dry weather conditions according to the k-C\* and N-k-C\* models.

When comparing dry weather and storm events design in a two-filter configuration one can see that the total surface required would be equal or bigger for a storm weather design than for dry weather (logically). However, as the inlet concentration is reduced

during storm events the resulting amount of replacements is lower than for dry season and, therefore, the total volume and mass of material required is also lower.

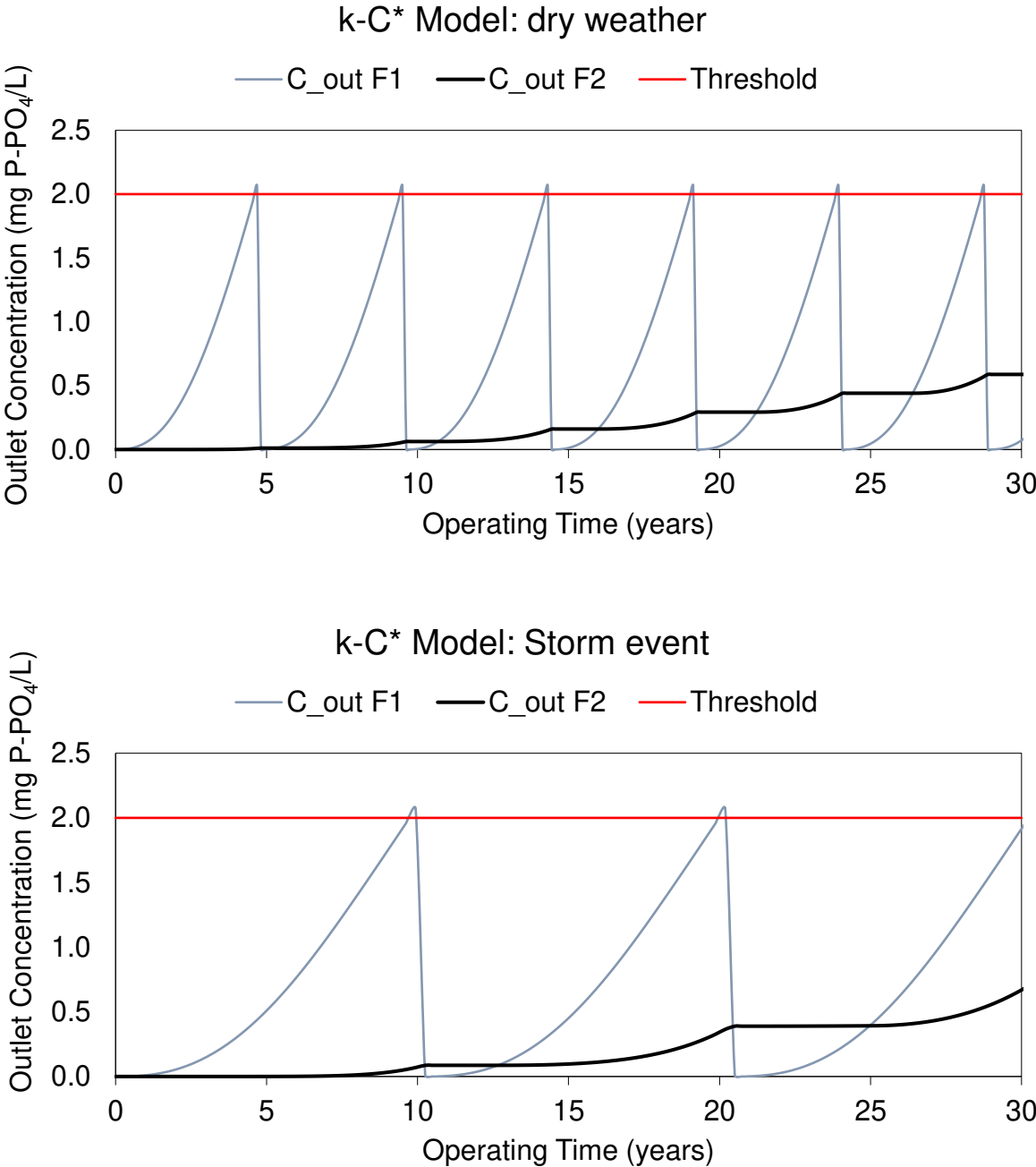


Fig. D.C. 5. Design of a two-filter system based on dry weather conditions and storm events according to the k-C\* model.

Table D.C. 2. Design characteristics of a two-filter in series configuration

	Design 2 filters (min. Vol)				Design 2 filters (Renewal every 10 years)			
	k-C* Model		N-k-C* Model		k-C* Model		N-k-C* Model	
	Dry weather	Storm Events	Dry weather	Storm Events	Dry weather	Storm Events	Dry weather	Storm Events
<b>Volume F1 (L/PE)</b>	133	133	140	137	280	133	263	137
<b>Max. Depth F1 (m)</b>	0.3	0.3	0.3	0.3	0.43	0.3	0.42	0.3
<b>Surface F1 (m<sup>2</sup>)</b>	433	433	467	457	651	433	626	457
<b>Nb. of replacements</b>	6	2	5	2	2	2	2	1.3
<b>Frq. replacements (years)</b>	4.7	9.9	5.2	12.8	9.9	9.9	9.7	12.8
<b>Volume F2 (L/PE)</b>	57	57	84	153	57	57	92	153
<b>Max. Depth F2 (m)</b>	0.3	0.3	0.3	0.3	0.3	0.3	0.42	0.3
<b>Surface F2 (m<sup>2</sup>)</b>	190	190	280	510	190	190	188	510
<b>Total footprint (m<sup>2</sup>)</b>	633	633	747	967	792	633	814	967
<b>Total Vol (m<sup>3</sup>)</b>	855	323	784	427	617	323	618	427
<b>Total mass (ton)</b>	1098	415	1007	548	792	415	794	548

In conclusion, the two-filter configuration allows a more compact system (reduced total footprint) than the one-filter configuration (reduced total footprint) and lower total

volume and mass required. However, the design choice will require to account for the costs associated with the replacements of the filter material of the two-filter configuration over the 30-year period and the costs associated with the greater footprint required for a one-filter configuration.

It can be observed as well that design set for dry-weather flow allow to respect outlet requirement for storm events. However, as hydraulic load is often a limiting factor for a two filter in series, higher storm events hydraulic loads could affect strongly the design. Consequently, it could be interesting to manage high storm event differently, e.g. by-passing a part of the flow as P concentrations are diluted.

Previous examples allowed illustrating the use of simple models to define different design strategies. Because the design is based on laboratory column results, it involves some limitations and direct extrapolation to full-scale systems might be done carefully, but in any case, such examples must be taken as design rules. One of the design limiting factors observed is the evolution of  $C^*$  with the PRC. The  $C^*$  values used for the design were determined in column experiments using low retention times ( $\sim 2$  hours), however, in full scale systems the hydraulic retention times can be much higher (10 to 24 hours). Real conditions may imply changes in the mechanisms and/or the rate-limiting steps. For instance, higher HRTs may involve the formation of hydroxyapatite instead of amorphous calcium phosphate, due to a greater time to attain equilibrium with benefits for the stability of the precipitate and reducing the  $C^*$  value, as well. On the other hand, if the velocity of the flow is that low that the thickness of the diffusive layer is much more important, the kinetic rate of the overall process may be reduced. As the  $C^*$  value strongly impact the replacement frequency as well as the possibility to use the full retention capacity of the material, determining more precisely its evolution in real condition appears to be of great importance. Secondly, it could be interesting to define PRC evolution to higher PRC values, which would allow to decrease the total volume of material to be used. Thus, laboratory experiments have validated the adequacy of these specific natural apatites for phosphorus retention from wastewater, however, in order to ensure the design of full-scale filters it would be necessary to conduct long-term experiments (several years) in a scaled-up system.

Hence, in order to better design and optimize full-scale systems, the combination of laboratory experiments with a mechanistic model would allow a better understanding

of processes and an improved control of the operation. On the other hand, such approach may involve an excessive complex model of difficult application. Thus, it should be an objective for future investigations on the development of a mechanistic model, to allow the better representation of complex processes possible while maintaining easy-to-use characteristics.

In conclusion, the results from this work have provided a better understanding of the retention process of calcium phosphates in apatite filters, showing a great potential for its application in wastewater treatment of small communities. The exploitation of such potential will demand to focus future research efforts in the development of a mechanistic model and the validation of laboratory results in up-scaled systems working in real conditions.

# References

---

## Chapter 1

- Amann, A., O. Zoboli, J. Krampe, H. Rechberger, M. Zessner and L. Egle (2018). "Environmental impacts of phosphorus recovery from municipal wastewater." *Resources, Conservation and Recycling* 130: 127-139. DOI: 10.1016/j.resconrec.2017.11.002.
- Andrieux-Loyer, F. (1997). Les formes de phosphore particulaire et sedimentaire en environnement cotier. Methodes d'analyse, biodisponibilite, echange. PhD Thesis Chimie Appliquée: Chimie Marine, l'universite de bretagne occidentale faculte des sciences et techniques.
- Ateeq, F. (2016). Chemical Removal of Total Phosphorus from Wastewater to Low Levels and Its Analysis Master of Science, Wilfrid Laurier University, .
- Barca, C., S. Troesch, D. Meyer, P. Drissen, Y. Andres and F. Chazarenc (2013). "Steel slag filters to upgrade phosphorus removal in constructed wetlands: two years of field experiments." *Environ Sci Technol* 47(1): 549-556. DOI: 10.1021/es303778t.
- Bellier, N., F. Chazarenc and Y. Comeau (2006). "Phosphorus removal from wastewater by mineral apatite." *Water Res* 40(15): 2965-2971. DOI: 10.1016/j.watres.2006.05.016.
- Bellin, I. (2016). "New markets emerge for plant purification [L'épuration végétalisée s'ouvre à de nouveaux marchés]." *Eau, l'Industrie, les Nuisances* 390: 67-76.
- Brix, H., C. A. Arias and M. del Bubba (2001). "Media selection for sustainable phosphorus removal in subsurface flow constructed wetlands." *Water Science and Technology* 44(11-12): 47-54. DOI: 10.2166/wst.2001.0808.
- Broberg, O. and G. Persson (1988). "Particulate and dissolved phosphorus forms in freshwater: composition and analysis." *Hydrobiologia* 170: 61-90.
- Chrispim, M. C., M. Scholz and M. A. Nolasco (2019). "Phosphorus recovery from municipal wastewater treatment: Critical review of challenges and opportunities

- for developing countries." *J Environ Manage* 248: 109268. DOI: 10.1016/j.jenvman.2019.109268.
- Cieślak, B. and P. Konieczka (2017). "A review of phosphorus recovery methods at various steps of wastewater treatment and sewage sludge management. The concept of "no solid waste generation" and analytical methods." *Journal of Cleaner Production* 142: 1728-1740. DOI: 10.1016/j.jclepro.2016.11.116.
- Comber, S., M. Gardner, J. Darmovzalova and B. Ellor (2015). "Determination of the forms and stability of phosphorus in wastewater effluent from a variety of treatment processes." *Journal of Environmental Chemical Engineering* 3(4): 2924-2930. DOI: 10.1016/j.jece.2015.10.002.
- Cordell, D. and S. White (2013). "Sustainable Phosphorus Measures: Strategies and Technologies for Achieving Phosphorus Security." *Agronomy* 3(1): 86-116. DOI: 10.3390/agronomy3010086.
- Egbuna, C. and J. Ifemeje (2015). "Biological Functions and Anti-nutritional Effects of Phytochemicals in Living System." *IOSR Journal of Pharmacy and Biological Sciences* 10(2): 10-19. DOI: 10.9790/3008-10231019.
- Egle, L., H. Rechberger, J. Krampe and M. Zessner (2016). "Phosphorus recovery from municipal wastewater: An integrated comparative technological, environmental and economic assessment of P recovery technologies." *Sci Total Environ* 571: 522-542. DOI: 10.1016/j.scitotenv.2016.07.019.
- Elliott, J. C. (2013). *Structure and Chemistry of the Apatites and Other Calcium Orthophosphates*, Elsevier Science.
- Fihri, A., C. Len, R. S. Varma and A. Solhy (2017). "Hydroxyapatite: A review of syntheses, structure and applications in heterogeneous catalysis." *Coordination Chemistry Reviews* 347: 48-76. DOI: 10.1016/j.ccr.2017.06.009.
- Garfí, M., L. Flores and I. Ferrer (2017). "Life Cycle Assessment of wastewater treatment systems for small communities: Activated sludge, constructed wetlands and high rate algal ponds." *Journal of Cleaner Production* 161: 211-219. DOI: 10.1016/j.jclepro.2017.05.116.
- Gilbin, R., E. Gomez and B. Picot (2000). "Phosphorus and organic matter in wetland sediments: analysis through gel permeation chromatography (GPC)." *Agronomie* 20(5): 567-576. DOI: 10.1051/agro:2000151.

- Gustafsson, J. P., A. Renman, G. Renman and K. Poll (2008). "Phosphate removal by mineral-based sorbents used in filters for small-scale wastewater treatment." *Water Research* 42(1-2): 189-197. DOI: 10.1016/j.watres.2007.06.058.
- Hamisi, R., G. Renman, A. Renman and A. Wörman (2019). "Modelling Phosphorus Sorption Kinetics and the Longevity of Reactive Filter Materials Used for On-Site Wastewater Treatment." *Water* 11(4). DOI: 10.3390/w11040811.
- Harouiya, N., S. Martin Rue, S. Prost-Boucle, A. Liénar, D. Esser and P. Molle (2011). "Phosphorus removal by apatite in horizontal flow constructed wetlands for small communities: pilot and full-scale evidence." *Water Science and Technology* 63(8): 1629-1637. DOI: 10.2166/wst.2011.250.
- Harouiya, N., S. Prost-Boucle, C. Morlay, D. Esser, S. Martin-Ruel and P. Molle (2011). "Performance evaluation of phosphorus removal by apatite in constructed wetlands treating domestic wastewater: column and pilot experiments." *International Journal of Environmental Analytical Chemistry* 91: 740-752.
- Hukari, S., L. Hermann and A. Nattorp (2016). "From wastewater to fertilisers-- Technical overview and critical review of European legislation governing phosphorus recycling." *Sci Total Environ* 542(Pt B): 1127-1135. DOI: 10.1016/j.scitotenv.2015.09.064.
- Jang, H. and S.-H. Kang (2002). "Phosphorus removal using cow bone in hydroxyapatite crystallization." *Water Research* 36 1324–1330. DOI: doi.org/10.1016/S0043-1354(01)00329-3.
- Jiang, C., L. Jia, B. Zhang, Y. He and G. Kirumba (2014). "Comparison of quartz sand, anthracite, shale and biological ceramsite for adsorptive removal of phosphorus from aqueous solution." *Journal of Environmental Sciences* 26(2): 466-477. DOI: 10.1016/s1001-0742(13)60410-6.
- Joko, I. (1984). "phosphorus removal from wastewater by the crystallization method." *Wat. Sci. Tech.* 17: 121-132.
- Kadlec, R. H. and S. D. Wallace (2009). *Treatment wetlands*. Boca Raton, FL, CRC Press.
- Kania, M., M. Gautier, A. Imig, P. Michel and R. Gourdon (2019). "Comparative characterization of surface sludge deposits from fourteen French Vertical Flow Constructed Wetlands sewage treatment plants using biological, chemical and thermal indices." *Sci Total Environ* 647: 464-473. DOI: 10.1016/j.scitotenv.2018.07.440.

- Kaplan, D. I. and A. S. Knox (2004). "Enhanced contaminant desorption induced by phosphate mineral additions to sediment." *Environmental Science and Technology* 38(11): 3153-3160. DOI: 10.1021/es035112f.
- Kim, B. (2014). Devenir du phosphore dans les filtres plantés de roseaux : étude de sa rétention / libération et des facteurs d'influence. PhD Thesis Sciences de l'Environnement Industriel et Urbain, Institut national des sciences appliquées de Lyon, Université de Lyon.
- Kim, B., M. Gautier, P. Michel and R. Gourdon (2013). "Physical-chemical characterization of sludge and granular materials from a vertical flow constructed wetland for municipal wastewater treatment." *Water Sci Technol* 68(10): 2257-2263. DOI: 10.2166/wst.2013.485.
- Lafon, J. P., E. Champion, D. Bernache-Assollant, R. Gibert and A. M. Danna (2003). "Thermal decomposition of carbonated calcium phosphate apatites." *Journal of Thermal Analysis and Calorimetry* 72(3): 1127-1134. DOI: 10.1023/a:1025036214044.
- Leroy, N. and E. Bres (2001). "Structure and Substitutions in Fluorapatite." *European Cells and Materials* 2: 36-48. DOI: 10.22203/eCM.v002a05.
- Martinez-Carvajal, G. D., L. Oxarango, J. Adrien, P. Molle and N. Forquet (2019). "Assessment of X-ray Computed Tomography to characterize filtering media from Vertical Flow Treatment Wetlands at the pore scale." *Sci Total Environ* 658: 178-188. DOI: 10.1016/j.scitotenv.2018.12.119.
- Melia, P. M., A. B. Cundy, S. P. Sohi, P. S. Hooda and R. Busquets (2017). "Trends in the recovery of phosphorus in bioavailable forms from wastewater." *Chemosphere* 186: 381-395. DOI: 10.1016/j.chemosphere.2017.07.089.
- Mercoiret, L. (2010). *Qualité des eaux usées domestiques produites par les petites collectivités: Application aux agglomérations d'assainissement inférieures à 2 000 Equivalent Habitants.*, Cemagref.
- Mihelcic, J. R., L. M. Fry and R. Shaw (2011). "Global potential of phosphorus recovery from human urine and feces." *Chemosphere* 84(6): 832-839. DOI: 10.1016/j.chemosphere.2011.02.046.
- Molle (2003). *Filtres plantés de Roseaux: Limites hydrauliques et rétention du phosphore.* PhD Génie de procédés, Université de Montpellier II.

- Molle, Liénard, Grasmick and Iwema (2003). "Phosphorus retention in subsurface constructed wetlands: investigations focused on calcareous materials and their chemical reactions." *Water Science and Technology* 48(5): 8.
- Molle, A. Liénard, A. Grasmick, A. Iwema and A. Kabbabi (2005). "Apatite as an interesting seed to remove phosphorus from wastewater in constructed wetlands." *Water Science & Technology* 51(9): 193-203.
- Molle, P., S. Martin, D. Esser, S. Besnault, C. Morlay and N. Harouiya (2011). "Phosphorus removal by the use of apatite in constructed wetlands: Design recommendations." *Water Practice and Technology* 6(3). DOI: 10.2166/wpt.2011.046.
- Morvannou, A., N. Forquet, S. Michel, S. Troesch and P. Molle (2015). "Treatment performances of French constructed wetlands: results from a database collected over the last 30 years." *Water Sci Technol* 71(9): 1333-1339. DOI: 10.2166/wst.2015.089.
- Prochaska, C. A. and A. I. Zouboulis (2006). "Removal of phosphates by pilot vertical-flow constructed wetlands using a mixture of sand and dolomite as substrate." *Ecological Engineering* 26(3): 293-303. DOI: 10.1016/j.ecoleng.2005.10.009.
- Quintana, M., M. F. Colmenarejo, J. Barrera, E. Sánchez, G. García, L. Travieso and R. Borja (2008). "Removal of phosphorus through struvite precipitation using a by-product of magnesium oxide production (BMP): Effect of the mode of BMP preparation." *Chemical Engineering Journal* 136(2-3): 204-209. DOI: 10.1016/j.cej.2007.04.002.
- Reijnders, L. (2014). "Phosphorus resources, their depletion and conservation, a review." *Resources, Conservation and Recycling* 93: 32-49. DOI: 10.1016/j.resconrec.2014.09.006.
- Roy, E. D. (2017). "Phosphorus recovery and recycling with ecological engineering: A review." *Ecological Engineering* 98: 213-227. DOI: 10.1016/j.ecoleng.2016.10.076.
- Scholz, R. W. (2019). Foreword: Phosphorus Recycling — Mending a Broken Biogeochemical Cycle. P. R. a. Recycling, Springer Nature Singapore Pte Ltd.
- Schoumans, O. F., F. Bouraoui, C. Kabbe, O. Oenema and K. C. van Dijk (2015). "Phosphorus management in Europe in a changing world." *Ambio* 44 Suppl 2: S180-192. DOI: 10.1007/s13280-014-0613-9.

- Science Communication Unit UWE, U. o. t. W. o. E. U., Bristol (2013). Sustainable Phosphorus Use. Science for Environment Policy Indepth Report:, European Commission.
- Senthilkumar, K., A. Mollier, M. Delmas, S. Pellerin and T. Nesme (2014). "Phosphorus recovery and recycling from waste: An appraisal based on a French case study." *Resources, Conservation and Recycling* 87: 97-108. DOI: 10.1016/j.resconrec.2014.03.005.
- Shepherd, J. G., S. P. Sohi and K. V. Heal (2016). "Optimising the recovery and re-use of phosphorus from wastewater effluent for sustainable fertiliser development." *Water Res* 94: 155-165. DOI: 10.1016/j.watres.2016.02.038.
- Spivakov, B. Y., T. A. Maryutina and H. Muntau (1999). "Phosphorus Speciation in Water and Sediments." *Pure and Applied Chemistry* 71(11): 2161-2176. DOI: 10.1351/pac199971112161.
- Stricker, A. E. and A. Héduit (2010). "Phosphore des eaux usées - Etat des lieux et perspectives."
- Troesch, S., D. Esser and P. Molle (2016). "Natural Rock Phosphate: A Sustainable Solution for Phosphorous Removal from Wastewater." *Procedia Engineering* 138: 119-126. DOI: 10.1016/j.proeng.2016.02.069.
- U.S.G.S (2020). Mineral commodity summaries, U.S Geological Survey.
- van Puijenbroek, P., A. H. W. Beusen and A. F. Bouwman (2019). "Global nitrogen and phosphorus in urban waste water based on the Shared Socio-economic pathways." *J Environ Manage* 231: 446-456. DOI: 10.1016/j.jenvman.2018.10.048.
- Venkiteshwaran, K., P. J. McNamara and B. K. Mayer (2018). "Meta-analysis of non-reactive phosphorus in water, wastewater, and sludge, and strategies to convert it for enhanced phosphorus removal and recovery." *Sci Total Environ* 644: 661-674. DOI: 10.1016/j.scitotenv.2018.06.369.
- Vohla, C., M. Kõiv, H. J. Bavor, F. Chazarenc and Ü. Mander (2011). "Filter materials for phosphorus removal from wastewater in treatment wetlands—A review." *Ecological Engineering* 37(1): 70-89. DOI: 10.1016/j.ecoleng.2009.08.003.
- Wang, Y., Z. Cai, S. Sheng, F. Pan, F. Chen and J. Fu (2020). "Comprehensive evaluation of substrate materials for contaminants removal in constructed wetlands." *Sci Total Environ* 701: 134736. DOI: 10.1016/j.scitotenv.2019.134736.

- Wilfert, P., P. S. Kumar, L. Korving, G. J. Witkamp and M. C. van Loosdrecht (2015). "The Relevance of Phosphorus and Iron Chemistry to the Recovery of Phosphorus from Wastewater: A Review." *Environ Sci Technol* 49(16): 9400-9414. DOI: 10.1021/acs.est.5b00150.
- Xu, S., X. Chen and J. Zhuang (2019). "Opposite influences of mineral-associated and dissolved organic matter on the transport of hydroxyapatite nanoparticles through soil and aggregates." *Environ Res* 171: 153-160. DOI: 10.1016/j.envres.2019.01.020.
- Yang, Y., Y. Zhao, R. Liu and D. Morgan (2018). "Global development of various emerged substrates utilized in constructed wetlands." *Bioresour Technol* 261: 441-452. DOI: 10.1016/j.biortech.2018.03.085.
- Ye, Y., H. H. Ngo, W. Guo, Y. Liu, J. Li, Y. Liu, X. Zhang and H. Jia (2017). "Insight into chemical phosphate recovery from municipal wastewater." *Sci Total Environ* 576: 159-171. DOI: 10.1016/j.scitotenv.2016.10.078.
- Yuan, Z., S. Pratt and D. J. Batstone (2012). "Phosphorus recovery from wastewater through microbial processes." *Curr Opin Biotechnol* 23(6): 878-883. DOI: 10.1016/j.copbio.2012.08.001.
- Zhang, W., P. Gago-Ferrero, Q. Gao, L. Ahrens, K. Blum, A. Rostvall, B. Bjorlenius, P. L. Andersson, K. Wiberg, P. Haglund and G. Renman (2019). "Evaluation of five filter media in column experiment on the removal of selected organic micropollutants and phosphorus from household wastewater." *J Environ Manage* 246: 920-928. DOI: 10.1016/j.jenvman.2019.05.137.
- Zhu, Y., X. Zhang, Y. Chen, Q. Xie, J. Lan, M. Qian and N. He (2009). "A comparative study on the dissolution and solubility of hydroxylapatite and fluorapatite at 25°C and 45°C." *Chemical Geology* 268(1-2): 89-96. DOI: 10.1016/j.chemgeo.2009.07.014.

## **Chapter 2**

- Agrawal, S. G. and A. H. J. Paterson (2015). "Secondary Nucleation: Mechanisms and Models." *Chemical Engineering Communications* 202(5): 698-706. DOI: 10.1080/00986445.2014.969369.
- Anderson, M. A. and A. J. Rubin (1981). *Adsorption of inorganics at solid-liquid interfaces*, Ann Arbor Science.

- Attia , Y. A. and D. W. Fuerstenau (1988). "The Equilibrium Composition of Hydroxyapatite and Fluorapatite-Water Interfaces." *Colloids and Surfaces* 34: 271-285.
- Baillon, F., F. Espitalier, C. Cogné, R. Peczalski and O. Louisnard (2015). Crystallization and freezing processes assisted by power ultrasound. *Power Ultrasonics*: 845-874.
- Barca, C., S. Troesch, D. Meyer, P. Drissen, Y. Andres and F. Chazarenc (2013). "Steel slag filters to upgrade phosphorus removal in constructed wetlands: two years of field experiments." *Environ Sci Technol* 47(1): 549-556. DOI: 10.1021/es303778t.
- Barone, J. P. and G. H. Nancollas (1977). "The seeded growth of calcium phosphates. The effect of solid/solution ratio in controlling the nature of the growth phase." *Journal of Colloid And Interface Science* 62(3): 421-431. DOI: 10.1016/0021-9797(77)90093-5.
- Bellier, N., F. Chazarenc and Y. Comeau (2006). "Phosphorus removal from wastewater by mineral apatite." *Water Res* 40(15): 2965-2971. DOI: 10.1016/j.watres.2006.05.016.
- Bengtsson, Å. (2007). Solubility and surface complexation studies of apatites, Umeå University,.
- Blanco, I., P. Molle, L. E. Saenz de Miera and G. Ansola (2016). "Basic Oxygen Furnace steel slag aggregates for phosphorus treatment. Evaluation of its potential use as a substrate in constructed wetlands." *Water Research* 89: 355-365. DOI: 10.1016/j.watres.2015.11.064.
- Botsaris, G. D. (1976). Secondary nucleation - A review. *Industrial Crystallization*. J. W. Mullin (ed.), Plenum Press.
- Castro, F., A. Ferreira, F. Rocha, A. Vicente and J. António Teixeira (2012). "Characterization of intermediate stages in the precipitation of hydroxyapatite at 37°C." *Chemical Engineering Science* 77: 150-156. DOI: 10.1016/j.ces.2012.01.058.
- Chow, L. C. (2001). "Solubility of Calcium Phosphate." *Monogr Oral Sci. Base* 18(Octacalcium phosphate): 94-111.
- Chung, S.-Y., Y.-M. Kim, J.-G. Kim and Y.-J. Kim (2008). "Multiphase transformation and Ostwald's rule of stages during crystallization of a metal phosphate." *Nature Physics* 5(1): 68-73. DOI: 10.1038/nphys1148.

- Claveau-Mallet, D., B. Courcelles, P. Pasquier and Y. Comeau (2017). "Numerical simulations with the P-Hydroslag model to predict phosphorus removal by steel slag filters." *Water Res* 126: 421-432. DOI: 10.1016/j.watres.2017.09.032.
- Dean, J. A. (1956). *Lange's handbook of chemistry*.
- Dorozhkin, S. V. (2010). "Amorphous calcium (ortho)phosphates." *Acta Biomater* 6(12): 4457-4475. DOI: 10.1016/j.actbio.2010.06.031.
- Elliott, R. (1988). *Solidification of cast irons*. Cast Iron Technology, Butterworth Heinemann: 91-125.
- Ertl, G. (2009). *Reactions at solid surfaces*, John Wiley and Sons Inc. Publication.
- Fowler, B. O. and S. Kuroda (1986). "Changes in Heated and in Laser-Irradiated Human Tooth Enamel and Their Probable Effects on Solubility." *Calcified Tissue International* 38: 197-208.
- Francis, M. D. (1969). "The Inhibition of Calcium Hydroxyapatite Crystal Growth by Polyphosphonates and Polyphosphates." *Calc. Tiss. Res.* 3: 151-162.
- Fritz, B. and C. Noguera (2009). "Mineral Precipitation Kinetics." *Reviews in Mineralogy and Geochemistry* 70(1): 371-410. DOI: 10.2138/rmg.2009.70.8.
- Gebrehiwet, T., L. Guo, D. Fox, H. Huang, Y. Fujita, R. Smith, J. Henriksen and G. Redden (2014). "Precipitation of calcium carbonate and calcium phosphate under diffusion controlled mixing." *Applied Geochemistry* 46: 43-56. DOI: 10.1016/j.apgeochem.2014.04.005.
- Godelitsas, A. and J. M. Astilleros (2011). *Dissolution, sorption/(re)precipitation, formation of solid solutions and crystal growth phenomena on mineral surfaces. Ion Partitioning in Ambient-Temperature Aqueous Systems*: 289-324.
- Han, C., Z. Wang, Q. Wu, W. Yang, H. Yang and X. Xue (2016). "Evaluation of the role of inherent Ca(2+) in phosphorus removal from wastewater system." *Water Sci Technol* 73(7): 1644-1651. DOI: 10.2166/wst.2015.642.
- Hermassi, M., C. Valderrama, J. Dosta, J. L. Cortina and N. H. Batis (2015). "Evaluation of hydroxyapatite crystallization in a batch reactor for the valorization of alkaline phosphate concentrates from wastewater treatment plants using calcium chloride." *Chemical Engineering Journal* 267: 142-152. DOI: 10.1016/j.cej.2014.12.079.
- Hlabse, T. and G. Walton (1965). "The nucleation of calcium phosphate from solution." *Analitica Chimica Acta* 33: 373-377.

- Joko, I. (1984). "phosphorus removal from wastewater by the crystallization method." *Wat. Sci. Tech.* 17: 121-132.
- Kallay, N., T. Preočanin, D. Kovačević, J. Lützenkirchen and M. Villalobos (2011). "Thermodynamics of the Reactions at Solid/Liquid Interfaces." *Croatica Chemica Acta*: 1-10. DOI: 10.5562/cca1864.
- Kamano, Y., K. Kadota, A. Shimosaka, Y. Shirakawa and J. Hidaka (2014). "Quantitative evaluation on the heterogeneous nucleation of amino acid by a thermodynamic analysis." *Journal of Molecular Liquids* 200: 474-479. DOI: 10.1016/j.molliq.2014.11.021.
- Karapinar, N., E. Hoffmann and H. H. Hahn (2006). "P-recovery by secondary nucleation and growth of calcium phosphates on magnetite mineral." *Water Res* 40(6): 1210-1216. DOI: 10.1016/j.watres.2005.12.041.
- Kellogg, R. M. and M. Leeman (2012). 9.16 Crystallization as a Tool in Industrial Applications of Asymmetric Synthesis. *Comprehensive Chirality*: 367-399.
- Lafon, J. P., E. Champion, D. Bernache-Assollant, R. Gibert and A. M. Danna (2003). "Thermal decomposition of carbonated calcium phosphate apatites." *Journal of Thermal Analysis and Calorimetry* 72(3): 1127-1134. DOI: 10.1023/a:1025036214044.
- Li, Z., X. Sun, L. Huang, D. Liu, L. Yu, H. Wu and D. Wei (2017). "Phosphate adsorption and precipitation on calcite under calco-carbonic equilibrium condition." *Chemosphere* 183: 419-428. DOI: 10.1016/j.chemosphere.2017.05.139.
- Liu, H. and S. D. Dandy (1995). *Theoretical and Modeling Studies on Diamond Nucleation. Diamond Chemical Vapor Deposition*

#### Nucleation and Early Growth Stages

- William Andrew Applied Science Publishers: 143-159.
- Liu, Y. C. (2001). "Generic mechanism of heterogeneous nucleation and molecular interfacial effects." *Advances in Crystal Growth Research*: 42-61.
- Mañas, A., M. Pocquet, B. Biscans and M. Sperandio (2012). "Parameters influencing calcium phosphate precipitation in granular sludge sequencing batch reactor." *Chemical Engineering Science* 77: 165-175. DOI: 10.1016/j.ces.2012.01.009.
- Mbamba, C. K., D. J. Batstone, X. Flores-Alsina and S. Tait (2015). "A generalised chemical precipitation modelling approach in wastewater treatment applied to calcite." *Water Res* 68: 342-353. DOI: 10.1016/j.watres.2014.10.011.

- McDowell, H., W. E. Brown and J. Sutter (1971). "Solubility Study of Calcium Hydrogen Phosphate. Ion-Pair Formation 111." *Inorganic Chemistry* 10(8): 1638-1643.
- Meyer, J. L. and E. D. Eanes (1978). "A Thermodynamic Analysis of the Amorphous to Crystalline Calcium Phosphate Transformation." *Calcif. Tiss. Res.* 25,: 59-68.
- Molle, A. Liénard, A. Grasmick, A. Iwema and A. Kabbabi (2005). "Apatite as an interesting seed to remove phosphorus from wastewater in constructed wetlands." *Water Science & Technology* 51(9): 193-203.
- Montastruc, L., C. Azzaro-Pantel, B. Biscans, M. Cabassud and S. Domenech (2003). "A thermochemical approach for calcium phosphate precipitation modeling in a pellet reactor." *Chemical Engineering Journal* 94(1): 41-50. DOI: 10.1016/s1385-8947(03)00044-5.
- Moreno, E. C., M. Kresak and R. T. Zahradnik (1977). "Physico chemical aspects of fluoride-apatite systems relevant to the study of dental caries." *Caries Res.* 11: 142-171.
- Nancollas, G. H. and M. S. Mohan (1970). "The growth of hydroxyapatite crystals." *Archs oral Biol.* 15: 731-745.
- Ohlinger, Young and Schroeder (1999). "kinetics effects on preferential struvite accumulation in wastewater." *Journal of Environmental engineering* 125(8): 730-737.
- Ostwald, W. Z. (1897). " Studien über die Bildung und Umwandlung fester Körper." *Phys. Chem.* 22: 289-330.
- Panfili, F. (2004). Etude de l'évolution de la spéciation du zinc dans la phase solide d'un sédiment de curage contaminé, induit par phytostabilisation, Université de Provence - Aix-Marseille I.
- Patel, P. R., T. M. Gregory and W. E. Brown (1974). "Solubility of CaHP04 · 2H20 in the Quaternary Ca(OHh - H3P04 - NaCl - H20 at 25°C \*." *URNAL OF RESEARCH of the National Bureau of Standards - A. Physics and Chemistry* Vol. 78A(No.6,).
- Peng, L., H. Dai, Y. Wu, Y. Peng and X. Lu (2018). "A comprehensive review of phosphorus recovery from wastewater by crystallization processes." *Chemosphere* 197: 768-781. DOI: 10.1016/j.chemosphere.2018.01.098.
- Prieto, M., A. FernandezGonzalez, A. Putnis and L. FernandezDiaz (1997). "Nucleation, growth, and zoning phenomena in crystallizing (Ba,Sr)CO3, Ba(SO4,CrO4), (Ba,Sr)SO4, and (Cd,Ca)CO3 solid solutions from aqueous

- solutions." *Geochimica Et Cosmochimica Acta* 61(16): 3383-3397. DOI: 10.1016/s0016-7037(97)00160-9.
- Prieto, M., F. Heberling, R. M. Rodríguez-Galán and F. Brandt (2016). "Crystallization behavior of solid solutions from aqueous solutions: An environmental perspective." *Progress in Crystal Growth and Characterization of Materials* 62(3): 29-68. DOI: 10.1016/j.pcrysgrow.2016.05.001.
- Richardson, J. F., J. H. Harker and J. R. Backhurst (2002). *Crystallisation*. Chemical Engineering: 827-900.
- Seckler, M. M. (1994.). *Calcium phosphate precipitation in a fluidized bed*, Technische Universiteit.
- Song, Y., H. H. Hahn and E. Hoffmann (2002). "The effect of carbonate on the precipitation of calcium phosphate." *Environ Technol* 23(2): 207-215. DOI: 10.1080/09593332508618427.
- Song, Y., H. H. Hahn and E. Hoffmann (2002). "Effects of solution conditions on the precipitation of phosphate for recovery." *Chemosphere* 48(10): 1029-1034. DOI: 10.1016/s0045-6535(02)00183-2.
- Sparks, D. L. (2003). *Sorption Phenomena on Soils*. Environmental Soil Chemistry E. Inc.
- Sposito, G., P. E. E. G. Sposito and O. U. Press (1989). *The Chemistry of Soils*, Oxford University Press.
- Tung, M. S., N. Eidelman, B. Sieck and W. E. Brown (1988). "Octacalcium Phosphate Solubility Product from 4 to 37-Degree-C." *Journal of Research of the National Bureau of Standards* 93(5). DOI: 10.6028/jres.093.153.
- Zhu, Y., X. Zhang, Y. Chen, Q. Xie, J. Lan, M. Qian and N. He (2009). "A comparative study on the dissolution and solubility of hydroxylapatite and fluorapatite at 25°C and 45°C." *Chemical Geology* 268(1-2): 89-96. DOI: 10.1016/j.chemgeo.2009.07.014.
- Zoltek, J. J. (1976). "Identification of Orthophosphate Solids Formed by Lime Precipitation." *Water Pollution Control Federation* 48(1): 179-182.

### **Chapter 3**

- Bellier, N., F. Chazarenc and Y. Comeau (2006). "Phosphorus removal from wastewater by mineral apatite." *Water Res* 40(15): 2965-2971. DOI: 10.1016/j.watres.2006.05.016.
- Blandin, A. F. (2013). Matériau granulaire à base de phosphate, son procédé de fabrication et son utilisation dans un dispositif de déphosphatation des eaux usées (Phosphate based granular material, process for manufacturing same and use thereof in a device for removing phosphates from wastewater). O. M. d. I. P. Intellectuelle, Compagnie financière et de participations Roullier.
- Bunaciu, A. A., E. G. Udristioiu and H. Y. Aboul-Enein (2015). "X-ray diffraction: instrumentation and applications." *Crit Rev Anal Chem* 45(4): 289-299. DOI: 10.1080/10408347.2014.949616.
- Croarkin, C. and P. Tobias (2013). NIST/SEMATECH e-Handbook of Statistical Method NIST U.S. Department of Commerce. .
- Harouiya, N., S. Prost-Boucle, C. Morlay, D. Esser, S. Martin-Ruel and P. Molle (2011). "Performance evaluation of phosphorus removal by apatite in constructed wetlands treating domestic wastewater: column and pilot experiments." *International Journal of Environmental Analytical Chemistry* 91: 740-752.
- Kadlec, R. H. and S. D. Wallace (2009). *Treatment wetlands*. Boca Raton, FL, CRC Press.
- Klute, A. (1986). *Methods of Soil Analysis: Part 1—Physical and Mineralogical Methods*. Madison, WI, Soil Science Society of America, American Society of Agronomy.
- Levenspiel, O. (2012). The Tanks-in-Series Model. *Tracer Technology*. 96: 81-97.
- Metcalf and Eddy (2003). *Wastewater Engineering Treatment and Reuse*, Mc Graw Hill.
- Molle, P., S. Martin, D. Esser, S. Besnault, C. Morlay and N. Harouiya (2011). "Phosphorus removal by the use of apatite in constructed wetlands: Design recommendations." *Water Practice and Technology* 6(3). DOI: 10.2166/wpt.2011.046.
- Patel, J. P. and P. H. Parsania (2018). Characterization, testing, and reinforcing materials of biodegradable composites. *Biodegradable and Biocompatible Polymer Composites*: 55-79.

Persson J., Somes N.G.L and Wong T.H.F. (1999). "Hydraulics efficiency of constructed wetlands and ponds." *Water Science and Technology* 40: 291-300.

Shackelford, C. D. (2013). *Geoenvironmental Engineering*. Reference Module in Earth Systems and Environmental Sciences.

Zhou, W., R. P. Apkarian, Z. L. Wang and D. Joy (2006). *Fundamentals of Scanning Electron Microscopy (SEM)*. *Scanning Microscopy for Nanotechnology*. W. Zhou and Z. L. Wang. New York, Springer: 1-40.

## **Chapter 4.2.**

Blandin, A. F. (2013). Matériau granulaire à base de phosphate, son procédé de fabrication et son utilisation dans un dispositif de déphosphatation des eaux usées (Phosphate based granular material, process for manufacturing same and use thereof in a device for removing phosphates from wastewater). O. M. d. I. P. Intellectuelle, Compagnie financière et de participations Roullier.

Bohart, G. S. and E. Q. Adams (1920). "Some aspects of the behavior of charcoal with respect to chlorine." *J. Am. Chem. Soc.* 42 523–544. DOI: doi.org/10.1016/S0016-0032(20)90400-3.

Chu, K. H. (2010). "Fixed bed sorption: Setting the record straight on the Bohart–Adams and Thomas models." *Journal of Hazardous Materials* 177: 1006–1012. DOI: 10.1016/j.jhazmat.2010.01.019.

Delgado-González, L., B. Lartiges, M. Gautier, S. Troesch and P. Molle (2021). "Phosphorous Retention by Granulated Apatite: Assessing Maximum Retention Capacity, Kinetics and retention processes." *Water Sci. Technol*(in press). DOI: doi: 10.2166/wst.2021.010.

Ebelegi, A. N., N. Ayawei and D. Wankasi (2020). "Interpretation of Adsorption Thermodynamics and Kinetics." *Open Journal of Physical Chemistry* 10(03): 166-182. DOI: 10.4236/ojpc.2020.103010.

Foo, K. Y. and B. H. Hameed (2010). "Insights into the modeling of adsorption isotherm systems." *Chemical Engineering Journal* 156(1): 2-10. DOI: 10.1016/j.cej.2009.09.013.

- Gajewska, M. H., M. J. Marcinkowski and H. Obarska-Pempkowiak (2013). *Environmental Engineering IV*, CRC Press.
- Harouiya, N., S. Martin Rue, S. Prost-Boucle, A. Liénar, D. Esser and P. Molle (2011). "Phosphorus removal by apatite in horizontal flow constructed wetlands for small communities: pilot and full-scale evidence." *Water Science and Technology* 63(8): 1629-1637. DOI: 10.2166/wst.2011.250.
- Harouiya, N., S. Prost-Boucle, C. Morlay, D. Esser, S. Martin-Ruel and P. Molle (2011). "Performance evaluation of phosphorus removal by apatite in constructed wetlands treating domestic wastewater: column and pilot experiments." *International Journal of Environmental Analytical Chemistry* 91: 740-752.
- Hu, Q., Y. Xie and Z. Zhang (2020). "Modification of breakthrough models in a continuous-flow fixed-bed column: Mathematical characteristics of breakthrough curves and rate profiles." *Separation and Purification Technology* 238. DOI: 10.1016/j.seppur.2019.116399.
- Kadlec, R. H. and S. D. Wallace (2009). *Treatment wetlands*. Boca Raton, FL, CRC Press.
- Klute, A. (1986). *Methods of Soil Analysis: Part 1—Physical and Mineralogical Methods*. Madison, WI, Soil Science Society of America, American Society of Agronomy.
- Kowacz, M., M. Prieto and A. Putnis (2010). "Kinetics of crystal nucleation in ionic solutions: Electrostatics and hydration forces." *Geochimica et Cosmochimica Acta* 74(2): 469-481. DOI: 10.1016/j.gca.2009.10.028.
- Lee, C.-G., J.-H. Kim, J.-K. Kang, S.-B. Kim, S.-J. Park, S.-H. Lee and J.-W. Choi (2014). "Comparative analysis of fixed-bed sorption models using phosphate breakthrough curves in slag filter media." *Desalination and Water Treatment* 55(7): 1795-1805. DOI: 10.1080/19443994.2014.930698.
- Martinez-Carvajal, G. D., L. Oxarango, J. Adrien, P. Molle and N. Forquet (2019). "Assessment of X-ray Computed Tomography to characterize filtering media from Vertical Flow Treatment Wetlands at the pore scale." *Sci Total Environ* 658: 178-188. DOI: 10.1016/j.scitotenv.2018.12.119.

- Molle, A. Liénard, A. Grasmick, A. Iwema and A. Kabbabi (2005). "Apatite as an interesting seed to remove phosphorus from wastewater in constructed wetlands." *Water Science & Technology* 51(9): 193-203.
- Molle, P., S. Martin, D. Esser, S. Besnault, C. Morlay and N. Harouiya (2011). "Phosphorus removal by the use of apatite in constructed wetlands: Design recommendations." *Water Practice and Technology* 6(3). DOI: 10.2166/wpt.2011.046.
- Parkhurst, D. L. and C. A. J. Appelo (2013). *Description of Input and Examples for PHREEQC Version 3—A Computer Program for Speciation, Batch-Reaction, One-Dimensional Transport, and Inverse Geochemical Calculations*, U.S. Geological Survey. U.S. Geological Survey Techniques and Methods: 497.
- Patel, H. (2019). "Fixed-bed column adsorption study: a comprehensive review." *Applied Water Science* 9(3). DOI: 10.1007/s13201-019-0927-7.
- Song, Y., H. H. Hahn and E. Hoffmann (2002). "The effect of carbonate on the precipitation of calcium phosphate." *Environ Technol* 23(2): 207-215. DOI: 10.1080/09593332508618427.
- Troesch, S., D. Esser and P. Molle (2016). "Natural Rock Phosphate: A Sustainable Solution for Phosphorous Removal from Wastewater." *Procedia Engineering* 138: 119-126. DOI: 10.1016/j.proeng.2016.02.069.
- Vohla, C., M. Kõiv, H. J. Bavor, F. Chazarenc and Ü. Mander (2011). "Filter materials for phosphorus removal from wastewater in treatment wetlands—A review." *Ecological Engineering* 37(1): 70-89. DOI: 10.1016/j.ecoleng.2009.08.003.
- Yan, G., T. Viraraghavan and M. Chen (2001). "A New Model for Heavy Metal Removal in a Biosorption Column." *Adsorption Science & Technology* 19(1): 25-43.
- Yang, Y., Y. Zhao, R. Liu and D. Morgan (2018). "Global development of various emerged substrates utilized in constructed wetlands." *Bioresour Technol* 261: 441-452. DOI: 10.1016/j.biortech.2018.03.085.

### **Chapter 4.3.**

- Anderson, M. A. and A. J. Rubin (1981). Adsorption of inorganics at solid-liquid interfaces, Ann Arbor Science.
- Barone, J. P. and G. H. Nancollas (1977). "The seeded growth of calcium phosphates. The effect of solid/solution ratio in controlling the nature of the growth phase." *Journal of Colloid And Interface Science* 62(3): 421-431. DOI: 10.1016/0021-9797(77)90093-5.
- Bellier, N., F. Chazarenc and Y. Comeau (2006). "Phosphorus removal from wastewater by mineral apatite." *Water Res* 40(15): 2965-2971. DOI: 10.1016/j.watres.2006.05.016.
- Blanco, I., P. Molle, L. E. Saenz de Miera and G. Ansola (2016). "Basic Oxygen Furnace steel slag aggregates for phosphorus treatment. Evaluation of its potential use as a substrate in constructed wetlands." *Water Research* 89: 355-365. DOI: 10.1016/j.watres.2015.11.064.
- Blandin, A. F. (2013). *Matériau granulaire à base de phosphate, son procédé de fabrication et son utilisation dans un dispositif de déphosphatation des eaux usées (Phosphate based granular material, process for manufacturing same and use thereof in a device for removing phosphates from wastewater)*. O. M. d. I. P. Intellectuelle, Compagnie financière et de participations Roullier.
- Bouwman, A. F., G. Van Drecht, J. M. Knoop, A. H. W. Beusen and C. R. Meinardi (2005). "Exploring changes in river nitrogen export to the world's oceans." *Global Biogeochemical Cycles* 19(1). DOI: 10.1029/2004gb002314.
- Claveau-Mallet, D., B. Courcelles, P. Pasquier and Y. Comeau (2017). "Numerical simulations with the P-Hydroslag model to predict phosphorus removal by steel slag filters." *Water Res* 126: 421-432. DOI: 10.1016/j.watres.2017.09.032.
- Drizo, A., C. A. Frost, J. Grace and K. A. Smith (1999). "Physico-chemical screening of phosphate removing substrates for use in constructed wetland systems." *Water Research* 33(17): 3595.

- Han, C., Z. Wang, Q. Wu, W. Yang, H. Yang and X. Xue (2016). "Evaluation of the role of inherent Ca(2+) in phosphorus removal from wastewater system." *Water Sci Technol* 73(7): 1644-1651. DOI: 10.2166/wst.2015.642.
- Harouiya, N., S. Martin Rue, S. Prost-Boucle, A. Liénar, D. Esser and P. Molle (2011). "Phosphorus removal by apatite in horizontal flow constructed wetlands for small communities: pilot and full-scale evidence." *Water Science and Technology* 63(8): 1629-1637. DOI: 10.2166/wst.2011.250.
- Kadlec, R. H. and S. D. Wallace (2009). *Treatment wetlands*. Boca Raton, FL, CRC Press.
- Martinez-Carvajal, G. D., L. Oxarango, J. Adrien, P. Molle and N. Forquet (2019). "Assessment of X-ray Computed Tomography to characterize filtering media from Vertical Flow Treatment Wetlands at the pore scale." *Sci Total Environ* 658: 178-188. DOI: 10.1016/j.scitotenv.2018.12.119.
- Molle, A. Liénard, A. Grasmick, A. Iwema and A. Kabbabi (2005). "Apatite as an interesting seed to remove phosphorus from wastewater in constructed wetlands." *Water Science & Technology* 51(9): 193-203.
- Molle, Martin, Esser, Besnault, Morlay and Harouiya (2011). "Phosphorus removal by the use of apatite in constructed wetlands: Design recommendations." *Water Practice and Technology* 6(3). DOI: 10.2166/wpt.2011.046.
- Montastruc, L., C. Azzaro-Pantel, B. Biscans, M. Cabassud and S. Domenech (2003). "A thermochemical approach for calcium phosphate precipitation modeling in a pellet reactor." *Chemical Engineering Journal* 94(1): 41-50. DOI: 10.1016/s1385-8947(03)00044-5.
- Parkhurst, D. L. and C. A. J. Appelo (2013). *Description of Input and Examples for PHREEQC Version 3—A Computer Program for Speciation, Batch-Reaction, One-Dimensional Transport, and Inverse Geochemical Calculations*, U.S. Geological Survey. U.S. Geological Survey Techniques and Methods: 497.
- Peng, L., H. Dai, Y. Wu, Y. Peng and X. Lu (2018). "A comprehensive review of phosphorus recovery from wastewater by crystallization processes." *Chemosphere* 197: 768-781. DOI: 10.1016/j.chemosphere.2018.01.098.

- Prieto, M., F. Heberling, R. M. Rodríguez-Galán and F. Brandt (2016). "Crystallization behavior of solid solutions from aqueous solutions: An environmental perspective." *Progress in Crystal Growth and Characterization of Materials* 62(3): 29-68. DOI: 10.1016/j.pcrysgrow.2016.05.001.
- Prochaska, C. A. and A. I. Zouboulis (2006). "Removal of phosphates by pilot vertical-flow constructed wetlands using a mixture of sand and dolomite as substrate." *Ecological Engineering* 26(3): 293-303. DOI: 10.1016/j.ecoleng.2005.10.009.
- Song, Y., H. H. Hahn and E. Hoffmann (2002). "The effect of carbonate on the precipitation of calcium phosphate." *Environ Technol* 23(2): 207-215. DOI: 10.1080/09593332508618427.
- Song, Y., H. H. Hahn and E. Hoffmann (2002). "Effects of solution conditions on the precipitation of phosphate for recovery." *Chemosphere* 48(10): 1029-1034. DOI: 10.1016/s0045-6535(02)00183-2.
- van Puijenbroek, P., A. H. W. Beusen and A. F. Bouwman (2019). "Global nitrogen and phosphorus in urban waste water based on the Shared Socio-economic pathways." *J Environ Manage* 231: 446-456. DOI: 10.1016/j.jenvman.2018.10.048.
- Van Santen, R. A. (1984). "The Ostwald step rule." *The Journal of Physical Chemistry* 88(24): 5768-5769. DOI: 10.1021/j150668a002.
- Vohla, C., M. Kõiv, H. J. Bavor, F. Chazarenc and Ü. Mander (2011). "Filter materials for phosphorus removal from wastewater in treatment wetlands—A review." *Ecological Engineering* 37(1): 70-89. DOI: 10.1016/j.ecoleng.2009.08.003.
- Wang, Z., J. Dong, L. Liu, G. Zhu and C. Liu (2013). "Screening of phosphate-removing substrates for use in constructed wetlands treating swine wastewater." *Ecological Engineering* 54: 57-65. DOI: 10.1016/j.ecoleng.2013.01.017.
- Yang, Y., Y. Zhao, R. Liu and D. Morgan (2018). "Global development of various emerged substrates utilized in constructed wetlands." *Bioresour Technol* 261: 441-452. DOI: 10.1016/j.biortech.2018.03.085.

## Chapter 5.2.

- Ádám, K., T. Krogstad, L. Vråle, A. K. Søvik and P. D. Jenssen (2007). "Phosphorus retention in the filter materials shellsand and Filtralite P®—Batch and column experiment with synthetic P solution and secondary wastewater." *Ecological Engineering* 29(2): 200-208. DOI: 10.1016/j.ecoleng.2006.09.021.
- Anthony, J. W., R. A. Bideaux, K. W. Bladh and M. C. Nichols (1995). *Handbook of Mineralogy. II (Silica, Silicates)*. Chantilly, VA, USA, Mineralogical Society of America.
- Barca, C., D. Meyer, M. Liira, P. Drissen, Y. Comeau, Y. Andrès and F. Chazarenc (2014). "Steel slag filters to upgrade phosphorus removal in small wastewater treatment plants: Removal mechanisms and performance." *Ecological Engineering* 68: 214-222. DOI: 10.1016/j.ecoleng.2014.03.065.
- Bellier, N., F. Chazarenc and Y. Comeau (2006). "Phosphorus removal from wastewater by mineral apatite." *Water Res* 40(15): 2965-2971. DOI: 10.1016/j.watres.2006.05.016.
- Castro, F., A. Ferreira, F. Rocha, A. Vicente and J. António Teixeira (2012). "Characterization of intermediate stages in the precipitation of hydroxyapatite at 37°C." *Chemical Engineering Science* 77: 150-156. DOI: 10.1016/j.ces.2012.01.058.
- Chung, S.-Y., Y.-M. Kim, J.-G. Kim and Y.-J. Kim (2008). "Multiphase transformation and Ostwald's rule of stages during crystallization of a metal phosphate." *Nature Physics* 5(1): 68-73. DOI: 10.1038/nphys1148.
- Dorozhkin, S. V. (2010). "Amorphous calcium (ortho)phosphates." *Acta Biomater* 6(12): 4457-4475. DOI: 10.1016/j.actbio.2010.06.031.
- Harouiya, N., S. Martin Rue, S. Prost-Boucle, A. Liénar, D. Esser and P. Molle (2011). "Phosphorus removal by apatite in horizontal flow constructed wetlands for small communities: pilot and full-scale evidence." *Water Science and Technology* 63(8): 1629-1637. DOI: 10.2166/wst.2011.250.
- Harouiya, N., S. Prost-Boucle, C. Morlay, D. Esser, S. Martin-Ruel and P. Molle (2011). "Performance evaluation of phosphorus removal by apatite in constructed

- wetlands treating domestic wastewater: column and pilot experiments." *International Journal of Environmental Analytical Chemistry* 91: 740-752.
- Hermassi, M., C. Valderrama, J. Dosta, J. L. Cortina and N. H. Batis (2015). "Evaluation of hydroxyapatite crystallization in a batch reactor for the valorization of alkaline phosphate concentrates from wastewater treatment plants using calcium chloride." *Chemical Engineering Journal* 267: 142-152. DOI: 10.1016/j.cej.2014.12.079.
- Jang, H. and S.-H. Kang (2002). "Phosphorus removal using cow bone in hydroxyapatite crystallization." *Water Research* 36 1324–1330. DOI: doi.org/10.1016/S0043-1354(01)00329-3.
- Joko, I. (1984). "phosphorus removal from wastewater by the crystallization method." *Wat. Sci. Tech.* 17: 121-132.
- Kadlec, R. H. and S. D. Wallace (2009). *Treatment wetlands*. Boca Raton, FL, CRC Press.
- Klute, A. (1986). *Methods of Soil Analysis: Part 1—Physical and Mineralogical Methods*. Madison, WI, Soil Science Society of America, American Society of Agronomy.
- Kõiv, M., M. Liira, Ü. Mander, R. Mõtlep, C. Vohla and K. Kirsimäe (2010). "Phosphorus removal using Ca-rich hydrated oil shale ash as filter material – The effect of different phosphorus loadings and wastewater compositions." *Water Research* 44(18): 5232-5239. DOI: 10.1016/j.watres.2010.06.044.
- Levenspiel, O. (2012). *The Tanks-in-Series Model. Tracer Technology*. 96: 81-97.
- Mañas, A., M. Pocquet, B. Biscans and M. Sperandio (2012). "Parameters influencing calcium phosphate precipitation in granular sludge sequencing batch reactor." *Chemical Engineering Science* 77: 165-175. DOI: 10.1016/j.ces.2012.01.009.
- McCabe, W. L., J. C. Smith and P. Harriott (2005). *Unit Operations of Chemical Engineering*, McGraw-Hill.
- Merriman, L., J. Hathaway, M. Burchell and W. Hunt (2017). "Adapting the Relaxed Tanks-in-Series Model for Stormwater Wetland Water Quality Performance." *Water* 9(9). DOI: 10.3390/w9090691.

- Meyer, J. L. and E. D. Eanes (1978). "A Thermodynamic Analysis of the Amorphous to Crystalline Calcium Phosphate Transformation." *Calcif. Tiss. Res.* 25,: 59-68.
- Molle, A. Liénard, A. Grasmick, A. Iwema and A. Kabbabi (2005). "Apatite as an interesting seed to remove phosphorus from wastewater in constructed wetlands." *Water Science & Technology* 51(9): 193-203.
- Molle, P., S. Martin, D. Esser, S. Besnault, C. Morlay and N. Harouiya (2011). "Phosphorus removal by the use of apatite in constructed wetlands: Design recommendations." *Water Practice and Technology* 6(3). DOI: 10.2166/wpt.2011.046.
- Nancollas, G. H. and M. S. Mohan (1970). "The growth of hydroxyapatite crystals." *Archs oral Biol.* 15: 731-745.
- Ostwald, W. Z. (1897). " Studien über die Bildung und Umwandlung fester Körper." *Phys. Chem.* 22: 289-330.
- Vohla, C., M. Kõiv, H. J. Bavor, F. Chazarenc and Ü. Mander (2011). "Filter materials for phosphorus removal from wastewater in treatment wetlands—A review." *Ecological Engineering* 37(1): 70-89. DOI: 10.1016/j.ecoleng.2009.08.003.

### **Chapter 5.3.**

- Hermassi, M., C. Valderrama, J. Dosta, J. L. Cortina and N. H. Batis (2015). "Evaluation of hydroxyapatite crystallization in a batch reactor for the valorization of alkaline phosphate concentrates from wastewater treatment plants using calcium chloride." *Chemical Engineering Journal* 267: 142-152. DOI: 10.1016/j.cej.2014.12.079.
- Herrmann, I., A. Jourak, J. P. Gustafsson, A. Hedstrom, T. S. Lundstrom and M. Viklander (2013). "Modeling phosphate transport and removal in a compact bed filled with a mineral-based sorbent for domestic wastewater treatment." *J Contam Hydrol* 154: 70-77. DOI: 10.1016/j.jconhyd.2013.08.007.
- Joko, I. (1984). "phosphorus removal from wastewater by the crystallization method." *Wat. Sci. Tech.* 17: 121-132.

- Mañas, A., M. Pocquet, B. Biscans and M. Sperandio (2012). "Parameters influencing calcium phosphate precipitation in granular sludge sequencing batch reactor." *Chemical Engineering Science* 77: 165-175. DOI: 10.1016/j.ces.2012.01.009.
- Meyer, J. L. and E. D. Eanes (1978). "A Thermodynamic Analysis of the Amorphous to Crystalline Calcium Phosphate Transformation." *Calcif. Tiss. Res.* 25,: 59-68.
- Montastruc, L., C. Azzaro-Pantel, B. Biscans, M. Cabassud and S. Domenech (2003). "A thermochemical approach for calcium phosphate precipitation modeling in a pellet reactor." *Chemical Engineering Journal* 94(1): 41-50. DOI: 10.1016/s1385-8947(03)00044-5.
- Nancollas, G. H. and M. S. Mohan (1970). "The growth of hydroxyapatite crystals." *Archs oral Biol.* 15: 731-745.
- Parkhurst, D. L. and C. A. J. Appelo ( 1999 ). User's Guide to PHREEQC (Version 2)— A Computer Program for Speciation, Batch-Reaction, One-Dimensional Transport, and Inverse Geochemical Calculations. *Water Resources Investigations Report*. Washington DC, U.S. Geological Survey, . 99-4259.
- Šimůnek, J., M. Šejna, H. Saito, M. Sakai and M. T. van Genuchten (2013). "The HYDRUS-1D Software Package for Simulating the One-Dimensional Movement of Water, Heat, and Multiple Solutes in Variably-Saturated Media."

# Communications

---

## Peer reviewed articles

---

Delgado-González L., Lartiges B., Gautier, M. Troesch S., Molle P (2021). Phosphorous Retention by Granulated Apatite: Assessing Maximum Retention Capacity, Kinetics and retention processes. *Water Science and Technology*. (in press)

Delgado-González L., Prost-Boucle S., Troesch S., Molle P (2021). Granulated apatite filters for phosphorous retention in treatment wetlands: experience from full-scale applications. *Water Science and Technology* 40 (2021) 101927 (Published article)

Delgado-González L., Lartiges B., Troesch S., Proietti A., Molle P. (2020) Seeded phosphorus retention in fixed-bed laboratory columns by apatites. (Submitted)

## Oral Communications

---

09/18

### **X Journées Techniques EPNAC, Lyon (France)**

Title : “La déphosphatation par apaties granulées Phosclean® : Retour d’expérience du projet APPROVE ”.

Delgado L., Prost-Boucle, S., Troesch, S, Molle, P.

**10/18 ICWS 2018, Valencia (Spain)**

Title: "Full scale experience of granulated apatite filters for phosphorous retention in treatment wetlands".

Delgado L., Prost-Boucle, S., Troesch, S, Molle, P.

**05/19 Journée Technique: "Valorisation des Ressources des Eaux Usées Urbaines et Industrielles » Pôle de compétitivité AXELERA.**

Title : "Le traitement et valorisation du phosphore pour les petites collectivités par filtres garnis d'apatite".

Delgado L., Molle, P.

**06/19 WETPOL 2019 Aarhus (Denmark)**

Title: "Phosphorous retention in granulated apatite: assessing capacity, kinetics and reaction mechanisms".

Delgado L., Troesch, S, Molle, P

**10/19 XI Journées Techniques EPNAC, Strasbourg (France)**

Title : " Rétention du phosphore sur matériaux spécifiques : les solutions en développement".

Delgado L., Molle, P.

## Other Communications

---

**10/17**

**S2SMALL 2017, Nantes (France)**

Poster title: "Phosphorous removal by apatite filters: lessons learned by full scale systems and a new apatite generation"

Delgado L., Prost-Boucle, S., Troesch, S, Molle, P.

**09/19**

**IWARR 2019, Venice (Italy) (*accepted*)**

Poster title: "Phosphorus recovery on apatite filters: developing a mechanistic model"

Delgado L., Troesch S., Blanc D., Gautier M., Molle, P.